SASAS 2019

CLIMATE MEETS AGRICULTURE
"THE INTERPLAY"

Peer Reviewed Conference Proceedings of the

35th Annual Conference of the South African Society for Atmospheric Sciences

Climate Meets Agriculture
– *The Interplay*

8-9 October 2019

Riverside Sun, Vanderbijlpark

SPONSORS

ARC • LNR
Excellence in Agricultural Research and Development

South African Weather Service

UN environment
United Nations Environment Programme

WATER RESEARCH COMMISSION

CAMPBELL SCIENTIFIC
WHEN MEASUREMENTS MATTER

PREFACE

It is a pleasure to welcome you to the 35th Annual Conference of the South African Society for Atmospheric Sciences (SASAS 2019) in Vanderbijlpark, Gauteng (8-9 October 2019). This conference is hosted by the Agricultural Research Council - Soil, Climate and Water (ARC-SCW) under the theme 'CLIMATE MEETS AGRICULTURE – THE INTERPLAY'. The main aim is to increase awareness on the connection between agriculture and climate. Thus, the interplay requires collaboration among researchers, government officials and farmers, not only as a vehicle to improve science but also to develop applications for food security, environmental sustainability and economic development, as well as to ensure household and community well-being.

SASAS 2019 promises to be both stimulating and informative, with a wonderful array of international keynote speakers and invited speakers. The programme covers topics on Agrometeorology; Air Quality and Aerosols; Remote Sensing Applications; Climate Change and Agriculture; Weather Forecasting and Climate Modelling; Climate Extremes – Impacts and Preparedness; Instrumentation and Data Collection; Atmospheric Wave Dynamics and aerosols, Impacts of Climate Variability and Change as well as Climate Services, Policy and Research Opportunities. Thus, delegates will have a wide range of sessions to attend at the conference. This programme also covers special invited talks discussing topical issues, as well as speed talks by students from various institutions. A total number of 100 abstracts were accepted for the conference. Each contributed abstract submitted for oral or poster presentation was edited and extended abstracts were peer reviewed.

We would like to thank the SASAS Council for allowing us to host the conference. Our sincere gratitude also goes to the organizing committee, review panel committee, and the Stanley Jackson award committee. We would also like to thank all the authors for contributing their research to the conference. Special thanks to South Africa Weather Service (SAWS), United Nations Environment Programme (UNEP), Water Research Commission (WRC) and Campbell Scientific Africa (CS Africa) for sponsoring the conference.

We wish you all a wonderful scientific experience and look forward to a fruitful conference.

Teboho Masupha and Phumzile Maluleke
SASAS Conference Co-Chairs

ISBN: 978-0-6398442-0-6

MESSAGE FROM THE PRESIDENT

Dear SASAS community,

The SASAS 2019 conference is taking place during a remarkable period in the history of climate science. Never before has climate related issues featured on the global stage as right now with actions such as the global climate strike that demands action at governmental levels to secure our sustainability on the Earth. In southern Africa our existence is closely linked with the agricultural sector, which is very vulnerable not just within a changing climate, but also from one season to the next, and even down to the daily time scale. This year, SASAS is hosted by the Agricultural Research Council – Soil, Climate and Water, with the theme of the conference, "CLIMATE MEETS AGRICULTURE – THE INTERPLAY". The common theme in the SASAS 2019 conference keynote addresses is sustainable food production and the role of the weather and climate in achieving food security. There is an increasing responsibility on the climate science community to provide a better service to all sectors, across all time scales. The annual SASAS conferences provide a platform where the climate science community can interact amongst ourselves to advance our research and to develop young scientists. Our conferences also provide opportunities to interact with other sectors in need of weather and climate information. This year, we welcome everyone from the agricultural community to join us and to share your expertise to fulfil the overarching responsibility of providing a service that can make a positive difference.

Welcome to SASAS 2019.

Christien Engelbrecht, SASAS President

COMMITTEES

EVENT ORGANISING COMMITTEE

Ms Maluleke, Phumzile	Agricultural Research Council
Ms Masupha, Teboho	Agricultural Research Council
Dr Tongwane, Mphethe	Agricultural Research Council
Prof Walker, Sue	Agricultural Research Council
Ms Laas, Adri	Agricultural Research Council
Dr Paterson, Garry	Agricultural Research Council
Ms Lombard, Christa	Agricultural Research Council
Dr Moeletsi, Mokhele	Agricultural Research Council
Mr Phahlane, Obed	Agricultural Research Council

EXTENDED ABSTRACT REVIEW PANEL MEMBERS

Dr Abiodun, Babatunde	University of Cape Town
Prof Archer, Emma	University of Pretoria
Mr Barnston, Tony	International Research Institute for Climate and Society
Dr Beraki, Asmerom	Council for Scientific and Industrial Research
Dr Botai, Joel	South African Weather Service
Dr Chikoore, Hector	University of Venda
Dr Crespo, Olivier	University of Cape Town
Mrs de Beer, Anika	University of Pretoria
Dr de Coning, Estelle	World Meteorological Organisation
Mrs de Lange, Anzel	University of Pretoria
Mr du Preez, Jean	University of Pretoria
Dr Dyson, Liesl	University of Pretoria
Dr Engelbrecht, Christien	South African Weather Service
Prof Engelbrecht, Francois	University of the Witwatersrand
Dr Feig, Gregor	South African Environmental Observation Network
Dr Garland, Rebecca	Council for Scientific and Industrial Research
Dr Johnston, Peter	University of Cape Town
Dr Kruger, Andries	South African Weather Service
Mrs Landman, Stephanie	South African Weather Service
Dr Lennard, Chris	University of Cape Town
Dr Malherbe, Johan	Council for Scientific and Industrial Research
Ms Maluleke, Phumzile	Agricultural Research Council
Mr Mkhwanazi, Musa	South African Weather Service
Dr Moeletsi, Mokhele	Agricultural Research Council
Ms Mpheshea, Lerato	Council for Scientific and Industrial Research
Mr Munghemezulu, Cilence	University of Pretoria
Mr Muthige, Mavhungu	Council for Scientific and Industrial Research
Dr Ndarana, Thando	University of Pretoria
Mr Phakule, Steven	South African Weather Service
Dr Ratnam, Venkata	Japan Agency for Marine-Earth Science and Technology
Dr Rixen, Michel	World Meteorological Organisation
Ms Serafini, Aimee	Independent
Dr Sweijd, Neville	Alliance for Collaboration on Climate and Earth Systems Science
Dr Tadross, Mark	University of Cape Town
Dr Terblanche, Deon	Consultant
Prof Venkataraman, Siva	University of KwaZulu-Natal
Ms Webster, Elizabeth	South African Weather Service
Dr Wolski, Piotr	University of Cape Town

ABSTRACTS LIST

ABSTRACTS

1. AGROMETEOROLOGY

Investigating the effect of solar radiation components on surface evaporation

P. Govender*, J.A. Ogunniyi and V. Sivakumar

School of Chemistry and Physics, University of KwaZulu-Natal, Durban, South Africa

*Corresponding author e-mail: GovenderP5@ukzn.ac.za; Tel: 031-2607661

The effect of solar radiation components on surface evaporation for successive summer and winter months were investigated over Durban, South Africa, using measurements from a pyrheliometer, pyranometer and MERRA reanalysis data during the 2014-2016 period. The results show significantly higher direct radiation during summer compared to winter which leads to increased surface evaporation. Durban generally has cloud free skies during winter, while most days in summer experience substantial cloud cover. This resulted in significant fluctuation in diffuse radiation during the summer, causing increased scattering and reflection, and which resulted in an increased evaporation rate.

Keywords: Direct normal; Diffuse; Scattering; Durban

Introduction

Solar radiation provides the fundamental requirements for plant growth i.e. heat and light. Radiation supplies the needed energy for certain metabolic processes within growing plants. It is required for various plant processes such as germination, leaf expansion, stem growth, flowering, and fruit growth and curing (Palmer, 1920; Yadav, 2016). In addition, radiation reaching the ground affects climatic conditions such as air temperature, humidity and rainfall as well as soil conditions, all which are important for agricultural purposes.

Durban (29.858º S; 31.021º E) is located on the east coast of South Africa, and experiences more than 100 sunny days annually (Govender *et al*., 2018). Within the KwaZulu-Natal province, there is a large expanse of sugar cane plantations, contributing to the production several million tons of sugar cane crops annually. The subtropical climate of province provides the ideal environment for their growth. An important factor responsible for the climate is the solar radiation, where the amount and intensity available depends on factors such as atmospheric conditions and season.

In this study, the effect of direct normal and diffuse solar radiation components on surface evaporation will be investigated. Evaporation describes the amount of water loss to the atmosphere from the Earth's surface. It is a major component in the computation of surface energy balance and in the hydrological cycle. It is therefore important to accurately determine the amount of water loss into the atmosphere for applications such as irrigation planning, water resource management among others (Syu *et al*., 2016).

Surface evaporation rate is one of the processes dependent on the amount of radiation received, and the direct normal and diffuse radiation components are major contributors to this process. Therefore, this study aims to investigate the relationship between these three variables.

Direct normal radiation is the component that is directly from the Sun's disk, and can be regarded as the amount of 'sunshine'. Diffuse radiation is the component that undergoes scattering and reflection from atmospheric components such and cloud aerosols, as well as from nearby surfaces (Govender, 2017). Through evaporation, direct and diffuse radiation has an effect on the amount of water contained in the soil (soil moisture) which is important for crop production.

Instrumentation and Method

Solar radiation and evaporation rate data for Durban, South Africa, for a period of two years during 2014-2016 were included in the analysis. For the measurement of the two solar radiation components, a pyrheliometer (200 nm to 4000 nm) and pyranometer (285 nm to 2800 nm) were used for the measurement of direct normal (*Dn*) and diffuse horizontal (*Dh*) radiation, respectively. A solar station consisting of the instruments are located at the University of KwaZulu-Natal (29.870º S; 30.976º E) on a roof platform that is 150 above sea level. A pyrheliometer measures the nearly collimated radiation within a narrow field of view, usually between 5.0º and 5.8º.

When the pyrheliometer is pointed at the Sun, only radiation within the field of view is captured by the detector. To continuously measure direct normal radiation, the pyrheliometer has to be constantly pointed at the Sun. This is achieved through the use of a solar tracker. The pyrheliometer (Model CHP1) mounted onto the Solys2 solar tracker is shown in Fig. 1. Diffuse horizontal radiation is measured using a pyranometer. A pyranometer measures radiation incident on it with the solid angle of 2π. A blackened thermopile sensor is housed in a glass domed structure, which allows transmission of radiation equally from all directions. Measurement of the diffuse radiation is achieved by using a shading device to cover the sensing element. The direct radiation is blocked out so that only the scattered and reflected radiation may be received. The pyranometer (Model CMP11) used in this study is shown in Fig. 2. Both instruments are subject to regular maintenance (i.e. cleaning of the optical windows) and data were manually check for quality. Radiation measurements were recorded at minute-resolution intervals, and averaged to produce daily averages. Daily averages of *Dn* and *Dh* measurements were then used for the present analysis.

Data for surface evaporation was obtained from Modern-Era Retrospective Analysis for Research and Applications (MERRA) model, through the Giovanni Earth Data portal. The model has a spatial resolution of $0.5^{o} \times 0.6^{o}$. Hourly measurements were averaged to produce daily estimates of surface evaporation. This was done to ensure that evaporation data matched the temporal resolution of the radiation data.

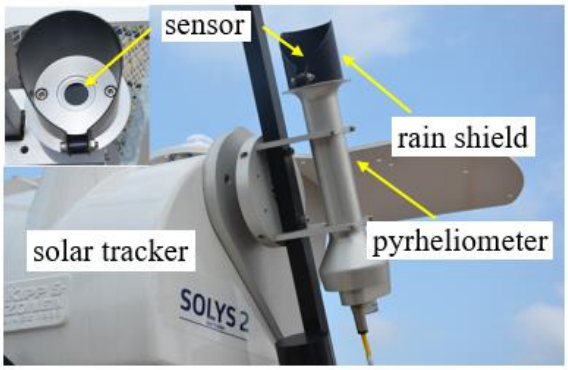

Figure 1: Pyrheliometer (CHP1) used to measure *Dn*, shown mounted onto the Solys2 solar tracker. Inset: Front view of the pyrheliometer which constantly points at the Sun.

Results and Discussion

Correlation between Dn, Dh and evaporation

Figs. 3 and 4 show the correlation between surface evaporation and *Dn* for winter and summer, for both

Figure 2: Pyranometer (CMP11) used to measure *Dh*. A shading ball device is used to block the *Dn* component, such that only *Dh* is received by the sensor.

years, respectively. For winter (), most days have an average *Dn* ranging from 600-900 W/m^2. The evaporation rate remains mostly below 3 kg/m^2/s, with a few instances that occur above. For summer (), *Dn* is significantly higher, as expected, and the surface evaoporation also shows a corresponding increase, however with a larger variation. Surface evaporation rate has a variation that is approximately between 3 kg/m^2/s and 7 kg/m^2/s. In addition *Dn* averages are mostly > 800 W/m^2.

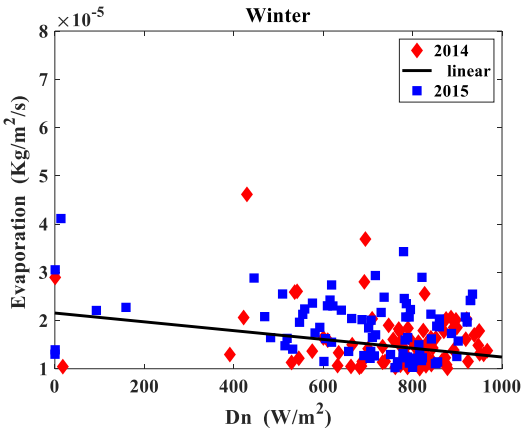

Figure 3: Correlation between surface evaporation and *Dn* for winter.

Correlation between surface evaporation and *Dh* are shown in Fig. 5 and 6. For winter (), *Dh* varies between 300-600 W/m^2. Similar to *Dn*, the evaporation rate is below 3 kg/m^2/s for most days. For summer (), *Dh* varies between 400-1000 W/m^2. In addition, evaporation rate also shows a large variation approximately between 3 kg/m^2/s and 7 kg/m^2/s.

Although, the contribution from the *Dn* component is larger than that of *Dh*, the surface evaporation rate does not show a significant increase.

The significant variation in *Dh* during summer is mainly due to the presence of clouds. Durban experiences substantial cloud cover during summer (Govender, 2017). Clouds result in subtantial scattering of *Dh* resulting in an increase of this component. Winter generally has clearer days and signifcantly less scattering.

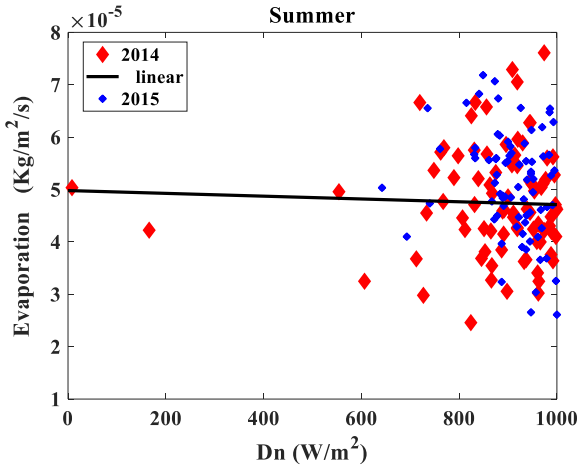

Figure 4: Correlation between surface evaporation and *Dn* for summer.

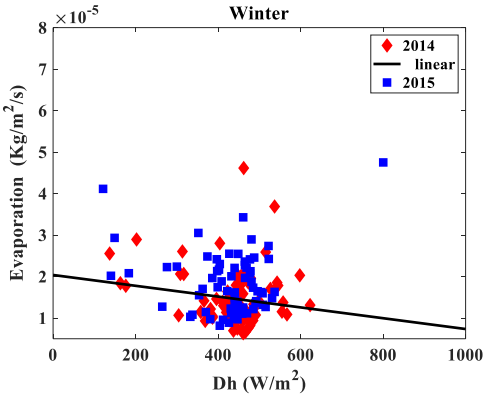

Figure 5: Correlation between surface evaporation and *Dh* for winter for 2014 and 2015.

Seasonal analysis

Shown in Fig. 7 (a)-(d) is the relationship between *Dn*, *Dh* and surface evaporation for the winter and summer seasons. For winter in both years, mean evaporation is relatively low (below 2×kg/m^2/s). On average, *Dn* is approximately 800 W/m^2. The *Dh* average is below 600 W/m^2, and shows little fluctuation during most days. This is due to Durban experiencing many cloud-free days in winter (Govender, 2017). There was one instance of missing data for *Dh* during the winter period of 2014, and some for 2015. Nevertheless, the trend of *Dh* during the 2015 winter was similar to that of the 2014 winter.

During the winter of 2015, there was an instance where the *Dn* and *Dh* decreased, but evaporation rate increased.

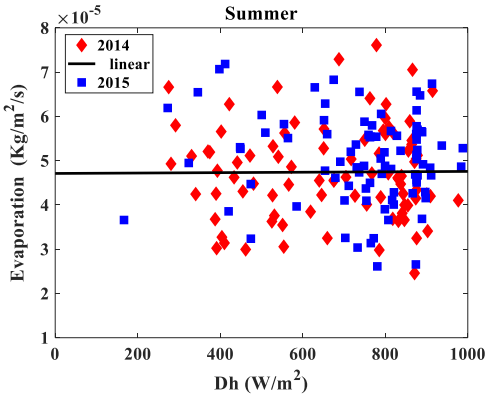

Figure 6: Correlation between surface evaporation and *Dh* for summer.

This could possibly be explained by the presence of high wind speed during these days that resulted in an increase in evaporation, despite the decreased radiation.

For summer in both years, evaporation rate is substantially higher (> 4× kg/m^2/s) for most days, due to the higher *Dn* (> 800 W/m^2). The *Dh* also shows an increase as well as significant variation. The variation in *Dh* during summer is mainly due to clouds. Durban experiences sunbstantial cloud cover during the months of November, December and January, particularly of the stratocumulus type (Govender, 2017), resulting in increased *Dh*. Correlation between surface evaporation and *Dn* and *Dh* were found to be low, which may be due to the coarse spatial resolution of the MERRA data, and which requires further investigation. Overall, for the summer season both components contribute to the higher evaporation rate, while during the winter season the direct component is the main contributor.

Conclusions

This study investigated the effect of individual solar radiation components on surface evaporation for Durban, South Africa. In summer, direct radiation is higher due to the higher solar altitude angle above the horizon. Diffuse radiation is higher due to increased scattering by clouds. Both these factors contribute to the higher evaporation rate during the summer season as compared to the winter season. During the winter, evaporation rate is mainly dependent on the direct component, since diffuse radiation is significantly lower due to clearer sky conditions.

Evaporation rate has a direct effect on soil moisture conditions, which in turn affects crop production. This study provides useful information on how the variation of solar radiation components can be a contributing factor to such conditions.

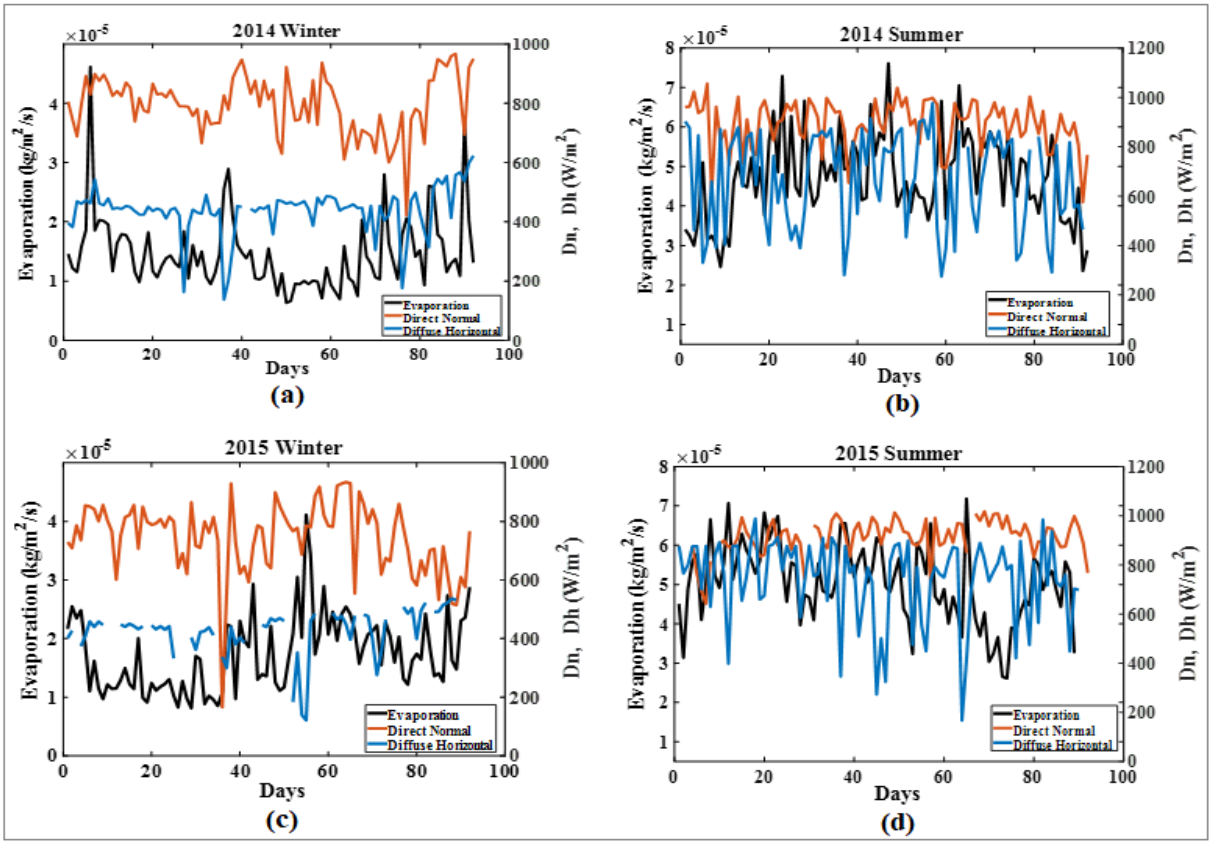

Figure 7: Relationship between *Dn*, *Dh* and evaporation for (a) winter season of year 2014, (b) summer season of year 2014, (c) winter season of year 2015 and (d) summer season of year 2015.

In addition, further work will include meteorological variables such as wind speed, temperature and humidity, combined with solar radiation components, in order to investigate the effect on evaporation rate.

Acknowledgements

The authors acknowledge the Southern African Universities Radiometric Network (SAURAN). Analyses of surface evaporation data were produced with the Giovanni online data system developed by NASA GES DISC. In addition, P. Govender and J.A. Ogunniyi acknowledge the National Astrophysics and Space Science Programme (NASSP) at the University of KwaZulu-Natal for bursary support.

References

Govender, P. (2017). Clustering analysis for classification and forecasting of solar irradiance in Durban, South Africa. PhD Thesis. University of KwaZulu-Natal, Durban, South Africa.

Govender, P., Brooks, M.J. and Matthews, A.P. (2018). Cluster analysis for classification and forecasting of solar irradiance in Durban, South Africa. *Journal of Energy in Southern Africa*. 29(2): 51- 62.

Palmer, A.H. (1920). The agricultural significance of sunshine as illustrated in California. *U.S. Monthly Weather Review*. 48:151-154.

Syu, M.R, Lee, P.H., Leou, T.M. and Shen, Y. (2016). Solar irradiance and Pan evaporation estimation from meteorological satellite data. *Terrestrial Atmospheric and Oceanic Sciences*. 27 (2): 221-239.

Yadav, B. (2016). Effect of reduced solar radiation on growth and yield of wheat. MSc Thesis. Indian Agricultural Research Institute, New Delhi, India.

2019 versus 2006: Improved yield potential for late planted maize in a warming climate

Johan Malherbe[1], Christien Engelbrecht[2], Francois Engelbrecht[3], Jacobus Van Der Merwe[1]
[1]Council for Scientific and Industrial Research (CSIR)
[2]Agricultural Research Council (ARC)
[3]University of the Witwatersrand

Corresponding author: jmalherbe@csir.co.za

The 2018/19 summer saw increased white maize production as projected by the National Crop Estimates Committee when weather conditions during the very late part of the growing season became uncharacteristically favourable for crop maturation. Rainfall started very late over the western production areas – long after the planting window. Here we contrast the crop development in 2018/19 to another summer with very late rainfall (2005/06) where the upward tendency in crop expectations was absent. We also note differences in temperature regimes and consider the potential effect of climate change to promote the occurrence of improved potential when planting occurs after the optimal planting window.

Keywords: Maize Production, South Africa, Climate Change, Crop Modelling

Introduction

The maize-production region in South Africa, particularly the western region, was negatively impacted by the recent drought in 2015/16. During this and earlier drought events that affected production negatively in the region, very high maximum temperatures during mid-to late summer occurring during the sensitive growth phase of the plant were instrumental (e.g. Malherbe et al. 2015, 2016). The growing risk of detrimental temperatures during mid-summer is underlined by an observed upward trend in temperatures, since the 1960's,in the order of 1 - 2°C per century over the region (Kruger 2004) and projected further increases under anthropogenic forcing (Engelbrecht et al. 2015).

The western maize production region of South Africa produces most of the country's white maize, used for human consumption. The 2018/19 summer rainy season saw extremely dry conditions dominating the central parts of the country, including the western maize production region, during the October – December period. The first widespread rain only occurred by the very end of December, and while conditions henceforth changed to periods with widespread rain and extensive cloud cover, totals were for the most part not exceeding the long-term mean in many areas, but were closer to the norm than during the early part of the summer. By April, widespread above-normal rain occurred. This was followed by unseasonably warm conditions during most of autumn, with frost only by the end of May, substantially later than the typical date of the first widespread frost. As the season developed during the January – May period, the very favorable conditions resulted in successive increases in the estimate for total production coming from the western production areas (CEC 2019), even though planting happened after – and in some cases several weeks after the planting window over the region. Based on the expectation of hot and dry conditions over the summer rainfall region towards mid- and late summer as indicated by the seasonal outlooks from a multitude of coupled climate models (http://iri.columbia.edu/our-expertise/climate/forecasts/seasonal-climate-forecasts/), together with a slow start to the season maize futures prices increased markedly towards early January. The unexpected favorable conditions towards late summer caused maize futures prices to decrease by 10 to 20% during the remainder of the growing season, reflecting the effect of an unrealistically negative outlook earlier and unexpected favorable conditions in late summer.

In the 2005/06 summer, a similar pattern occurred in terms of rainfall. However, during that summer, there was no upward trend in estimated production, despite rainfall totals being higher than in 2018/19. We observe the difference in temperatures between the two summers and consider the potential effect of climate change on the production potential of very late planted maize.

Data and Methods

Daily weather data and soil profile information from the Agricultural Research Council – Institute for Soil, Climate and Water (ARC-ISCW) climate and soil databanks respectively were used as input data to a crop simulation model. The research presented here focused on one specific area in the western maize production region, located near Potchefstroom (26.75°S, 27.05°E).

The DSSAT Crop System Model (previously known as CERES-maize - Jones et al. 2003; Hoogenboom et al. 2010) was used to simulate the effect of different planting dates and using a long versus medium growing season cultivar. Table 1 represents the crop management considerations together with the 3 planting dates after the normal planting window. Application of fertilizers was assumed to be 60 kg Ha^{-1} Nitrogen, a typical fertilizer strategy for dryland cultivation in the area.

Table 1 Variables considered during modeling

Variable	Experiment
Soil Type	Pinedene Klerksdorp
Row Width (m)	1.0
Plant Population (plants m^{-2})	1.5
Planting date	10 January, 25 January, 5 February
Cultivar type	Medium growing-season, Long growing-season

The sum total of combinations considered was 6 – resulting in a total of 240 experiments when executed for each year in the time series (1980 – 2019). The soil type is a common type found in the area of interest, as indicated by the land type inventories of the dominant land types (ARC-ISCW Land Type Inventory and soil descriptions). It has a reddish fine sandy loam to sandy clay loam textured upper horizon. The upper horizon of the soil is of medium depth (520 mm - Pinedene Klerksdorp). The 3 planting dates outside the normal planting window are sometimes used in the event of dismal failure of rainfall during October – December, as observed during both 2005/06 and 2018/19. Model simulations for all growing seasons started 150 days before planting.

To evaluate the possible increased probability of warmer late-summer / autumn conditions, we consider an AMIP-style run of the Conformal Cubic Atmospheric Model, with surface temperature modelled at 8 km spatial resolution in an AMIP-style CCAM downscaling with observed greenhouse gas concentrations and SSTs consistent with the observed.

Results and Discussion

Fig. 1 shows the monthly total rainfall during 2005/06 and 2018/19, together with the long-term average per month.

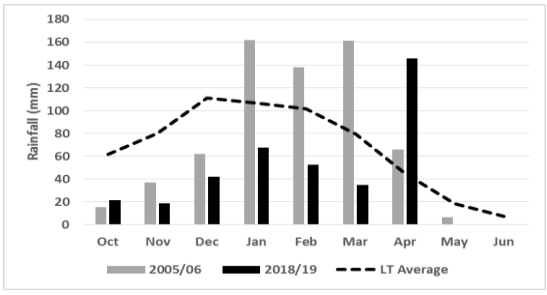

Fig. 1 Monthly rainfall in 2005/06 (grey bars) and 2018/19 (black bars) as well as the long-term average per month (broken line).

It is clear that during both these summers, drought characterized the October-December periods while the latter part of summer saw near-normal or above-normal rainfall. It is also clear that rainfall during 2005/06 was mostly higher than during 2018/19 during the latter part of summer potentially supporting higher production. Rainfall during the October-December period was only 45% (32%) of the long-term average during 2005/06 (2018/19). During January to April it was 158% (90%) in 2005/06 (2018/19). Table 2 shows various climate parameters during the 2005/06 and 2018/19 summers during the growing season as determined by the DSSAT simulations.

Table 2 Rainfall, average maximum temperature and average minimum temperature during the growing seasons for the long-season and medium-season cultivars during 2006 and 2019, for the planting dates as indicated.

Cultivar	Plant Date	Year	Harvest Date	Rainfall (mm)	TX av (°C)	Tn av (°C)
Long season	10-Jan	2006	01-Jun	455.8	24.5	11.8
		2019	14-Jun	316.3	27	11.6
	25-Jan	2006	01-Jun	382	24.1	11.1
		2019	14-Jun	302.8	26.4	11.1
	05-Feb	2006	01-Jun	371.3	23.7	10.6
		2019	14-Jun	267.5	26.2	10.6
Medium season	10-Jan	2006	01-Jun	455.8	24.5	11.8
		2019	04-Apr	151.6	30.2	15.7
	25-Jan	2006	01-Jun	382	24.1	11.1
		2019	14-Jun	302.8	26.4	11.1
	05-Feb	2006	01-Jun	371.3	23.7	10.6
		2019	14-Jun	267.5	26.2	10.6

According to model output data (Table 2), that rainfall in 2006 during the growing seasons was much higher than in 2019 for all planting dates and cultivars indicated. On average, maximum temperatures were 2 – 3 °C higher in 2019. While minimum temperatures were fairly similar, it should be noted that the 2019 harvest date is 2 weeks later than in 2006 (simulated) and therefore indicates warmer night-time/early morning conditions on a day-to-day basis.

A clear problem during 2006 was the occurrence of relatively low temperatures during the latter part of summer, specifically towards the March-May period, while temperatures remained very mild towards the very end of the growing season in 2018/19 (Fig. 2).

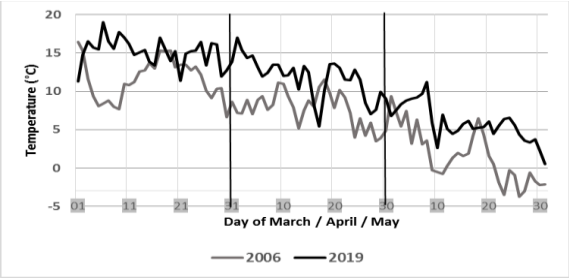

Fig. 2 Daily minimum temperatures during the March-May periods in 2006 (grey) and 2019 (black).

Temperatures falling below 10°C results in significantly slower crop development. During most of April 2006, minimum temperatures were below this value while it remained above 10°C for most of April 2019. If one considers the first day when minimum temperature dropped below 5°C, it occurred about 2 weeks earlier in 2006 than in 2019 (23 April vs. 10 May). Figs. 3a and 3b show the modelled results for long and medium growing season cultivars and different very late planting dates during 2006 and 2019.

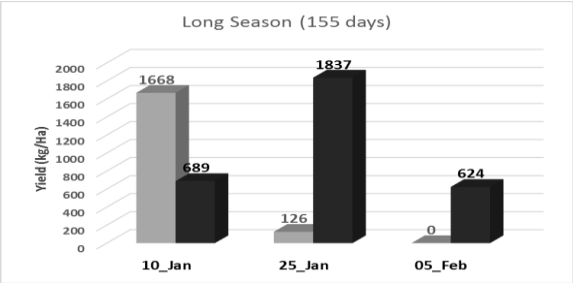

Fig. 3a: Yield simulated for the long growing-season maize cultivar on the Hutton Pinedene soil type per planting date (left to right) and plant population of 1.5 plants/m^2 during 2006 (grey) and 2019 (charcoal).

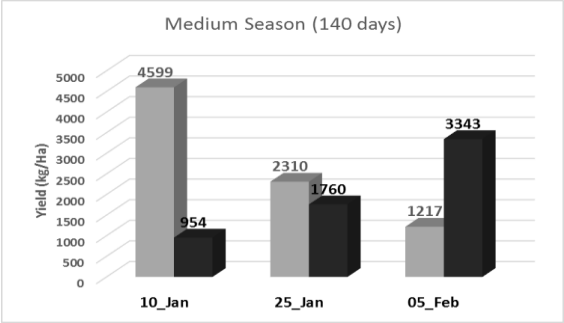

Fig. 3b: Same as Fig. 3a, but for a medium growing season cultivar.

The strong positive impact of the very late part of the 2019 summer, compared to that of 2006, is clear by the contrasting trends in yields obtained, with decreases (increases) noted with later planting dates during 2006 (2019). In fact, of all the experiments, the second highest yield was obtained by a medium growing season cultivar, planted at the latest date considered – in 2019. Moreover, for the long growing season cultivar, the highest yield obtained for any planting date, was in 2019 – despite much lower rainfall – again showing the important role played by the higher temperatures towards autumn.

Given the very wet conditions during JFM 2006, it is fair to question the role of water-logged conditions versus temperature regime in determining the outcomes of that production season. To gain an understanding of the importance of temperatures in determining the trends observed, Fig. 4 shows, for the same experiments as in Fig. 3, the results when the March – May temperature records for 2006 and 2019 are swopped while other variables are kept as in the original dataset.

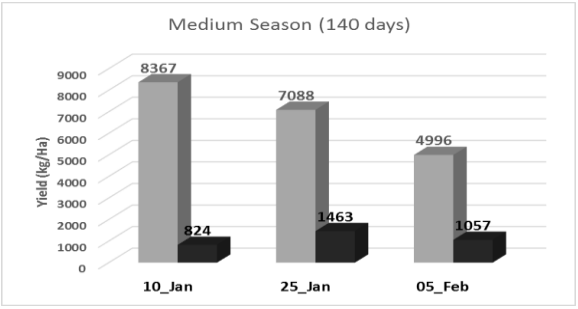

Fig. 4: Same as Fig. 3b, but for these experiments, the temperature records in 2006 (2019) were replaced with the temperature records of 2019 (2006).

It is clear that, given temperatures as in 2019, the 2006 season would have seen greatly increased yields for all planting dates. Given the relatively dry March period in 2019, one would assume that the lower temperatures as observed in March 2006 could have been beneficial. However, Fig. 4 shows that the lower temperatures would have resulted in lower yields in 2019 also, with no strong increase in production if planting happened extremely late (as model results indicate for planting only by 5 February 2019). This highlights the importance of the higher temperatures for increased production during the latter part of the 2019 production season.

Fig. 5 shows the model-simulated (as per AMIP simulation) change in the first day of the year when

minimum temperature falls below 5°C at the area of interest, for a historic (1871 – 1899) and recent (1979 – 2016) period.

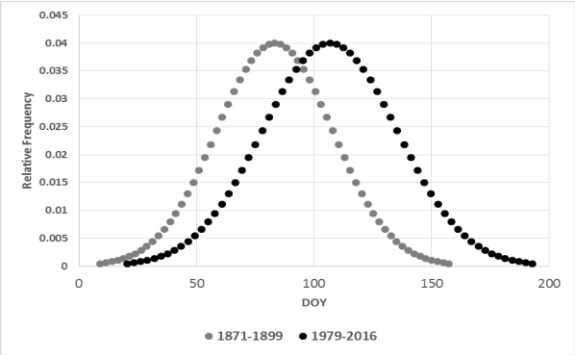

Fig. 5: Frequency distribution of the first day of the year when minimum temperature falls below 5°C over the focus area, for 1871-1899 (grey) and for 1979-2016 (back), as per AMIP-style high-resolution simulation, using CCAM.

Associated with changing atmospheric greenhouse gas concentrations and SST trends, the CCAM-AMIP style simulation indicates a likely postponement of the first day during the year when minimum temperature reaches 5°C. According to the simulation, the first instance with minimum temperature falling below this cut-off value, has on average moved later with about 3 weeks during the 20th century.

Conclusions

Both 2005/6 and 2018/19 can be characterised as summers with very late-occurring rainfall over the western maize-production region. For dryland maize-production, this essentially means that cultivation occurred after the normal planting window. While crop development during 2005/06 occurred during a period with 30 – 50% more rain than in 2018/19, estimated production increased during the January – June period in 2018/19 – not in 2005/06. The very positive impact on crop production in 2018/19 versus 2005/06, is strongly related to the unseasonably mild conditions during autumn in 2018/19, as opposed to cool conditions in 2005/06. Minimum temperatures below 5°C occurred 2 weeks later in 2018/19 than in 2005/06. According to an AMIP-style simulation by CCAM, this is equivalent to the simulated shift in occurrence of such low temperatures, as a function of changes associated with anthropogenic forcing. This is indicative of a potential opportunity to utilise late summer rain coupled with relatively high autumn temperatures, potentially with increasing frequency during the 21st century. Given the lead time essential for decision support in agriculture, this potential can only be unlocked with the further improvement of existing temperature forecast skill (e.g. Lazenby et al. 2014) still largely lacking as demonstrated by the opposite trend in observed versus predicted seasonal rainfall and temperature trends during 2018/19.

References

CEC (2019) Crop Estimates Committee, Department of Agriculture, Forestry and Fisheries, Pretoria.

Engelbrecht, F., Adegoke, J., Bopape, M.J., Naidoo, M., Garland R, Thatcher M, McGregor J, Katzfey J, Werner M, Ichoku C and Gatebe C (2015) Projections of rapidly rising surface temperatures over Africa under low mitigation. Environmental Research Letters, 10(8), p.085004.

Hoogenboom G, Jones JW, Wilkens PW, Porter CH,.Boote KJ, Hunt LA, Singh U, Lizaso JL, White JW, Urasev O, Royce FS, Ogoshi R, Gijsman AJ and Tsuji GY (2010) Decision Support System for Agrotechnology Transfer (DSSAT) Version 4.5 [CD-ROM]. University of Hawaii, Honolulu, Hawaii.

Jones JW, Hoogenboom G, Porter CH, Boote KJ, Batchelor WD, Hunt LA, Wilkens PW, Singh U, Gijsman AJ and Ritchie JT (2003) DSSAT Cropping System Model. European Journal of Agronomy, 18, 235-265.

Kruger AC and Shongwe S (2004) Temperature trends in South Africa: 1960–2003. International Journal of Climatology: A Journal of the Royal Meteorological Society, 24(15), pp.1929-1945.

Lazenby MJ, Landman WA, Garland RM and DeWitt DG (2014) Seasonal temperature prediction skill over Southern Africa and human health. Meteorological Applications, 21, 963-974. DOI: 10.1002/met.1449

Malherbe J, Durand W and Engelbrecht CJ (2015) Acknowledging decadal to intraseasonal variability in support of agriculture – the 2014/15 maize production season. 31st Annual Conference of the South African Society for Atmospheric Sciences, Potchefstroom, 21–22 September 2015. ISBN 978-0- 620-67825-4.

Malherbe J and Durand W (2016) How would current advice benefit maize farmers with respect to historical associations with El Niño events. 32nd Annual Conference of the South African Society for Atmospheric Sciences, Potchefstroom, 31 October – 1 November 2016. ISBN 978-0-620-72974-1.

Time series analysis of climate impacts on sugarcane yield in south-eastern Africa

Thulebona W. Mbhamali[1], Mark R. Jury[1, 2], Nkanyiso B. Mbatha[1]

[1]Department of Geography, University of Zululand, KwaDlangezwa, South Africa
[2]Department of Physics, University of Puerto Rico, Mayagüez, USA

Corresponding author: *twmbhamali@gmail.com, Tel: +27 76 898 9128*

The study explored the statistical links between climate variables and indices and sugarcane yield using the time series analysis. Climate datasets derives from KNMI climate explorer, and extracted from 1970-2016. The main datasets are GPCC8 rainfall, CRU4 temperature, SST patterns and SLP datasets. The statistical analysis was performed through scientific programming by following the R procedures. The methods employed are: Mann-Kendall test, Pearson correlation and MLR time series analysis. Annual sugarcane yield has been decreasing since 1980s, partial due to climate impacts but there are also non-climatic influences. The study found a strong relationship between local crop-drivers and the yield due to its long-cycle (12-24 months) in contrast to short-lived crops such as maize (3-4 months). Surface air temperature is the main climatic factor for sugarcane production in both rainfed and irrigated sugarcane. It is evident that in rainfed agro-climatic regions, soil moisture availability as a function of precipitation in the preceding season is essential for sugarcane growth and development, and this accelerates the yield in the upcoming season. Hence, sugarcane prediction technique that will incorporate PDSI is desired to improve the forecast skill.

Keywords: Climate impacts, Sugarcane yield, Statistical link, programming and Southeastern Africa

Introduction

Yamori *et al.* (2014) reported that sugarcane (*Saccharum officinarum* L.) is a C_4 crop which is grown in both tropical and subtropical agro-ecological zones, mainly for the production of sugar and bioenergy. Plants and crops are spatially distributed according to climate responses. Hence, C_3 (temperate plants), C_4 (tropical plants) and CAM (semi-arid condition plants) plant species are reported to have different abilities for temperature acclimation of photosynthesis. Sugarcane yield and production have been reported to be directly and ultimately affected by crop drivers such as evapotranspiration, rainfall, temperature, pests and diseases (Everingham, *et al*., 2003). Gbetibouo and Hassan (2005) estimated the economic impacts of climate change on the major South African crops using the Ricardian model. The model was based on agricultural data for sugarcane, maize, wheat, sorghum, soybean, groundnut and sunflower. The study revealed that field crops are more sensitive to increased temperatures than to precipitation, and thus to greenhouse warming.

This study explores the statistical association between climate and sugarcane yield using the time series analysis. Figure 1 shows the study area and the area which was averaged over south-eastern Africa for time series (31-23°S and 28-33°E). The study area comprises parts of KwaZulu-Natal, Mpumalanga (in South Africa-SA) and Eswatini-ES. It has been found that the sugar-belt is vulnerable to rainfall variability (Gbetibouo & Hassan, 2005), which affects the annual output.

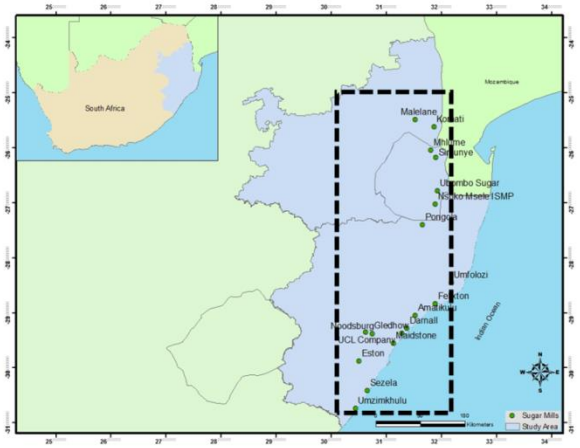

Figure 1: Map of southeastern Africa and the sugarcane growing region. Individual sugar mills are green dots. The dashed box indicates the area-which was averaged for time series analysis (modified from: Mbhamali, et al., 2018).

Data and methods

The station-based monthly GPCC8 rainfall (Schneider, *et al*., 2018), is available through the KNMI climate explorer (KNMI-CE) website. An area average was calculated over south-eastern Africa (Figure 1) for the period from 1970-2016. The rainfall and yield time series were compared, statistical links explored using the Multi-variate Linear Regression (MLR) and correlation methods. PDSI is precipitation (P) minus potential evaporation (E), where E is the function of temperature and soil moisture content over

time in a given location (Dai, *et al.*, 2004). Monthly averaged CRU4 station-based temperature data (Harris, *et al*., 2014), rainfall, PDSI and temperature were related to the yield and tested for its impact on the yield over the study area. Sea level pressure (SLP) data was obtained from KNMI-CE, and it was used to compute the heatmap and perform variable importance through MLR.

The HadSLP2 reanalysis interpolation system provides SLP time series as discussed in Allan and Ansell (2006). The Southern Oscillation Index (SOI) from Climate Prediction Center was employed to explore the statistical association between the Pacific El Niño-Southern Oscillation (ENSO) and sugarcane yield. SOI data was extracted from KNMI-CE for the period 1970-2016, and used as defined in the study of Ropelewski and Jones (1987).

Niño4 is defined as a monthly ENSO index which is calculated by averaging SST anomalies (SSTA) (Rayner, *et al.*, 2003) in the central equatorial Pacific (5°N-5°S and 160°E and 150°W). The SSTAs that exceed 0.5 °C are used to define La Niña and El Niño signatures. The Niño4 time series derives from averages of Met Office Hadley Centre SST datasets in KNMI-CE. In this study it was useful for scrutinising ENSO influence in the yield over southeastern Africa. The monthly NOAA reconstructed SST V4 (Rayner, *et al*., 2003), has been interpolated to 1°, and was drawn from KNMI-CE from 1970-2016. This was used for Pearson correlation and MLR analysis to test the statistical link with the yield and evaluate its importance to sugarcane production.

National sugarcane yield data was extracted from the United Nations (UN) Food and Agriculture Organisation's (FAO) database for the period 1970-2016. The South Africa and ESwatini yield time series were used independently because in SA sugarcane is largely rainfed while in ES it is 100% irrigated. Hence, in Eswatini the storage dams provide a buffer during the dry seasons.

The Mann-Kendall test is used to calculate the monotonic trends in a time series, and here this technique is used as described in previous studies (Kendall, 1975). The Mann-Kendall test is non-parametric and rank based, and is often used for detecting monotonic trends in the time series of geophysical data (environmental sciences, climate and hydrological data). Non-parametric techniques are robust and resistant to time series with outliers (Lanzante, 1996), hence in this study it was paramount to employ this technique. With reference to the -transformation equation outlined above, this study considered a 5% confidence level, by which the null hypothesis of no trend was rejected if The test also provides the Mann-Kendall tau () that measures the correlation. The Mann-Kendall test was used to detect trends in sugarcane yield. However, the former, only detects whether the monotonic trend is upward or downward. Thus, to quantify for the onset of the trend and approximate the potential trend turning points (PTTPs) in the time series, the Sequential Mann-Kendall (Seq.MK) test is robust (Chatterjee, *et al*., 2014). The forward sequential (Prog) values ()) of the standardised time series derive from the original data (), and the backward sequential (Retr) values are approximated using the same approach but beginning with the last value of the original time series. In the plot of) and) curves their intersection shows the PTTPs, and the trend is considered significant when and .

In this study the Pearson correlation method used the Pearson correlation coefficient to explore the statistical links between climate variables and the yield. Multi-variate Linear Regression (MLR) analysis revealed the relationship between the yields and climate variables using the level of significance. The MLR is given by:

$$y = \beta_0 + \beta_1 x_1 + \beta_2 x_2 + \cdots \beta_n x_n + \in \qquad (1)$$

where is the dependant variable (sugarcane yield), denote the independent variables (rainfall, temperature, PDSI, SLP, SST patterns, SOI, Niño4), is the intercept from the model output, are the coefficients of terms and is the standard error. In this study it was used to test the importance of climate variables in sugarcane yield. The Pearson correlation and MLR are also explained in the study of NDVI and drought impact by Mbatha and Xulu, (2018).

Results and discussion

Table 1 presents a summary of the Mann-Kendall statistics for sugarcane yield time series from FAO database for the two countries. In South Africa the yield exhibits a declining yield trend with -transformation of -4.604 and the value of and in ESwatini the yield ha -transformation of 4.631 and thevalue of .

Table 1: Mann-Kendall (MK) test statistics for sugarcane yield (ton/ha) trends over South Africa and ESwatini, and bold -transformation values are significant at the 95% level.

South Africa and ESwatini (FAO yields)		
SA_FAO	*z*	**-4.604**
SA_FAO	*p*-value	4.15E-06
SA_FAO	Tau (τ)	-0.465
Swazi_FAO	*z*	**-4.631**
Swazi_FAO	*p*-value	3.63E-06
Swazi_FAO	Tau (τ)	-0.468

Figure 2 shows the trends detected from a Sequential Mann-Kendall trend test method and from the analysis there is no potential trend turning points detected. It should be noted that these results might be due to the time series employed, and demarcating this analysis to different agro-climatic zones could produce different outcomes. The Mann-Kendall statistic test indicated that sugarcane yields have been decreasing since 1980s over south-eastern Africa. A huge decline of the yield was observed during the period from 2010-2016, where z-score values were observed to be below -4, which is an indication of a significant downward trend (see Figure 2). The trend is declining due to increased temperature and reduced rainfall (Figures 2a and b; Mbhamali, *et al.*, 2017). However, there are additional influences which are non-climatic such as pests and diseases (Dube & Jury, 2000). These climate variables and indices were chosen because of their interdependence and potential role in climate variability over the study area.

The Pearson correlation coefficients of 0.68 and0.48 between temperature and yield were observed illustrated in Figures 3a and b. Rainfall and yield have a statistical association of PCC = 0.50 and PCC = 0.45 for South Africa (a) and ESwatini (b), respectively. This further indicates that sugarcane farmers must use climate prediction for their farm management practices, decision-making and policy formulation. The abrupt temperature and potential evapotranspiration increase tends to reduce the amount of soil moisture which then suppress sugarcane yield. This implies that despite potential rainfall increasing or decreasing, temperature has the ability to deplete soil moisture and surface water through potential evapotranspiration, which then results to crop failure.

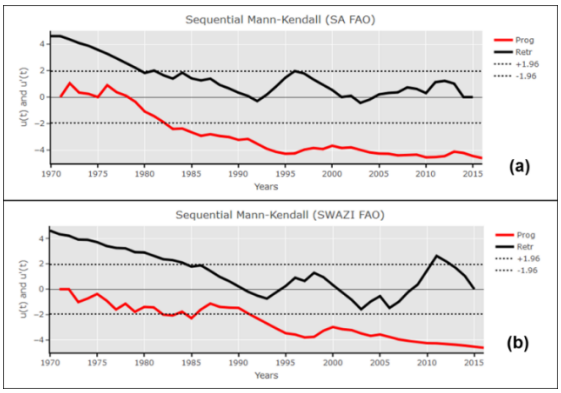

Figure 2: Trends detection in sugarcane yield, where $u(t)$ is a forward sequential curve represented in solid-black line and $u'(t)$ is a backward sequential curve represented in solid-red line over a) SA and b) Swazi (Eswatini).

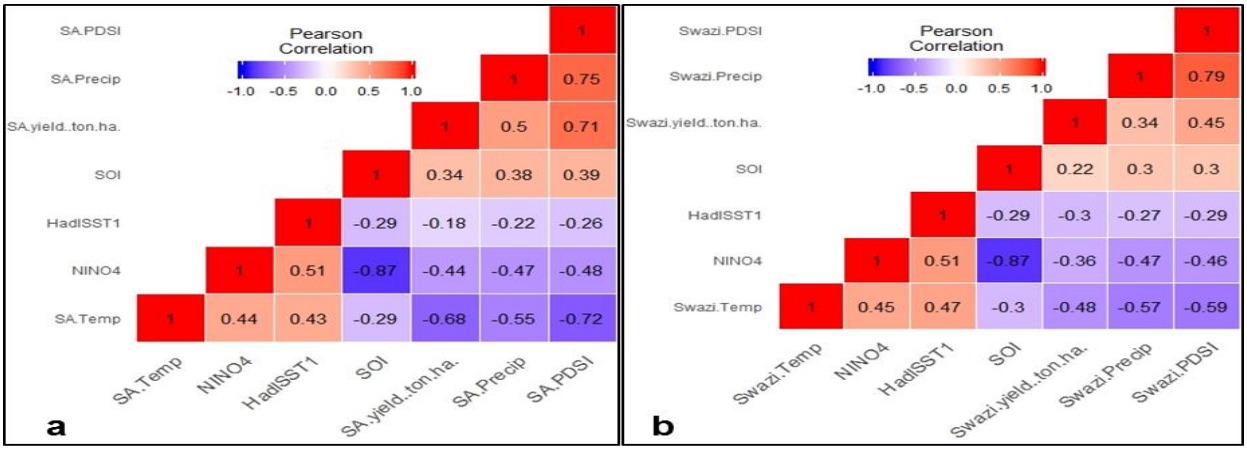

Figure 3: Heatmap of Pearson Correlation representing statistical association between climatic factors and sugarcane yield from 1970-2016 in a) South Africa and b) ESwatini. PCC is defined as +1 for strong positive correlation, 0 indicates that there is no linear relationship, and -1 means strong anti-correlation.

These interactions are incorporated in the PDSI, and the study affirms this drought index as a good proxy for sugarcane yield because these two are strongly correlated (0.7) in South Africa. In ESwatini this index explains 50% of cane variation from season-to-season, due to irrigation as expected.

Niño4 has of -0.44 and 0.36 with the yield in SA and ES, respectively. These indicate that warming of the South-west Indian Ocean (SWIO) decelerates sugarcane growth one year after the warm phase of ENSO. This was also substantiated with the negative relationship between SST patterns and the yield, where the was -0.18 and 0.30 over SA and ES, respectively. This suggests that – local climate parameters (rainfall and temperature) provide large explanation about sugarcane variability in comparison to global or remote influences such as ENSO as illustrated in Figure 3.

In the summary of MLR analysis, a statistically significant relationship between the drought index (PDSI) and surface air temperature with the sugarcane yield was observed at 1% level of confidence and the -values of 0.01 (PDSI and yield) and 0.03 (temperature and yield) over South Africa (Table 2). This statistical connection also exist between surface temperature and the yield in ESwatini. Although, this is slightly weaker than in South Africa as indicated with a -value of 0.10 at 5% level, and this was expected due to irrigation.

Table 2: Model output from MLR for FAO sugarcane yields (dependant variables) and climatic variables and indices are independent variables for the period 1970-2016.

MLR for South Africa					
	Estimate	Std. Error	t-value	-value	Signif. Codes
(Intercept)	4.851e+01	1.004e+02	0.483	0.6318	
SA_PDSI	5.842e-02	2.248e-02	2.599	0.0131	*
SA_Precip	-1.505e-04	2.009e-04	-0.749	0.4584	
SA_Temp	-1.260e-01	5.499e-02	-2.291	0.0274	*
HadlSST1	1.486e-01	8.900e-02	1.670	0.1029	
HadSLP	-4.473e-02	9.905e-02	-0.452	0.6541	
Niño4	-6.986e-02	7.438e-02	-0.939	0.3534	
SOI	-2.863e-02	6.432e-02	-0.445	0.6586	
MLR for Eswatini					
	Estimate	Std. Error	t-value	-value	Signif. Codes
(Intercept)	2.413e+01	5.086e+01	0.474	0.6378	
Swazi_Precip	-5.737e-05	8.396e-05	-0.683	0.4985	
Swazi_Temp	-4.073e-02	2.408e-02	-1.691	0.0987	.
Niño4	-4.310e-02	3.871e-02	-1.113	0.2724	
SOI	-3.193e-02	3.209e-02	-0.995	0.3260	
HadSLP	-1.843e-02	5.016e-02	-0.367	0.7153	
HadlSST1	5.250e-03	4.446e-02	0.118	0.9066	
Swazi_PDSI	1.268e-02	9.581e-03	1.323	0.1935	

Signif. codes: 0 '***' 0.001 '**' 0.01 '*' 0.05 '.' 0.1 ' ' 1 where these numbers from 0-1 are -values and the order of significant is strongest at and denoted with '***' while -value = 1 means that the independent variable is not statistically significant.

Conclusion

Sugarcane yield trends are significantly declining as indicated with -transformation far less than -4 in both countries. This is partial due to drought conditions, but it should be noted that there are additional influences which are non-climatic in nature. This includes sugarcane pests and diseases, monetary policy and land-use change. There is a strong statistical connection between rainfed sugarcane and climate than its counterpart irrigated sugarcane. There is a heterogeneous and intermittent intercomparisons detected in the statistical links between climate and sugarcane yield over southeastern Africa. The increasing temperature and reduced rainfall as a result of anticyclonic circulation tends to suppress the annual sugarcane yields. However, PDSI appears to explain much of the sugarcane variability over time at 1-5% level in southeast Africa. The results revealed a clear evidence of detrimental impacts of drought in sugarcane yield, as confirmed with the strong dip of the yield during 1992/93 season (*sugarcane time series not shown*). The minimum yields (41.7 ton/ha for SA and 90.8 ton/ha for Swazi) were reached. The

surface air temperature reveals itself as a key feature for sugarcane production, which provides the evidence of ENSO induced drought impacts over the sugar-belt of southeastern Africa. In addition to other crop-drivers employed in seasonal climate forecasting and sugarcane monitoring and modelling systems, the PDSI could be added to improve to forecast skills. It should be noted that PDSI uses both temperature and precipitation as inputs in contrast to other drought indices which use precipitation only.

Acknowledgements
I thank the KNMI climate explorer and FAO for archiving data in public domains to facilitate research. I also appreciate Carslaw (2015), for developing a free guide to use R procedures.

References

Allan, R. and Ansell, T., 2006. A new globally complete monthly historical gridded mean sea level pressure dataset (HadSLP2): 1850–2004. Journal of Climate, 19(22), pp.5816-5842.

Carslaw, D.C., 2015. The openair manual — open-source tools for analysing air pollution data. Manual for version 1.1-4, King's College London.

Chatterjee, S., Bisai, D. and Khan, A., 2014. Detection of approximate potential trend turning points in temperature time series (1941–2010) for Asansol Weather Observation Station, West Bengal, India. India. Atmospheric and Climate Sciences, 4, pp.64-69.

Dai, A., Trenberth, K.E. and Qian, T., 2004. A global dataset of Palmer Drought Severity Index for 1870–2002: Relationship with soil moisture and effects of surface warming. Journal of Hydrometeorology, 5(6), pp.1117-1130.

Dube, L.T. and Jury, M.R., 2000. The nature of climate variability and impacts of drought over KwaZulu-Natal, South Africa. South African Geographical Journal, 82(2), pp.44-53.

Everingham, Y.L., Muchow, R.C., Stone, R.C. and Coomans, D.H., 2003. Using Southern Oscillation Index phases to forecast sugarcane yields: a case study for northeastern Australia. International Journal of Climatology: A Journal of the Royal Meteorological Society, 23(10), pp.1211-1218.

Gbetibouo, G.A. and Hassan, R.M., 2005. Measuring the economic impact of climate change on major South African field crops: a Ricardian approach. Global and Planetary Change, 47(2-4), pp.143-152.

Harris, I.P.D.J., Jones, P.D., Osborn, T.J. and Lister, D.H., 2014. Updated high-resolution grids of monthly climatic observations–the CRU TS3. 10 Dataset. International Journal of Climatology, 34(3), pp.623-642.

Kendall, M.G., 1975. Rank correlation methods. 2nd impression. Charles Griffin and Company Ltd. London and High Wycombe.

Mbatha, N. and Xulu, S., 2018. Time Series Analysis of MODIS-Derived NDVI for the Hluhluwe-IMfolozi Park, South Africa: Impact of Recent Intense Drought. Climate, 6(4), pp.95-118.

Mbhamali, T.W., Jury, M.R., Motsa, N.M. and Mbatha, N.B., 2017. Climate impacts on sugarcane yield in the eastern part of southern Africa, Proc. of 33rd Annual conference of South African Society for Atmospheric Sciences, ISBN 978-0-62077401-7, 21-22 September 2017, Polokwane, Limpopo (South Africa), pp. 58-61.

Mbhamali, T.W., Jury, M.R., Motsa, N.M. and Mbatha, N.B., 2018. Statistical prediction of sugarcane yields over south-eastern Africa, Proc. of 34th Annual conference of South African Society for Atmospheric Sciences, ISBN 978-0-620-80825-5, 20-21 September 2018, Durban, KwaZulu-Natal (South Africa), pp. 114-116.

Rayner, N.A., Parker, D.E., Horton, E.B., Folland, C.K., Alexander, L.V., Rowell, D.P., Kent, E.C. and Kaplan, A., 2003. Global analyses of sea surface temperature, sea ice, and night marine air temperature since the late nineteenth century. Journal of Geophysical Research: Atmospheres, 108(D14), pp.4407-4443.

Ropelewski, C.F. and Jones, P.D., 1987. An extension of the Tahiti–Darwin southern oscillation index. Monthly Weather Review, 115(9), pp.2161-2165.

Schneider, U., Becker, A., Finger, P., Meyer-Christoffer, A., Rudolf, B. and Ziese, M., 2018. GPCC Full Data Monthly Product Version 8 at 0.5°: Monthly Land-Surface Precipitation from Rain-Gauges built on GTS-based and Historical Data.

Yamori, W., Hikosaka, K. and Way, D.A., 2014. Temperature response of photosynthesis in C3, C4, and CAM plants: temperature acclimation and temperature adaptation. Photosynthesis Research, 119(1-2), pp.101-117.

2. ATMOSPHERE – OCEAN INTERACTIONS

Spatial variability in coastal winds over the Cape Peninsula region from Synthetic Aperture Radar observations

M. Krug[1,2,3], M. Rouault[2,3], P. Willmott[4]

[1]Council for Scientific and Industrial Research, Natural Resources and the Environment, Cape Town, South Africa.
[2]Department of Oceanography, Mare Institute, University of Cape Town, South Africa.
[3]Nansen Tutu Center for Marine Environmental Research, University of Cape Town, South Africa.
[4]Stellenbosch University, Stellenbosch, South Africa.

Corresponding author:

High resolution (1 km) winds derived from satellite-based Synthetic Aperture Radar (SAR) acquisitions are used to better understand the spatial variability of coastal winds over the larger Cape Peninsula. Using outputs from a global reanalysis, we showed that 80% of the wind variability over the larger Cape Peninsula can be explained by winds blowing from either the north-west or south-east. The high-resolution SAR observations are then grouped across these two dominant wind directions to characterize the typical surface ocean wind signatures associated with the south-eastern and north-western wind regimes. We find that the south-easterly wind regime is associated with distinct wind shadows across the middle section of False Bay as well as in the lee of Table Mountain. A region of accelerated winds extending from Cape Hangklip and across False Bay is also observed. In contrast, north-westerly winds show a sheltered region in the north-west corner of False Bay and a region of accelerated winds south-west of Cape Hangklip. Spatial variations in ocean winds over the larger Cape Peninsula which are clearly linked to the orography, are not represented in global reanalyses products such as the National Center for Environmental Prediction (NCEP) Climate Forecast System Reanalyses (CFSR) used in this study. The global reanalysis product also strongly over-estimates wind speeds over the shelf regions located between the Cape Peninsula and Cape Columbine, particularly during the south-easterly wind regime. The rapid spatial variations in ocean winds observed with the SAR lead to the presence of strong and localized wind gradients whose impact on the ocean circulation remains to be studied.

Keywords: satellite oceanography, coastal winds, Synthetic Aperture Radar, Cape Peninsula, wind shadows

Introduction

Accurate wind observations are essential for the monitoring and management of our cities, harbours and marine resources. Due to the difficulties associated with deploying and maintaining sensors at sea, wind observations over the ocean rely quasi-exclusively on satellite observations. Most observations of ocean winds over the ocean are done using satellite-based sensors such as scatterometers. The existing constellation of scatterometers in space provides global coverage of the world's ocean wind fields at a spatial resolution of 25 km but the signal observed by scatterometers is contaminated near land boundaries, resulting in a loss of data within 20 to 70 km from the coast (Verhoef et al., 2012).

The Larger Cape Peninsula (LCP) is located south of Africa, in the Western Cape province (Fig. 1). It encompasses the city of Cape Town, one of the largest cities in South Africa and forms part of the southern Benguela upwelling region, one of the four major coastal upwelling ecosystem in the world. In the southern Benguela, winds control the process of enrichment, concentration and retention, which are fundamental to the survival and recruitment of pelagic fish (Lett et al., 2006). Previous studies have shown that resolving spatial variations in nearshore winds is essential to understand and model the ocean circulation and bio-physical interactions in coastal upwelling systems (Capet et al., 2004). This is particularly true for the Larger Cape Peninsula (LCP) region, where the strongest upwelling occurs on the narrow inner shelf and productivity is maximum within distances of 20 to 80 km from the coast (Weeks et al., 2006). Changes in coastline orientation and elevation directly impact on the coastal wind fields and on the oceanography of the LCP region. Using aircraft observations, Jury (1987) found that during deep South Easterly (SE) regimes, when the depth of the flow exceeded 1000 m, winds flowing over the Cape Peninsula and Cape Hangklip would be accelerated with little directional shearing, resulting in stronger winds to the northwest of the capes. In shallow SE regime, when the SE wind were capped beneath a stable inversion layer located between 500 m - 1000 m, Jury (1987) found that a pronounced wind

shadow would develop on the eastern side of False Bay and that mountains near Cape Hangklip (Fig. 1(b)) would steer the SE winds seawards. The strong impact of the orography and coastline orientation on the winds demonstrated by Jury (1987) emphasises the need for high resolution observations of ocean winds in the LCP region.

The aircraft observations analysed by Jury (1987) were collected at a height of 150 m and with a spatial resolution of 10 – 30 km and to date, the impact of the orography on the surface oceanic wind fields in the LCP has never been quantified at resolutions below 10 km. In this study, high resolution (1 km) wind estimates derived from Envisat Advanced Synthetic Aperture Radar (ASAR) acquisitions are used to map for the very first time spatial variations in surface ocean winds over the LCP. The impact of the rugged topography on the surface ocean winds under the predominant SE and North Westerly (NW) wind regimes is assessed.

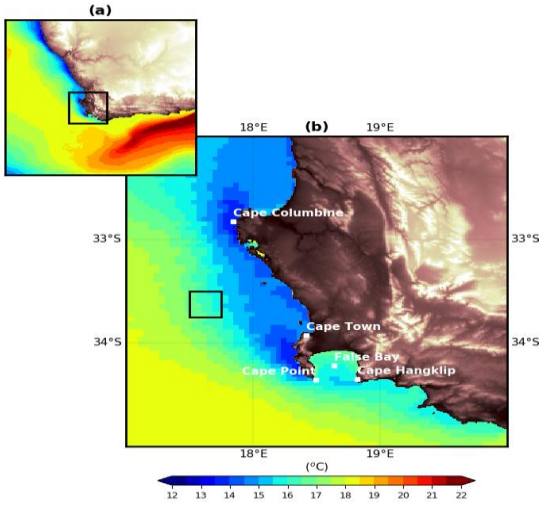

Figure 1: Colour map of the annual SST climatology from a 10 year archive of MODIS-TERRA satellite observations. Blue shades indicate colder waters and yellow shades indicate warmer waters. The black rectangle in (a) shows the Larger Cape Peninsula (LCP) region, south of Africa. In (b) the black rectangle shows the location of the Cape Town offshore box.

Data and method

An archive of ASAR Wide Swath Medium (WSM) resolution images acquired over the LCP between 2008 and 2012 is used to derive high resolution (1 km) ocean surface winds, hereafter referred to as SAR winds. Extracting ocean surface winds from SAR images requires a-priori knowledge of the wind direction, the angle between the wind direction and the radar look direction, the SAR incidence angle as well as accurate Normalised Radar Cross Section (σ0) measurements. These parameters were directly derived from the ASAR images except for the wind directions which were sourced from the National Center for Environmental Prediction (NCEP) Climate Forecast System Reanalyses (CFSR). The CFSR reanalyses are available at an hourly temporal resolution and a spatial resolution of 0.3° between 1979 and March 2011 and 0.2° beyond March 2011 (CFSv2 product) (Saha et al., 2014). CFSR therefore has a much lower spatial resolution than the ASAR dataset and is not expected to show much spatial variability near the coast. All ASAR images were calibrated to units of σ0 using the open-source NanSat (https://github.com/nansencenter/nansat) 22 python module. For each image, the σ0 was down-sampled from a resolution of 150 m x 150 m to 1 km x 1 km grid using Lanczos spatial interpolation. Wind directions from the CFSR dataset were interpolated onto the ASAR NRCS 1 km grid and the predicted wind direction closest in time to the ASAR image acquisition were selected. The CMOD5.N Geophysical Model Function (GMF) (Verhoef et al., 2008) was then applied to provide estimates of the equivalent neutral wind speeds 10 m above the ocean's surface. Winds from the CFSR product were bi-linearly interpolated onto the 1 km ASAR grid to allow inter-comparisons between the ASAR and CFSR wind speeds. The post-processing of the data involved removing spurious data present along the edge of the ASAR image swath associated with wind speeds below 1 $m.s^{-1}$.

Hourly values of the CFSR wind speed and direction inside the Cape Town offshore box (Fig. 1(b)) are extracted to identify the predominant offshore wind directions. The SAR winds derived over the LCP area are then grouped into these 2 predominant wind directions and averaged over time to provide composite images. These composites are then used to image the typical spatial variability experienced over the LCP during the 2 predominant wind direction regimes. The differences between the model (CFSR) and observed (SAR) winds speeds are then derived to quantify the mean bias between the modelled and the observed dataset.

Results

Winds offshore Cape Town between 2008 and 2012 were predominantly aligned along a NW/ SE axis with a larger proportion of SE winds occurring during the summer season (Fig. 2). Using the hourly CFSR product, we estimate that about 80% of the variability can be explained by wind variations occurring along that axis. In a recent review on False Bay, Pfaff et al., (2019) used 20 years of daily CFSR winds to show that

seasonal shifts in the latitude of the South Atlantic Anticyclone cause winds to reverse from a predominant SE direction in summer to a NW direction in the winter, with 80% of the variance explained by winds blowing along the NW/SE axis. Based on these findings, the SAR wind data were therefore grouped into the two dominant SE and NW wind regimes. The main objective of this approach was to provide maps of the typical spatial variability experienced over the LCP region during both SE and NW wind conditions. Over the 2008-2012, a total of 63 ASAR images were collected during SE wind conditions over the LCP region, with most acquisition occurring over the False Bay region and to the south and south-east of False Bay. Less ASAR images were available during NW wind conditions, with a total of 24 images over the LCP region. Based on Fig. 2(d), the range of wind speeds observed by ASAR is diverse enough and the composites should provide an accurate representation of the time-averaged spatial wind distribution over the LCP region during both SE and NW wind regimes.

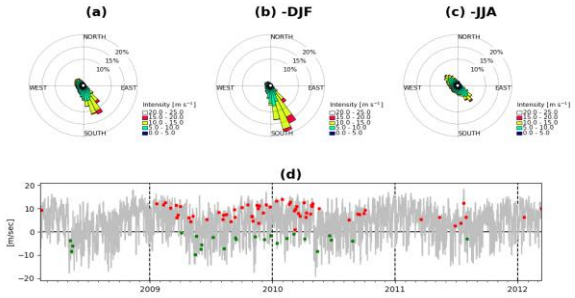

Figure 2: Wind Roses from the hourly CFSR product extracted at the offshore Cape Town box and over 2008-2012 period. The legend indicates wind speeds in m/sec. (a) shows the frequency distribution of the winds for all data points. (b) shows the winds distribution over the austral summer months of December-January-February (DJF) and (c) over the austral winter months of June-July-August (JJA). (d) Time-series of the CFSR winds at the offshore Cape Town box aligned along a NW/SE axis. Markers showing instances of SAR SE (red) and NW (green) winds.

Figs. 3(a) and (c) show wind speeds dropping off towards the coast in both SE and NW wind conditions with stronger winds generally experienced in water depths greater than 200 m and the gradient in the wind speed directed along the predominant wind direction (along a NW/SE axis). This drop in wind speed is significant for both SE and NW wind conditions, with offshore wind speeds typically 4 $m.s^{-1}$ stronger or more. During SE winds (Fig. 3(a)), the strongest winds occur over the south-west of the LCP region, south of False Bay. SE winds are generally associated with calm conditions in the north-west region of the LCP, near the Cape Columbine headlands (33°S) and further north. During NW winds (Fig. 3(b)), the strongest winds are generally found in the south and south-eastern LCP region. Calm conditions during NW wind events are encountered north of the Cape Peninsula and in over water depth shallower than 200 m.

Since the CFSR product shows little spatial variability over the region (not shown) due to its coarse spatial resolution, the differences between the ASAR and the CFSR wind speeds can be used to reveal the magnitude and extent of the spatial variability in the LCP region. One of the most striking features observed in the SE regime, is a fan-shaped wind shadow in False Bay which extends from Kogel-Bay to Kalk Bay, over a length of about 30 km. It is approximately 25 km at its widest along the western coastline of the bay. The lower winds within the shadow are only blowing at around 5 $m.s^{-1}$, compared to the surrounding winds which blow at over 12 $m.s^{-1}$ (Fig. 3(a)). As seen in Fig. 3(b), variations in wind speeds of about 10 $m.s^{-1}$ can be experienced within a few kilometers as one travels from the north-east corner of False Bay to the mouth of the bay. Another wind shadow, visible in the lee of Table Mountain, extends about 15 km at sea and is approximately 10 km wide (Figs. 3(a) and (b)). In the lee of Table Mountain winds are typically 2$m.s^{-1}$ weaker than in surrounding waters during SE winds.

During SE winds there appears to be a region of accelerating winds extending from Cape Hangklip to the tip of the Cape Peninsula. When the offshore winds blow from the south-east, the winds over the eastern LCP regions have a most easterly component. It is thought that the presence of the Hottentot Mountain range near Cape Hangklip causes the predominantly easterly winds to accelerate and be deflected towards the south-west along Cape Hangklip. We note that this topographic steering of the winds by the orography is clearly not captured in the CFSR product.

The spatial variability patterns during NW winds are not as distinct as those observed during SE wind events. Variations in wind speeds are however present in False Bay with the north-western corner of the bay being more sheltered from the winds (Figs. 3(c) and (d)). Winds in the north-west corner of the bay are typically 4 to 5 $m.s^{-1}$ weaker than those on the eastern side of the bay. We note that NW winds are also associated with locally intensified winds in the lee of Cape Hangklip.

Figs. 3(b) and (d) show large discrepancies between the CFSR and SAR wind speeds. CFSR tends to largely over-estimate the winds in the region north-west of the Cape Peninsula, and under-estimates the winds further at sea. In a SE wind regime, the region of discrepancy between the CFSR and SAR winds extends further north towards the north-west, from 34°S to 32°S (Fig. 3(b)).

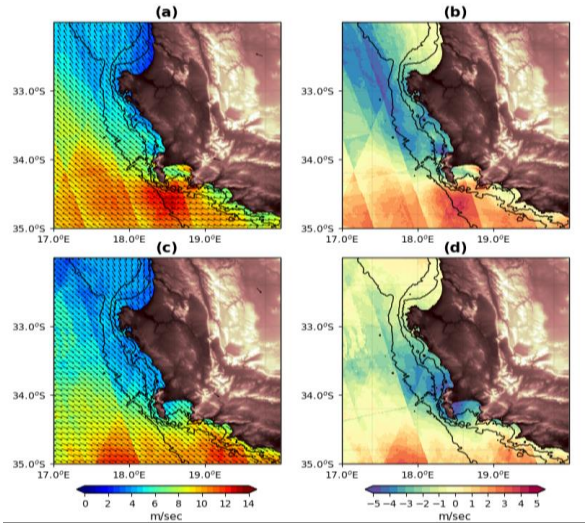

Figure 3: Composite of SAR winds during (a) SE and (c) NW winds. The overlaid arrows represent wind directions interpolated from the CFSR product. Panels (b) and (d) are time-averages of the differences between the ASAR and CFSR windspeeds during (b) SE and (d) NW winds. The black contour lines in all panels show the location of the 50m, 100m and 200m isobaths.

Conclusions

Winds are the strongest driver of sea state, ocean circulation and upwelling in the LCP region. Local orography, coastal geometry and differences in temperature between the ocean and the adjacent land masses drive a high spatial and temporal variability in coastal winds through processes such as land/sea breezes, wind shadows or funnelling effects. The high spatial variability which characterises the LCP regions is not captured in the low resolution (25 km) and land contaminated (within 50 km of the coast) wind products, which are currently used to force all oceanic and atmospheric South African numerical models. This impedes our ability to monitor and predict the coastal marine environment. Using observations collected over 5 years, we demonstrated the ability of satellite-based SAR sensors to image and characterise small scale spatial variations in coastal regions. The development of an improved observing capability for high resolution wind observations near the coast will lead to better sea-state monitoring and predictions and serve a wide a range of users such as the South African Maritime Safety Authority (SAMSA), Fishery industry, Shipping or Port Authorities. Examples of downstream benefits include improved predictions of harmful algal blooms, coastal erosion, storm surge, and wave propagation.

Acknowledgement

Dr. Krug was funded by the CSIR-NRE PG project EEEO057. The ASAR wind data was processed using the CSIR Centre for High Performance Computing (CHPC) infrastructure with support from the ACE Lab.

References:

Capet, X. J., Marchesiello, P., & McWilliams, J. C. (2004). Upwelling response to coastal wind profiles. Geophysical Research Letters, 31(13).

Jury, M. R. (1987). Aircraft observations of meteorological conditions along Africa's West Coast between 30–35 South. Journal of climate and applied meteorology, 26(11), 1540-1552.

Lett, C. , Roy, C. , Levasseur, A. , Van Der Lingen, C. D. and Mullon, C. (2006), Simulation and quantification of enrichment and retention processes in the southern Benguela upwelling ecosystem. Fisheries Oceanography, 15: 363-372. doi:10.1111/j.1365-2419.2005.00392.x.

Pfaff, M. C., Logston, R. C., Raemaekers, S. J., Hermes, J. C., Blamey, L. K., Cawthra, H. C., & Van Niekerk, L. (2019). A synthesis of three decades of socio-ecological change in False Bay, South Africa: setting the scene for multidisciplinary research and management, Elementa: Science of the Anthropocene, 7: 32. doi: https://doi.org/10.1525/elementa.367.

Saha, S., Moorthi, S., Wu, X., Wang, J., Nadiga, S., Tripp, P., ... & Ek, M. (2014). The NCEP climate forecast system version 2. Journal of Climate, 27(6), 2185-2208.

Verhoef, A., Portabella, M., Stoffelen, A., & Hersbach, H. (2008). CMOD5. n-the CMOD5 GMF for neutral winds.

Verhoef, A., Portabella, M., & Stoffelen, A. (2012). High-resolution ASCAT scatterometer winds near the coast. IEEE Transactions on Geoscience and Remote Sensing, 50(7), 2481-2487.

Weeks, S. J., Barlow, R., Roy, C., & Shillington, F. A. (2006). Remotely sensed variability of temperature and chlorophyll in the southern Benguela: upwelling frequency and phytoplankton response. African Journal of Marine Science, 28(3-4), 493-509.

The annual cycle of turbulent latent heat flux in the Agulhas current system

M. Rouault[1,2], A. S. Nkwinkwa Njouodo[1,2,5], J. A. Johannessen[3,4]

[1]Department of Oceanography, Mare Institute, University of Cape Town, South Africa.
[2]Nansen Tutu Center for Marine Environmental Research, University of Cape Town.
[3]Nansen Environmental and Remote Sensing Research Center, Bergen, Norway.
[4]Geophysical Institute, University of Bergen, Bergen, Norway.
[5]GEOMAR Helmholtz Centre for Ocean Research Kiel, 2405 Kiel, Germany

Corresponding author :

We are using data from in-situ observations, climate reanalysis and satellite remote sensing to study the annual cycle of the turbulent flux of moisture from ocean to atmosphere also called the turbulent latent heat flux (LHF). We first assess if the various datasets adequately represent the intense exchange of moisture that occurs above the Agulhas Current system. We are using monthly fields of turbulent latent heat flux and various parameters used to calculate the LHF: sea surface temperature (SST), surface wind speed, saturated specific humidity at the temperature of the sea surface (Qsst) and air specific humidity at 10 m height (Qa). We use MODIS SST and the satellite derived QuikSCAT SCOW wind climatology as reference for SST and surface wind. Compared to MODIS SST, all products underestimate the SST in the core of the Agulhas Current. The differences in LHF are due to the difference in Qa and surface wind speed. We study the annual cycle of the LHF and its drivers in four locations of the Agulhas Current system: offshore Durban; offshore Port Elizabeth; in the Retroflection area and in the shelf water offshore Cape Town outside of the Agulhas Current system. The highest LHF of about 250 W/m² is found in the Retroflection area in winter. The lowest LHF is 100 W/m² off Port Elizabeth in summer. In Durban, Qsst - Q10 is the main driver of the amplitude of the annual cycle of LHF. The annual cycle of LHF follows the wind speed in the Retroflection area. Both Qsst - Q10 and wind speed variations drive the annual cycle of LHF off Port Elizabeth.

Introduction

The greater Agulhas Current system is composed of the core of the Agulhas Current which is about 100 km wide; the Retroflection region with a loop diameter of 350 and the Agulhas Return Current that meanders in an eastward direction. Substantial turbulent latent heat fluxes as well as marine boundary layer modification were measured above the core of the Agulhas Current, the Retroflection region and the Agulhas Return Current (Rouault et al., 2000)]. These measurements show that the turbulent latent heat flux which is akin to the turbulent flux of moisture at the air-sea interface increases substantially in the Agulhas Current system. Gimeno et al., (2010) showed that the Agulhas Current system is a source of moisture for the Southern Africa rainfall. Nkwinkwa Njouado et al. (2018) linked the high LHF to higher rainfall above the current and at the coast adjacent to the current. The turbulent latent heat flux is underestimated in models if the resolution does not represent the SST field within the core of the current that is about 100 km wide (Rouault et al., 2003). The core of the Agulhas Current is important because of its thermal contrast with the surrounding water leading to a fivefold increase in the turbulent fluxes of latent heat. Radiosondes launched during the ACASEX cruise show that the core of the current literally produces a wall of moisture (Rouault et al., 2000) that can reach up to 2000 m above the Agulhas Current. The LHF measured above the Agulhas Current were not well reproduced in older climate reanalysis (NCEP1, NCEP2 and ERA40). However, recent reanalysis for ERA-Interim, ERA5, CFSR and MERRA-2 are now available at a higher resolution. At the same time numerous new air sea interaction datasets derived from satellite remote sensing such as SEAFLUX (Curry et al., 2004) have been produced at a resolution that allows to represent the core of the Agulhas Current. The aim of this study of the air-sea exchanges in the Agulhas Current system is threefold: (i) explore whether the new climate reanalysis and satellite derived datasets have sufficient spatial resolution and representations of the LHF; (ii) examine the magnitude of uncertainties in the basic parameters (wind, SST, surface specific humidity) used to calculate the LHF; and (iii) quantify the annual cycle of the LHF and its drivers in the Agulhas Current system.

Data and method

Various parameters are analysed including, latent heat flux, sea surface temperature (SST), surface wind speed at 10 m, specific humidity of air at 10 m (Qa) and saturated specific humidity (Qsst). Saturated specific humidity is not available for all products and is calculated using the Clausius-Clapeyron relation and the SST. The averaging periods are ranging from monthly to seasonal and are constrained by the availability of satellite datasets. When datasets were

not available at the same period, for example ERA-40 we used the same amount of time (8 years) for the averaging to have a consistent result. We analysed the gridded monthly data (version 2) derived from the National Oceanography Centre Southampton (NOCS) based on Voluntary Observing Ship (VOS). Two satellite-based data products are used, notably the third version of the Hamburg Ocean Atmosphere Parameters and Fluxes (HOAPS3) product with a spatial resolution of 0.5° x 0.5°, and the high-resolution air-sea turbulent fluxes (SEAFLUX) available on a grid of 0.25° x 0.25° (Curry et al., 2004). The Moderate Resolution Imaging Spectroradiometer (MODIS) is used to provide reference SST data because of its very high resolution (4 x 4 km) that evidently represents the fine spatial structures of the Agulhas current, especially near the coast. The Scatterometer Climatology of Ocean Winds (SCOW) is used as reference wind speed and direction in this study. Five reanalysis products are used. The Climate Forecast System Reanalysis (CFSR, MERRA-2, ERA-Interim, ERA 40 and NCEP)

Results

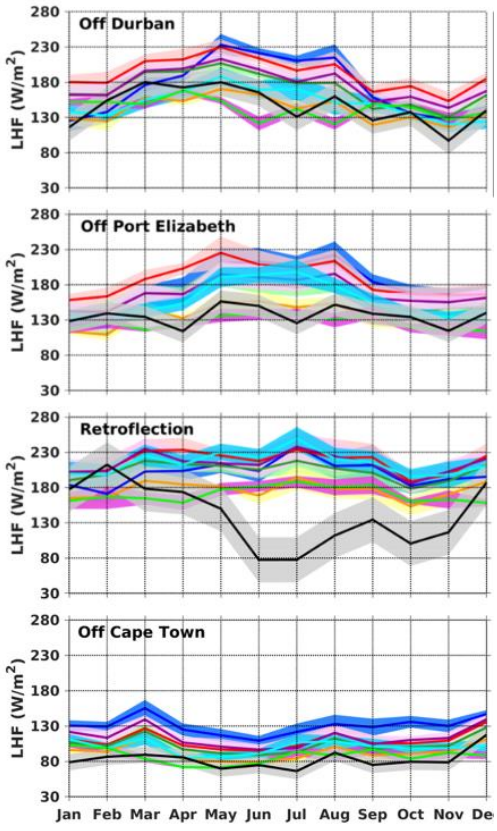

Figure 1: Annual cycles of latent heat flux (W/m²). In Agulhas Current off Durban (31.5-32.5°E; 30-31°S), off Port Elizabeth (25-26°E ; 34.5-35.5°S), Agulhas Retroflection (19-20°E ; 38-39°S) and off Cape Town (16-17°E ; 33.5-34.5°S) for SEAFLUX (blue), CFSR (red), MERRA-2 (green), ERA-5 (purple), ERA-Interim (yellow), NCEP2 (cyan), ERA-40 (purple), and NOCS (black). Shades areas represent the standard errors calculated as the standard deviation divided by the square root of the number of years.

In this paper, the first objective is to investigate whether the recent climate reanalyses (CFSR, MERRA-2, ERA-5 and ERA-Interim), satellite-based (SEAFLUX and HOAPS3) and in-situ observation-based (NOCS) LHF products have a good representation of the intense turbulent flux of moisture that occurs above the Agulhas Current, compared to older reanalyses (ERA-40 and NCEP2), because the Agulhas Current is not adequately resolved in the coarser-resolution (ERA-40 and NCEP2). HOAPS3 compares quite well with SEAFLUX, but HOAPS3 does not have data along the coast. Compared to the SEAFLUX LHF, the ERA-40 and NCEP2 LHF fail to represent the structure of the Agulhas Current. The new reanalysis products, on the other hand, have a better representation of the current, therefore, can adequately represent the LHF in the Agulhas Current system, except ERA-Interim that underestimates the fluxes. CFSR is relatively like MERRA-2 and ERA-5 but has higher LHF. Between the four new reanalyses, surprisingly ERA-Interim has the lowest fluxes (100-200 W/m²). This result is unexpected in view of the higher spatial resolution of the ERA-Interim (0.75° x 0.75°) compared to ERA-40 (2.5° x 2.5°). It is most likely due to its low wind speed although the LHF is compensated by high values of Qsst-Qa. The improved version of ERA-Interim (ERA-5) represents better the LHF in the Agulhas region. The phase of the seasonal cycle of NOCS LHF is reversed in the Retroflection region compared to other products. This might indicate that not enough vessels pass through the Agulhas Retroflection region. Another reason for the uncertainties in NOCS is due to measurement uncertainty. To conclude, CFSR, MERRA-2, and ERA-5 show good representation of the Agulhas Current and will be used for further analysis to investigate the relation between the intense flux of moisture over the Agulhas Current and the weather and climate in Southern Africa, and to validate mesoscale atmospheric models such as the Weather Research and Forecasting model (WRF)

The second aim of this study is to identify the level of uncertainties introduced by the basic parameters: SST, wind (U), surface specific humidity (Qa), ocean current (Us) used to estimate the LHF (e.g. Equation 1)

$$LHF = \rho_a C_E l_v |U - U_S|(Qsst - Qa) \quad (1)$$

The differences between each product and the reference products from MODIS are calculated for SST, SCOW for wind speed and SEAFLUX for Qsst-Qa. CFSR SST is higher than MERRA-2 SST compared to MODIS SST. This may explain higher values of the LHF from CFSR compared to MERRA-2, as SST is used to compute Qsst. Between all the new reanalyses, MERRA-2 has the highest wind speed and CFSR the highest Qsst-Qa. ERA-Interim has the weakest wind speed in the Agulhas system compared to SCOW. This explains the lowest values of the ERA-Interim LHF. In the Agulhas Current system, CFSR and MERRA-2 wind speed are similar. ERA-Interim has the strongest Qsst-Qa compared to other reanalyses. This compensates for the low wind speed in the calculation of ERA-Interim LHF but not enough. Qsst-Qa variability is mostly influenced by the variation of Qa. The differences in Qa between the products clearly have a greater impact than the discrepancies in wind speed and ocean surface temperature. For the satellite-based products, the retrievals of air temperature (Ta) and specific humidity (Qa) at the surface continue to be problematic in regions with strong vertical gradients. Another source of specific uncertainties for the reanalyses is incomplete account of the surface current speed. Looking at the annual mean of the Agulhas Current from the GlobCurrent data repository, the surface current speed can be more than 1.5 m/s. During the ACASEX (Rouault el al., 2003), Surface current speeds of up to 2 m/s were measured. Thus, neglecting a 2 m/s current speed at a near-surface wind speed of 4 m/s may lead to a 50% error in the LHF estimation.

Finally, the annual cycle of the LHF and its drivers in the Agulhas Current system is investigated using SEAFLUX. SEAFLUX is used to recalculate the LHF using a climatology Qsst-Qa and/or wind speed, as it has a high spatial resolution (0.25° x 0.25°) and reliable SST and wind speed [45]. Three locations, representative of various regions of the Agulhas Current system (off Durban, off Port Elizabeth and Retroflection) and one point outside the Agulhas system (off Cape Town) were selected for the comparison. In the Agulhas Current system, the lowest LHF of 100 W/m² is found off Port Elizabeth in late summer. In contrast, the largest LHF of ~250 W/m² is in the Retroflection region in winter. In the Agulhas Retroflection region, large values of LHF are due to stronger wind speed in the Retroflection area. Off Durban higher values of the LHF can be explained by the difference of specific humidity. Off Port Elizabeth and Cape Town, values of LHF can be explained by the combination of Qsst-Qa and the wind speed. On a shorter timescale (5-day averages climatology), correlation between LHF and wind speed is higher off Port Elizabeth, in the Retroflection region and off Cape Town. Off Durban, the correlation is low. Therefore, the wind speed could not be the main driver of the amplitude of the annual cycle of LHF in this region. To summarize, off Durban, LHF is mostly driven by the surface specific humidity. In the Retroflection region LHF is mostly driven by the wind speed. Off Port Elizabeth it is a combination of the specific humidity and the wind speed.

References

Curry et al. (2004), SEAFLUX. Bull. Amer. Meteor. Soc., 85,409-424.

Gimeno, L., A. Drumond, R. Nieto, R. M. Trigo, and A. Stohl (2010), On the origin of continental precipitation. Geophysical Research Letters, 37(13).

Nkwinkwa Njouado, A.S., Koseki, S., Keenlyside, N. and Rouault, M., 2018. Atmospheric signature of the Agulhas Current. Geophysical Research Letters. 45, 5185-5193, doi:10.1029/2018GL077042.

Rouault, M., A. M. Lee-Thorp, and J. R. E. Lutjeharms (2000), Observations of the atmospheric boundary layer above the Agulhas Current during along current winds. Journal of Physical Oceanography, 30, 70-85

Rouault, M., C. J. C. Reason, R. E. Lutjeharms, and A. Beljaars (2003), NCEP Reanalysis and ECMWF operational model underestimation of latent and sensible heat fluxes above the Agulhas Current, Journal of. Climate, 16, 776-782

3. ATMOSPHERIC AIR QUALITY

Investigating the role of near-surface atmospheric boundary layer moisture flux in supercellular tornadogenesis over Gauteng during December 2017

Lesetja E Lekoloane, Mary-Jane M Bopape and Tshifhiwa G Rambuwani

Research and Development, South African Weather Service, Pretoria, South Africa

Corresonding author:

The state-of-the-art ERA5 reanalysis dataset from the European Centre for Medium-Range Weather Forecasts (ECMWF) is used to investigate the role of near-surface atmospheric boundary layer (ABL) moisture flux in supercellular tornadogenesis over Gauteng in December 2017. It was found that negative near-surface ABL moisture flux, in association with maximum water vapour concentration, played a role in tornadogenesis of the two supercells examined. This may be a significant pattern but more cases need to be analysed to come to a substantial statistical conclusion, including an examination of the influence of ABL turbulent fluxes of thermodynamic and kinematic parameters in inducing higher amounts of water vapour needed for tornadogenesis.

Keywords: Tornadoes, Surface fluxes, Climatology, South Africa, Severe thunderstorms

Introduction

Tornadogenesis, a process by which a tornado initiates, is one of the most complex and less understood physical phenomena. This is especially attributed to the various thunderstorms and environments from which tornadoes could initiate, and the difficulty in observing the very fine scale processes at high temporal resolutions (Doswell III *et al.*, 1993). Besides well-funded field projects like VORTEX (www.vortex2.org), the advent of high performance computing has allowed numerical modelling of tornadoes at grid spacing of several meters, making it possible to study the evolution of some of the most destructive tornadoes on record.

An increasing number of studies utilising numerical models (e.g. Yokota *et al.*, 2018; Markowski and Richardson, 2009; Thompson *et al.*, 2003) agree on at least two important ingredients needed for tornadogenesis in supercell thunderstorms: an abundance of water vapour concentration and large vertical vorticity in the atmospheric boundary layer. These two ingredients have been found to contribute to tornadogenesis by modifying the environment to allow the formation of intense vortices associated with tornadoes.

The atmospheric boundary layer (ABL) is the lowest part of the troposphere which is directly influenced by the presence of the Earth's surface making it variable in space and time (Stull, 1988). Horizontal and vertical transportation within the ABL, which allows for mixing and exchange with the free atmosphere above, is highly driven by turbulent fluxes of heat, moisture, and momentum (Stull, 1988).

Turbulent near-surface fluxes in particular, serve as sinks or sources of thermodynamic and kinematic parameters and significantly impacts the evolution of the entire ABL, cloud formation, concentration of pollutants and the initiation of some thunderstorms (Sun *et al.*, 2017). This means that to further understand tornadogenesis, there needs to be an investigation of the influence of these fluxes. An understanding of these turbulent fluxes in relation to tornadic supercell thunderstorms is also important for improved parametrisation of the ABL in numerical models, which acts as a coupler between surface processes and the rest of the free atmosphere and its evolution at all timescales.

The Highveld region of South Africa is notoriously known for its severe convective weather, which is especially in the form of severe thunderstorms during summer months (Gijben, 2012). Some of these severe thunderstorms are distinguished by a deep rotating updraft, and are therefore specifically classified as supercell, from which some result in tornadoes.

The month of December 2017 saw two tornadic supercell thunderstorms impact the Highveld of Gauteng Province. The first was on the 11th from which a tornado was observed in the Vaal Marina area at around 1530 UTC and destroyed much property, leaving at least 1100 people displaced (SAWS, 2018). The second resulted in a tornado in Protea Glen, Soweto, on the 30th, at around 1440 UTC from which reports indicate that property was damaged and a few people got injured (eNCA, 2017). The main objective of this study is to investigate the role of near-surface

ABL moisture fluxes in the tornadogenesis of these two supercell thunderstorms.

Data and Methods

ERA5 monthly averaged and hourly data on single levels from the European Centre for Medium-Range Weather Forecasts (ECMWF) are utilised in this study. The ERA5 dataset is the state-of-the-art atmospheric reanalysis of the global climate produced by the ECMWF (Hersbach and Dee, 2016). This reanalysis is performed using the 2016 ECMWF model cycle (41r2) and an assimilation of hundreds of thousands of daily global observations, including those from the South African observational network through the World Meteorological Organisation's (WMO's) Global Telecommunication System (GTS) (Haiden *et al.*, 2018). Some of the data collected over the southern African domain and the surrounding oceans include those from synops, METAR's, satellites, radiosondes, buoys, weather stations, ships and aircrafts. Table 1 lists a summary of the dataset used in this study.

Table 1: Description of ERA5 dataset used in this study.

Coverage	Global (in this study: 18° to 38° S, 15° to 45° E)
Horizontal resolution	0.25°×0.25°(atmosphere) 0.5°×0.5°(ocean waves)
Vertical levels	137 up to 1 Pa
Temporal resolution	Hourly
Assimilation system	2016 ECMWF model cycle (41r2), 4D-Var

The dataset is analysed for the southern African domain, including the immediate oceans south and south-east of the continental coastline (18° to 38° S, 15° to 45° E). A particular focus of the analysis is also given to Soweto (coordinates: -26.27, 27.85) and Vaal Marina (coordinates: -26.88, 28.23) in the Gauteng Province of South Africa. The meteorological parameters contained in the data are the surface pressure, 2-metre dewpoint temperature, 10-metre meridional and zonal wind components.

The near-surface ABL moisture flux is computed by taking the product of saturation specific humidity and horizontal wind vectors respectively at 2 and 10 metres above the surface as indicated in Eq. 1 below.

$$\vec{Q} = q_{sat}\overrightarrow{V_h} \qquad (1)$$

q_{sat} is used in order to represent the maximum amount of water vapour reached at saturation and is measured in gkg^{-1} while $\overrightarrow{V_h}$ is measured in ms^{-1}.

For measuring $\vec{Q}$, q_{sat} is converted to $kgkg^{-1}$, so that it is measured in $kgkg^{-1} \cdot ms^{-1}$.

The near-surface saturation specific humidity is calculated as a function of saturation water vapour pressure

$$q_{sat} = \frac{\frac{R_{dry}}{R_{vap}} e_{sat}(T)}{p - \left(1 - \frac{R_{dry}}{R_{vap}}\right) e_{sat}(T)} \qquad (2)$$

where the saturation water vapour pressure is expressed with the Teten's formula and measured in .

$$e_{sat}(T) = a_1 exp\left\{a_2\left(\frac{T - T_0}{T - a_3}\right)\right\} \qquad (3)$$

where constants $a_1 = 611.21\,Pa$, $a_2 = 17.502$ and $a_3 = 32.19\,K$are set for saturation over water, and $T_0 = 273.16\,K$. The gas constants$R_{dry} = 287.0597\,J\,kg^{-1}\,K^{-1}$ and $R_{vap} = 461.5250\,J\,kg^{-1}\,K^{-1}$ are respectively for dry air and water vapour. The variable T represents dewpoint temperature at 2-meters above the surface, while p is the surface pressure which is approximately equal to the pressure at 2-meters above the surface.

These equations, variables and constants are together used to calculate specific humidity which represents the amount of ABL near-surface water vapour. A 32-year climatology of ABL near-surface water vapour and moisture flux for the month of December is then created for the study area from 1985 to 2016, with hourly data used for the analysis of the environments of two tornadic supercell thunderstorms in Vaal Marina and Soweto during December 2017.

Results and Discussion

A 32-year climatological analysis for the month of December captures near-surface ABL moisture content that is variable especially between the western and eastern parts of South Africa. Fig. 1a indicates that areas east of the Drakensburg mountain range of Limpopo, Mpumalanga and KwaZulu Natal provinces have relatively higher values of near-surface specific humidity compared to the rest of South Africa during the December month. This is an indicator that those areas have statistically higher amounts of near-surface water vapour in South Africa during December. The analysis also indicates that the western parts of South

Africa are relatively drier near the surface during the analysis period. Within the analysis domain, it was also found that most of the water vapour near the surface is located in the Mozambique Channel.

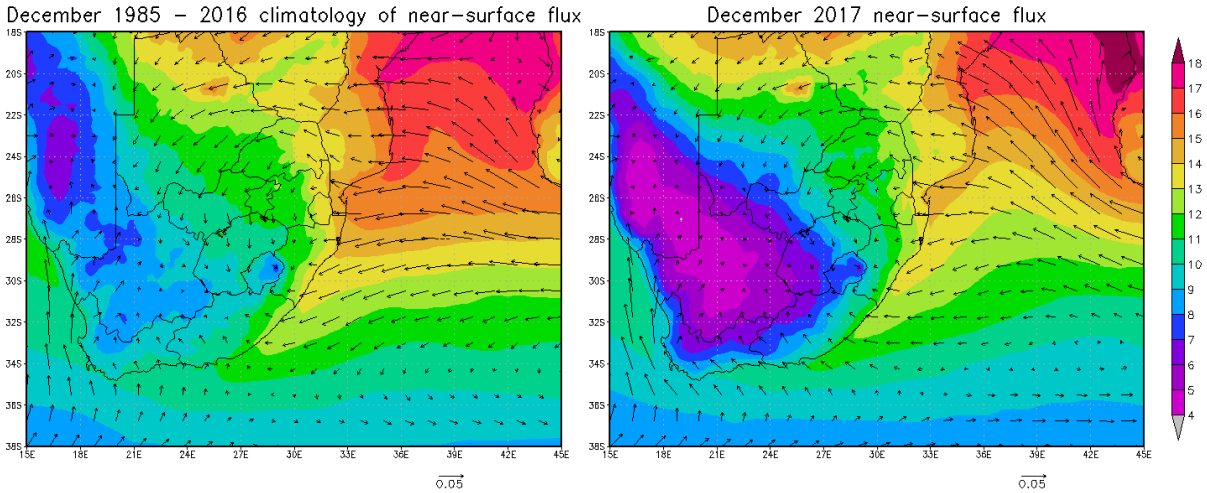

Figure 1: An analysis of near-surface ABL specific humidity (shaded, interval of $1 g kg^{-1}$) and moisture flux (vector, in $kg kg^{-1} \cdot ms^{-1}$). (a) Indicates a December 32-year climatology from 1985 to 2016, while (b) indicates a December 2017 mean.

Computations of the near-surface moisture flux indicates that, climatologically, most of the water vapour in the North West, Limpopo, Free State, Mpumalanga, KwaZulu Natal and Gauteng Provinces (hereafter together referred to as eastern parts of South Africa) during the December month originates particularly from the southern part of the Mozambique Channel and the South West Indian Ocean (SWIO). On average, the near-surface specific humidity in Soweto during the December month is 11.55 g/kg while in Vaal Marina is 11.65 g/kg.

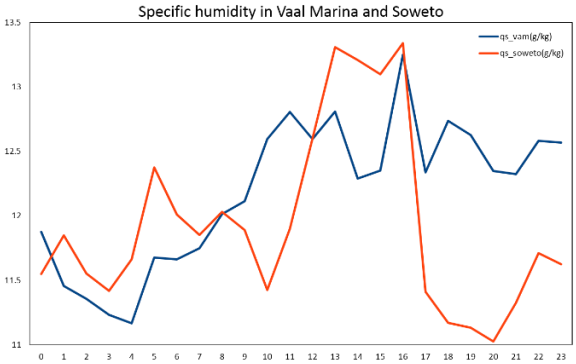

Figure 2: A time series for near-surface ABL specific humidity (in) in Vaal Marina (blue) and Soweto (red) on 11 December 2017 (for Vaal Marina) and 30 December 2017 (for Soweto).

Fig. 1b indicates that during December 2017, on average, the South African inland and southern part of the Mozambique Channel ABL near the surface were less moist compared to the climatology. Soweto and Vaal Marina were about 1 g/kg less moist (respectively about 10.55 g/kg and 10.65 g/kg). This suggest that less moisture was being advected into Gauteng Province.

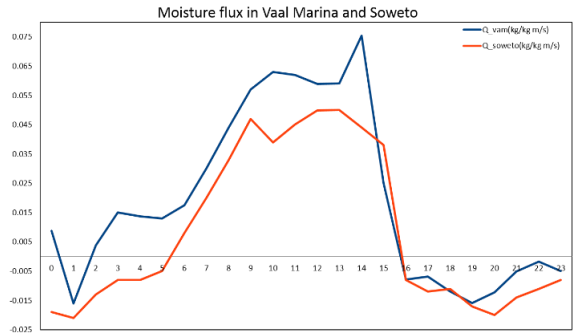

Figure 3: A time series for near-surface ABL moisture flux (in) in Vaal Marina (blue) and Soweto (red) on 11 December 2017 (for Vaal Marina) and 30 December 2017 (for Soweto).

On the contrary, Vaal Marina and Soweto, were relatively more moist compared to the climatology and the 2017 mean on 11 December and 30 December respectively. On those respective days, the average near-surface specific humidity in Vaal Marina was 12.19 g/kg and in Soweto was 11.94 g/kg.

An analysis of Vaal Marina ABL near-surface on 11 December indicates that a maximum specific humidity of 13.25 g/kg was reached at 1600 UTC which is higher than the day mean of 12.19 g/kg (Fig. 2). The same analysis in Soweto on 30 December also

indicates that maximum specific humidity was reached at 1600 UTC, but was 13.34 g/kg (with an almost equal spike of 13.31 g/kg at 1300 UTC) and also higher than the day mean of 11.94 g/kg. This is significant because tornadoes in Vaal Marina and Soweto were respectively observed around 1530 UTC and 1440 UTC. This suggest that around the time of tornadogenesis in supercell thunderstorms reported in those two areas, there was a maximum increase in the ABL near-surface water vapour.

Fig. 3 respectively indicates a time series for near-surface ABL moisture flux () in Vaal Marina and Soweto on 11 and 30 December 2017. This reveals that at 1600 UTC (during the time of maximum water vapour in both areas) there was a sudden reversal of moisture flux from positive to negative. Mathematically, positive flux indicates that the area is acting as a source of moisture, while negative flux implies that it is a sink of moisture. Hence positive (negative) flux indicates that there is more moisture leaving (entering) the area than entering (leaving) it.

This is a significant pattern, as it suggest that in the near-surface ABL, negative moisture flux corresponds to maximum water vapour during the time of supercell tornadogenesis. This means that for the two cases examined, for a tornado to initiate, the near-surface ABL had to contain relatively higher amounts of water vapour which are associated with negative moisture fluxes, at least in the storm's or near the storm's environments. Therefore, near-surface ABL moisture fluxes, in association with water vapour concentration, seem to have played a role in the December 2017 supercellular tornadogenesis over the Gauteng Province.

Conclusion

A 32-year climatological analysis during the December month indicates that moisture fluxes are important for near-surface water vapour transport into the eastern parts of South Africa, and seem to originate from SWIO and the Mozambique Channel.

An examination of two cases of observed tornadoes in Vaal Marina and Soweto during December 2017, revealed that negative near-surface ABL moisture fluxes, in association with maximum water vapour concentration, played a role in supercellular tornadogenesis. This role may be significant, but more cases of tornadic supercell thunderstorms need to be analysed to make a substantial statistical conclusion.

The results of an extended study similar to this may contribute toward a probabilistic prediction of tornadogenesis in supercell thunderstorms over South Africa. It is of interest to also look at the role of ABL heat (sensible and latent) and momentum fluxes in supercellular tornadogenesis (and their relationship with moisture flux), including the influence of turbulence on these parameters. This may help improve the parametrisation of the ABL in the numerical modelling and prediction of severe thunderstorms at different timescales.

Reference

Doswell III, C.A, Weiss, S.J. and Johns, R.H. (1993). In *The Tornado: Its Structure, Dynamics, Prediction, and Hazards*, Vol. 79, Church, C., Burgess, D. and Davies-Jone, R. (Eds.), American Geophysical Union, 557 – 571.

eNCA. (2017). Joburg mops up after storm devastation, eNCA, 31 December 2017. Available at: https://www.enca.com/south-africa/joburg-mops-up-after-storm-devastation (Acessed: 1 July 2019).

Gijben, M. (2012). The lightning climatology of South Africa. *South African Journal of Science*. 108: 1-10.

Haiden, T., Dahoui, M., Ingleby, B., de Rosnay, P., Prates, C., Kuscu, E., Hewson, T., Isaksen, L., Richardson, D., Zuo, H. and Jones, L. (2018). Use of in situ surface observations at ECMWF. *ECMWF Technical Memoranda*. 834: 1 – 26.

Hersbach, H. and Dee, D. (2016). ERA5 reanalysis is in production. *ECMWF Newsletter*. Vol. 147, p. 7. Available at: https://www.ecmwf.int/en/newsletter/147/news/era5-reanalysis-production (Accessed: 14 February 2019).

Markowski, P.M. and Richardson, Y.P. (2009). Tornadogenesis: Our current understanding, forecasting considerations, and questions to guide future research. *Atmospheric Research*. 93: 3-10.

SAWS. (2018). *Climate Summary of South Africa*. South African Weather Service. 28: 1 - 5.

Stull, R.B. (1988). *An introduction to boundary layer meteorology*. Kluwer Academic Publishers, Dordrecht.

Sun, X., Holmes, H.A., Osibanjo, O.O., Sun, Y. and Ivey, C.E. (2017). Evaluation of Surface Fluxes in the WFR Model: Case Study for Farmland in Rolling Terrain. *Atmosphere*. 8: 197 – 219.

Thompson, R.L., Edwards, R., Hart, J.A., Elmore, K.L. and Markowski, P. (2003). Close Proximity Soundings within Supercell Environments Obtained from the Rapid Update Cycle. *Weather and Forecasting*. 18: 1243 – 1261.

Yokota, S., Niino, H., Seko, H., Kunii, M. and Yamauchi, H. (2018). Important Factors for Tornadogenesis as Revealed by High-Resolution Ensemble Forecasts of the Tsukuba Supercell Tornado of 6 May 2012 in Japan. *Monthly Weather Review*. 146: 1109 – 1132.

Using different health-based metrics to assess ambient surface-ozone concentrations in South Africa

Nontsikelelo C Maduna[1] and Rebecca M. Garland[1,2]

[1]Department of Geography Geoinformatics and Meteorology, University of Pretoria
[2]Council for Scientific and Industrial Research, Pretoria

*Corresponding author:

Surface-ozone is a created in the atmosphere through photochemistry (i.e. secondary pollutant) and can negatively impact human health. In South Africa, the state of ozone pollution is assessed by using the number of exceedances of the ambient (outdoor) concentrations of the South African National Ambient Air Quality Standards (NAAQS). Using three of the Tropospheric Ozone Assessment Report exposure metrics: i) maximum daily 1-h average ozone value over the entire calendar year, ii) maximum daily 8-h average over the entire calendar year, iii) the 4th highest daily maximum, were assessed together with the number of exceedances per year of South African NAAQS, ambient surface-ozone concentrations in South Africa were assessed. The study looked at four stations, Diepkloof, Ermelo, Lephalale and Witbank. The different metrics assessed different aspect of the impact of ozone on human health. . From the study it was shown that the four stations have more years that do not comply to the NAAQS than years that do comply. When the Department of Environmental Affairs set the standard for ozone, it was meant to protect human health; thus, levels that surpass that standard put health at risk. It was found here that that there are differences in the inter-annual variability between the different metrics and the exceedance count of the NAAQS, As all four of these metrics are health-based, they should be considered together when describing surface-ozone concentrations, their inter-annual variability, and trends in South Africa.

Keywords: Near-surface ozone, Human health, Air pollution, Air quality

Introduction

Ozone is a secondary pollutant that is created through complex photochemical reactions that take place in the atmosphere (Monks, et al., 2015).. Surface-ozone can have variable atmospheric lifetimes (Monks, et al., 2015).In the free troposphere, it can have an atmospheric lifetime of weeks, which can lead to long-range transport (Young, et al., 2013).However, in urban areas, the atmospheric lifetimes are generally shorter (i.e. hours) due in part to increased removal (Monks, et al., 2015).Ambient ozone concentrations can vary greatly in time and space, particularly in urban areas. Ozone has a general diurnal cycle, with very low levels at night, and a peak in the early afternoon when solar radiation (and thus formation through photochemistry) is highest.

Despite its variation in time and space and the complexity of its production, ozone's negative impact on human health is well understood and has been established. Health impacts include decreased lung function (WHO, 2000)). In an effort of improving air quality in the country, the Department of Environmental Affairs signed the Air Quality Act in 2009 and in that the National Ambient Air Quality Standards (NAAQS) were established. The standard for ozone is 61 ppb over an averaging period (running) of 8 hours, and the allowable frequency of exceedance is 11 times per calendar year. The allowable frequency of exceedance is the number of times the ambient concentrations can exceed the standard and still be in compliance with NAAQS. This metric only assesses if the 8-hr running average is above 61 ppb, and does not give information on by how much the NAAQS was exceeded. As health impacts worsen with exposure to increasing ozone, it is important to also understand the maximum levels that people are exposed to.

In this study, the health-based metrics used to assess surface-ozone concentrations in South Africa were taken from the international Tropospheric Ozone Assessment Report (TOAR) (Fleming, et al., 2018). TOAR provided an assessment of various metrics used to estimate the health risk and impacts from ozone globally.

The three chosen TOAR metrics looked at different aspects of the impact to get a holistic understanding of the ozone impacts on health.
These metrics are:

- Maximum daily 1-h average ozone value over the entire year.
- Maximum daily 8-h average over the entire year. Twenty-four 8-h running means were calculated per day, as the average concentration during that hour and the preceding 7 hours. An 8-h running mean was valid if at least 6 hours had valid O_3 measurements during the 8-hour period. A valid daily maximum 8 -h concentration was

calculated if there were at least 18 valid 8-h running means during that day.

- The 4th highest daily maximum, was computed if there was a valid daily maximum 8-h concentration on at least 70% each day (Lefohn, et al., 2016).

In addition, the number of exceedances per year of the South African NAAQS 8-hr standard of 61 ppb was used.

Data and Methods

Ground-level ozone is measured at numerous monitoring sites in South Africa. As this study focused on impacts on human health, the sites were selected by their proximity to high population centres A population density map (data from Stats SA) (Statistics South Africa, 2016) was generated using ArcGIS. This map was overlain with the South African map that has the South African Air Quality Information System (SAAQIS) monitoring sites. From that it was seen clearly that the areas with the most population and monitoring sites were in the Highveld area and Limpopo. Areas of high population density are important to look at because more people will be exposed to the measured concentrations.

The three monitoring networks that had data available for this study were Highveld Priority Area (HPA), Vaal Triangle Priority Network (VTAPA) and Waterberg-Bojanala Priority Area (WBPA). Managed by the South African Weather Service (SAWS). Since these networks did not start operating at the same time, different years were received from the networks. However, all data that the sites have collected since the beginning of their operation were received from SAAQIS (operated by SAWS). The data received were hourly averages. Once the data were received, a quality check was done to ensure all the data points represented realistic observations. The quality check involved removing negative values, repeating values and values that were way higher than the values that were in their vicinity. Then data completeness was calculated and only sites that had years with at least 70% data completeness (using hourly values) were considered. Data completeness was calculated before and after quality check was done. From the networks only four stations within these three networks (Table 1) met the criteria. When calculating the metrics, years with 70% completeness were used, which means that different years were used for each station. The years used are shown in Table 1. All calculations, including the metrics, were done using Matlab ©.

Table 1: Summary of the stations used.

Station	Coordinates	Network	Years used
Diepkloof	26.2446°S, 27.9542°E	VTAPA	2008,2009,2012,2013, 2014,2015,2016,2017, 2018
Ermelo	26.5124°S, 29.9856°E	HPA	2009,2010,2011,2012, 2013,2014,2015,2016, 2017
Lephalale	23.6665°S, 27.7448°E	WBA	2013,2014,2015,2016
Witbank	25.8728°S, 29.2553°E	HPA	2009,2010,2012,2013, 2014,2015,2016

Results and discussion

In Figure 1 it can be seen that for all four stations, the maximum daily 1-h ozone value (blue) has the highest values, followed by the maximum daily 8-h average (red) then finally the 4th highest MDA8 ozone value (green). It must be noted that the 1-h ozone value is not a true representative of how ozone is actually distributed throughout the day; instead, it only indicates the highest reading of the day.

Lephalale has the lowest ozone values with values just below 90 ppb followed by Ermelo values with values just above 110 ppb, which is then followed by Witbank with values over 140 ppb and lastly Diepkloof has the highest values with the highest being 315 ppb.

a) Diepkloof

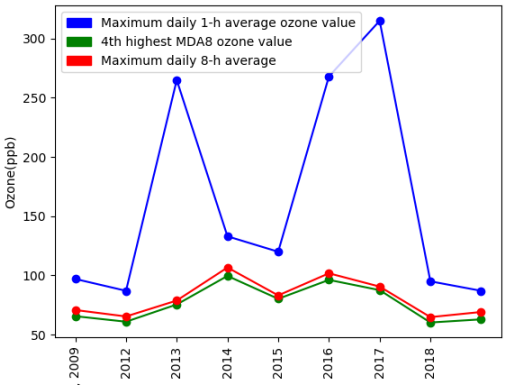

b) Ermelo

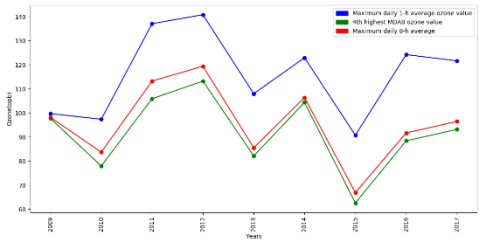

c) Lephalale

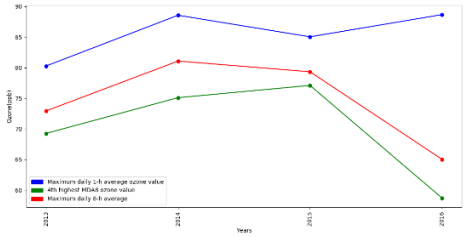

d) Witbank

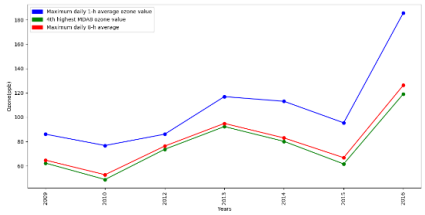

Figure 1: Maximum daily 1-h average ozone value, 4th highest MDA8 ozone value and Maximum daily 8-h average for a) Diepkloof b) Witbank c) Lephalale and d) Witbank

Figure 1 shows the three metrics calculated at the four sites. The next metric to be calculated for the stations was the number of exceedances per year of the South African NAAQS 8-hour running average greater than 61 ppb. Table 2 summarizes results for the metric. The allowable frequency of exceedance is 11, and thus all years with a value higher than 11 are seen to be out of compliance of NAAQS. As the NAAQS were set to protect health, these exceedances also indicate that health may be at risk.

Table 2: Number of exceedances of daily maximum 8-h running average values greater than 61 ppb. The gray shaded cells are years without data and the red shaded cells are years above 11 exceedances.

	2008	2009	2010	2011	2012
Diepkloof	7	3			13
Ermelo		45	21	13	62
Lephalale					
Witbank		3	0		22

	2013	2014	2015	2016	2017	2018
Diepkloof	109	54	67	65	4	2
Ermelo	42	53	11	30	25	
Lephalale	10	5	16	8		
Witbank	64	29	5	14		

All sites saw numerous exceedances of NAAQS, with 18 values above 11 out of 29 in Table 2. These exceedance counts are used by policy makers in South Africa to understand if and when ozone is a problem. If the concentrations do not exceed NAAQS, then ozone is seen to be within regulated values for that year.

However, to get a clear picture of what was happening at all the stations, all four metrics need to be used hand in hand. The number of exceedances just shows how many 8-hour running averages exceeded the standard, but it doesn't communicate by how much exactly. From a health perspective, exposure to ambient concentration of 62 ppb of ozone is not the same as 140 ppb. When calculating the number of exceedances, it is considered to be the same, which may then lead to incorrect assumptions if other metrics are not considered. A low exceedance value does not mean that the ambient ozone concentration levels were also low. With the three TOAR metrics used here (Figure 1) peak values are also considered, and different trends are seen.

Diepkloof used nine years to calculate the metrics, five out of those nine years had the number of exceedances above 11 (2012, 2013,2014, 2015 and 2016). The most exceedances were recorded in 2013. However, from Figure 1a, it can be seen that 2013 also had high values for the maximum daily 1-h average (blue line) but not for the maximum daily 8-h average (red) nor the 4th highest MDA8 ozone value (green), which peaked in 2014 and 2016. In addition, the maximum daily 1-h average (blue line) also had high levels in 2016 and 2017; the number of exceedances, however, were not the highest those years. Thus, while the number of exceedances may have been low those years, the maximum peaks were among the highest for the time period study (all three lines in Figure 1a).

Ermelo used nine years to calculate the metrics, eight out of those nine years had the number of exceedances above 11 (2009, 2010,2011, 2012, 2013, 2014, 2016, 2017). The most exceedances were recorded in 2012 From Figure 1b it can also be seen that the highest values for the other three metrics were recorded in 2012 as well. The maximum daily 1-h average (blue line) had high levels in 2011 and 2012. Similarly, both the maximum 8-h average (red) and the 4th highest MDA8 ozone value (green) also had high values in 2011 and 2012.Unlike Diepkloof, the maximum peaks for Ermelo were highest in 2012 and so was the number of exceedances.

Lephalale used four years to calculate the metrics, one year out of those four years had number of

exceedances above 11 and that year was 2015. However, from-Figure 1c, it can be seen that 2015 also had high values for the 4th highest MDA8 ozone value (green line) but not for the maximum daily 8-h average(blue). The maximum daily 8-h average peaked in 2014 and the maximum daily 1-h average peaked in 2016. However, 2014 and 2016 recorded one of the lowest exceedance values. Thus, while the number of exceedances may have been low in those two years, it was those two years that had maximum peaks for the maximum 8-h average and maximum 1-h average respectively.

Witbank used seven years to calculate the metrics, four years out of those seven years had the number of exceedances above 11(2012, 2013,2014,2016). The most exceedances were recorded in 2013. However, from -Figure 1d, it can be seen that 2013 was not the year that had the highest values for any of the three metrics. All three lines in Figure 1d show that the maximum peaks were in 2016 during the time period study. Although 2016 had a number of exceedances above 11, its 22 is lower than the number of exceedance in 2013 which was 64. Thus, while the number of exceedances may have been high in 2013 the maximum peaks were not the highest in that year. It was in 2016 that saw the highest maximum peaks.

Conclusion

From the study it was shown that the four stations have more years that do not comply to the standards than years that do comply with the standard. When the Department of Environmental Affairs set the standard for ozone it was meant to protect human health thus levels that surpass that standard become a health problem. However, to get a clear picture of what is happening different metrics need to be used. It was found here that that there are differences in the inter-annual variability between the different metrics and the exceedance count of the NAAQS, As all four of these metrics are health-based, they should be considered together when describing surface-ozone concentrations, their inter-annual variability, and trends in South Africa.

Acknowledgements

The data used in this research project was received from the South African Air Quality Information System (SAAQIS) from SAWS. The authors thank the DEA and SAWS for access to these data.

References

Fleming, Z. L. et al., 2018. Tropospheric Ozone Assessment Report: Present-day ozone distribution and trends relevent to human health. *Elementa: Science of the Anthropocene*, 6(12), pp. 1-41.

Lefohn, A. S. et al., 2016. Responses of human health and vegetation exposure metrics to changes in ozone concentratio distributions in the European Union, United States and China. *Atmospheric Environment*, Volume 152, pp. 123-145.

Monks, P. S. et al., 2015. Tropospheric ozone and its precursors from urban to global scale from air quality to short-lived climate forcer. *Atmospheric Chemistry and Physics*, Volume 15, pp. 8889-8973.

Statistics South Africa, 2016. *Statistics South Africa Data.* [Online] Available at: http://superweb.statssa.gov.za/webapi/jsf/dataCatalogueExplorer.xhtml [Accessed 23 March 2019].

WHO, 2000. *Air Quality Guidelines.* 2nd ed. s.l.:WHO Regional Publications.

Young, P. J. et al., 2013. Pre-industrial to end 21st century projections of tropospheric ozone from the Atmospheric Chemistry and Climate Intercomparison Project (ACCMIP). *Atmospheric Chemistry and Physics*, Volume 13, pp. 2063-2090.

4. ATMOSPHERIC WAVE DYNAMICS AND AEROSOLS

Investigating the correlation between surface ultraviolet radiation and Aerosol Optical Depth over Pretoria, South Africa

Bohlale Kekana and David J. du Preez

Department of Geography, Geoinformatics and Meteorology, University of Pretoria, South Africa

Corresponding author:

Surface ultraviolet (UV) radiation is affected by many factors such as ozone and aerosols. An increase in natural and anthropogenic aerosols has been observed in Pretoria over the years. Therefore, it is important to understand the effects of aerosols on UV radiation. This study will investigate the relationship between UV and aerosol optical depth over Pretoria using one year (i.e. 2016) of data. The relationship between AOD and UV was explored through a simple methodology. Firstly, the AOD and UV annual cycle was defined through graphical representation. The relationship between AOD and UV was expressed through the use of the RAF equation before the results were tabulated. Both steps used monthly averages of AOD and UV. The RAF method confirmed an undeniable relationship between AOD and UV (0.06% increase of UV caused by a 1% decrease in AOD). AOD and UV values in summer months are larger compared to the rest of the year. Since clouds play a large role in affecting the amount of UV radiation that reached the earth's surface, by considering only cloud-free days, a stronger relationship between UV and AOD can possibly be found.

Keywords: AOD, Correlation, Pretoria

Introduction

The effect of aerosols on ultraviolet (UV) radiation has not been studied as well as the effect of ozone on UV radiation (Lee, et al., 2013). With the increase of aerosols over recent years the effects of aerosols on UV radiation has become more important (Kim, et al., 2014).

UV radiation is defined as a band in the electromagnetic spectrum (Chesnutt, 2019). UV has a wavelength of 100 – 400 nm which can be divided into three categories: UV-C (100-280 nm), UV-B (280-315 nm) and UV-A (315-400 nm). UV-B radiation is a function of aerosols, cloud cover, solar zenith angle (SZA), ozone, altitude and latitude (Sahai, et al., 2000). All these parameters affect the amount of UV that penetrates the atmosphere, but aerosols, in particular, can absorb or scatter more than 50% of UV-B (NASA, 2019). Overexposure to UV-B has significant health implications on human beings including skin cancer and immunologic response (Goettsch, et al., 1998). Measuring UV radiation using the UV Index can raise public awareness on excess exposure to UV radiation (Lopo, et al., 2014).

Aerosols are fine matter suspended in the air, which are predominantly in the troposphere (Tesfaye, et al., 2011). Some aerosols are produced in nature (examples are fog, dust, and volcanic eruptions) while some are a product of human activities such as fossil fuel emissions. The degree to which aerosols hinder the transfer of light in the atmosphere is referred to as the aerosol optical depth (AOD). The long-lived effect of aerosols on the earth radiation balance happens in areas where the largest accumulation of aerosols such as smoke and dust is found (Ross, et al., 2003). The highest AOD values occur mostly in spring, predominantly in the southern parts of the hemisphere while South Africa in particular, has its highest record in mid-winter to mid-spring (June-September) (Adesina, et al., 2016).

This project aims to investigate the annual cycle of UV and AOD and to investigate the correlation between surface UV-B radiation and AOD over Pretoria, South Africa. Studies like the one of Kim, et al (2014) found that there was a negative correlation between the same parameters. By defining the cycle of UV and AOD, the investigation will get one step closer in determining if the results will match the information presented in the recently mentioned study.

Data and methods

The AOD daily data was collected from the National Aeronautics and Space Administration (NASA) online Giovanni portal for 2016. The AOD data was measured using an instrument designed for air quality and ozone measurements called the Ozone Measuring Instrument (OMI) (Ozone Monitoring Instrument, 2018).

The hourly UV-B radiation data was for a period of one year (2016) from the South African Weather Service (SAWS) for the Erasmusrand, Pretoria station. The weather station at Pretoria, South Africa (25.81° S, 28.49° E) had an altitude of 1228 m above sea level. The instrument that was used to measure UV-B was the solar light 501 UV-Biometer instrument (Cadet, et al., 2017). The UV-B data was converted from minimum erythemal dose (MED) to UV index (UVI) values. UVI describes the level of UV radiation. The equation to calculate UVI is as follows:

$$\text{UVI} = \left(\frac{\text{x}}{3600}\right) \times 40 \qquad \text{…Equation 1}$$

Where 1 MED is equal to 210 Jm^{-2}, 3600 is the number of seconds in an hour, $x = MED \times 210$ in h^{-1} and Jm^{-2} respectively.

In this paper, the radiation amplification factor (RAF) (Eq. 2) (Massen, 2013) was used to approximate the effects of a small percentage change of AOD on UV radiation. RAF is the logarithmic ratio of the comparative variations between AOD and UV radiation. The interpretation will be as follows; an increase in the percentage of UV is caused by a 1% reduction of AOD. Monthly averages of these RAFs were produced. Note that only cloudy days were used for this analysis. The following equation was used to calculate the RAF;

$$\text{-RAF} = \frac{\ln\left(\frac{UVB_1}{UVB_0}\right)}{ln\left(\frac{AOD_1}{AOD_0}\right)} \qquad \text{… Equation 2.}$$

Where UVB0 and UVB1 are the first and second UV-B radiation respectively, similarly AOD.

Results and discussion

AOD was evaluated for only one year (i.e. 2016). It can be seen (Fig. 1) that AOD average values vary from 1.10 - 1.71 throughout the year. February has the highest mean AOD value with a maximum of 2.07; while November has a peak of 4.07. Approximately 60% of 2016 has an AOD value of above 0.72. AOD seems to increase in September and thus becoming extremely high as summer sets in. The increase might be due to dust accumulation within the atmosphere, as spring is a windy dry season in South Africa. In this case, the highest AOD values do not occur in spring, but rather, spring is when the values began to increase. However, just like the article by Adesina, et al. (2016), winter (June-August) seems to carry the lowest AOD values in the year. AOD values are normally higher in areas of high population and industrialization like the study area chosen for this study (Roy, 2007). Furthermore, these factors (including cloud cover) are already at play in rising the overall average AOD values before considering the seasonal climate.

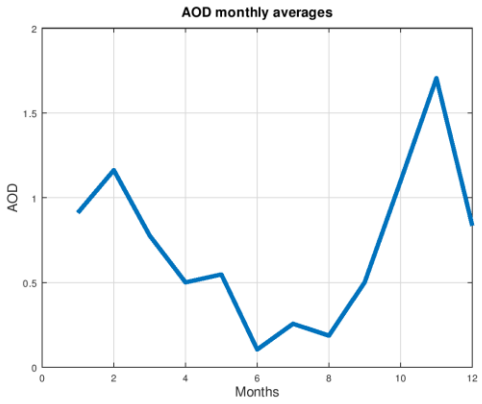

Figure 1. Monthly mean for 2016 AOD at 483.5 nm over Pretoria.

It can be observed that UV radiation (Fig. 2) has its highest (lowest) reading in summer (winter), particularly in January (June) being the month with the highest (lowest) UV average. 12 pm values are the highest because sunlight has a more direct path and passes through less atmosphere. This pattern is similar to that shown in other studies (Cadet et al. 2018).

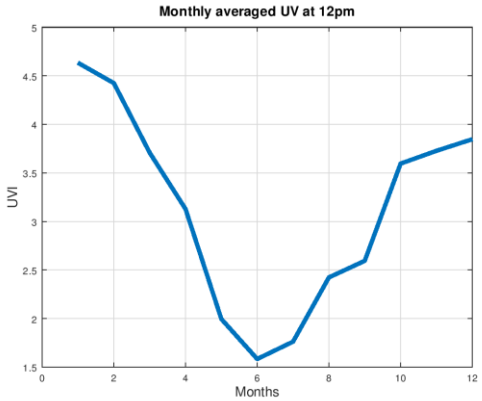

Figure 2. The monthly mean (12:00 local time) for UVI at Pretoria.

Table 1, shows that the RAF values are slightly higher in December. There are no drastic changes in the values of RAF throughout the year, except for negative values. June has the lowest value in the whole year, this could mean that the month experienced fairly low values of AOD (mean=0.1) while the UV values (mean=1.6) are relatively high (Fig. 1 and 2). Furthermore, according to research done by Prakash, et al. (2015), RAF can explain sensitivity, with large values of RAF indicating greater sensitivity of UV to AOD changes. Therefore, this could be the reason for

November having extremely high values of UV and vice versa for lower values.

June and December are minimum and maximum months of the year respectively. This means that a 1% decline in AOD led to a 0.02 - 0.65% increase in UV. The average RAF for all months is 0.06 is the year RAF average, i.e. 0.06% increase in UV with a reduction in AOD.

Table 1. Calculated RAF values for each month

Month	RAF
January	0.07
February	0.11
March	0.15
April	-0.25
May	0.08
June	0.03
July	-0.12
August	-0.12
September	0.07
October	0.15
November	-0.11
December	0.65

Conclusion

This study investigated the annual cycle of AOD and UV during 2016 as well as the relationship between AOD and UV using RAF. During summer, both AOD and UV values are the highest.

According to the RAF, there is a negative relationship between AOD and UV i.e. when UV increases, AOD tends to decrease. Even though the UV range is smaller as opposed to the AOD range in this relationship. It is apparent that cloud cover plays a major role on surface UV, so further investigations will produce a better quality of results by removing the effects of clouds. There are 134 clear-sky days that will used as the analysis proceeds.

Acknowledgements

The authors acknowledge the SAWS for providing solar UV-B radiation data for this study. The South African society of atmospheric science is also thanked for the sponsorship.

References

Adesina, A. J., Kumar, K. R. & Sivakumar, V., 2016. Aerosol-Cloud-Precipitation Interactions over Major Cities in South Africa: Impact on Regional Environment and Climate Change. *Aerosol and Air Quality Research*, Volume 16, p. 195–211.

Cadet, J.-M., Bencherif, H., Portafaix, T., Lamy, K., Ncongwane, K., Coetzee, G. J., & Wright, C. Y. (2017). Comparison of Ground-Based and Satellite-Derived Solar UV Index Levels at Six South African Sites. *International Journal of Environmental Research and Public Health*, *14*(1384), 1-15.

Diffey, B. L., 2002. Sources and measurement of ultraviolet radiation. *Methods*, Volume 28, pp.4-13.

du Preez, D., Ajtic, J., Bencherif, H., Begue, N., & Wright, J. C. (2019). Spring and summer time ozone and solar ultraviolet radiation variations over Cape Point, South Africa. *Ann. Geophys*(37), 129-141.

Earth Data NASA, 2019. *GES DISC.* [Online] Available at: https://disc.gsfc.nasa.gov/datasets/OMAERUVd_003/summary [Accessed 29 April 2019].

Goettsch, W., Garssen, J., Slob, W., de Gruijl, F. R., & Van Loveren, H. (1998). Risk assessment for the harmful effects of UVB radiation on the immunological resistance to infectious diseases. *Environmental Health Perspectives*, *106*(2), 71-77.

Kerr, J. & Fioletov, V., 2008. Surface ultraviolet radiation. *Atmosphere-Ocean*, 46(1), pp. 159-184.

Khan, N., Shahid, S., Ahmed, K., Ismail, T., & Son, N. N. (2018). Performance Assessment of General Circulation Model in Simulating Daily Precipitation and Temperature Using multiple gridded datasets. *water*, *10*, 1-18.

Kim, W., Kim, J., Park, S. S. & Cho, H.-K., 2014. UV Sensitivity to Changes in Ozone, Aerosols, and Clouds in Seoul, South Korea. *JOURNAL OF APPLIED METEOROLOGY AND CLIMATOLOGY*, Volume 53, pp. 310-320.

Lee, J., Choi, W., Kim, D. R., Kim, S.-Y., Song, C.-K., Hong, J. S., . . . Lee, a. S. (2013). The Effect of Ozone and Aerosols on the Surface Erythemal UV Radiation. *Korean Meteorological Society and Springer*, *49*(3), 271-278.

Lopo, A. B., Spyrides, M. H., Lucio, P. S. & Sigró, J., 2014. Ozone and Aerosol Influence on Ultraviolet Radiation on the East Coast of the Brazilian Northeast. *Atmospheric and Climate Sciences*, 4(1), p. 8.

NASA, 2010. *earth observatory.* [Online] Available at: https://earthobservatory.nasa.gov/global-maps/MODAL2_M_AER_OD [Accessed 11 march 2019].

Massen, F. (2013). *Computing the Radiation Amplification Factor RAF using a sudden dip in Total Ozone Column measured at Diekirch, Luxembourg*. Retrieved Semptember 16, 2019, from

https://www.researchgate.net/profile/Francis_Massen/publication/303250480_Radiation_Amplification_Factor_from_sudden_dip_in_Total_Ozone_Column/links/5739fb6508ae298602e36c46.pdf

NASA, 2019. *Ultraviolet Radiation: How it Affects Life on Earth.* [Online] Available at: https://www.earthobservatory.nasa.gov/features/UVB/uvb_radiation3.php [Accessed 6 September 2001].

Ozone Monitoring Instrument, 2018. *OMI aerosol measurements: OMAERO (Aerosol absorption optical thickness and Aerosol types).* [Online] Available at: http://projects.knmi.nl/omi/research/product/product_generator.php?&info=page&product=aerosol&flavour=OMAERO&long=Aerosol%20absorption%20optical%20thickness%20and%20Aerosol%20types [Accessed 29 April 2019].

Phakula, S., Landman, W. A. & Beraki, A. F., 2018. Forecasting seasonal rainfall characteristics and onset months over South Africa. *INTERNATIONAL JOURNAL OF CLIMATOLOGY*.

Prakash, S., Singhal, A., Sharma, R. & Giri, R. K., 2015. RADIATION AMPLIFICATION FACTOR (RAF) AND ULTRAVIOLET INDEX (UVI) OVER INDO GANGETIC PLAINS. *International Journal of Advanced Research in Engineering and Applied Sciences*, 4(2), pp. 99-115.

Ross, K. E., Piketh, S. J., Bruintjes, R. T., Burger, R. P., Swap, R. J., & Annegarn, H. J. (2003). Spatial and seasonal variations in CCN distribution and the aerosol-CCN relationship over southern Africa. *JOURNAL OF GEOPHYSICAL RESEARCH, 108*(17), 1-18.

Roy, S. S., 2007. Impact of aerosol optical depth on seasonal temperatures in India: a Spatio-temporal analysis. *International Journal of Remote Sensing*, 29(3), pp. 727-740.

Sahai, Y., Kirchhoff, V. W. J. H. & Casiccia, N. P. L. a. C., 2000. OBSERVATIONS OF W-B RADIATION DURING BIOMASS. *Pergamon*, 26(12), pp. 1979-1982.

Slevin, T., 2015. *What does a UV Index mean?.* [Online] Available at: https://www.iol.co.za/lifestyle/health/what-does-a-uv-index-mean-1958251 [Accessed 1 May 2019].

Solar Light, 2019. *Solar Light.* [Online] Available at: https://solarlight.com/product/uvb-biometer-model-501-radiometer/ [Accessed 29 April 2019].

Tesfaye, M., Sivakumar, V., Botai, J. & Mengistu, G. T., 2011. Aerosol climatology over South Africa based on 10 years of Multiangle Imaging Spectroradiometer (MISR) data. *JOURNAL OF GEOPHYSICAL RESEARCH*, Volume 116, pp. 1-17.

5. CLIMATE EXTREMES – IMPACTS AND PREPAREDNESS

Potential Impact of 2018/2019 Extreme Weather events on the meeting of Sustainable Development Goals 2, 3 and 6 in the SADC region

Kaitano Dube,

Department of Hospitality Tourism and PR., Vaal University of Technology

Corresponding author: dubekaitano@gmail.com, Tel: +27710096290

The study argues that hydro-meteorological events experienced in the SADC region are a threat to progress made towards attainment of Sustainable Development Goals namely, SDG2- Zero Hunger, SDG3- Good Health and SDG 6-clean water and sanitation. The study found that extreme weather events in 2018/19 posed a threat to SADC socio-economic progress of the region and progress made on SDGs. The paper recommends adoption of public and private partnership investment in high-resolution early warning systems, smart agriculture and indigenous knowledge systems to ensure, continued progress on SDGs and household food security for rural and urban households who are increasingly vulnerable to extreme weather events

Keywords: SDGs, SADC, Food security, Hunger, Cyclones, Malnutrition, Weather extremes, Droughts, Floods

Introduction and Background

When the world transitioned from Millennium Development Goals to Sustainable Development Goals in 2015, global leaders set in motion a new development trajectory set to lapse 2030 and beyond. The Agenda 2030 on Sustainable Development set in motion an ambitious plan to chase after 17 global goals and 169 targets in 15 years. Achievement of these set goals and targets would inadvertently result in a better future for all, across the world with the promise of leaving no one behind (United Nations, 2015). Over the past four years, many organisations and states have channelled resources in order to ensure the achievement of these goals. Some significant progress has been realised in some parts of the world, including in Africa. According to the UN (2019), the world was still off track in meeting the set goals with need to revamp action. The attainment of these goals is particularly the imagined ideal for many states in Africa, particularly in the SADC region where stakes were very high.

There is an increase in extreme weather events as if we were living in the post 2°C era already. The world is experiencing some of the most unprecedented extreme weather events that could be attributed to climate change such as extreme flooding, cyclones, runaway fires and extreme droughts to mention but a few (World Meteorological Organization - WMO, 2019). Munich RE (2019), noted that in the first half of 2019 already global losses of $42 billion was incurred with Cyclone Idai's cost pegged at $2 billion. The devastating cyclone left 1.85 million people in need and 1.9 million people in need of food aid, according to (United Nations Office for the Coordination of Humanitarian Affairs- OCHA, 2019). Given that the world is still battling to come up with concrete plans for climate adaptation and resilience, the current events present challenges for many marginalised communities without a proper livelihood and food security safety nets as such events increase their climate vulnerability.

The SADC region is grappling with several environmental challenges such as pollution, climate change, poverty and inequality which threatens the region's economic and livelihood security (Omisore, 2018; Mubecua & David, 2018; Muchuru & Nhamo, 2019; Nhamo & Agyepong, 2019). There is a fear that failure to achieve the SDGs can result in social and political instability. The stakes for SDGs for Africa are therefore much higher with only ten years left to achieve the set goals. This paper seeks to highlight the implications of extreme weather events that were experienced during the 2018/19 summer rainfall season in Southern Africa on selected SDGs.

The little progress that has been made in achieving SDGs thus seems to be under threat, notably in Africa, where we have witnessed a wide range of extreme weather events affecting the SADC region and beyond in the past five years. The Intergovernmental Panel on Climate Change-IPCC's Special Report (2018) made an essential acknowledgement that climate change-related extreme weather events are indeed a threat to the achievement of SDGs.The report noted that climate change would scuttle efforts to achieve sustainable development and poverty. In support of that notion, the World Economic Forum (2019), highlighted that extreme weather events are the biggest threat to the global economy in 2019.

Methodology

Given that this study is focused on the 2018-2019 rain season, the data used for this study is focussed on that period only. In that regard, the study made use of data from Copernicus GDO- Global Drought Observatory to map the precipitation amounts and to detect chlorophyll levels during the 2018/2019 agricultural season. The database also provided a platform to cross-compare seasons with previous years. GDO also provide a Risk of Drought Impact for agriculture Index that showed the expected impact of the drought on agricultural production. Other sources of data include hydrological data from the Zambezi River Authority and data from South Africa's Department of Water and Sanitation. Secondary data analysis of the United Nations, its agencies and other member state agencies were used to complement the data from the Copernicus Emergency Management Service.

Results and Discussion

The research found that there are two extremes that have implications on agriculture and food security in the region which threaten the achievement of SDG 2, 3 and 6. The region faces drought in at least nine of SADC member states with drought magnitude ranging from High, Medium and Low. The drought is set to affect about 19.5 million people at varying magnitude, as shown in Figure 1 and Figure 2.

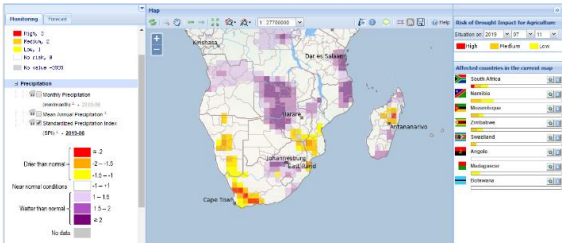

Figure 1: Hydrometeorological Extremes in SADC Region during the 2018/2019 rainfall season
Source: Copernicus Global Drought Observatory (2019)

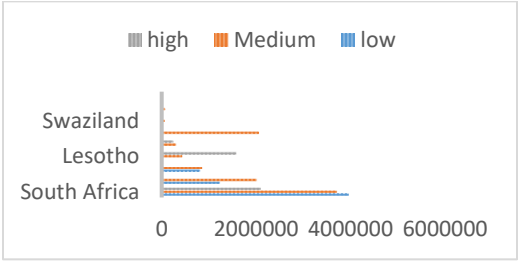

Figure 2: Population under drought risk within the SADC region 2018/2019 rain season
Source: Author Based on Copernicus Global Drought Observatory (2019).

The other extreme that is shown in Figure 1 is the higher than average rainfall that was received in the late summer season mainly between April and May especially over the area around Mozambique, Malawi and Zimbabwe due to the double effect of Tropical Cyclone Idai and Kenneth. Evidence shows that the record sea surface temperature that has been observed by Copernicus Climate missions and also NOAA led to the development of high category cyclones in the Mozambique channel. The compounded effect of rising sea level, storm surges and tropical cyclones led to disastrous floods that affected 4 SADC countries in March and April of 2019. An extremely high amount of rainfall was also received in the Eastern Cape particularly in Port St Johns as well as parts of the Kwa Zulu Natal province especially in around eThekwini metropolitan area.

The higher than usual rainfall that was received in the area led to flooding in some of the countries mentioned resulting in loss of lives, property, infrastructure and livelihood security. Due to flooding some homes and granaries were swept away triggering a food and health crisis. Vast tracks of near harvest stage crops were swept away triggering instant food insecurity as the harvest and livestock were swept away.

The flooding that occurred in 2019 occurred during the harvest period, which is usually around March stretching to April According to a SADC report. Tropical Cyclone Idai, led to the destruction of 778,822 hectares of cropland which further worsened the challenge of food insecurity due to drought in other parts of southern Africa (See Figure 1) (SADC, 2019). The two tropical cyclones Idai and Kenneth added about 1.8 million people onto the food insecurity figure. This is problematic as southern Africa is one of the few regions where food insecurity is increasing (Food and Agricultural Organization- FAO, 2019). Statistics from FAO shows that food insecurity has been increasing in Southern Africa and parts of Asia while the rest of the world food insecurity is decreasing.

According to Dube and Nhamo (2018), over the last five years, the region experienced one of the worst El Niño droughts in history which led to severe water and food shortages in the region. The region only managed a 0.5% food insecurity decline in 2018. The prospects of achieving Zero hunger – SDG 2, therefore, remains a pipe dream that is unlikely to be met, given the ravaging meteorological droughts and extreme rainfall that are on the increase in the SADC regions both in terms of intensity and magnitude. This is even more so when one considers that due to Idai crops were wiped off and livestock destroyed. In addition, farming assets

such as farming equipment were also swept away, which affected and will affect the capacity for communities to produce their food in the 2019/2020 rainfall season unless tillage services provided through other means.

A combination of drought and flooding have been the key drivers of malnutrition food insecurity and malnutrition in the region amongst children, pregnant women and HIV positive and TB patients (FAO, 2019). Figure one and two shows that several people will be affected by the droughts that affected the 2018/19 agricultural season. Reports indicate that as a result of the droughts in Mozambique 8,7 million will suffer as a consequent of drought exposing them to hunger and malnutrition between 2019 and 2020. In Zimbabwe, the drought and post-impact of the Cyclone Idai induced floods that were expected to have a devastating impact on the economy and employment patterns which would further render the population vulnerable to food insecurity, disease and malnutrition (see Figure 1 and 2).

The drought in the parts of Angola which is part of the catchment of the Zambezi River had seen far too low water flow in the Zambezi River and consequently one of the worst record low water levels Lake Kariba which is an essential source of electricity for Zambia and Zimbabwe as can be seen in Figure 3. Due to low water levels, Zimbabwe has been forced to go under persistent load shedding, which lasts anything between 18 and 24 hours in some instances. The energy regulator in Zimbabwe reported that as of September energy production at Kariba Power station had fallen from 1050MW to a 245MW owing to low water levels. Electricity shortage, among other things, will severely affect winter cropping and market gardens as it would be almost impossible to complete irrigation schedules for cropping further worsening the impact of the drought and food insecurity. Food price hikes are inevitable, which will further reduce access to both quantity and quality food for the marginalised. The impact will be mostly felt by vulnerable groups of people who include: the elderly, the sick and pregnant women, with lasting impact on their health and nutrition status.

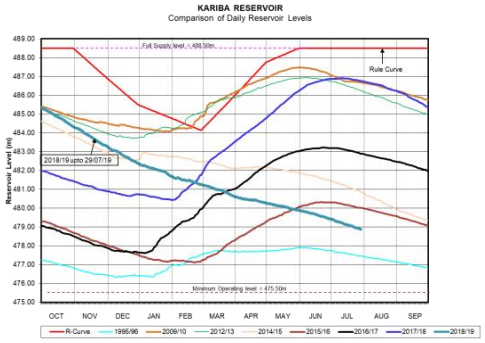

Figure 3: Lake Kariba water levels as of 29 July 2019 in comparison to the last ten years
Source: Zambezi River Authority (2019)

The uncertainties brought about by the land debate in South Africa compounded with drought will likely see food prices going up in a country that is battling poverty, inequality, HIV and TB. Such a scenario will increase morbidity, which will hamper progress towards SDGs 2,3 and 6. Figure 4 shows that several areas in South Africa are water-stressed, which can also affect irrigation, agriculture and water and sanitation provision, further heightening food insecurity in South Africa and the region. The map shows that drought areas that have been identified in Figure 1 have surface water problems as signified by the red and orange dots to yellow dots in South Africa, Lesotho and also Swaziland (Eswatini). The drought across South Africa will result in water supply challenges in the mostly urban population imposing challenges for the country to reach its water and sanitation needs, which can worsen diseases and sickness.

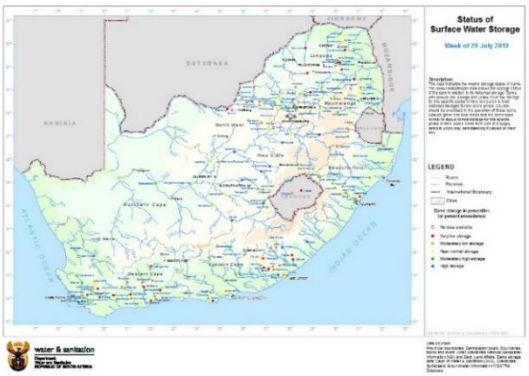

Figure 4: Surface water storage as of July 2019 in South Africa.
Source: Department of Water and Sanitation (2019)

Increased incidences of drought are concerning in SADC, which calls for a new approach to agricultural practice in order to ensure community climate resilience for sustainability, in light of increased

frequency of drought and severity. There is need for academics and communities to come up with better ways of dealing with repeated occurrence of droughts in the region given their knock-on effect on livelihood security. The rural and urban populace can pursue various options. A call to return to combined use of agro-ecologically based management strategies and the use of traditional small grains crops, that are adapted to the climate can be an option that can be explored to abate hunger and malnutrition. Hadebe et al. (2017), noted that some of the traditional and indigenous crops such as sorghum which is grown in almost every SADC countries have high water efficiency which makes it good climate adaptation crop. This will call for the protection of traditional seedbanks which are currently being contaminated and depleted.

Urban agriculture can take advantage of the inexpensive use of hydroponics and drip irrigation to ensure a buffer for hunger and be a sustainable supply for nutritious, healthy foods. Venter (2019), supports the use of hydroponics in climate change areas to ensure food security for a healthy society, given the numerous advantages offered by this farming system which offers an all year cropping season, better yields, a 40% less water usage compared to traditional cropping methods and better disease management amongst other advantages.

Conclusions and Recommendations

The SADC region is facing severe challenges caused by hydrometeorological challenges such as flooding and extreme drought, which undermines the capacity for household food security and national food security. Due to interlinkages with other SDGs, failure to ensure food security will result in failure to meet other SDGs such as SDG3 and also SDG6. The impact of hydrometeorological droughts is far-reaching as previous records indicate that in years of drought the GDP of the SADC region tends to decline with a spiralling effect on employment patterns given that regional economies are agro-based. There is, therefore, need to come up with projects that ensure household food security in both rural and urban migration that are water efficient. Governments also need to come up with plans to ensure that poor peasants are insured from increased droughts and flooding. Most households, consequently, fail to meet their food needs. Recent droughts have also resulted in most urban areas failing to meet their water and sanitation needs. SADC member states need to come up with inexpensive plans that budgets for most recurring droughts and put measures to build community resilience. Most importantly there is need for meteorological service departments to invest in robust system with capacity to undertake seasonal to decadal predictions so as to meet and better manage extreme disaster in a manner that does not disrupt progress made towards meeting SDGs.

References

Copernicus Global Drought Observatory . (2019). *Emergency Management Service* . Retrieved July 30, 2019, from http://edo.jrc.ec.europa.eu/gdo/php/index.php?id=2001

Department of Water and Sanitation . (2019). *Status of Surface Water Storage* . Retrieved July 31, 2019, from http://www.dwa.gov.za/Hydrology/Weekly/Storage.aspx

Dube, K., & Nhamo, G. (2018). Climate change and potential impacts on tourism: evidence from the Zimbabwean side of the Victoria Falls. *Environment Development and Sustainability*, 1-17.

FAO. (2019). *The State of Food Security and Nutrition in the World 2019.* FAO. Retrieved July 30, 2019, from https://sustainabledevelopment.un.org/index.php?page=view&type=20000&nr=5678&menu=2993

Hadebe, S. T., Modi, A. T., & Mabhaudhi, T. (2017). Drought tolerance and water use of cereal crops: A focus on sorghum as a food security crop in sub-Saharan Africa. *Journal of Agronomy and Crop Science, 203*(3), 177-191.

IPCC. (2018). *Global Warming of 1.5°C An IPCC Special Report on the impacts of global warming of 1.5°C above preindustrial related global greenhouse gas emission pathways, in the context of strengthening the global response to the threat of climate change, sustainable.* Intergovernmental Panel on Climate Change. Retrieved July 26, 2019, from https://www.ipcc.ch/sr15/

Mubecua, M. A., & David, O. J. (2018). So far so good? Tracking the poverty eradication goal of SDGs in Kenya, Nigeria, and South Africa. *Journal of Public Affairs*, e1964.

Muchuru, S., & Nhamo, G. (2019). A review of climate change adaptation measures in the African crop sector. *Climate and Development*, 1-13.

Munich RE. (2019). *Thunderstorms, cyclones and heatwaves: the natural disaster figures for the first half of 2019.* Retrieved September 18, 2019, from https://www.munichre.com/en/media-relations/publications/press-

releases/2019/2019-07-30-press-release/index.html
Nhamo, G., & Agyepong, A. O. (2019). Climate change adaptation and local government: Institutional complexities surrounding Cape Town's Day Zero. *Jàmbá: Journal of Disaster Risk Studies, 3*(9), 11.
Omisore, A. G. (2018). Attaining sustainable development goals in sub-Saharan Africa; The need to address environmental challenges. *Environmental development, 25*, 138-145.
SADC. (2019). *SADC Regional Humanitarian Floods Appeal In Response to Tropical Cyclone Idai 11 April 2019.* SADC. Retrieved July 30, 2019, from https://reliefweb.int/report/mozambique/sadc-regional-humanitarian-floods-appeal-response-tropical-cyclone-idai-enpt
UN. (2019). *Global Sustainable Development Report 2019: The Future is Now – Science for Achieving Sustainable Development.* New York: United Nations. Retrieved from https://sustainabledevelopment.un.org/content/documents/24797GSDR_report_2019.pdf
United Nations . (2015). *Sustainable Development Goals Knowledge Platform Transforming our world: the 2030 Agenda for Sustainable Development*. Retrieved July 30, 2019, from https://sustainabledevelopment.un.org/post2015/transformingourworld
United Nations Office for the Coordination of Humanitarian Affairs- OCHA. (2019). *Mozambique Cyclone Idai Six Months After.* United Nations Office for the Coordination of Humanitarian Affairs. Retrieved from https://reliefweb.int/sites/reliefweb.int/files/resources/OCHA_MOZ_SIX_Months_After_Idai_20190912_EN.pdf
Venter, C. (2019). Undercover farming can overcome climate change challenges. *FarmBiz, 5*(7), 25-27.
Wootton-Beard, P. (2019). Producing fodder crops using hydroponics. *Farming Connect*.
World Economic Forum. (2019). *The Global Risks Report 2019 14th Edition.* Geneva: World Economic Forum. Retrieved September 16, 2019, from https://www.weforum.org/reports/the-global-risks-report-2019
World Meteorological Organization- WMO. (2019). *WMO Statement on the State of the Global Climate in 2018.* CH-1211 Geneva 2, Switzerland: World Meteorological Organization.
Zambezi River Authority. (2019). *Lake Kariba Weekly Levels in Meters*. Retrieved July 31, 2019, from http://www.zambezira.org/hydrology/lake-levels

Improvements in predicting the likelihood of severe events

Stephanie Landman and Estelle Marx

South African Weather Service, Pretoria, South Africa

*Corresponding author: stephanie.landman@weathersa.co.za

During March 2019, a Unified Model convective-scale ensemble prediction system over the South African domain was implemented at the South African Weather Service for testing and verification. During the same time, a multi-model ensemble prediction system was also under development, covering the Southern Africa Developing Community domain. Using the case of the KwaZulu-Natal floods in April 2019, it was found that the convective scale ensemble indicates more localised and concentrated regions of heavy rain, whereas the multi-model system predicted higher rainfall totals over a much larger area.

Keywords: convective scale ensemble, multi-model, probability forecasts, predictability

Introduction

Most Numerical Weather Prediction (NWP) systems provide a good enough representation of the predicted weather that they can be used to provide fundamental automated weather forecasts directly from the model output. However, in general, it is recommended that some post-processing should be used to calibrate computerised forecasts (Robertson *et al.*, 2013). Any NWP process is dependent on the observations assimilated with the generation of the analysis (e.g., field representing the current state of the atmosphere). Due to this sensitivity to these initial conditions, any inherent error in the initial assimilation process or observations data can result in a significant error in the resulting forecast. Therefore, even with the best observations and data assimilations techniques, a perfect analysis is not possible, and consequently, neither is a perfect forecast (Kalnay, 2003). An additional error in NWP is the inherent modelling errors due to the understanding, simplifications and assumptions made in the dynamic and physics calculations. These errors differ between different NWP systems due to the differences in the applications of the dynamical and physical processes. An ensemble of forecasts addresses these weaknesses in NWP. The uncertainty in a weather forecast can vary widely from day to day according to the synoptic situation, and the ensemble approach provides an estimate of this day-to-day uncertainty.

Convective instability adds a new scale of forecast uncertainty, which convective permitting ensemble systems can also address (Stein *et al.*, 2019). The ensemble is designed to sample the spread of the forecast and results in probability forecasts to assess the likelihood that certain outcomes will occur.

An ensemble is attained by adding or subtracting small perturbations to the analysis field to attempt to address the uncertainty within the initial conditions. The resulting difference or size of the spread in the forecasts from the different initial conditions will either increase or decrease the confidence in the forecasts. Due to the computational costs of running an ensemble (multiple forecasts), the resolution of the convective scale ensemble members is generally double that of the deterministic (single) forecast. An alternative approach to reduce the costs of creating an ensemble, a poor man's ensemble (Ebert, 2001) is created by combining the forecasts from different deterministic forecasts generated from different NWP systems at various operational centres (Landman *et al.*, 2012).

Data and Methodology

During March 2019, a Unified Model (UM) convective-scale ensemble prediction system (CSEPS) with a 4.5 km horizontal resolution was implemented and had since been running regularly at the South African Weather Service (SAWS) for testing and verification. The ensemble domain covers South Africa and consists of 12 members, with each member receiving initial- and lateral boundary conditions from the Met Office's global ensemble prediction system (MOGREPS-G) (Hagelin *et al.*, 2017). In addition to the UM-CSEPS, a multi-model ensemble (MMENS) prediction system is also under development and testing within SAWS, covering the whole Southern Africa Developing Community (SADC) domain. The global deterministic NWP models used in the MMENS are from the 1) German Weather Service's (DWD) ICON, 2) Met Office's Global Atmosphere (GA), 3) Global Forecasting System (GFS) and 4) the SAWS in-house regional UM 4.4 km deterministic run. All members are resampled to a common ~6 km horizontal grid, and additional members are achieved through pseudo-ensemble methods (Theis *et al.*, 2005)

The resulting ensemble, therefore, also consists of 12 members, similar to the CSEPS.

The KwaZulu-Natal flood in April 2019 is used as a case study to evaluate the performance of both the CSEPS and MMENS performance. During the evening of 22 April and into the morning of 23 April, a significant amount of rainfall fell over the southern parts of the KwaZulu-Natal (KZN) coast. The rain was the result of a cut-off low which developed over the Eastern Cape Province but intensified along the KZN coast. The resulting floods and mudslides led to 67 fatalities, the displacement of ~1260 people and an estimated cost of R1 trillion in damages (Dailymaverick, 2019). In Fig. 1 the four rainfall stations from SAWS which observed the highest amount of rainfall during these 24 hours are plotted, and the accumulated rainfall plotted. It is noted that Port Edward recorded 398.2 mm and almost 100 mm during the evening of the 23rd.

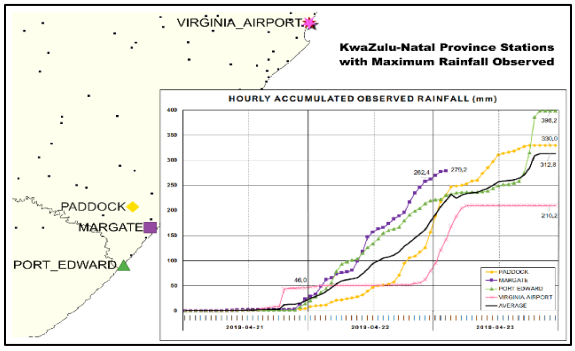

Figure 1: Map indicating the location of the four rainfall stations and the corresponding hourly, accumulated observed rainfall from 21 to midnight on the 23rd of April 2019

Results

During the time of the event, operational forecasters at SAWS had access to UM deterministic NWP guidance for issuing of warnings (SAWS currently have 4 km, and 1.5 km horizontal resolution UM deterministic runs operationally). However, in this study, we are looking into the spread of possibilities the two ensemble systems provided. In Fig. 2, the CSEPS 00Z forecast from the 22nd shows the 12-member accumulated rainfall predicted for the 48 hours from midnight 22 April to midnight of the 24th of April 2019. All members indicate the high amounts of rain over the southern parts of the KZN coast, with member nr. 7 indicating the largest area expecting rainfall greater than 150 mm over the two days.

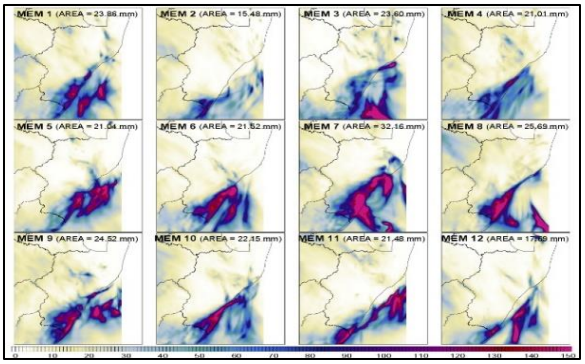

Figure 2: The 12 members of the CSEPS: total rainfall (mm) predicted for the 48-hour period of 00Z 22 April to 00Z 24 April 2019. Indicated is also the area average rainfall for the KwaZulu-Natal Province

The corresponding forecasts made by the members of the MMENS are shown in Fig. 3. Due to the lower native horizontal resolution grids of the global NWP models contributing to the MMENS, the predicted rainfall areas are generally larger and the rainfall patterns less defined. It is also evident that more MMENS members are predicting larger areas of rainfall greater than 150 mm, than the members of the CSEPS.

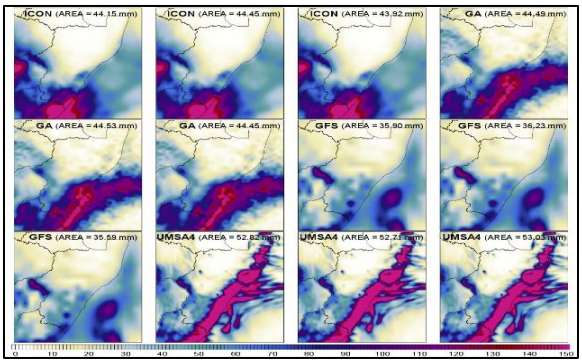

Figure 3: The 12 members of the MMENS: total rainfall (mm) predicted for the 48-hour period of 00Z 22 April to 00Z 24 April 2019. Indicated is also the area average rainfall for the KwaZulu-Natal Province

The ensemble average of both systems was calculated and compared to the regional, high-resolution deterministic SA4 forecast (Fig. 4). The CSEPS average indicates the more distinct, concentrated region of significant rainfall over the southern KZN coast. The SA4 forecast is one of the members of the MMENS, but it is seen in the MMENS average rainfall that the other members of the ensemble lessen the intense rainfall predicted by SA4 along the KZN coast. Fig. 5, in turn, indicates the actual, gridded interpolated rainfall observed by the automatic rainfall and weather stations (ARS) over the KZN Province. It

is seen that the high rainfall event was concentrated over the southern parts of the coast.

The observations show that the highest amount of rainfall was concentrated from Durban southwards. As much as 163 mm was observed at Amanzimtoti during the 24 hours of 06Z 22 April to 06Z 23 April.

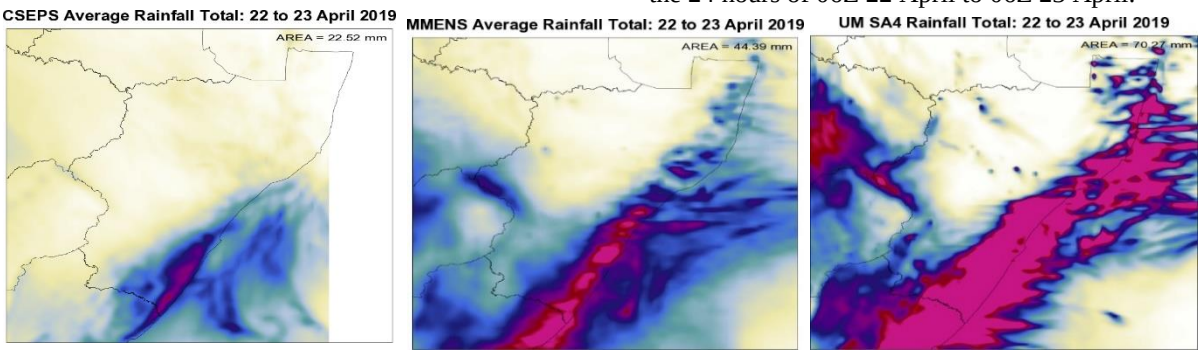

Figure 4: Ensemble averages for the CSEP and MMENS forecasts, including the single high-resolution forecast of UM SA4

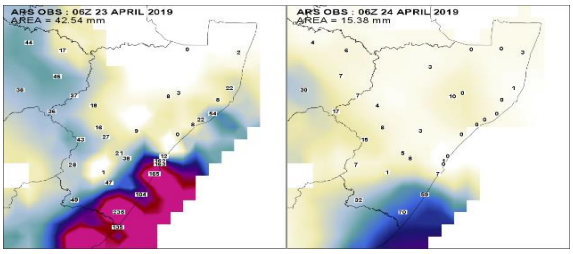

Figure 5: Gridded daily rainfall totals from the automatic rainfall stations in the KwaZulu-Natal Province, with observations from 06Z-06Z on 23 April and 06Z-06Z on 24 April 2019

Conclusion

When comparing the average rainfall of the two ensemble systems, both forecasts have strength and weaknesses. The CSEPS indicates more localised and concentrated regions of heavy rain as was observed, whereas the MMENS predicted the higher rainfall totals but over a much larger area. However, both ensemble systems performed better than the single deterministic forecast. Since the ensemble of forecasts forms typically a good representation of the most likely expected weather, these ensemble systems may be used to provide reliable probabilistic forecasts of such weather.

Acknowledgements

The CSPES was implemented at SAWS together with the Met Office under the WCSSP, funded by the Newton Fund (https://www.metoffice.gov.uk/research/approach/collaboration/newton/wcssp-southafrica and https://www.newtonfund.ac.uk/about/about-partner-countries/south-africa/).

References

https://www.dailymaverick.co.za/article/2019-04-25-deadly-kzn-floods-bring-tales-of-tragedy-and-sorrow/

Ebert, E., 2001: Ability of a Poor Man's Ensemble to Predict the Probability and Distribution of Precipitation. *Monthly Weather Review*. 129. doi:10.1175/1520-0493

Hagelin, S., Son, J., Swinbank, R., McCabe, A., Roberts, N., Tennant, W., 2017: The Met Office convective-scale ensemble, MOGREPS-UK. *Quarterly Journal of the Royal Meteorological Society*. 143. doi:10.1002/qj.3135

Kalnay, E., 2003: *Atmospheric Modeling, Data Assimilation and Predictability*. Cambridge University Press, UK

Landman, S., Engelbrecht, F.A., Engelbrecht, C.J., Dyson, L.L., Landman, W.A. (2012). A short-range weather prediction system for South Africa based on a multi-model approach. *WaterSA*, **38**, 765-773

Robertson, D., Shrestha, D., Wang, Q., 2013: Post-processing rainfall forecasts from numerical weather prediction models for short-term streamflow forecasting. *Hydrology and Earth System Sciences*. doi:17. 17.10.5194/hess-17-17-3587-2013

Stein, T.H., Keat, W., Maidment, R.I., Landman, S., Becker, E., Boyd, D.F., Bodas-Salcedo, A., Pankiewicz, G., Webster, S., 2019: An Evaluation of Clouds and Precipitation in Convection-Permitting Forecasts for South Africa. *Weather and Forecasting*. 34, 233-254. Doi:10.1175/WAF-D-18-0080.1

Theis, S.E., Hense, A. and Damrath, U., 2005: Probabilistic precipitation forecasts from a deterministic model: a pragmatic approach. *Meteor. Appl.*, 12, 257-268

Investigation of spatio-temporal changes of drought in the Eastern Cape Province

Kgalalelo Letshwiti[1], Christina Botai[1], Joel Botai[1,2] and Jaco de Wit[1]

[1]South African Weather Service
[2]Department of Geography, Geoinformatics and Meteorology, University of Pretoria

*Corresponding author:

This research study evaluated drought characteristics in Port Elizabeth (PE) and Makhanda regions of the Eastern Cape Province from 1968 to 2018, based on the computation of the Standardized Precipitation Index (SPI) at 6 and 12 months accumulation periods. Results indicate that drought conditions are persisting in these regions. Both PE and Makhanda exhibit negative SPI trends, suggesting that the SPI values are becoming more negative, leading to persistent dry conditions. Mild to moderate drought conditions dominated over the 50 years of the study period. In addition, drought severity has increased over the years. The severity was less in 1983 and reached its maximum in 1995. The results reported in this study is supported by significant decrease of water levels in some of the major dams supplying water to the two regions. Appropriate water use planning and other saving measures are therefore required to alleviate further water supply crises and for future management and planning of water resources in the region.

Keywords: Rainfall trend, Standardized Precipitation Index, Drought

Introduction

South Africa has been experiencing recurrent drought (Botai et al., 2018) that are impacting various sectors of the country's economy, e.g. water and agriculture, among others. For instance, water supply has been disrupted in various areas of the country, including the Western Cape, Limpopo, Mpumalanga, and the Eastern Cape provinces. Water crisis in the Eastern Cape Province, particularly in Port Elizabeth (PE) and Makhanda, has reached the worst level in its history. The water levels in most of the reservoirs have drastically dropped, leaving the government with an uncertain future, and the possibility of "day zero".

Drought is one of the factors contributing to water supply shortages in the Eastern Cape Province. This natural phenomenon is attributed to various factors, including insufficient or delay in rainfall coupled with climatic conditions such as warm temperature and increase evapotranspiration. Research studies have projected a shift as well as a decrease in rainfall across different parts of South Africa, including the western areas of the country (Cook et al., 2014). Such changes are likely to exacerbate the occurrence of drought events in those affected regions. For effective management and planning of water resources, there is a need to monitor drought, particular in the most affected areas like the Eastern Cape, where the drought impacts are already evinced in water reservoirs. The aim of this research study is to evaluate spatial and temporal characteristics of drought based on the Standardized Precipitation Index (SPI), focusing mainly on PE and Makhanda regions of the Eastern Cape Province. In particular, the study aims to analyse the historical patterns of drought in the selected region from 1968 – 2018. Such information may contribute towards the development and implementation of drought monitoring tools or early warning systems.

Study area

The Eastern Cape is one of the nine provinces of South Africa and it is situated along the south coast of the country. The climate of the province varies adversely, e.g. the northern areas are characterized by semi-arid conditions, whereas climate towards the south slightly differ, where an ample supply of water is provided by the rivers trickling down from mountains. Generally, the northern areas of the Eastern Cape exhibit hotter and colder nights while the southern areas experience a higher rainfall. The eastern coast along the study area experience all year rainfall (Engelbrecht et al 2014). The selected areas for the study are the PE and Makhanda region, see Fig. 1, for their locations in the map.

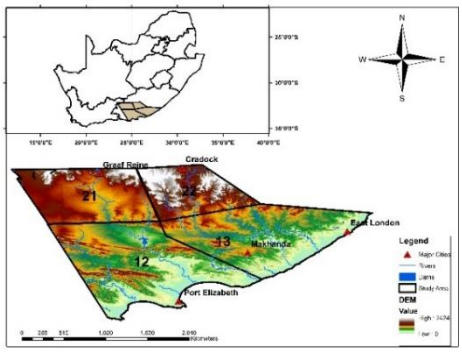

Figure 1: Map of the Eastern Cape Province with the distribution of the selected district stations

Data and methodology

The data used in this study is the monthly rainfall totals from South African Weather Service (SAWS) rainfall district stations. The analysed monthly totals spanned from 1968 to 2018 (50 years). In total, 4 district stations were considered, whereby two stations are located in PE (dis12 and dis21) and the other two (dis13 and dis22) are in Makhanda.

Characteristics of the rainfall measurements across the four district stations were based on computation of basic statistical parameters, e.g. the mean, standard deviation, coefficient of variation, kurtosis and skewness. Trends in rainfall were analysed and detected based on the non-parametric Mann-Kendall (MK) test (Mann, 1945; Kendall, 1975). The derived trends were tested with a statistical significance level of $p = 0.05$.

Drought analysis was based on the calculation of the Standardized Precipitation Index (SPI) series. The computation of SPI time series across the stations was based on the SPI method proposed by McKee (1993). In general, the SPI was computed by fitting a gamma distribution function to the monthly rainfall time series, accumulated to 6 and 12 months, from January of each year, and estimate the parameters of the distribution. These parameters are used to calculate the cumulative probability function of rainfall at 6 and 12 months accumulated periods. The resulting accumulative probability is then transformed into a standardized normal distribution, with mean and standard deviation of zero and 1, respectively (Edwards and McKee, 1997). The output is a SPI time series, consisting of both negative values (corresponding to dry conditions) and positive values (wet conditions). The computed SPI values were analyse to assess drought conditions in the selected regions of the Eastern Cape Province.

The 6 and 12 months accumulation periods were selected because they correspond to agricultural (or mid-term trends in precipitation) and hydrological (long-term precipitation patterns) impacts of drought, respectively. For the purpose of this study, the drought characteristics considered are the annual trends, general features of the SPI series, drought duration and severity in the selected regions. In particular, the drought duration and severity were calculated as per their definitions in the literature, i.e. the number of months with continuously negative SPI corresponding to below-average water resources and the accumulated negative SPI in a given drought event, respectively (Dayal et al. 2018)

Results

Precipitation characteristics

Table 1 gives a summary of rainfall time series characteristics across the districts. The mean annual rainfall range between 27 and 54. The highest mean is recorded in dis12 and dis13 stations, which are located in PE and Makhanda, along the coastal area. The coefficient of variation is approximately 1 across the stations. The distribution of rainfall is extremely skewed at an annual time scale, with skewness coefficient of greater than 1, across the stations. In addition, rainfall time series exhibits thick-tailed distribution (e.g. positive coefficient of kurtosis) across the stations.

Table 1. Characteristics of monthly rainfall totals across the stations

Station	Mean	STD	CV	Kurt.	Skew.
12	41.15	33.23	0.80	4.66	1.90
13	53.85	43.83	0.81	6.64	1.96
21	27.32	26.43	0.97	3.30	1.59
22	38.47	33.25	0.86	4.68	1.66

Trends in precipitation

Fig. 2 depicts annual trends in rainfall across the districts. Based on the results, three of the four districts exhibit positive trends. The only station exhibiting negative trends is dis22 located in Makhanda region. The standardized test statistics across the stations is $Z = 0.5395$. The positive value suggests that, overall, the two regions have experienced an increasing trend in rainfall. However, the trends across the stations are not statistically significant at 0.05 significance level.

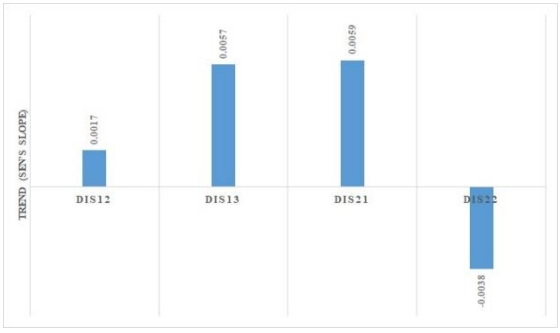

Figure 2: Annual precipitation trends across the stations

Drought characteristics

Fig. 3 depicts SPI 6 time series across the 4 stations in PE and Makhanda regions. The SPI exhibits seasonal and inter-seasonal drought variability pattern. Port Elizabeth seem to be experiencing more prolonged drought whereas Makhanda experiences highly variable drought. Mild to moderate drought predominates across the regions. Based on the SPI 6 time series, drought was still persisting by the end of 2018.

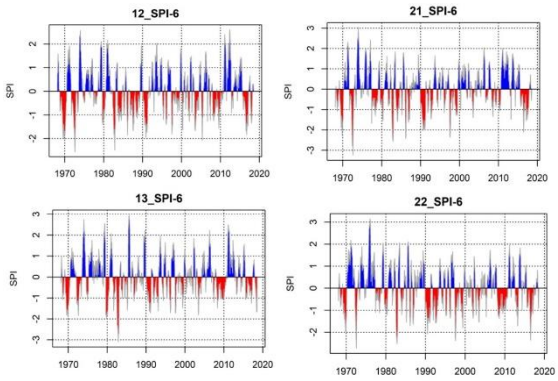

Figure 3. SPI 6 time series for the selected districts in Eastern Cape

The SPI 12 time series results are depicted in Fig. 4. There exists seasonal and annual drought variation across the stations. In some cases drought seem to exhibit decadal variation. Mild to moderate drought predominates in the regions, although there are few cases of severe drought occurrences. The longest drought duration occurred in PE between 1983 and 1988. Based on the SPI 12 time series across the stations, drought in PE and Makhanda was still persisting by the end of the study period, with no sign of recovery.

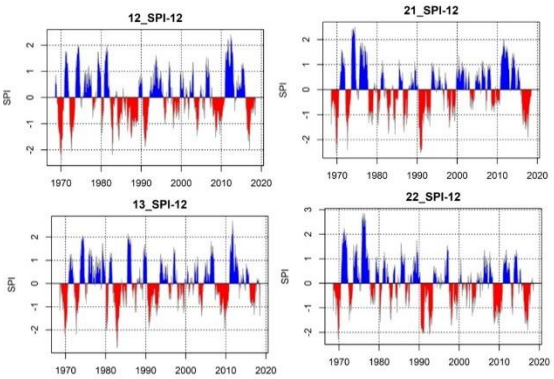

Figure 4. Same as Figure 3 but for SPI 12

SPI trend characteristics

Table 2 summarises results of SPI trends and the corresponding significant trends, for both the SPI 6 and 12 accumulation periods. The observed trend pattern is similar in both the accumulation periods. Thus, dis12 and dis13 exhibit positive trends whereas dis21 and dis23 exhibit negative trends in both the SPI 6 and 12. The stations exhibiting negative trends are found along the coast, but covering both PE and Makhanda areas. In addition, trends based on SPI 6 are statistically significant in three of the district stations while for SPI 12 half of the stations depict statistically significant trends and the other half statistically insignificant trends. Based on the Z values (Z = -1.0239 and Z = -1.1546 for SPI 6 and 12, respectively), both PE and Makhanda depict a decreasing trend in the SPI. This suggests that the SPI values are getting more and more negative, hence drought persistence in selected regions.

Table 2. SPI trends across the stations

SPI 6		
Station	Trend (Sen's slope)	*p*-value
12	0.0005	0.04
13	0.0003	0.27
21	-0.0012	<<0.00
22	-0.0004	0.07
Across the stations	-1.0239	0.31
SPI 12		
12	0.0007	0.01
13	0.0003	0.17
21	-0.0015	<<0.00
22	-0.0003	0.17
Across the stations	-1.1546	0.25

The SPI 6 and 12 were used to calculate yearly drought severity across the district stations. This gives the sum of severities of the drought events occurred in each year from 1968 to 2018, expressed in a dimensionless drought severity score. The results for drought severity are depicted in Figs. 5(A) and (B), for the SPI6 and 12 respectively. Drought severity varies between approximately 0.7 and 11.5 (SPI 6) and 1 and 10 (SPI 12) across the stations. Drought severity derived from SPI 6 depicts an increasing linear trend. In PE drought reached maximum severity in 1988, 1992, 1995 and 2013. On the other hand, drought reached maximum severity in 1988, 1992, 1995, 2005 and 2013 in Makhanda. The SPI 12 drought severity also depicts a clear increasing linear trend. In particular, drought was more severe between 1990 and 2005. In PE and Makhanda, drought reached maximum severity in 1994. Between 2005 and 2015 drought was less severe. However, based on results, it is possible that drought in both regions has again become more severe, this is based on the increasing trend observed from 2016 to 2018.

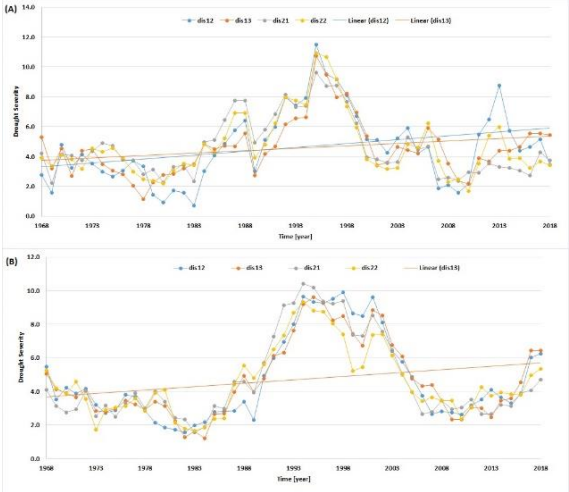

Figure 5. Drought severity across the stations, A: corresponds to SPI 6 and B: to SPI 12

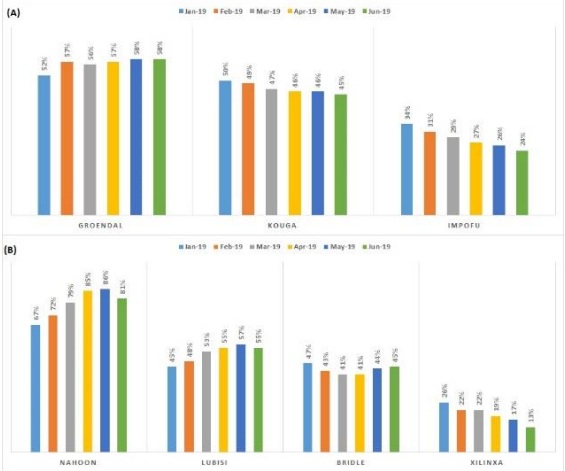

Figure 6. Dam levels in (A) Nelson Mandela Bay and (B) Makhanda

Discussion

Drought is significantly affecting water resources in the Eastern Cape Province. Based on the results obtained in the current research study, drought in the province, particularly in PE and Makhanda areas, exhibit seasonal and annual variability. The drought is predominantly mild to moderate. The impacts of drought in the selected study area are likely to exacerbate. This is because the SPI time series seem to suggest that drought is still persisting in PE and Makhanda regions. In particular the there is a tendency of increase in drought severity in those regions. The Eastern Cape Provincial government has stated that the water shortage particularly in Makhanda has stabilised and that the water is now sufficient for the community. However, results obtained in this study suggest that the water resources are still under pressure, due to persistent drought. For instance, the dam levels supplying water to PE and Makhanda continue to drop in an alarming rate, see the current state of dams in Fig 6. As noted in Fig. 6, one of the major dams supplying water to PE has dropped to 24% and the other in Makhanda to 14% by the end of June 2019. In addition, persistent drought is likely to affect agricultural production, given that most farmers, particularly small-scale, rely on rainfed farming. Remedial measures (including drilling of boreholes) are therefore needed to alleviate future water related impacts.

Conclusion

This research study evaluated drought characteristics in the Eastern Cape Province, focusing mainly on the PE and Makhanda regions, from 1968 to 2018. Results indicate that the areas have experienced mild to moderate drought during the study period. Occurrences of drought severity depicted an increasing pattern from 1990 to 2004. Drought in PE and Makhanda was less severe in 1983 and reached maximum severity in 1995. While the SPI 6 depicts a decrease in drought severity from 2017, the SPI 12 suggest that the severity is increasing during the period. This is confirmed by the continued water crisis in the regions, whereby the dams supplying water are continually dropping.

References

Botai, C. M., Botai, J. O., & Adeola, A. M. (2018). Spatial distribution of temporal precipitation contrasts in South Africa. South African Journal of Science, 114(7-8), 70-78.

Cook, B. I., Smerdon, J. E., Seager, R., & Coats, S. (2014). Global warming and 21 st century drying. Climate Dynamics, 43(9-10), 2607-2627.

Deyal, K.S., Deo, R.C., Apan, A.A. (2018). Investigating drought duration-severity-intensity characteristics using the Standardized Precipitation Evapotranspiration Index: Case studies in drought-prone Southeast Queensland. Journal of Hydrologic Engineering. Vol .23(1)

Edwards, D.C. & McKee, T.B. (1997) Characteristics of 20th Century Drought in

the United States at Multiple Times Scales. Atmospheric Science Paper, 634, 1-30.

Engelbrecht, C.J., Landman, W.A., Engelbrecht, F.A., Malherbe, J. (2015). A synoptic decomposition of rainfall over the Cape south coast of South Africa. Climate Dynamics 44: 2589-2607. DOI: 10.1007/s00382-014-2230-5

Kendall, M.G. (1975) Rank Correlation Methods. 4th Edition, Charles Griffin, London.

Madadgar, S., & Moradkhani, H. (2011). Drought analysis under climate change using copula. Journal of hydrologic engineering, 18(7), 746-759.

Mann, H. B. (1945). Nonparametric tests against trend. Econometrica: Journal of the Econometric Society, 245-259.

McKee, T. B., Doesken, N. J., & Kleist, J. (1993). The relationship of drought frequency and duration to time scales. In Proceedings of the 8th Conference on Applied Climatology (Vol. 17, No. 22, pp. 179-183). Boston, MA: American Meteorological Society.

Sensitivity Analysis of the SPI to Statistical Distribution Functions: A case study of the Western Cape Province

Nkosinathi M. Masango[1,*], Christina Botai[2], and Cilence Munghemezulu[1]

[1]South African Weather Service
[2]Department of Geography, Geoinformatics and Meteorology, University of Pretoria

*Corresponding author: u15139809@tuks.co.za

Drought indices are often used for drought-risk assessments, monitoring and prediction. The Standardized Precipitation Index (SPI) is one of the most commonly used index and is generally calculated by fitting a suitable probability distribution function (PDF) to the observed precipitation data. Users often select their own distribution function, although in most cases the Gamma distribution has been selected as the default function. The aim of this research study is to assess the sensitivity of SPI to the choice of different PDFs. For this purpose, four PDFs, namely, the Gamma, Normal, Weibull and Pearson Type 3, were assessed. The results depict minimal differences across the PDFs, with the Gamma and Pearson Type 3 distributions almost similar patterns in the SPI time series. Generally, the results confirm the utility of using the Gamma distribution when computing SPI for drought monitoring. However, due to close correlation between the Gamma and Pearson type 3, the Pearson Type 3 distribution can be used as an alternative to compute SPI values for drought monitoring and prediction, without much lost in content.

Keywords: Rainfall trend, Standardized Precipitation Index, Drought.

Introduction

Drought is considered as a slowly, reoccurring natural phenomenon that develops after a lengthy period of insufficient or delayed precipitation over a large area (McKee et al., 1993). This natural hazard has an adverse effect on key socio-economic sectors such as water, agriculture, energy, tourism and recreation. Drought monitoring and prediction plays an essential role for mitigation as well as for effective planning measures to alleviate the inherent impacts of drought. The Standardized Precipitation Index (SPI) is the most commonly used drought index for monitoring and prediction of drought (Potop et al., 2012; Chen et al., 2013; Svensson, 2016). In particular, the SPI is recommended by the World Meteorological Organization for drought monitoring and has key advantages that include spatial consistence, simplicity and flexibility as it can be tailored into time scales of user's interest (e.g. 1, 2, 3…, 24 months) (Hong et al., 2007).

The SPI is computed by fitting a statistical probability distribution function (PDF) to the monthly precipitation observations. The selected PDF is often considered as the most appropriate function that fits well to the precipitation time series. The Gamma statistical distribution function has in most cases been a natural selection choice when computing SPI (Alam et al., 2012; Botai et al., 2016; Ghamghmai et al., 2016; McKee et al., 1993). However, there are other research studies that recommend the use of other distribution functions, such as the Log-Normal (Angelidis et al., 2012), the Generalized Normal distribution (Blain et al., 2015), Log-Pearson (Gutterman, 1999) and Generalized Logistic distribution (Stagge et al., 2015). These studies seem to suggest that the selection of PDF plays virtual role in the computation of the SPI time series, implying that that the selection of PDF has an effect on the outcome of the derived SPI. Despite the importance of PDF in SPI computation, it is not very clear whether the PDF exhibits any spatial dependency characteristics.

The SPI is used in South Africa, particularly by the South African Weather Service to monitor drought conditions in the country. This research study aims to assess the sensitivity of SPI to various statistical PDFs and identify the most suitable distribution function that can be used when computing the SPI series for drought monitoring in the Western Cape Province, of South Africa.

Study area

The Western Cape Province (WCP), depicted in Fig. 1 is located on the south-western part of South Africa. It has a surface area of 129,462 km which boarders both the Northern Cape and the Eastern Cape provinces in the north and east, respectively. Furthermore, the province is surrounded by the Atlantic Ocean on the west and the Indian Ocean in the south (Census, 2011). The Province has the highest rainfall variations compared to other provinces of the country, with a minimum of 60 mm and a maximum of 3345 mm per annum, while most areas receive roughly between 350 and 1000 mm per annum (Gasson, 1998).

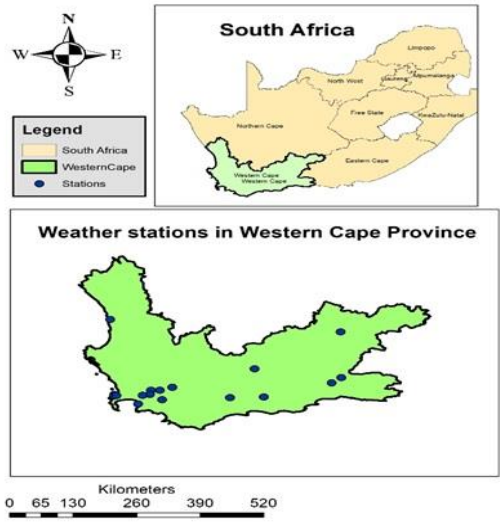

Figure 1: Map of the Western Cape Province with the distribution of the selected meteorological stations

Data and methodology

Daily precipitation data for the years 1985-2018(33 years) from 11 meteorological weather stations was collected from the Department of Water and Sanitations website http://www.dwa.gov.za/Hydrology/Verified/hymain.aspx. The selection of meteorological weather stations in the Western Cape Province was based on the availability of continuous datasets, allowing not more than 5% of missing data per station. Seven of the stations are located along the west coast which receive rainfall in winter, the remaining stations are found along the Eastern interior where most of rainfall occur in late summer and autumn season.

Characteristics of the annual precipitation data across the selected stations were based on the mean, standard deviation, coefficient of variation, kurtosis and skewness. The non- linear Mann-Kendall statistical method was used to test if there was a positive or negative trend in the rainfall time series. For details on how the MK- test is computed refer to Yue et al., (2002). The derived trends were tested with a statistical significance level of $p = 0.05$.

In total, four, different statistical distribution functions (e.g. Normal, Weibull, Gamma and Pearson Type 3) were used to assess the sensitivity of the SPI series to these PDFs. The computation of the SPI time series across the stations was based on the methodology proposed by McKee (1993). In general, the SPI was computed by first fitting each of the four selected PDFs to the monthly precipitation series from 11 meteorological weather stations, all distributed within the Western Cape Province, over a 12-month accumulation period. Fitting the PDFs resulted in the estimation of PDFs' parameters that describe the relation of the distribution functions to the rainfall observations. The fitted PDFs were then transformed into a normal distribution so that the mean SPI and standard deviation are 0 and 1, respectively (McKee, 1993). The resulting SPI is a set of positive and negative values corresponding to wet and dry conditions, respectively.

Once the SPI series for each PDF was computed, the sensitivity of the computed SPI to each PDF was assessed across the stations. This was achieved by comparing the SPI series across different PDFs with drought features, particularly, the duration and severity, derived from the streamflow drought index. The streamflow drought index was calculated using data from three stream-gauge stations distributed in the central and south-eastern part of the Western Cape Province. The selection of the best suitable PDF was based on the ability of the SPI to detect and reflect similar drought conditions as those observed from the streamflow drought analysis.

Results

Precipitation characteristics

Table 1 summarizes characteristics of rainfall data across the stations. The mean varies across the stations, ranging between approximately 1 to 5 mm/day. The standard deviation is high (16 mm/day) for G1E006, followed by G2E005 and G2E005 and H1E007 with standard deviation of ~13 and ~11 mm/day, respectively. The coefficient of variation was greater than 2 across all stations, with station H4E007 exhibiting the highest coefficient of variation. The distribution of rainfall is extremely skewed, with skewness coefficient of greater than 4, across all stations. In addition, rainfall time series exhibits thick-tailed distribution (e.g. positive coefficient of kurtosis) across all stations. In particular, station H4E007 exhibits the highest kurtosis value (169 units), suggesting the data might have more outliers.

Table 1. Characteristics of rainfall observations across the stations. STD = standard deviation, CV = coefficient of variation, Kurt = kurtosis, Skew = skewness

Meteorological weather stations	Mean mm/day	STD mm/day	CV	Kurt Units	Skew
G1E003	2.59	8.64	3.34	55.5	5.82
G1E006	4.93	16.2	3.28	80.1	6.41
G2E003	2.30	6.66	2.90	36.5	4.95
G2E004	4.23	11.1	2.61	29.8	4.4
G2E005	4.34	12.7	2.29	33.1	4.68
G3E003	0.61	2.29	3.81	79.6	7.57
G4E001	2.58	7.56	2.92	55.6	5.52
H1E007	2.89	10.9	3.78	162	8.92
H4E007	0.87	4.33	4.95	169	10.1
H6E001	1.47	5.54	3.75	120	8.59
H7E002	2.02	6.85	3.39	120	8.21

Trends in precipitation

Fig. 2 depicts annual trends in rainfall across the stations. Based on the results, all the analysed stations exhibit negative trends. The observed negative trends suggest that, there's has been a decrease in rainfall over the 33-year period of study. The trends in four stations (indicated in red) are statistically significant at 0.05 significance level.

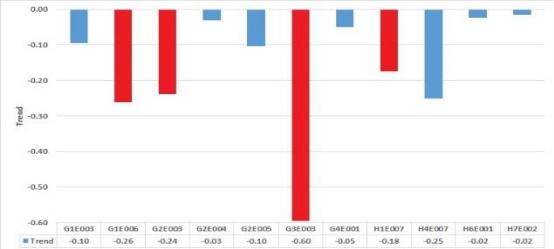

Figure 2: Annual precipitation trends across the stations, red indicates stations exhibiting statistically significant trends at 95% significant level.

Characteristics of the SPI series

Fig. 3 depicts the SPI time series for two selected stations. The corresponding time series were calculated using 12 months' accumulation period. The time series depicts both wet and dry conditions over the 33-year study period. Both, set of figures (top corresponding to G1E006 and bottom to G2E004 stations) depict highly variable wet and dry conditions. Drought across the stations range from mild (e.g. SPI values greater than -1.00 but less than 0) to moderate (e.g. SPI values greater than -1.50 but less -1.00), although there are few cases where severe drought (SPI greater than -2.00 but less than -1.50) is detected. Prolonged drought is observed between 2015 and 2018.

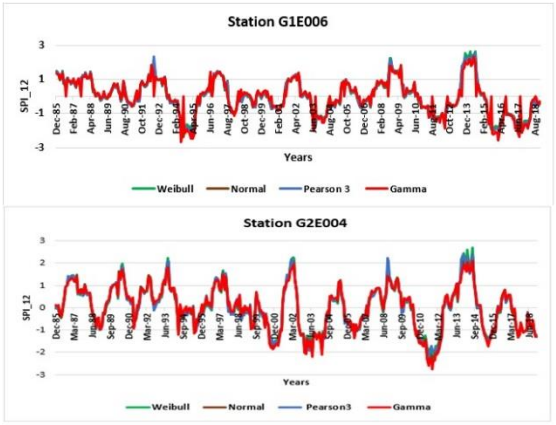

Figure 3. Monthly SPI time series of selected meteorological stations showing a detailed trend of how drought events processed over the years.

Sensitivity of SPI to PDFs

The sensitivity of the SPI to different PDFs was evaluated by comparing the SPI series for each PDF with the drought duration and severity computed from streamflow drought index. Results for drought characteristics as derived from streamflow drought index and utilized for SPI inter-comparisons are presented in Table 2. Three major drought duration and severity events occurred with G1H008 station, whereas the other two stations experience two major events per station.

Based on the results for annual average SPI time series across the selected stations (see Fig. 4) it is noted that the all the selected distribution functions are able to detect the drought durations shown in Table 2. The Weibull (green) distribution tends to underestimates the severity of each event compared to the three other distributions. The Gamma (red) and Pearson Type 3 (blue) tend to show similar characteristics, in terms of detecting drought duration as well as the severity of each event. In some cases, however, Pearson Type 3 seem to under-estimate the severity, while, Gamma distribution slightly over-estimate the severity, particularly, the events that occurred between 2015-2017 years for stations G2E004.

Table 2. Streamflow drought characteristics. DD=drought duration DS=drought severity.

Stream-gauge stations	No of events	Start	End	DD	DS
G1H008	1	2004-11-04	2005-05-29	187	4
	2	2015-04-03	2016-03-26	358	98
	3	2016-10-29	2018-04-18	518	115
G1H003	1	1994-11-01	1995-06-08	219	4
	2	2017-01-11	2018-04-22	438	28
H1H006	1	2015-08-11	2015-12-25	136	126
	2	2017-06-18	2017-10-14	118	118

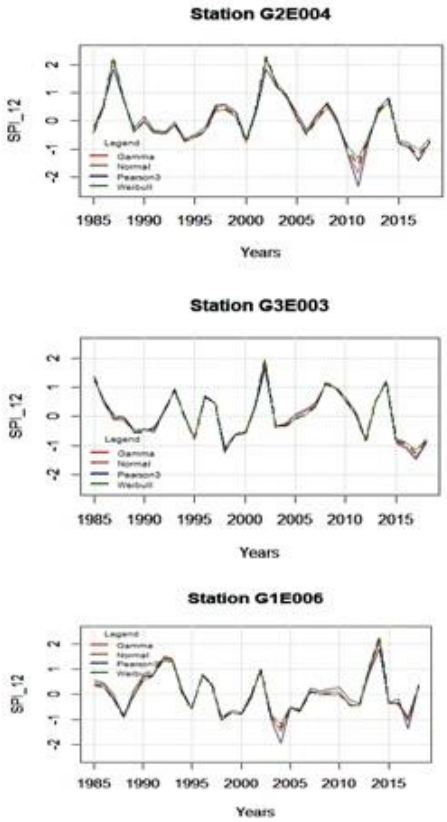

Figure 4. Annual average SPI time series for selected meteorological stations (G2E004, G3E003, G1E006).

Conclusion

The SPI was computed using the default Gamma distribution and alternative distribution functions (Normal, Weibull, and Pearson Type 3) to monthly precipitation data of 33 years, from 11 meteorological weather stations. In general, the results depict minimal differences between the four selected PDFs. Major drought duration that occurred between 2016 and 2017 (see Table 2, station G1H008) are clearly detected, particularly, by Gamma and Pearson Type 3 distributions, although there are small differences in the estimation of the drought severity. This study has confirmed the significance of using Gamma distribution for the computation of the SPI for drought monitoring, as suggested in the literature. However, based on the results, Pearson Type 3 can also be used as an alternative distribution function for the same purpose, without much lost in information content.

References

Alam, A.T.M.J., Rahman, M.S., Saadat, A.H.M & Huq.M.M.(2012). Gamma distribution and its application of spatially monitoring meteorological drought in Barind, Bangladesh. *Journal of Environmental Science and Natural Resources, 5(2): 287-293*.

Angelidis, P., Maris, F. Kotsovinos, N & Hrissanthou, V. (2012). Computation of drought index SPI with alternative distribution functions. Water resources management journal. 26(9): 2453-2473.

Blain, G.M & Meschiatti, C.M. (2015). Inadequacy of the gamma distribution to calculate the Standardized Precipitation Index, Revista Brasileira de Engenharia Agrícola Ambiental.19(12): 1129–1135.

Botai, C.M., Botai, J.O, Dlamini L.C., Zwane, N.S & Phaduli, E. (2016). Characteristics of Droughts in South Africa. A Case Study of Free State and North West Provinces. Water Journal .439(8):1-23.

Gasson, B. 1998. The Biophysical Environment of the Western Cape Province in relation to its economy and settlements, School of Architecture and Planning, University of Cape Town for the Department of Local Government and Housing (Directorate of Development Promotion) of the Province of the Western Cape https://www.westerncape.gov.za/text/2005/12/4a_wc_pages_51-114_web.pdf (URL),1 May 2019.

Gudmumundsson, L& Stagge, J.H. 2016. Standardized Climate Indices such as SPI, SRI or SPEI. SCI- package

Ghamghami, M., Hejabi, S., Rahimi, J., Bazarafshan, J & Olya, H. (2016). Modelling a drought index using a nonparametric approach. Global Nest Journal.19:58-68.

Hong W. U., Hayes M.J., Weiss, A & QI HU. 2001: Calculation of the Standardized Precipitation Index, the China-Z index and the statistical Z-score, International Journal of Climatology, 21: 745-758. http://webapps.daff.gov.za/AmisAdmin/upload/Western%20Cape%20Provincial%20Profile%20-%2005Aug14.pdf (URL), date accessed 1 May 2019.

McKee, T.B., Doesken, N.J & Kleist, J.(1993). *The Relationship of Drought Frequency and Duration to Time Scales.* Proceeding of the Ninth Conference on Applied *Climatology*. *American Meteorological Society*: Boston; 179–184.

Potop, V., Boronean, T. C., Možný, M., Štěpánek, P & Skalák, P. 2012. Observed spatiotemporal characteristics of drought on various time scales over the Czech Republic, Springer, Inc.

Stagge, J.H., Tallaksen, L.M., Gudmundsson, L., van Loon, A.F & Stahl, K. (2015). Candidate distributions for climatological drought indices (SPI and SPEI), International journal of Climatology. 35 (13): 4027–4040

Yue, S., Pilon, P., Phinney, B & Cavadias, G. (2002). The influence of autocorrelation on the ability to detect trend in hydrological series. Hydrological processe.16:1807 – 1820.

Projected changes of wildfire risks in South Africa under climate change scenarios and temperature thresholds

Anna E Wiese[1,*] and Asmerom F. Beraki[1,2]

[1]University of Pretoria - Department of Geography, Geoinformatics and Meteorology, Pretoria, South Africa
[2]CSIR - Smart Places, Global Change, Climate and Air Quality Modelling (CAQM), Pretoria, South Africa

*Corresponding author: *u15130348@tuks.co.za

Interactions between weather, fuels and humans spur wildfires which has many negative impacts. Research indicates increased numbers of wildfire days in South Africa due to global warming, but effects on wildfire regimes is unknown. This study investigates this using the conformal-cubic atmospheric model simulations constrained with a Representative Concentration Pathway (RCP) trajectory. The study explores projected changes of wildfire regimes under a low mitigation scenario and 1.5°C, 2.0°C and 3.0°C global temperature goals using the Canadian Forest Fire Danger Rating System. Results suggest that the size and severity of wildfires may increase with potential changes in positioning of risk areas.

Keywords: Wildfire regimes, fire season, representative concentration pathway, South Africa, CCAM

Introduction

Wildfires are global phenomena that result in destruction of agriculture and habitats, pollution and loss of life. This occurrence is a product of the interactions between weather, fuels and humans (De Groot et al., 2009). Research has indicated that fire weather seasons have lengthened, frequency has increased, and more burnable areas are affected (Bowman et al., 2015). It is however difficult to determine future trends due to complex and nonlinear interactions between the weather, vegetation and humans (De Groot et al., 2009). Fire danger indices are developed based on weather variables that influence ignitability, spread rate and controllability of wildfires. A Fire Weather Index can predict the seriousness of the fire conditions and the threat it may pose if not controlled.

Wildfires severely affect the biodiversity of an area as it causes the loss of forestry and plant life (Das et al., 2010). Changes in wildfire regimes may also affect the distribution of agriculture and housing as wildfire is a direct threat to human life and livestock. A fire management system is set in place by the government to control fires using fire suppression measures, to set and implement evacuation plans and to plan prescribed burning events (South Africa, 2013). Researching the number of occurrences of natural wildfires, fire season length and the affected areas aids in understanding the change of wildfire regimes due to climate change. Due to the drier conditions, wildfire events occur more frequently and effect a larger area in some parts of the world (Henley et al., 2015, Engelbrecht et al., 2015). In southern Africa it is projected that high fire days will increase with the increase in temperatures, but the effects on wildfire season length, intensity and the affected areas is unclear (Engelbrecht et al., 2015).

In 2015 the Paris Agreement was formed that aims to keep the increase in global temperatures under 2°C above pre-industrial levels as well as to further limit this temperature increase to 1.5°C (United Nations, 2019). The Intergovernmental Panel on Climate Change (IPCC) Fifth Assessment Report (AR5) developed models to simulate climate under future emission scenarios. These Representative Concentration Pathways (RCPs) are used to simulate what climate extremes may look like (Canadell et al., 2016). The RCPs represent greenhouse gas (notably CO_2) concentration futures, which are all considered possible trajectories depending on the concentration of greenhouse gases that are emitted to the atmosphere. The model is forced with RCP8.5 to assess the impact of climate change on wildfire regimes.

This attempt to link climate change to wildfire changes is crucial for the understanding of the effect of climate change. Looking closely at the change in weather conditions that now prevail when wildfires occur, it might be possible to identify a trend. For this research data from 1960 to 2099, in accordance with the RCP simulated scenario time, is used over the domain of South Africa. The hypothesis for this study is "*there is a change in wildfire activity due to climate change*". The study thus tests the hypothesis under low mitigation and different global temperature goals using Daily Severity Ratings and Fire Weather Indices with the ultimate objective of assessing the extent and scale of future projected wildfire risks.

Data and Methodology

This research project was conducted over the domain of South Africa which lies between 20°S to 36°S and 15°E to 35°E. High resolution model simulations for the present day and future projections incorporating climate change parameters was analysed along with variables such as temperature, humidity, precipitation and wind speed. The simulations for the period of 1960 to 2099 was used.

Model description

The regional climate model used is the conformal-cubic atmospheric model (CCAM; McGregor & Dix, 2008). The CCAM is a variable resolution global climate model (GCM). The model is developed by the Common-wealth Scientific and Industrial Research Organization (CSIRO) (Thatcher & McGregor, 2009). CCAM runs coupled to the dynamic land-surface

model CSIRO Atmosphere Biosphere Land Exchange (CABLE) (Kowalczyk et al., 1994).

Model simulations and observation data
Six sets of GCM simulations of CMIP5 and AR5 of the IPCC were downscaled to 50 km resolutions globally. The simulations span the period 1960-2099 (Archer et al., 2018). The CCAM downscales the Australian Community Climate and Earth System Simulator (ACCESS1-0); Geophysical Fluid Dynamics Laboratory Coupled Model (GFDL-CM3); National Centre for Meteorological Research Coupled Global Climate Model version 5 (CNRM-CM5); Max Planck Institute Coupled Earth System Model (MPI-ESM-LR); Norwegian Earth System Model (NorESM1-M) and Community Climate System Model (CCSM4).

The model simulations were conducted at the Centre for High Performance Computing (CHPC) at the Meraka Institute at the Council for Scientific and Industrial Research (CSIR) (Archer et al., 2018). Bias-corrected monthly sea-surface temperatures and sea-ice concentration forcings are used for each simulation. Carbon dioxide, ozone and sulphate forcing was implemented in line with the RCP scenarios. The bias is computed by subtracting for each month the Reynolds et al. (2002) SST climatology (for 1961-2000) from the corresponding CGCM climatology (Muthige et al., 2018).

The project makes use of observational data compiled from various sources to assess how the model baseline simulations represent observed features of wildfires. Data sources include reanalysis data from the National Centers for Environmental Prediction (NCEP; Kanamitsu et al. 2002) which can also be used as a proxy for observations.

Canadian Forest Fire Danger Rating System
The Canadian Forest Fire Danger Rating System (CFFDRS) is a well-known system for predicting and assessing wildfire risks globally (Van Wagner 1987). It consists of two components: the fire weather index (FWI) and the fire behaviours prediction system. This study will concentrate on the FWI component. This system has often been used to plan fire management schemes, to train fire management personnel and to research the association between climate change and changing fire weather.

Four climate variables which play a key role in wildfire potential are: daily maximum temperatures, daily relative humidity, total precipitation and mean maximum 10m wind speed (Bowman et al., 2015). These variables are taken at noon daily and are used as input in the CFFDRS package in RStudio to calculate the Fine Fuel Moisture Code (FFMC), Duff Moisture Code (DMC), Drought Code (DC), Initial Spread Index (ISI), Build-up Index (BUI), Fire Weather Index (FWI) and Daily Severity Rating (DSR). The FFMC expresses the moisture content of fine and dry fuels and indicates sustained burning ignition and spread rate of fires. DCM expresses moisture content of dead, loose organic matters and indicates the relationship between probability of ignition by lightning and fuel consumption. DC expresses deep, heavy, dry organic matter and indicates the relationship between fire extinguish potential and heavy fuel consumption. ISI is calculated by combining FFMC and wind to express the spread rate excluding the impact of fuels. BUI is calculated by combining DMC and DC and expresses the amount of fuels present used by the fire to spread. FWI is calculated by combining ISI and BUI and express the fire spreading intensity in energy rate/unit length of fire front. DSR is a function of FWI that expresses the difficulty to control a fire. The FWI indicates growth, intensity and suppression difficulty of wildfires.

Fire statistics and ensemble means of DSR were created using Climate Data Operators (CDO) for seasonal and monthly time scales. The DSR averaged over many seasons is described as the Seasonal Severity Rating (SSR) and is a better representation of fire climate characteristics over many seasons and regions. The Seasonal Severity Rating are projected by RCP 8.5 for 1.5 ºC, 2 ºC and 3ºC temperature threshold. This component is analysed below to show characteristics of the fire regime that is projected to change.

Results and Discussion
Wildfire regimes consist of the area affected, the season in which the most fire events occur as well as the frequency of fire events and its level of danger or intensity. The current climate for South Africa defines its fire seasons to be in the summer months (December, January, February) for the Western Cape and in the spring months (September, October) for the rest of the country which as these are the driest months (Engelbrecht et al., 2015). However, this study looks at the winter months (June, July, August) season.

The first figure looks at the DJF season which is relevant to the Western Cape fire season. The 3ºC temperature threshold is expected to be reached by the end of the 21st century if no action is taken towards mitigation. The area most effected, as shown in Fig. 1, is concentrated to the western part of South Africa as well as to the north into Namibia. The DJF season wildfire risk is thus projected to be more related to the Northern Cape by the simulations. The data also shows that the burnable area increases in size with the increase in temperature towards the end of the 21st century. The size of the burnable area affected for the 3ºC temperature threshold is much larger than the area for 1.5ºC temperature threshold.

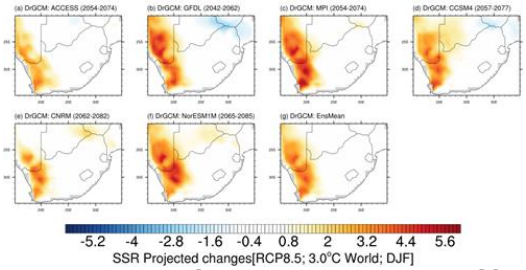

Figure 1: Seasonal Severity Rating projected by RCP 8.5 for 3 ºC temperature threshold for the DJF season. The figure shows all six simulations as well as the ensemble mean.

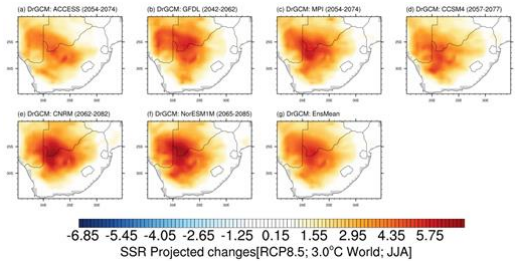

Figure 2: Seasonal Severity Rating projected by RCP 8.5 for 3 ºC temperature threshold for the JJA season. The figure shows all six simulations as well as the ensemble mean.

The second figure looks at the JJA season relating to the winter. The area most expected to be affected, as shown in Fig. 2, is concentrated to the central and western parts of South Africa as well as a great part intruding into neighbouring countries. This deviates from the current risk classification which is that the highest risk occurs over the central and eastern parts of South Africa (Forsyth et al., 2010).

The data also shows that, similarly to the DJF season, the size of the burnable area increases with the increase in temperature towards the end of the 21st century. The size of the burnable area affected for the 3ºC temperature threshold is much larger than the area for 1.5ºC temperature threshold. For the JJA season, the area affected during the time period when the 2ºC temperature threshold is reached is, however, smaller than both the areas of the 1.5ºC temperature threshold (not shown) and 3ºC temperature threshold. Thus, there may be some effect or forcing present when the 2ºC temperature threshold is reached that reduces the number of wild fire events or it could be as a result of model deficiency and is to be investigated further.

The DJF season has a lower frequency of fire events in comparison to the JJA season in South Africa which remains the same for the future projections. In both figures it is, however, evident that the intensity for both seasons increases towards the end of the simulation period. The severity of the JJA season is far greater than that of the DJF season. For both seasons the severity of wildfire events increases gradually from the 1.5ºC temperature threshold to the 3ºC temperature threshold.

When comparing the size of the burnable areas affected for the two seasons the JJA season poses a greater threat than the DJF season in terms of fire danger and is projected to be quite larger than the current area and the DJF area. Both burnable areas increase in risk to the west and northward presumably posing a serious problem for areas that previously did not expect wildfire events in that season. The north western region of South Africa is currently classified as a low risk area but projected to be the area with the greatest wildfire severity towards the end of the century (Forsyth et al., 2010). This makes the western part of the country more susceptible to fire events in both seasons which influences infrastructure, agriculture, safety, wildfire management systems etc. for this region. The severity of the wildfire seasons may exacerbate problems for South Africa under the low mitigation scenario.

Conclusions

The DJF SSR shows a projected increase in wildfire risk over the western parts of the Northern Cape and increased intensity. The JJA SSR shows a similar projected increase in wildfire risk over the northern central parts of South Africa as well as a great increase in intensity. The JJA season has both a larger extent and stronger severity in comparison to the DJF season. Wildfire risk may greatly increase over South Africa under the RCP 8.5 scenario and temperature thresholds. Wildfire regimes are projected to change considerably.

It should be noted that this work is part of an ongoing research project and the results presented here are based on preliminary analysis. The comparison of model historical wildfire simulations against the corresponding NCEP, and assessment of projected changes in frequency of wildfire dangers are underway.

Acknowledgements

Acknowledgement is due to the Center for High Performance Computing (CHPC) for providing computational facility. The R Project for Statistical Computing (https://www.r-project.org) and NCAR Command Language (NCL) (http://www.ncl.ucar.edu) were used for analysis and graphics.

References

Amiro, B.D., Logan, K.A., Wotton, B.M., Flannigan, M.D., Todd, J.B., Stocks, B.J. & Martell, D.L. (2004). Fire weather index system components for large fires in the Canadian boreal forest. *International Journal of Wildland Fire*, 13, pp. 391-400.

Archer, E., Engelbrecht, F., Hänsler, A., Landman W.A., Tadross, M. & Helmschrot, J., (2018). Seasonal prediction and regional climate projections for southern Africa. In: Climate change and adaptive land management in southern Africa – assessments, changes, challenges, and

solutions (ed. by Revermann, R., Krewenka, K.M., Schmiedel, U., Olwoch, J.M., Helmschrot, J. & Jürgens, N.), pp. 14-21, *Biodiversity & Ecology*, 6, Klaus Hess Publishers, Göttingen & Windhoek. doi:10.7809/b-e.00296.

Bowman, D.M.J.S., Brown, T.J., Cochrane, M.A., Freeborn, P.H., Holden, Z.A., Jolly, W.M. & Williamson, G.J. (2015). Climate-induced variations in global wildfire danger from 1979 to 2013. *Nature Communications*, 6 (7537).

Canadell, P., Dix, M., Jubb, I. (2016). Representative Concentration Pathways. *Australian Climate Change Science Program.*

Das, S., De Klerk, H., Forsyth, G.G., Khuluse, S., Schmitz, P. & Van Wilgen, B.W. (2010). Fire management in Mediterranean-climate shrublands: a case study from the Cape fynbos, South Africa. *Journal of Applied Ecology*, 47, pp. 631-638.

De Groot, W.J., Flannigan, M.D., Gowman, L.M., Krawchuk, M.A. & Wotton, B.M. (2009). Implications of changing climate for global wildland fire. *International Journal of Wildland Fire*, 18, pp. 483-507.

Engelbrecht, F., Adegoke, J., Bopape, M-J., Naidoo, M., Garland, R., Thatcher, M., McGregor, J.L., Katzfey, J., Werner, M., Ichoku, C. & Gatebe, C. (2015). Projections of rapidly rising surface temperatures over Africa under low mitigation. *Env. Res. Letters.* 10 085004.

Forsyth, G.G., Kruger, F.J. & Le Maitre, D.C. (2010). National veldfire risk assessment: Analysis of exposure of social, economic and environmental assets to veldfire hazards in South Africa. *CSIR Report No: CSIR/NRE/ECO/ER/2010/0023/C.*

Fusco, E.A. (2016). Quantifying the human influence on fire ignition. *Ecological Applications*, 383.

Henley, B.J., Karoly, D.J. & King, A.D. (2017). Australian climate extremes at 1.5°C and 2°C of global warming. *Nature Climate Change.*

Holtslag, A.A.M. & Boville, B.A. (1993). Local versus non-local boundary layer diffusion in a global climate model. *Journal of Climate*, 6, pp. 1825-1842.

Kowalczyk, E.A., Garrat, J.R. & Krummel, P.B. (1994). Implementation of a soil-canopy scheme into the CSIRO GCM-regional aspects of the model response. *CSIRO Division of Atmospheric Research Technical Paper, 32 (59).*

Lawson, B.D. & Armitage, O.B. (2008). Weather guide for the Canadian Forest Fire Danger Rating System. *Natural Resources Canada, Canadian Forest Service North Forestry Centre.*

Kanamitsu, M., Kumar, A., Schemm, J.K., Juang, H.M.H., Wang, W., Yang, F., Hong, S.Y., Peng, P., Chen, W. & Ji, M. (2002). NCEP dynamical seasonal forecast system 2000. *Bull. Amer. Meteor. Soc*., **83**: 1019-1337.

McGregor, J.L. & Dix, M.R. (2008) An updated description of the conformal-cubic atmospheric model. *High Resolution Numerical Modelling of the Atmosphere and Ocean*, pp. 51–75. Available at https://doi.org/10.1007/978-0-387-49791-4_4 . [Accessed 9 May 2019]

McGregor, J.L. (2005). Geostrophic adjustment for reversibly staggered grids. *Monthly Weather Review*, 133, pp. 1119-1128.

Muthige, M.S., Beraki, A., Englebrecht, F.A., Grab, S., Maisha, T.R., Malherbe, J. & Van der Merwe, J. (2018). Projected changes in tropical cyclones over the South West Indian Ocean under different extents of global warming. *Environmental Research Letters*, 13 (065019).

Reynolds, R.W., Rayner, N.A., Smith, T.M. & Stokes, D.C. (2002). An improved in situ and satellite SST analysis for climate. *Journal of Climatology*, 15, pp. 1609–1625.

Rotstayn, L.D. (1997). A physically based scheme for the treatment of stratiform clouds and precipitation in large-scale models: Description and evaluation of the microphysical processes. *Royal Meteorological Society*, 123, pp. 1227-1282.

South Africa. (2013). Fire Danger Rating System. *Department of Agriculture, Forestry and Fisheries, Staatskorant*, 37014 (37).

Thatcher, M. & McGregor, J.L. (2009). Using a Scale-Selective filter for dynamical downscaling with the Conformal Cubic Atmospheric Model. *Monthly Weather Review; Washington*, 137(6), pp. 1742 - 1752.

Wang, X., Wotton, M.B., Cantin, A.S., Parisien, M., Anderson, K., Moore, B. & Flannigan, M.D. (2017). Cffdrs: An R package for the Canadian Forest Fire Danger Rating System. *Ecological Processes*, 6(5).

Working on Fire (2019). Fire in the South African Landscape. *Department of Environmental Affairs* [Online]. Available at https://workingonfire.org/fire-in-the-south-african-landscape/ . [Accessed 25 June 2019]

United Nations. (2019). *The Paris Agreement* [Online]. Available at https://unfccc.int/process-and-meetings/the-paris-agreement/what-is-the-paris-agreement . [Accessed 28 February 2019]

Van Wagner, C.E. & Pickett, T.L. (1985). Equations and FORTRAN program for the Canadian Forest Fire Weather Index System. *Can. For. Serv., Ottawa, Ont. For. Tech. Rep*, 33, pp. 18

6. CLIMATE SERVICES, POLICY AND RESEARCH OPPORTUNITIES

How costly are poor seasonal forecasts?

Willem A. Landman, Department of Geography, Geoinformatics and Meteorology, University of Pretoria
Emma Archer, Department of Geography, Geoinformatics and Meteorology, University of Pretoria
Mark Tadross, Climate Systems Analysis Group, University of Cape Town

Corresponding author: Willem.Landman@up.ac.za, Tel: +27-12-420-3713;

Seasonal forecast system development has made significant advances in recent years, including the development of models for hydrological, agricultural and health applications utilising forecast output from complex global climate models. The skill levels of these models are in some cases (location and season) found to be promising when evaluated over an extended period of time – notwithstanding the fact that during some years forecasts may still be wrong even for skilful models. In this study, we investigate what the financial implications might be when forecast crop-yields are wrong in consecutive years. The paper first introduces a linear statistical dry-land crop-yield model that uses output from a coupled ocean-atmosphere climate model as a predictor of crop-yield. The crop model is shown to be skilful, but produced poor forecasts for three consecutive years during the test period. We evaluate what the possible cost implication might be for a farmer who makes financial investments or takes financial risks in proportion to the crop-yield forecasts.

Keywords: crop-yield forecasts, coupled ocean-atmosphere model, El Niño and La Niña, accumulated profit

Introduction

The seasonal forecast community has developed complex climate models for operational seasonal forecasting in South Africa (Beraki et al., 2014). For optimal seasonal forecast production, atmospheric models are coupled to similar models for the ocean, the land surface and sea ice. Notwithstanding their demonstrated accuracies, statistical correction methods are recommended even for today's coupled climate model forecasts (Barnston and Tippet, 2017). The use of such multi-tiered forecast systems have shown to be more accurate for seasonal rainfall forecasts, at least for SADC (Landman et al., 2012). Recently, hindcasts (or re-forecasts) over a period spanning several decades have been used in the development of application models for agriculture in southern Africa (Malherbe et al., 2014) and hydrology (Muchuru et al., 2014). In some cases, the developed application models have been used in an operational seasonal forecasting environment (see the archived forecasts produced by the University of Pretoria for examples: https://tinyurl.com/ybrb3a72). As is the practice with operational seasonal forecasting, these forecasts, including applications forecasts, are accompanied by some indication of forecast skill evaluated over an independent test period. The skill estimates represent a general statement on the overall skill of the forecast system. In this study, we want to develop an application model, and more specifically a model for the prediction of dry-land crop-yields at a single farm in South Africa. We then determine the skill levels of the model, followed by an assessment of possible financial implications for the forecast user (in the agricultural sector) when there is a succession of poor or "missed" forecasts produced by the model.

Data and Methodology

a. Data

A set of coupled model hindcasts (or re-forecasts) and end of season crop-yield data are used in the following analysis. The climate model data have been used already for a number of predictability studies (e.g. Landman et al, 2012) and consists of ensemble mean (from 12 members) 850 hPa geopotential height (i.e. near-surface atmospheric circulation) as a proxy for rainfall hindcasts. This geopotential height field has long since been established as a predictor that can replace a climate model's predicted rainfall fields in statistical downscaling for southern Africa (Landman and Goddard, 2002). The geopotential height anomalies are forecast using the ECHAM4.5-MOM3 coupled model (DeWitt, 2005) for December to February (DJF) seasons, with a model initialization month of November. Since DJF is often the best forecast skill season over the region and the rainfall during this season plays a significant role during grain filling and tasselling, it was decided to use only climate model data for DJF as a predictor of end of season dryland crop-yield. Even though additional atmospheric variables (e.g. relative or specific humidity) might improve forecast skill, we leave aside additional variables as our focus is on demonstrating the impact of poor forecasts, and geopotential height is sufficient for deriving a reasonably skilful model.

The crop-yield data have been obtained from a farm near Bapsfontein (26°0′0″S 28°26′0″E) in South Africa. The period over which the analysis is done is the 21 years from 1987/88 to 2007/08. This period consists of 7 El Niño, 7 La Niña and 7 ENSO-neutral seasons according to the Oceanic Niño Index for cold and warm episodes. The crop yields are first detrended to remove the linear upward trend often associated with crop-yield data. To ensure that the yield data are from a normal distribution for optimal statistical modelling to be performed, the natural logarithm of the yield values are calculated and referred to in the following text. The Lilliefors (Wilks, 2011) goodness-of-fit test shows that the newly derived crop yield values are indeed from an unspecified normal distribution.

b. Methods

The IRI's Climate Predictability Tool (CPT) is used for producing crop-yield hindcasts and for verification. The predictor set is the ensemble mean 850 hPa geopotential height field of the coupled model, and the predictand the Bapsfontein crop yields. The canonical modes of the hindcasts are used in a multiple linear regression model as predictors. The forecast skill level of the statistical crop-yield model is first tested using a cross-validation setup with a 5-year-out window. Then the crop model is used to produce retro-active crop-yield forecasts for the two periods from 1999 to 2008 and from 2003 to 2008. The retro-active forecast process of the CPT creates probabilistic forecasts over these periods for three equi-probable categories with thresholds defined by respectively the 33.3rd (below which is the low yield category) and 66.7th (above which is the high yield category) tercile values of the climatological record. For a comprehensive description of the retro-active forecast process, refer to Landman et al. (2012).

We only show Pearson correlation values between cross-validated forecast and observed time series in order to represent the deterministic skill level of the crop model. Two sets of retro-active probabilistic forecasts are used to determine the potential economic value of the crop forecast system (Hagedorn and Smith, 2009). For this purpose we make use of the cumulative profit (CP) values generated by the CPT software. The CP values evaluate probabilistic forecasts by means of quantifying the skill of the forecast using an effective daily interest rate. Some capital is invested into the first of a series of consecutive probabilistic forecasts, say for example ZAR1,000. Depending on the outcome of how well the forecast performs, a return is obtained on the investment. This return is calculated based on 'fair odds' and assuming that the ZAR1,000 is spread across the forecast categories in proportion to the forecast probabilities. This means that for the observed category (above, below or normal), the farmer is returned three times the amount of money invested in that category each year. The CP results can be interpreted as follows: for the CP value of, say, 20 found for a specific retro-active forecast year, it means that an initial investment of ZAR1,000 in the first year would be worth ZAR(1,000x20=)20,000 in the specified year. One would subsequently invest all of the ZAR20,000 on the next year's forecast, and so forth. See Mason (2018) for a comprehensive explanation on the calculation of CP values.

Results

The cross-validation hindcasts and observed values, both normalised here, are presented in Fig 1. On the figure El Niño and La Niña years are respectively shown as "El" and "La". Also presented in the figure are the differences between the observed and predicted crop indices.

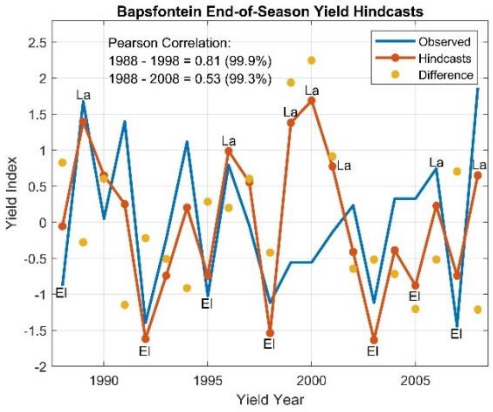

Figure 1. Cross-validation crop-yield hindcasts vs. observed values. The time series have been normalised. The Pearson correlation values for the first 11 years (1988 to 1998) and for all the years are presented on the figure, along with their levels of statistical significance.

Two features of the cross-validated results are immediately apparent. The first is that all the El Niño years are associated with below average predicted yields, and all the La Niña seasons are associated with above average predicted yields. One may thus deduce that ENSO phases play a significant part in this crop model's yield predictions for the Bapsfontein farm. Second, although all but one (2005) of the El Niño years are found to be actual low-yield years, a number of La Niña years are also actual low-yield years. For example, for the three-year period of 1999 to 2001 the observed yields are below average. The reasons for the forecast failures during these three seasons may be related to the observed rainfall outcomes during those

summers: the 1998/99 and 2000/01 seasons were not wet La Niña years over parts of SADC leading to low levels of soil moisture, and during 1999/00 the larger part of the region was flooded and possible damages to crops occurred.

The deterministic skill level of the cop-yield model is typical for southern Africa (c.f. Landman et al., 2012). Moreover, the correlation between forecasts and observed for the first half of the test period is very high (correlation > 0.8), suggesting that future forecasts may turn out to be skilful. However, the yield forecasts associated with the three La Niña seasons of 1998/99 to 2000/01 turned out to be poor. The question we want to answer in this study is whether or not these poor yield forecasts could have had a detrimental effect on the finances of a farmer basing decisions on them – specifically investment decisions, for the sake of the example. We address this question by first calculating the CP values for the seasons following the first 11 years of the data, i.e. from 1999 to 2008 as shown in Fig. 2. Negative CP values are found for the majority of the years, with positive values found only for 2005, 2007 and 2008. In fact, it was only at the end of the retro-active period when the farmer obtained substantial and positive CP's. The second retro-active period that excludes the poor forecasts associated with the three consecutive La Niña seasons present much better CP outcomes. In fact, it was primarily only during the 2005 season when there is a big difference between the forecast and observed anomalies where the CP value of this retro-active period is negative. Take note how the inclusion of the poor forecasts in the CP calculations has significantly delayed financial recovery, and how much less of a detrimental effect a single poorly forecast season (2005) has on profits compared to when consecutive seasons of poor forecasts are included. The above is a simple example, which can be expanded to include more realistic investment and planting strategies e.g. including maize prices and input costs.

Summary and Conclusions

Southern Africa ranks poorly against the majority of regions where ENSO has an effect on seasonal-to-interannual climate variability (Landman et al., 2019). Notwithstanding, seasonal forecasts have been found skilful over certain areas of the region and in particular during certain times of the year (Landman et al., 2012; Archer et al., 2019). Moreover, the majority of end-of-season crop yields over areas which include the Bapsfontein farm, are likely to be predictable when there is an ENSO event taking place (Landman and Beraki, 2012). Here we presented a linear statistical crop-yield prediction model that uses output from a coupled climate model that is linked with dry-land crop-yields at a single farm. The results presented may not be representative for all crop farms in the SADC region, since not all end-of-season yields may be equally influenced by ENSO events.

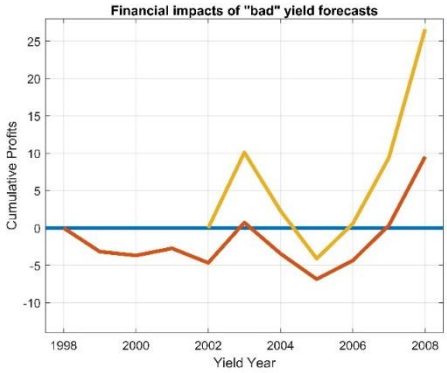

Figure 2. Cumulative profits as determined over the two retro-active forecast periods. Red: results from the retro-active period from 1999 to 2008; Orange: results from the retro-active period from 2003 to 2008.

Verification of the hindcasts produced by the crop model shows significant levels of skill. In fact, the first half of the 21-year deterministic verification period shows an unprecedented level of skill (corr > 0.81). Notwithstanding, the model performed poorly for three consecutive seasons during a series of La Niña events. We wanted to find out how such a sequence of poor forecasts may have affected the farmer during these three and subsequent years. The main conclusions that may be derived from this study are that the consecutive poor forecasts could have devastating consequences for the farmer, and that a possible financial recovery may only have happened a good number of years after the three poorly predicted years. We also show that a single poorly predicted season does not necessarily have the same negative financial impact.

So what implications does this result hold for seasonal forecast model developers, as well as those concerned with applying seasonal forecasts? There are several immediate implications, including:

- Even using a skilful seasonal forecast model may not immediately translate into tangible benefits to the user (or farmer as in this case), but may require sustained use of skilful forecasts over a period of several years;
- The yield forecasts and ENSO are symmetrical (low yields predicted during El Niño; high yields predicted during La Niña), but this symmetry is not as evident in the observed outcomes since not all La Niña seasons produced high yields;

- Even the hedging that takes place in CP calculations for each year (the capital is spread across the three categories according to the predicted probabilities) does not guarantee positive benefits. However, placing all resources on the assumption of single category outcome is even riskier.

It is clear that we may have to shift our priorities towards addressing user needs through tailored forecasting and the honest conveyance of model forecast caveats to users (including communication of uncertainty). Focussing our limited resources on demonstrating our capabilities as a modelling community, to address technical modelling challenges such as the production of high-resolution forecasts, risks ignoring fundamental limitations in using all seasonal forecasts. This is especially concerning in light of recent research which demonstrates that high resolution seasonal forecasts may hold very little benefit (Scaife et al., 2019). There are also some potentially relatively easy gains, such as exploring the benefit of using other prediction variables (e.g. pre-season soil moisture, evaporation-related variables etc), or combining a wider range of publicly available seasonal forecasts.

We need to be much more honest and transparent about our prediction capabilities even with skilful models such as the one presented here. Indeed, communicating how to use and interpret seasonal forecasts, as well as linking them to variables and impacts of interest to specific user groups in particular locations may hold as much, if not more benefit. Importantly, the process of producing responsible seasonal forecasts goes beyond producing the forecast itself and must not undermine trust between forecast producers and users through overblown promises of forecast accuracy and skill. To do so is to risk our efforts being misunderstood and ultimately ignored.

Acknowledgements

The work is a result of collaboration between South Africa and the IRI, supported by the National Research Foundation of South Africa (NRF) through their financial support of rated researchers, and the ACyS-ACCESS project funded by the NRF.

References

Archer, E., Landman W.A., Malherbe, J., Tadross, M. and Pretorius, S. (2019). South Africa's winter rainfall region drought: a region in transition? Climate Risk Management. **25**, 100188. DOI: 10.1016/j.crm.2019.100188.

Beraki, A., DeWitt, D., Landman, W.A. and Olivier, C. (2014) Dynamical seasonal climate prediction using an ocean-atmosphere coupled climate model developed in partnership between South Africa and the IRI. Journal of Climate. **27** 1719–1741. DOI:10.1175/JCLI-D-13-00275.1.

Barnston, A.G. and Tippett, M.K. (2017). Do statistical pattern corrections improve seasonal climate predictions in the North American Multimodel Ensemble models? Journal of Climate. **30**, 8335-8355. DOI: 10.1175/JCLI-D-17-0054.1.

DeWitt, D. G. (2005). Retrospective forecasts of interannual sea surface temperature anomalies from 1982 to present using a directly coupled atmosphere–ocean general circulation model. Monthly Weather Review. **133**, 2972–2995.

Hagedorn, R. and Smith, L.A. (2009). Communicating the value of probabilistic forecasts with weather roulette. Meteorological Applications. **16**, 143–155, DOI: 10.1002/met.92.

Landman, W.A. and Beraki, A. (2012). Multi-model forecast skill for mid-summer rainfall over southern Africa. International Journal of Climatology.**32**, 303–314. DOI: 10.1002/joc.2273.

Landman, W.A. and Goddard, L. (2002). Statistical recalibration of GCM forecasts over southern Africa using model output statistics. Journal of Climate, 15, 2038-2055.

Landman, W.A., Barnston, A.G., Vogel, C. and Savy, J. (2019). Use of El Niño-Southern Oscillation related seasonal precipitation predictability in developing regions for potential societal benefit. International Journal of Climatology, DOI: 10.1002/JOC.6157.

Landman, W.A., DeWitt, D. Lee, D.-E., Beraki, A. and Lötter, D. (2012). Seasonal rainfall prediction skill over South Africa: 1- vs. 2-tiered forecasting systems. *Weather and Forecasting*. **27**, 489-501. DOI: 10.1175/WAF-D-11-00078.1.

Malherbe, J., Landman, W.A., Olivier, C., Sakuma, H and Luo, J.-J. (2014) Seasonal forecasts of the SINTEX-F coupled model applied to maize yield and streamflow estimates over north-eastern South Africa. Meteorological Applications. **21**, 733–742. https://doi.org/10.1002/met.1402.

Mason, S.J. (2018). *Guidance on Verification of Operational Seasonal Climate Forecasts*. World Meteorological Organization, Commission for Climatology XIV Technical Report 1220.

Scaife, A.A., Camp, J., Comer, R., Davis, P., Dunstone, N., Gordon, M., MacLachlan, C., Martin, N., Nie, Y., Renm H.-L., Roberts, M., Robinson, W., Smith, D. and Vidale, P.L. (2019). Does increased atmospheric resolution improve seasonal climate predictions? Atmospheric Science Letters. e922, https://doi.org/10.1002/asl.922.

Wilks, D.S. (2011). Statistical Methods in the Atmospheric Sciences, 3rd edition. Academic Press: Amsterdam, pp. 676.

The Umlindi Newsletter: disseminating climate-related information for agriculture and natural disaster in South Africa

R. Maake*, T.E. Masupha, G.J Chirima, M.E. Moeletsi Chirima, P. Beukes

Agricultural Research Council (ARC) - Soil, Climate and Water, Private Bag X79, Pretoria 0001, South Africa

Corresponding author:

Disseminating climate-related information is an important aspect of managing the negative impacts caused by climate change and variability; as well as improving agricultural productivity in South Africa. However, in order for this information to be beneficial, it must be accurate, timely, and cost effective. Thus, the Agricultural Research Council developed a Newsletter, called Umlindi, which is distributed freely on a monthly basis to a variety of users. Overall, the Umlindi Newsletter serves as channel for disseminating useful indicators such as rainfall which provide a measure of the qualitative state of drought conditions country-wide.

Keywords: Drought, Vegetation conditions, Information dissemination, Umlindi Newsletter, Natural disasters

Introduction

Climate-related disasters, such as drought, floods and heat waves, have previously had adverse implications on the agricultural sector in South Africa. Various efforts have been undertaken by government officials and policy developers to reduce the resulting impacts of these disasters, however, the lack of data and information is an issue that affects a greater extent of the decision-making process. Decision-makers are mainly concerned about monitoring the agricultural season to help the farmers in adverse years and to provide timely and informed decisions for proper planning.

In light of this, the Agricultural Research Council - Soil, Climate and Water (ARC-SCW) developed and implemented a Newsletter in 2004, called the Umlindi – a Zulu word for "the watchman". The main aim of the Newsletter is to provide information on drought conditions, as well as climate advisories to the agricultural sector and the country as a whole. This Newsletter compiles information obtained from scientific research in a simplified manner that decision and policy makers as well as the general public can understand and use. The Umlindi Newsletter is distributed to subscribing individuals on a monthly basis and published on the ARC website (http://www.arc.agric.za/ARC%20Newsletters).

There are approximately 300 individuals subscribed to the Umlindi Newsletter ranging from farmers, university lecturers, private organizations such as insurance companies, consulting agencies, farmer's associations to Government entities at multiple scales (i.e. national, provincial and local).

Data and Methods

a. Data Acquisition

The content of the Umlindi Newsletter includes value-added products such as rainfall, Standardized Precipitation Index derived from agrometeorological data as well as Vegetation Conditions, Rainfall, Fire Watch, and Surface Water Resources derived from remotely-sensed data covering South Africa. The remotely-sensed data used to generate the above-mentioned products derived from remote sensing data was obtained from the Coarse Resolution Satellite Image Archive and Information System/Database (CRID). In addition, the data used to generate the Surface Water Resources is derived from the GeoTerraImage's 'Msanzi Amanzi' web-information service (https://www.water-southafrica.co.za. Meanwhile, the rainfall products offered include those obtained from combined inputs of 800 + automatic weather stations or rainfall recording stations from the ARC-SCW, South African Weather Service and Kruger National Park weather station networks. Thereafter, the maps are generated using continually improved automated scripts in Python scripting language and ArcGIS Geographic Information System developed by ESRI https://www.arcgis.com/features/index.html.

b. Rainfall mapping

Rainfall GIS surfaces covering South Africa (Malherbe *et al*, 2016) are produced from data within the ARC-SCW Climate Databank as well as the external sources mentioned above. The databank holds historical data from the South African Weather Service and the ARC-SCW. Monthly rainfall GIS surfaces covering the period 2009-2013 are produced from the historical rainfall data. The rainfall indices calculated to produce rainfall products for the month in consideration, include total rainfall, percentage of

long-term mean, cumulative total rainfall of the preceding 12 months expressed as a percentage of the long-term mean, and total rainfall of the preceding three months as compared to same period of the previous season. Rainfall deciles (Gibbs and Maher, 1967) are also calculated, and they are used to express the ranking of rainfall for a specific period in terms of the historical time series.

Drought conditions are monitored using the Standardized Precipitation Index (SPI - McKee et al., 1993), calculated per quaternary catchment. This index was developed to monitor the occurrence of droughts using only rainfall data. The index quantifies precipitation deficits on different time scales and therefore also drought severity. With regards to the Newsletter, the SPI is calculated for different time scale namely 1-, 3-, 6-, 9-, 12-, 24-, 36- and 40-month period based on a program (http://drought.unl.edu/archive/climdiv_spi/spi/program/spi_sl_6.exe) developed by the National Drought Mitigation Centre.

c. Vegetation Mapping

An archive of various vegetation monitoring products derived from satellite data is updated operationally at the ARC-SCW through the Coarse Resolution Imagery Database (CRID). The vegetation monitoring products are all derived from the Normalized Difference Vegetation Index (NDVI) which was developed by Rouse *et al* (1974). NDVI images describe the vegetation activity represented by values ranging between 0 and 1. The Normalized Difference Vegetation Index (NDVI) utilizes differential absorption and reflectance in the Red and Near-Infrared bands of the electromagnetic spectrum, linked to vegetation activity. It is computed from the following equation:

$$NDVI=(IR-R)/(IR+R) \qquad \text{Equation (1)}$$

where:
IR = Infrared reflectance &
R = Red reflectance

The Standardized Difference Vegetation Index (SDVI) is the standardized anomaly (according to the specific time of the year) of the NDVI.

The Vegetation Condition Index (VCI) developed by Kogan (1990), is represented as a percent value and provides a measure to determine drought conditions. A VCI of 50% reflects normal conditions while those below 50% reflects drought conditions and higher values reflects optimal conditions for vegetation. It is computed as follows:

$$VCI=100*(NDVI–NDVI_{MIN})/(NDVI_{Max}-NDVI_{MIN}) \qquad \text{Equation (2)}$$

where:
$NDVI_{MIN}$ = minimum pixel value for a given period
$NDVI_{Max}$ = maximum pixel value for a given period

d. Fire detection

Remote sensing-based detection of active fire relies on detecting the thermal signature of fires using a contextual algorithm (Giglio et al., 2003). Actively burning fires can be identified and located by detecting the elevated energy released relative to their non-burning surroundings at middle-infrared to thermal wavelengths (i.e. 3.6 μm - 12 μm), which depends on the combustion temperature even when the fire covers small fractions of the pixel (Lentile *et al*., 2006). The 8-day MODIS active fire product distributed by the Land Processes Distributed Active Archive Center (LP DAAC), located at the U.S. Geological Survey's EROS Data Center, is used to derive active fires. The images are downloaded in a HDF file format where the point represents the center of the MODIS pixel, being 1 km at nadir (Giglio, 2010), which are then converted to GeoTIFF using the Modis conversion tool. The 8 day images are used to build up the monthly datasets. The number of fire pixels observed in each 8-day Terra MODIS images are then averaged to generate a monthly fire image and ultimately the yearly fire image (figure 4) using a Geographic Information Systems software. Statistics such as the sum of all pixels with active fire activity in the satellite overpass are also extracted.

Results and Discussion

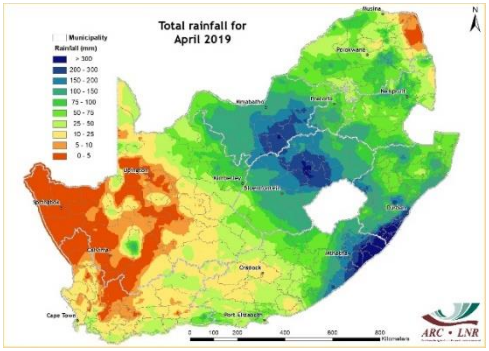

Figure 1: Total rainfall during April 2019 over South Africa

Various types of maps are produced to describe drought conditions the 10 day or month in consideration .The rainfall map (Figure 1) can easily be interpreted as the different values are represented by different colours in terms of the corresponding millimeters (mm) and percentages (%).

On the rainfall deciles maps shown by Figure 2, a value of 1 refers to the rainfall being as low or lower than experienced in the driest 10% of a particular month historically (even possibly the lowest on record for some areas). A value of 10 represents rainfall as high as the value recorded only in the wettest 10% of the same period in the past (or even the highest on record). It therefore adds a measure of significance to the rainfall deviation.

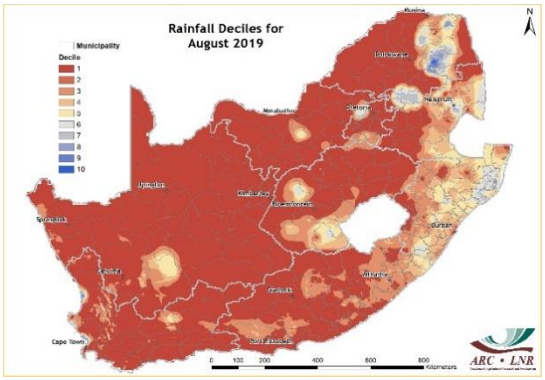

Figure 2: Rainfall decile during August 2019 over South Africa

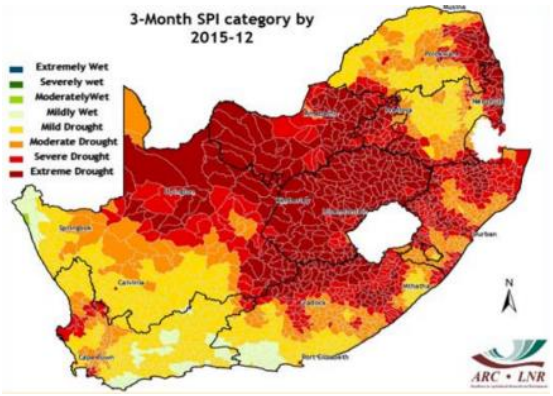

Figure 3: 3-month SPI during December 2015 over South Africa.

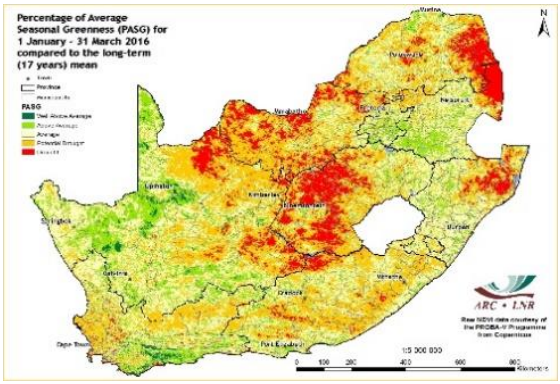

Figure 4: 3-month PASG for January-March 2016 over South Africa.

The Standardized Precipitation Index provides an indication of rainfall conditions per quaternary catchment based on the historical distribution of rainfall. Figure 3 shows the drought that occurred during the 2015/16 summer. The map (Figure 3) show severe to extreme drought conditions that occurred at the 3-month time scale by December 2015, in which agricultural productivity over most part of the country was affected.

The Normalized Difference Vegetation Index (NDVI) values are incorporated in the legend of the difference maps, ranging from -1 (lower vegetation activity) to 1 (higher vegetation activity) with 0 indicating normal/the same vegetation activity or no significant difference between the images. A dekadal NDVI image shows the highest possible "greenness" values that have been measured during a 10-day period. Vegetated areas will generally yield high values because of their relatively high near infrared reflectance and low visible reflectance. For better interpretation and understanding cumulative vegetation activity anomalies over extended time, a Percentage of Average Seasonal Greenness (PASG – Figure 4) is created where the cumulative vegetation activity, as represented by the cumulative NDVI of the current period, is expresseed as a percentage of the long-term aveage for the same period. Figure 4 shows the vegetation activity in response to the drought that occurred during the 2015/16 summer. At this period, vegetation activity was extremely poor over much of the North West, Free State and Limpopo. Finally, a temporal image difference approach for change detection is also used. NDVI images of the year under observation (e.g. 2019) is compared to the long-term average (2000 - 2018) in order to indicate how vegetation has changed over the given time. The NDVI difference map is depicted in Figure 5. The

resulting difference map (Figure 5) shows poor vegetation conditions for central parts of the country.

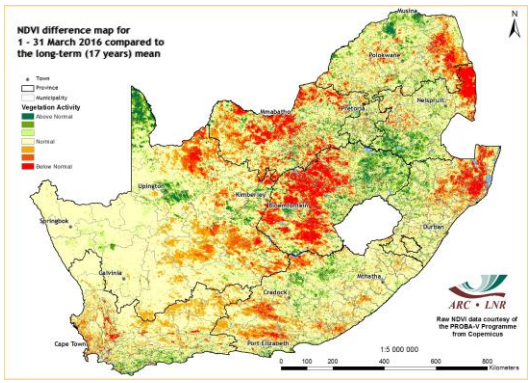

Figure 5: NDVI difference map for 2016 over South Africa

Figure 6 shows the location of active fires detected over a 3-month period, compared to other severe fire activities since 2000. The resulting map shows that fire activity was higher in Easter Cape, Western Cape and KwaZulu-Natal

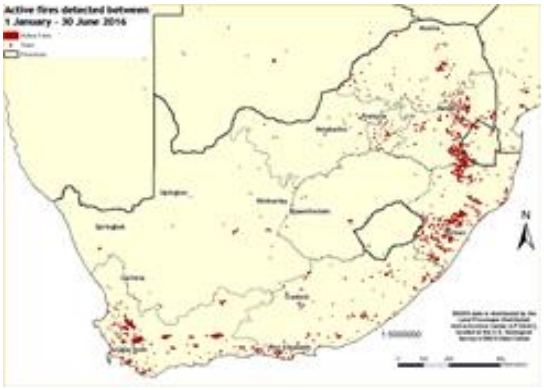

Figure 6: Active fires detected between 1 January - 30 June 2016 per province in South Africa.

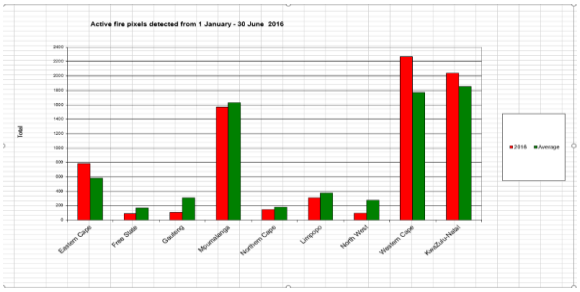

Figure 7: The total number of active fires detected between 1 January - 30 June 2016 per province in South Africa.

Conclusions

The Umlindi Newsletter developed by the ARC provides climate-related monitoring products obtained from an integration of remote sensing and *in-situ* data from weather stations. The remotely-sensed products, viz. vegetation conditions (NDVI) are used to complement the purely meteorological products (Rainfall), and other products, such as the occurrence of bush fires. The Newsletter is distributed to a variety of users on a monthly basis, through subscriptions as well as on the ARC website. The newsletter makes sound scientific information available to Policy-makers and decision-makers to respond to drought and other disasters.

Acknowledgements

The Newsletter is a product of the operational Coarse Resolution Imagery Database (CRID) project of ARC-SCW, funded by the National Department of Agriculture, Forestry and Fisheries. Development of the monitoring system was made possible at its inception through LEAD funding from the Department of Science and Technology.

Reference*s*

Gibbs, W.J. & Maher J.V. (1967). Rainfall Deciles as Drought Indicators. Bureau of Meteorology Bulletin No. 48, Melbourne, Australia.

Giglio, L. (2010). MODIS collection 5 active fire product user's guide version 2.4. *Science Systems and Applications, Inc*.

Giglio, L., Descloitres, J., Justice, C. O., & Kaufman, Y. J. (2003). An enhanced contextual fire detection algorithm for MODIS. *Remote sensing of environment*, *87*(2-3), 273-282.

Kogan, F. N. (1990). Remote sensing of weather impacts on vegetation in non-homogeneous areas. *International Journal of Remote Sensing*, *11*(8), 1405-1419.

Lentile, L. B., Holden, Z. A., Smith, A. M., Falkowski, M. J., Hudak, A. T., Morgan, P., ... & Benson, N. C. (2006). Remote sensing techniques to assess active fire characteristics and post-fire effects. International Journal of Wildland Fire, 15(3), 319-345.

Malherbe, J., Dieppois, B., Maluleke, P., Van Staden, M., & Pillay, D. L. (2016). South African droughts and decadal variability. *Natural Hazards*, *80*(1), 657-681.

McKee, T.B.N., Doesken, J. & Kleist, J. (1993). The relationship of drought frequency and duration to time scales. In: Proceedings of the eighth conference on Applied Climatology, Boston, *MA: American Meteorological Society*, p.179-184.

Rouse Jr, J., Haas, R. H., Schell, J. A., & Deering, D. W. (1974). Monitoring vegetation systems in the Great Plains with ERTS.

7. IMPACTS OF CLIMATE VARIABILITY AND CHANGE

Influence of climate on the spatiotemporal distribution of malaria at Thulamela municipality, Limpopo

Anthony L. Makondo[1] and Abiodun Adeola[2,3]
[1]Department of Geography, Geoinformatics and Meteorology, University of Pretoria
[2]South African Weather Service
[3]School of Health Systems and Public Health, Faculty of Health Sciences, University of Pretoria, Private Bag X20, Hatfield 0028, South Africa

Corresponding author:

Malaria, though curable continues to be a major health and socioeconomic challenge. Malaria cases have been on the rise for the last two years in the malaria-endemic region of South Africa. Thulamela municipality in Limpopo, South Africa falls within several municipalities at Vhembe district which is affected by malaria. It had 33 448 malaria cases over a period of 20 years (1998 January-2018 December). This study aims to determine the influence of climate on the spatiotemporal distribution of malaria cases for two decades (1998 January-2018 December). The Ordinary Least Squares (OLS) regression, exploratory regression, spatial autocorrelation, spearman's correlation and graphical plotting were performed to analyse the distribution of malaria and the relationship between malaria cases and climate variables. In addition, environmental variables were taken into consideration. The study found that malaria cases have a positive linear relationship with climate variables. The results further suggest that the climate variables were not strongly significant to the distribution of malaria with rainfall, maximum and minimum temperatures only able to account for 49%, 39% and 56% of the variations of malaria cases respectively in the villages of Thulamela. It was found that malaria distribution is also influenced by other local environmental variables (river, cultivated land and altitude). The identification of the drivers of the spatiotemporal distribution of malaria is essential for adequate malaria control. Such knowledge can aid in the development of a predicting system. This could inform possible earlier mitigation plan to stop malaria effects on the communities of Thulamela municipality.

Keywords: Malaria, Thulamela municipality, Epidemiology, Ordinary Least squares, Exploratory regression, Geostatistics.

Introduction

Malaria is regarded as a life-threating disease in the world with approximately 3.4 billion people recorded to be vulnerable to the disease in 2012 (Xia, et al., 2015). Approximately 207 million malaria cases were recorded with an estimated 627000 deaths globally. Malaria epidemiology in South Africa has been well researched (Adeola, et al., 2016). The objectives of this study were to determine the distribution, intensity, seasonality and environmental drivers of the spatial and temporal distribution of malaria.

Records have shown that Mpumalanga, Limpopo and Kwazulu-Natal provinces, and districts of Zimbabwe and Mozambique were mostly affected by malaria (Ikeda, et al., 2017). However, Limpopo districts were highly affected than other provinces (Maharaj, et al., 2013; Behera, et al., 2018). In Limpopo, between the year 1998 and 2007, a total of 58 768 malaria cases were reported with 628 deaths (Gerritsen, et al., 2008). High malaria outbreaks occur during warm and rainy seasons between September and February (Behera, et al., 2018).

Studies have shown that climatic, environmental, biological factors and drug resistance contributed to malaria transmission. Climatic factors such as temperature, rainfall, and relative humidity are mostly reported in studies to be positively correlated with malaria outbreaks (Lingala, 2017; Adeola, et al., 2016; Arab, et al., 2014). However, other local environmental factors such as rivers, cultivated land and altitude play a role in the distribution of malaria.

Despite the Limpopo Province accounting for the most malaria cases in South Africa, more studies have been done over Mpumalanga and KwaZulu-Natal. In addition, there is no existing study that has investigated the driving factors of the spatiotemporal distribution of malaria at the village level. As indicated in the National Climate Change Adaptation Strategy for South Africa (Environmental affairs, 2017), effective climate change adaptation and mitigation will require information at a very high resolution. Therefore, conducting malaria research at local level is imperative. More so, despite having good malaria control measure in South Africa, the number of malaria cases continued to rise between 2012 and 2014 (Behera, et al., 2018). Hence, understanding the influence of climate and environmental factors on the

transmission of malaria at a local scale will improve the control measures.

Data and methods

a. Data

Malaria data

Daily data of malaria cases at the official geographical and administrative boundary of villages in the Vhembe district from 1998-2018 was obtained from malaria control programme located in Tzaneen, Limpopo. Each year has a range of data from January-December. The data was exported from the malaria information system. Each data report contains both passive and active malaria data; the passive data are obtained from patients who tested positive of the plasmodium at the hospital while the active data are those that were collected through screening methods. Cases diagnosed via screening methods that were included in the study were those from people that lived close to or in the same areas with recently confirmed malaria cases. The malaria data contained records of facility name, date of diagnosis, number of cases, deaths, age, gender, infection, and the facility coordinates.

Climate data

Climate data consists of daily climate variables of daily maximum temperature, daily minimum temperature, and daily total rainfall amounts from two AWS stations in Thohoyandou and Phunda Maria. The data was collected from the South African Weather Service (SAWS) with a data period from 1998-2018. Each year has data ranges from January-December.

Spatial and environmental data

South African boundaries of local municipalities and village boundaries were acquired from the Municipal Demarcation Board which was recently updated by 2016. Land cover data was obtained from the Department of Environmental Affairs which was recently updated in 2013. Hydrology shapefiles were obtained from the Department of Water and Sanitation which was recently updated in 2012.

b. Methodology

The R statistical package was used to present malaria data and climate data through graphical methods and to find the correlation between malaria cases with each climatic factor monthly. The spearman's correlation was used to consider the monotonic relationship within the data (Lingala, 2017). The correlation coefficient ranges from -1 to 1, which indicates the strength of the relationship between the two datasets. The closer it is to 1 (or -1), suggest a strong positive relationship, otherwise, strong negative relationship between two datasets.

Using ArcGIS software (ArcMap 10.6) and spatial analyst tools, two stations with climate variable values (maximum temperature, minimum temperature, and total rainfall) were interpolated using Inverse Distance Weight (IDW) interpolation method to get climate values (maximum temperature, minimum temperature and total rainfall) for each village at Thulamela municipality, Vhembe district (Pimpler, 2017).

Through spatial join in ArcGIS, malaria data and climate data were joined with the shapefile (Villages) to perform further statistical analysis. The distribution maps of malaria from 1998-2018 were evaluated using ArcMap (Pimpler, 2017). The Moran's I values for malaria distribution was obtained through Geoda statistical software. The spatial weight type of distance weight was used with distance metric method of Euclidean distance of a distance bandwidth of 0.046202.

The exploratory regression and OLS regression were performed to obtain the climatic factors that are significant and that describe the distribution of malaria at Thulamela municipality of the year with the highest malaria cases of a range from January to march and a range from September to November (Pimpler, 2017; Behera, et al., 2018). If none of the climate factors is significant to the distribution of malaria, then other local environmental factors (rivers, cultivated land, and altitude) will be taken into consideration (Adeola, et al., 2016). The OLS regression model and exploratory regression model results contain probability fields, VLF values, Jarque-Bera statistics (JB stats), Jarque-Bera p-value (JB p-value), R-squared and Adjusted R-Square values to check if the model is biased and if it performed well (Pimpler, 2017). Spatial Autocorrelation Moran's I for residuals is conducted with a spatial weight of inverse distance weighting since majority of the villages are not connected.

Results and discussion

Throughout the years from 1998-2018 (20 years), there have been 33 448 malaria cases reported at Thulamela municipality. The year 2017 had the highest number of malaria cases (6 793) (Fig.1a), followed by 2000, 2003, 2006, 2015, then 2008 respectively. Malaria throughout the years was relatively randomly distributed with the Moran's I value of less than 0.5 (Tab. 1). Seasonally, as shown in Fig.1b, malaria cases occur more frequently in the summer season of December to February (DJF) including March with peaks in January. Malaria cases are low in the winter season of June to August (JJA).

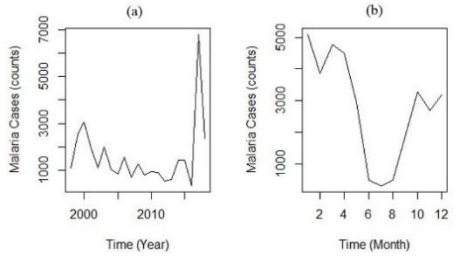

Figure 1. Monthly and yearly malaria case

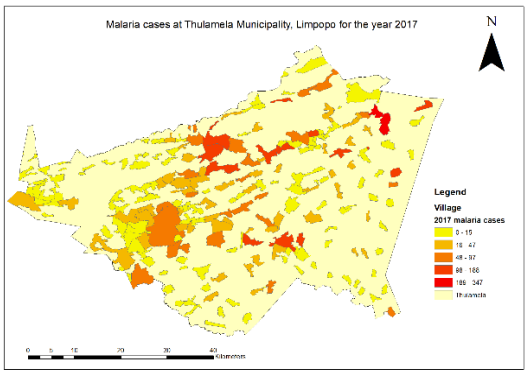

Figure 2. Malaria distribution for 2017. Red means high, otherwise low malaria cases.

Figure 2 illustrate that malaria cases were randomly distributed.

Table *1.* Year malaria cases Moran's I coefficient

Year	Moran's I coefficient
1998	0.198919
1999	0.168539
2000	0.143164
2001	0.141894
2002	0.106928
2003	0.126237
2004	0.14066
2005	0.183876
2006	0.093537
2007	0.0861056
2008	0.0496228
2009	0.0978582
2010	0.149647
2011	0.1921105
2012	0.132255
2013	0.162482
2014	0.143247
2015	0.0942481
2016	0.247506
2017	0.153692
2018	0.132608

Through R statistics, the linear relationship was evaluated using the Spearman correlation. Considering malaria cases and climate variables and monotonic relationship of both variables (Spearman correlation) (Lingala, 2017), monthly malaria cases and climate variables have a relatively positive correlation. Thus, amplifying the influence of climate variables (monthly maximum temperature, minimum temperature, and total rainfall) is the rise of malaria cases at Thulamela (Fig. 3). The results indicated that the minimum temperature has the strongest positive correlation than other climate variables (Table 2).

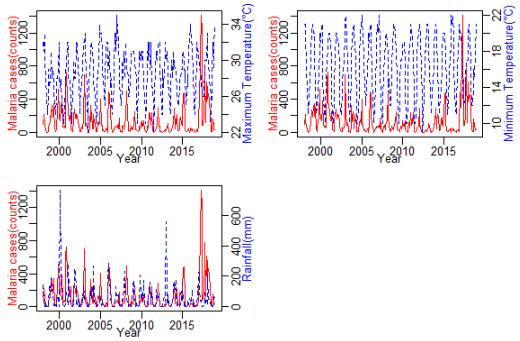

Figure 3. Malaria distribution in relation to climate variables

Table 2. Spearman correlation analysis of relationship between malaria and climatic factors

	Malaria	Rain	Tmax	Tmin
Malaria	1.00	0.49	0.39	0.56
Rain	0.50	1.00	0.41	0.73
Tmax	0.39	0.41	1.00	0.83
Tmin	0.56	0.73	0.83	1.00

The spearman correlation cannot show how climate variables statistically significantly influence the number of malaria cases at Thulamela. Therefore, the OLS regression is performed to check whether the climate variables are statistically significant influencers of malaria case distribution around the area (Pimpler, 2017).

Since the year 2017 had the highest number of malaria cases than any other year at Thulamela municipality, that year was considered for the OLS regression model. The regression model was conducted over the range of January-march and September-November (Behera, et al., 2018). For the January-March period, residuals were randomly distributed with Moran's Index of 0.059, z score of 1.452 and a p-value of 0.146 with a spatial weight of inverse distance weighting. Since the residuals are randomly clustered then OLS results are thus reliable.

The JB stats implies that the OLS regression is reliable. The climate factors were significant between the period of January-March 2017 however; the probability values indicate that the level of significance is not strong. JB p-value suggests that the residuals are far from reaching normality (Table 3). Hence, their influence may be jointly explained by

other local environmental factors additionally influence of the distribution of malaria. Hence, the relationship between local environmental factors and climate factors jointly influence the distribution of malaria (Adeola, et al., 2016).

Table 3. OLS diagnostics

	Probability	VIF	JB Stats	R-Square	JB P-value
	Malaria	Malaria	Malaria	Malaria	Malaria
Max T	0,80	>7.5	2623,33	0,09	0,000
MinT	0,80	>7.5	2623,33	0,09	0,000
Rain	0,80	>7.5	2623,33	0,090	0.000

When performing OLS regression for September-November 2017, residual distribution was found to be clustered with Moran' s index of 0.069 and z-score of 1.715 and p-value of 0.086, and OLS regression was not deemed as reliable.

Considering environmental factors, terrain, rivers, dams and land use types were taken into consideration. The result agrees with previous results by previous researchers (Adeola, et al., 2016). When villages are located at altitudes that are equal or less than 400m above MSL, closer than 2km from a water body, and cultivated land, malaria cases are relatively high (Adeola, et al., 2016).

A buffer of 2 km around rivers was made, and it was found that all the villages that have high malaria cases were within the river buffer (Fig. 5). The relatively high number of malaria cases were located lower or equal to 400m altitudes (Fig. 4) and closer to cultivated land (Fig.6). This implies local environmental factors contributed to the distribution of malaria and that the OLS regression model was biased since some of the independent variables from environmental factors were not imported in the model.

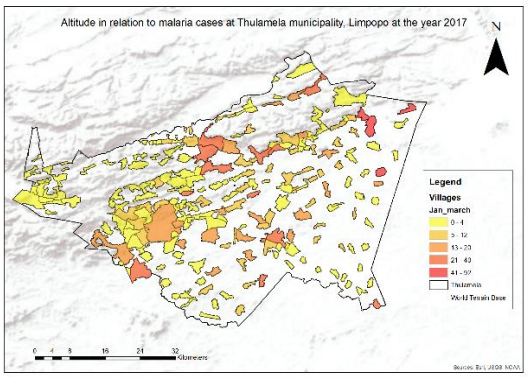

Figure 4. Terrain in relation to malaria cases in the year 2017

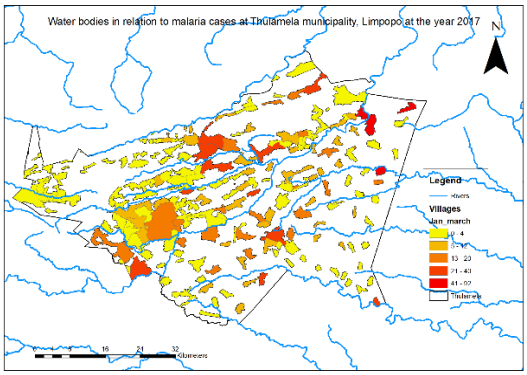

Figure 5. Rivers in relation to malaria cases in the year 2017

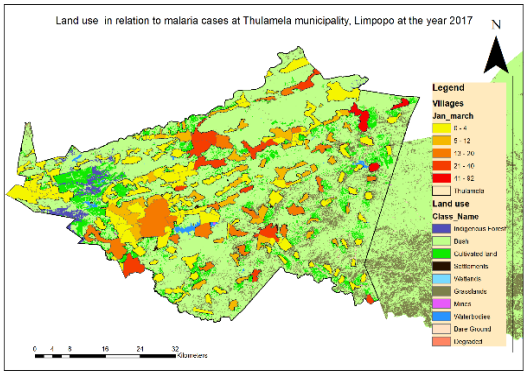

Figure 6. Land use in relation to malaria cases in the year 2017

Conclusion

The study demonstrate that for efficient malaria prediction, climate variables alone are not sufficient but should be combined in appropriate weight with environmental and socioeconomic (although not considered in this study) variables. The study showed that the pattern of occurrence can be analysed through spatial analysis. The OLS regression method helps in depicting a significant pattern of malaria. Since monthly changes in malaria cases, climate and environmental variables are evaluated, predictions of malaria for monthly occurrences are predictable and early malaria warnings can be issued to the public. Mitigation by different agencies of malaria control can be plan early before the outbreak and poor communities at Thulamela municipality will be saved from the effects of the disease early.

References

Adeola, A. M. et al., 2016. *Environmental factors and population at risk of malaria in Nkomazi municipality, South Africa.* [Online] Available at: https://repository.up.ac.za/bitstream/handle/226

3/56004/Adeola_Environmental_2016.pdf?sequence=1&isAllowed=y [Accessed 09 July 2019].

Arab, A., Jackson, C. M. & Kongoli, C., 2014. Modelling the effects of weather and climate on malaria distributions in West Africa. *Malaria Journal*, pp. 1-9.

Behera, S. K. et al., 2018. Malaria Incidences in South Africa linked to a climate mode in southwestern Indian Ocean. *Science Direct*, pp. 47-57.

Environmental affairs, 2017. *National Climate Change Adaptation Strategy Republic of South Africa.* [Online] Available at: https://www.environment.gov.za/sites/default/files/reports/nationalclimate_changeadaptation_strategyforcomment_nccas.pdf [Accessed 19 July 2019].

Gerritsen, A. A., Kruger, P., Van der Loeff, M. F. S. & Grobusch, M. P., 2008. Malaria incidence in Limpopo province, South Africa, 1998-2007. *Malaria Journal*, pp. 1-8.

Ikeda, T. et al., 2017. Seasonally lagged effects of climate factors on malaria incidence in South Africa. *Scientific reports*, 7(1), p. 2458.

Lingala, M. A., 2017. Effect of meteorological variabls on Plasmodium vivax and Plasmodium falciparum malaria outbreak in prone districts of Rajasthan, India. *Science Direct*, pp. 875-880.

Maharaj, R. et al., 2013. Epidemiology of malaria in South Africa. In: *From control to elimination*. s.l.:Epidemiology, pp. 779-783.

Pimpler, E., 2017. *Spatial Analystics with ArcGIS*. Birmingham: Packt Publishing.

Xia, J. et al., 2015. Spatial, temporal, and spatiotemporal analysis of malaria in Hubei Province, China from 2004–2011. *Malaria Journal*, pp. 1-10.

Rainfall variability in relation to the frequency of dry and wet years in the Luvuvhu River Catchment Area, Limpopo Province

S.M. Mazibuko[1, 2,*], G. Mukwada[2] and M.E. Moeletsi[1]

[1]Agricultural Research Council – Institute for Soil, Climate and Water, Private Bag X79, Pretoria 0001, South Africa
[2]Afromontane Research Unit, University of the Free State, Private Bag X13, Phuthaditjhaba, 9866, South Africa

*Corresponding author: mazibukosm@arc.agric.za

Rainfall variability in south Africa is reported to be influenced by El Nino Southern Oscillation (ENSO) and its effects also affects the Limpopo Province. The study was conducted to identify the relationship between Standardised Precipitation Index (SPI) and Sea Surface Temperature (SST) to identify the influence of SST in bringing rainfall variability in the Luvuvhu River Catchment Area (LRCA) and determine the probability of extreme rainfall events associated with SST. The results indicate that most of the time SST influence could results in high frequency of wet conditions. The study recommends the use of seasonal focus before planting and development of proper drainage systems and storage of water.

Keywords: ENSO, Sea Surface Temperature, SPI, drought and Floods

Introduction

Rainfall variability in South Africa is reported to be influenced by ENSO and its effects also impact the Limpopo Province (Odiyo *et al.,* 2019). The ENSO phenomenon is the oscillation between warm phases which is referred to as El Niño characterised by abnormal warming of surface ocean waters of the central and eastern pacific and enhanced convection in the atmosphere above; and a cold phase which is referred to as La Nina characterised by abnormal cooling of the ocean waters and supressed convection in the atmosphere above (Ganguli and Reddy, 2013). Considering some studies ENSO is identified as the main driver of rainfall variability in Southern Africa, however ENSO fails to explain seasonal rainfall variability(Crétat *et al.,* 2019). The relationship between ENSO and rainfall over southern Africa is proven to be strong but there are some ambiguities which still need to be clarified (Crétat *et al.,* 2019). For example, the relationship between ENSO and rainfall is not linear which means not every El Niño leads to dry conditions, the below average dry conditions failed to occur over southern Africa during the strong 1997/98 El Niño and in contrast the weaker El Niño of 1991/92 and 2002/2003 were related to severe summer droughts (Rapolaki *et al.,* 2019). The study adopted the use of SPI to achieve the following objective, (1) identify the relationship between SPI and SST to identify the influence of SST in bringing rainfall in the LRCA. (2) Determine the probability of extreme rainfall events associated with SST.

Instrumentation and Methods

The SPI programme was downloaded from the National Drought Mitigation Centre (NMDC) website (http://drought.unl.edu/MonitoringTools/DownloadableSPIProgram.aspx.) and used to compute SPI values. The meteorological data used in this study consist of gridded monthly rainfall data and Sea Surface Temperature (Nino 3.4) from the Climate Research Unit (CRU TS4.01), available online at http://www.cru.uea.ac.uk/_mikeh/datasets/global. The latitude and longitude grid points covering the LRCA for which monthly rainfall data were downloaded.

Identifying the occurrence of extreme dry and wet events and the relation with SST.

The SPI classification that was developed by Mckee (1993) was used to identify extreme dry and wet events. A drought year was identified when SPI values are consistently below -1.0, which shows that rainfall was below normal. Positive SPI values above 1.0 indicate the beginning of a wet period. Rainfall anomalies respond to ENSO extreme, the relationship between SPI and ENSO index was used to identify the influence of SST on rainfall variability.

Determining the probability of the occurrence of extreme rainfall events

After computing the SPI values for three months' time scale in all 15 grid points that cover the LRCA, STATISTICA software was used to determine the probability of extreme rainfall events. Firstly, the data was fitted to determine which distribution best represent the data. The kolmogorov Smirnov test was selected to analyse the probability of non-exceedance for all the data points.

Results and Discussion

Assessing the influence of SST on rainfall variability

The relationship between SPI and SST (Niño 3.4) indicate high positive correlation with a correlation coefficient above 0.90 for all the grid points. The results are also statistically significant with $p < 0.0001$. The results indicate that rainfall variability in the catchment is highly influenced by ENSO, resulting in either the El Niño, neutral or La Nina phases. A study by Ganguli and Reddy (2013) compared ENSO indices at different phases with drought variables and the results indicated high correlations and the corresponding p-values were less than 0.0001. Positive relationship between Sea Surface Temperature Anomalies (SSTA) and 12-months SPI was observed by (Nguyen et al., 2014).

Identify the probability of occurrence of extreme rainfall events

The results indicate the probability of the occurrence of dry and wet conditions in the LRCA. The probability of experiencing extremely dry conditions which is indicated by SPI values below -2 is indicated by 20% probability of non-exceedance. In relation to severe to moderately dry conditions, the probability of approximately 25% in grind points (A-H) was identified which represents data points in the lower to middle part of the catchment. Moreover, the grid points (I-O) from the middle of the catchment to the upper part of the catchment also indicated severe to moderate dry conditions with 40% probability of non-exceedance. The results suggest that there is variability in the intensity of dry conditions in the catchment, with moderately to severely dry occurring mostly in the middle to upper parts of the catchment. However, (Odiyo et al., 2015) suggested that high rainfall in the catchment occur in the upper most part where the Soutpansberg Mountains are found. These findings also show that drought could occur in both low and high rainfall areas, therefore water management strategies are required across the catchment.

Conclusions

The study was aimed at determining the influence of SST in cause variability in rainfall in the LRCA. The use of SPI and ENSO index showed that indeed rainfall variability could have associated with the influence of ENSO. Therefore, using weather forecast and advisories could help farmers to better prepare their planting activities based on the projected weather systems identified during the particular season. Development of water harvesting and storage methods is essential as the frequency of wet conditions is shown to be high. However, dissemination of information on cultivar selection based on the seasonal rainfall is recommended.

References

Odiyo, J., Mathivha, F.I., Nkuna, T.R. and Makungo, R., 2019. Hydrological hazards in Vhembe district in Limpopo Province, South Africa. *Jàmbá: Journal of Disaster Risk Studies*, *11*(2), p.13.

Rapolaki, R.S., Blamey, R.C., Hermes, J.C. and Reason, C.J., 2019. A classification of synoptic weather patterns linked to extreme rainfall over the Limpopo River Basin in southern Africa. *Climate Dynamics*, pp.1-15.

Crétat, J., Pohl, B., Dieppois, B., Berthou, S. and Pergaud, J., 2019. The Angola Low: relationship with southern African rainfall and ENSO. *Climate Dynamics*, *52*(3-4), pp.1783-1803.

Ganguli, P. & Reddy, M. J. 2013. Analysis of ENSO-based climate variability in modulating drought risks over western Rajasthan in India. *Journal of earth system science,* 122**,** 253-269.

Nguyen, L., Li, Q. & Nguyen, V. 2014. Effects of ENSO on SPEI/SPI drought indices in the Vietnam Songcai basin. *Advanced civil, urban and environmental engineering,* 2**,** 453-464.

Odiyo, J. O., Makungo, R. & Nkuna, T. R. 2015. Long-term changes and variability in rainfall and streamflow in Luvuvhu River Catchment, South Africa. *South African Journal of Science,* 111**,** 1-9.

Influence of the variability of hydro-meteorological parameters on dam levels in the Western Cape Province

Katekile L. Shivambu[1*], Christina M. Botai[2], Cilence Munghemezulu[1]

[1]Department of Geography Geoinformatics and Meteorology, University of Pretoria
[2]South African Weather Service, Private Bag X097, Pretoria 0001

*Corresponding author: katy.shivambu@gmail.com

Water reservoirs such as rivers, lakes and dams are influenced by various factors, including climatic conditions. This study sought to investigate the relationship between dam levels, precipitation, evaporation and streamflow in the Western Cape Province. Four major dams in the Western Cape Province were considered for the study. A linear regression and multivariate analysis were used to assess the relationship between dam levels and the selected driving variables, as well the dependence of dams on these climatic variables. Based on the results, the influence of precipitation, evaporation and streamflow on the changes of dam levels appear to be localized, with streamflow dominating in three of the selected dams. In addition, a multi-linear regression model used to model the influence of combined effects of precipitation, streamflow and evaporation suggest that changes in dam levels in Theewaterskloof and Voilvlei dams are more attributed to mainly streamflow and combined effects from streamflow and evaporation, respectively. This is expected given that streamflow is the main input that feeds the dams. The final model relating to variations in Kwaggaskloof Dam reflects a combined effects of precipitation, streamflow and evaporation, and these effects account up to 26%. The results, presented in this study assumed that the dam levels are solely affected by the three driving hydro-meteorological variables. It is acknowledged, however, that dams are also affected by other factors such as water consumption, land-use, and vegetation cover, among others. The inclusion of some of these factors is necessary for the purpose of increasing our understanding on the relationship between dam levels and hydro-meteorological variables, although most of water use data are not easily accessible.

Keywords: Dam levels, precipitation changes, streamflow, evaporation, multivariate analysis

Introduction

Dams provide numerous socio-economic benefits. For instance, dams contribute to socio-economic development by supplying water to various stakeholders for numerous purposes, such as irrigation, flow regulation for flood and drought control, navigation, house-hold consumption, recreation and hydroelectricity generation (World Commission on Dams, 2000). Despite their benefits, dams often have negative impacts on the river ecosystems. For instance, dams may block upstream and downstream fish passage, as well as increasing water temperatures (Gore and Petts, 1989; Trout Unlimited, 2002). The hydroelectricity generation process can result in the loss of fish (Alexander, 2 1999). Furthermore, dams may lead to a decrease in water oxygen levels and obstruct the potential movement of nutrients and sediments along streams (Kanehl et al., 1997; Bednarek, 2001).

In general, the registered impacts are two-way. Thus, while the dams may pose significant impacts on the ecosystems, climate change and variability on the other hand affects the stability of the dams, including the infrastructures as well as water levels. For instance, reduced rainfall intensity coupled with prolonged dry-spells under climate change may affect streamflow, runoff as well as sub-surface flows in the catchments, thereby affecting water availability in the dams (Immerzeel et al., 2010). In addition, warm temperatures are likely to exacerbate evaporation processes, (e.g. more water exposed to air and direct sunlight), hence increasing evaporation rates and reducing natural water flow (Bowen, 1926).

The ability of a dam to supply water for various purposes depends on the dam's water gain and its loss. Hydro-meteorological parameters such as precipitation, streamflow, temperature, evaporation and runoff play a significant role in the amount of water gain and losses within a dam. Hence these variables play a significant role in water resource management and planning, including the determination of water availability in most of water reservoirs (Van Koppen, 2005). For the purpose of effective water resources management and planning, it is necessary to assess the extent to which various hydro-meteorological variables affect the stability of dams, including the changes in water levels. The aim of this research study is to assess the influence of precipitation, evaporation and streamflow on the changes of dam levels in Western Cape Province.

Study area and Data

Four dams distributed across the Western Cape Province (WCP) were considered in this study, see their distribution in Figure 1. The WCP is the fourth largest of the nine provinces of South Africa, located on the south-western part of the country, where it boarders the Northern Cape and the Eastern Cape provinces in the north and east, respectively. The selection of four dams was based on Full Storage Capacity (FSC) of greater than 30 Mm^3 and the availability of recorded data. These dams are Gamkapoort, Kwaggaskloof, and Theewaterskloof and Voivlei. Based on the selection criteria, the four dams are therefore considered the major dams that supply water to the community of the WCP.

The datasets used are the weekly-recorded dam levels, and daily rainfall, evaporation and streamflow observations, all acquired from the Department of Water and Sanitation. Only meteorological and stream-gauge stations distributed within/near the dams were considered. In particular, the selected stations were those located in the upstream of the dams. All the datasets were analysed for the period from 2000 – 2017.

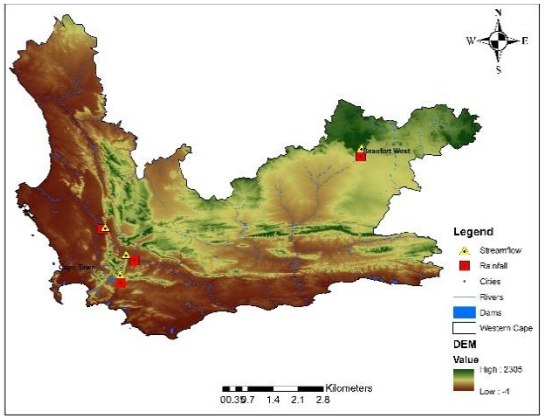

Figure 1: Distribution of the selected dams in the Western Cape Province.

Methodology

Table 1 lists the rainfall and stream-gauge stations selected for data analysis. Firstly, precipitation, evaporation and streamflow time series were analysed to assess the spatial and temporal characteristics of each variable across the stations. Features were described based on the mean, standard deviation, coefficient of variation and skewness statistical parameters. Trends were not considered due to the shorter period considered.

Table 1. Selected rainfall and stream gauge stations

Rainfall		
Stations	Latitude	Longitude
G1E002	-33.34178	19.04105
J2E004	-32.35017	22.5745
H4E007	-33.76	19.47
H6E001	-34.07591	19.29189
Streamflow		
G1H008	-33.31388	19.07472
J2H018	-32.24027	22.58583
H1H029	-33.68	19.36
H6H012	-34.09222	19.29416

A linear regression analysis was used to determine the relationship between the dam levels and the selected hydro-meteorological variables. Simple linear regression involves one independent variable and one dependent variable and a straight line approximates the relationship between the two variables (Lourk, 2017).

The equation that describes how y is related to x and an error term is called the regression model and described by Equation 1.

$$y = \beta_0 + \beta_1 X + \varepsilon \quad (1)$$

In order to determine the strength of the relationship and to characterize the extent to which hydro-meteorological parameters affect changes of water levels in the dams, coefficient of determination was calculated using the total sum of squares (SST), the sum of squares due to regression (SSR) and the sum of squares due to error (SSE) (Lourk, 2017) see Equation 2.

$$r^2 = \frac{SST - SSE}{SST} \quad (2)$$

Multivariate linear regression analysis of precipitation, evaporation and streamflow and the dam levels was used to determine the dependence of the dam levels on the selected parameters. Multivariate regression considers situations involving two or more independent variables (Lourk, 2017). The equation that describes how the dependent variable y, for instance the dam level in this study, is related to the independent variables, which are precipitation, evaporation and streamflow, $x_1, x_2, \ldots x_p$ and an error term is given in Equation 3:

$$y = \beta_0 + \beta_1 X_1 + \beta_2 X_2 + \cdots + \beta_p X_p + \varepsilon \quad (3)$$

Results

Characteristics of precipitation, evaporation and streamflow

Table 2 gives a summary of precipitation, evaporation and streamflow characteristics in terms of the mean, the standard deviation (STD), coefficient of variation (CV) and skewness (Skew.). The mean is highly variable across the stations and variables, with minimum of 0.02 mm for evaporation and maximum of 5.71 mm for streamflow. The CV is significantly high for precipitation and less for both evaporation and streamflow. The distribution of all the variables is positively skewed across the stations.

Table 2. Statistical characteristics of hydro-meteorological parameters

Precipitation				
Station	Mean	STD	CV	Skew.
Gamka.	0.71	3.86	5.43	9.36
Kwagg.	0.86	4.14	5.07	10.62
Theew.	0.65	3.53	5.42	10.78
Voilv.	0.66	3.50	5.32	9.20
Evaporation				
Gamka.	5.31	3.19	0.60	0.70
Kwagg.	6.57	12.3	1.87	2.24
Theew.	0.02	0.03	1.15	33.4
Voilv.	5.24	3.19	0.56	0.79
Streamflow				
Gamka.	0.43	0.86	2.00	2.18
Kwagg.	5.71	3.23	0.56	0.44
Theew.	5.76	3.11	0.54	0.60
Voilv.	0.51	0.90	2.30	1.89

The relationship between dam levels and hydro-meteorological parameters

Figure 2 depicts results from the simple linear regression analysis, which aimed to assess the relationship between dam levels and the selected hydro-meteorological parameters, e.g. Dam Levels (DL) versus Pre (Precipitation); DL vs. Evap (Evaporation); and DL vs. SF (Streamflow). Based on the results, a change in one variable results in change in dam levels, although in some cases such changes are significantly small. It can also be noted that streamflow changes play a significant role in the stability of dam levels, with changes ranging from 9% and up to 36% in three of the dams, namely Kwaggaskloof, Theewaterskloof and Voilvlei. . Precipitation changes contribute about 20% to the changes in water levels in Gamkapoort Dam. Generally, evaporation changes contribute less across all the four dams in the Western Cape.

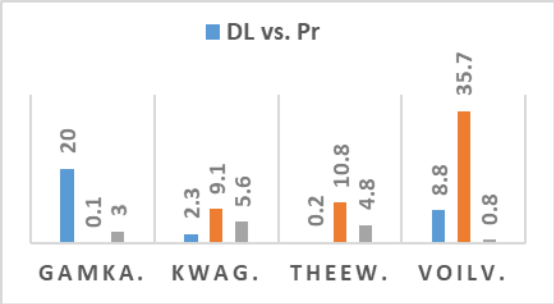

Figure 2: Relationship between dam levels and hydro-meteorological parameters, described in terms of linear regression model (R-Squared (%).

Multivariate linear regression analysis

Results for multivariate analysis are summarised in Table 3. In this analysis, the initial model is assumed to be the sum of precipitation, streamflow and evaporation, as shown in column 2 of Table 3. The final model that describes the main contributing parameters to the changes of dam levels is given in the third column of Table 3, with the percentage contribution given in column four. Based on the results it is noted that precipitation and evaporation are the main contributing factors to the changes in Gamkapoort dam levels, with a percentage contribution amounting to 26%. For Kwaggaskloof Dam all the three parameters appear to be contributing to the changes in water levels, with up to 25% contribution. In addition, water levels changes in Theewaterskloof Dam are mainly affected by streamflow changes, and this amounts to 12% contribution. Lastly, water levels in Voivlei Dam are affected by changes in streamflow and evaporation, with a combined contributions of 46%.

Table 3: Multivariate analysis results

Dam	Initial model	Final model	R^2 (%)
Gamka	*dl ~ Pre + EV + SF*	*dl ~ Pre + EV*	26
Kwagga	*dl ~ Pre + EV + SF*	*dl ~ Pre + EV + SF*	25
Theewat	*dl ~ Pre + EV + SF*	*dl ~ SF*	12
Voilv.	*dl~ Pre + EV + SF*	*dl ~ EV + SF*	46

Discussion

The linear regression analysis determined the relationship between the dam levels and each of the hydro-meteorological parameters (see for example Figure 2). Based on the linear regression results, streamflow is found to be the main input of water into the dams; therefore, the relationship between dams and streamflow has an *R*-squared percentage ranging from 9% to a maximum of 36% in three of the selected

dams, thus showing a stronger relationship between dam levels and streamflow.

The results presented in this study suggest that the impacts of precipitation, evaporation and streamflow on the changes of dam levels is localized and dependent on the climatology within the area. The data analysis was carried out with the assumption that hydro-meteorological variables are the only factors that influence water level fluctuations in the selected dams. In reality, dam levels are influenced by many other factors such as the area of the dam, land cover, vegetation, soil type, water consumption, upstream and downstream flows and its velocity, temperature etc. Other factor to be considered is the shape of the dams, as this can potentially affect the rate of evapotranspiration. Nevertheless, the results derived from this analysis can serve as a stepping-stone in an effort to understand the relationship between dam levels, precipitation, streamflow and evaporation, based on linear regression analysis. A similar approach to linear regression analysis used in this study is the use of simple water balance model. However, this approach cannot be considered here due to lack of water use data, a predicament faced by most researchers in hydrometeorology. As a result, this study only illustrate the relationship between dam levels and three driving hydro-meteorological variables.

Conclusion

Dam levels fluctuations are influenced by the climatology within the area. This study assessed the relationship between changes in dam levels and three driving hydro-meteorological variables, namely, precipitation, streamflow and evaporation. Results, based on linear regression analysis, indicate that streamflow is the main factor that influence the changes in water levels in three of the selected dams, followed by evaporation. Precipitation seem to dominate in Gamkapoort Dam, followed by evaporation. The results reported in this study are based on the assumption that dam levels are mainly affected by the three selected variables, although in reality this is not the case. Nevertheless, the research can contribute to effective water resources management and planning, as the relationship between dam levels, precipitation, streamflow and evaporation is clearly illustrated.

References

Alexander, J. (1999). The Muskegon River, Unnatural Wonder. The Muskegon Chronicle. Muskegon. pp. 1-20.

Bednarek, A.T., 2001. Undamming rivers: a review of the ecological impacts of dam removal. Environmental management, 27(6), pp.803-814.

Bowen, I.S., 1926. The ratio of heat losses by conduction and by evaporation from any water surface. Physical review, 27(6), p.779.

Gore, J.A. and Petts, G.E., 1989. Alternatives in regulated river management. CRC Press.

Immerzeel, W. W., Van Beek, L. P. and Bierkens, M. F., 2010. Climate change will affect Asian water towers. Science, 328(5984).pp.1382-1385.

Kanehl, P. D., J. Lyons, et al. (1997). "Changes in the Habitat and Fish Community of the Milwaukee River, Wisconsin, Following Removal of the Woolen Mills Dam." North American Journal of Fisheries Management 17: 387-400.

Lourk, J. 2017. Statistics for business and Economics (13e). Edwards University.

Trout Unlimited (2002). Small Dams Campaign, Trout Unlimited.

Van Koppen, B., Butterworth, J.A. and Juma, I., 2005, January. African water laws: Plural legislative frameworks for rural water management in Africa. In Proceedings of a workshop held in Johannesburg, South Africa (pp. 26-28).

World Commission on Dams, 2000. Dams and Development: A New Framework for Decision-making: The Report of the World Commission on Dams. Earthscan.

Variability of diffuse solar fraction and its relationship with atmospheric water vapour pressure deficit in South Africa

Mphethe I. Tongwane[a,b,*]

[a]Soil-Plant-Atmosphere Continuum Research Unit, School of Agricultural, Earth and Environmental Sciences, University of KwaZulu-Natal, Private Bag X01
Scottsville, 3209, South Africa
[b]Agricultural Research Council – Institute for Soil, Climate and Water, Private Bag X79, Pretoria, 0001, South Africa

*Corresponding author: tongwanem@arc.agric.za

Diffuse fraction (*K*) is a good indicator of the ratio of diffuse to global irradiance of a place. This study investigates characteristics of *K* at different locations in South Africa. The effect of atmospheric water vapour pressure deficit (VPD) on *K* is also studied. *K* is highest and lowest at coastal and inland locations respectively. It variable at low VPDs less than 1.6 kPa and generally constant for dry atmosphere.

Keywords: Global irradiance; Aerosols

Introduction

Solar irradiance drives the energy balance at the earth's surface, the hydrological cycle and the climate system (Stjern et al., 2009; Wild, 2009). Recent observations suggest that substantial changes in global irradiance occur over time and may profoundly affect our environments (Wild, 2009). Solar irradiance measurements show a consistent global dimming from the 1960s, when reliable data sets became available, through to the 1980s (Streets et al., 2009).

Changes in solar energy reaching the surface of the earth can be of natural origin, such as those induced by a major volcanic eruption on time scales of a few years, up to time scales of many millennia due to changes in the earth orbital parameters (Wild, 2009). On the other hand, anthropogenic activities have increased the aerosol content in the atmosphere that have affected characteristics of terrestrial solar irradiance (Kvalevag and Myhre, 2007; Wild, 2009). Aerosols reduce the amount of solar irradiance reaching the surface of the earth (Streets et al., 2009).

Extinction of solar irradiance in the atmosphere is done by two principal ways. Atmospheric aerosols scatter incident solar irradiance in all directions through the principles of Mie theory (Wang, 2019). Extinction of solar irradiance by gaseous elements is described by Rayleigh scattering (Wang et al., 2006). Both these scattering processes increase the amount of solar irradiance that is either reflected back to space or absorbed by the atmospheric constituents but increases the downward flux of diffuse radiation at the Earth's surface (Unsworth and Monnteith, 1972). Atmospheric constituents that affect transmission of direct solar irradiance include ozone absorption, molecular scattering, uniformly mixed gas (G) absorption, water vapor absorption, aerosol absorption and scattering, stratospheric and tropospheric nitrous oxide absorption (Allen *et al.*, 2006; Wang *et al.*, 2006).

Southern Africa is not only a region of abundant sunshine, but also a significant source of ozone precursors and a dominant anticyclonic circulation that suppresses vertical mixing and promote the accumulation of pollutants. Aerosols play an important role, reducing incoming solar irradiance by between 10 and 40% during times of local biomass burning and at the industrialized and populated regions (Kvalevag and Myhre, 2007). Few studies on trends of solar irradiance have been conducted in the southern atmosphere (Power and Mills, 2005). The objective of this study is to investigate temporal and spatial variability of diffuse fraction, *K* index in South Africa. The study also investigated the characteristics of the relationship of *K* and VPD. The variability of this index during the morning and afternoon periods will be analyzed. The study also establishes the relationship of *K* with water vapour pressure deficit, a measure of atmospheric dryness.

Study area, data and methodology

Data

Solar irradiance, air temperature and relative humidity data from six stations with longest datasets were used in this study. The hourly data for the stations (Bloemfontein, Cape Town, Durban, Port Elizabeth, Pretoria and Upington) representative of climatic conditions in the country were obtained from the South African Weather Services. Start and end dates as well as geographical descriptions of the data used

in analysis are provided in Tongwane et al. (2019). These data were of sufficient quality for research and were monitored using Kipp and Zonen pyranometers which were later replaced with Li-Cor pyranometers from the 1950s to the 1990s (Power and Mills, 2005). Disaggregated data for total (global) solar and diffuse recorded at various locations in the country irradiance data was not available after the mid-1990s.

Methodology

Average monthly values of *K* for mornings and afternoons were calculated separately. Hourly data from 0600hrs to 1100hrs were considered for morning calculations while 1200hrs to 1900hrs were used for the afternoons. *K* was described as a ratio of diffuse irradiance to global irradiance.

Hourly atmospheric water vapour pressure deficit (VPD) for each station were calculated using Eqn. 1. For each interval in VPD of 0.2, the corresponding values of *K* were averaged. These average values of *K* were then plotted against the value of VPD for the interval mid-point.

$$VPD\ (kPa) = e_o(T) - e_a(T) = 0.6108 exp\left[\frac{17.27T}{T+237.3}\right]\left\{1 - \frac{RH\%}{100}\right\} \quad (1)$$

where e_o and e_a are saturation vapour pressure and actual vapour pressure respectively; T is the hourly air temperature; RH is the hourly relative humidity.

Results and discussion

Components of solar irradiance received on the surface vary significantly between locations. Global irradiance is highest at Upington and Cape Town in summer, Upington, Pretoria and Bloemfontein in winter but diffuse irradiance is highest along the coastal locations throughout the year (Table 1, Tongwane et al., 2019). *K* is generally higher in the coastal areas where they can reach more than 0.6 at both Cape Town and Durban (Fig. 1a). This is caused by relatively moist conditions that are predominant in the coastal locations. *K* is highest at Durban in all the seasons except winter. This is consistent with the results of Power and Mills (2005) who found that Durban and Pretoria had the lowest global irradiance but highest diffuse irradiance in South Africa. However, at the arid Upington, diffuse irradiance is less than 40% of global irradiance and it can reach rates below 0.2 in winter. The lower *K* rates at Upington show that the sky is much clearer there than at any location in the country. Similar to coastal locations, *K* values are also higher at Pretoria. This is because Pretoria is located in the region of the country that is heavily polluted by air pollutants that originate from industries in Gauteng and Mpumalanga (Tesfaye et al., 2011). The high *K* values on the coastal locations and Pretoria reflect the Mie and Rayleigh effects respectively (Roman et al., 2013).

The gradient of decrease of *K* with VPD is steep until 1.6 kPa after which the rate of change is nearly constant at approximately 0.3 (Fig. 1b). The relationships of *K* and VPD after 1.6 kPa are generally similar except for all the locations except Cape Town during drier atmospheric conditions. This shows that composition of solar irradiance changes rapidly at low VPDs (i.e. moist atmospheric conditions) than at high VPDs which indicate dry conditions. Dry atmospheric conditions with daily and hourly VPDs greater than 1.6 kPa in the eastern interior of South Africa are predominant in the afternoons of the spring season (Tongwane et al., 2017). Diffuse fraction is gradually decreasing with time in most parts of the country (Fig. 2). Its change varies according to the month of the year, time of the day and a location. Cloud data at the stations during the observations of the solar irradiance were not available to investigate the relationship of K with cloudy conditions.

Conclusions

The amount of diffuse fraction of solar irradiance depends on location. The coastal areas have higher fractions than the inland locations. Port Elizabeth and Upington have highest and lowest fractions respectively. Cape Town with Mediterranean climate has a different diffuse fraction profile. Diffuse fraction decrease rapidly for vapour pressure deficits less than 1.6 kPa but remains nearly constant at 0.3 thereafter.

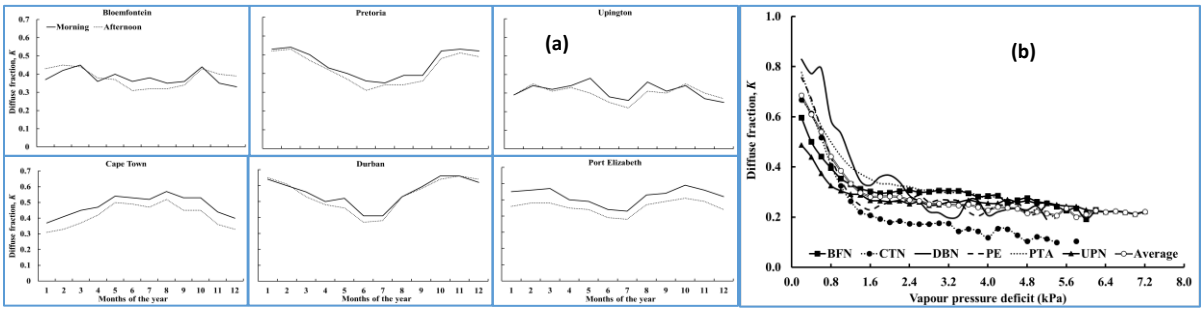

Fig. 1: (a) Temporal and spatial variability of diffuse fraction in South Africa, (b) Variability of diffuse fraction with atmospheric water vapour deficit (BFN – Bloemfontein; CTN – Cape Town; DBN – Durban; PE – Port Elizabeth; PTA – Pretoria; UPN – Upington; Average – Average of all stations)

Table 1: Average monthly global and diffuse irradiance at different locations in South Africa

	Global irradiance						**Diffuse irradiance**					
Month	**BFN**	**CTN**	**DBN**	**PE**	**PTA**	**UPN**	**BFN**	**CTN**	**DBN**	**PE**	**PTA**	**UPN**
1	27.55	29	20.7	25.48	23.87	29.65	7.35	6.59	8.94	8.61	8.58	5.42
2	24.84	25.9	20.1	22.86	22.47	26.62	6.83	5.90	7.84	7.73	8.20	5.52
3	21.59	21.4	17.9	18.74	20.17	22.99	5.85	5.00	6.52	6.22	6.83	4.85
4	17.98	15.2	14.9	14.74	17.70	18.71	4.36	4.37	4.74	4.62	5.12	4.03
5	15.27	10.6	12.2	11.38	15.71	15.63	3.19	3.66	3.63	3.44	3.51	3.05
6	13.57	8.69	10.9	9.88	14.32	13.67	2.73	3.17	3.02	2.95	3.09	2.71
7	14.64	9.64	11.5	10.69	15.14	14.69	2.88	3.36	3.36	3.11	3.24	2.67
8	17.83	12.60	13.5	13.31	17.82	17.90	3.55	4.39	4.43	4.22	3.97	3.56
9	21.37	17.10	15.00	16.81	20.80	21.86	5.18	5.79	5.97	6.13	5.24	4.60
10	24.84	22.70	17.50	21.09	22.59	26.13	6.45	6.85	7.49	7.63	6.81	5.79
11	27.78	27.60	19.50	24.61	23.47	29.88	6.85	7.26	8.59	8.82	7.98	5.36
12	29.13	29.30	21.40	26.75	24.69	30.98	7.00	7.19	9.12	8.72	8.50	5.15

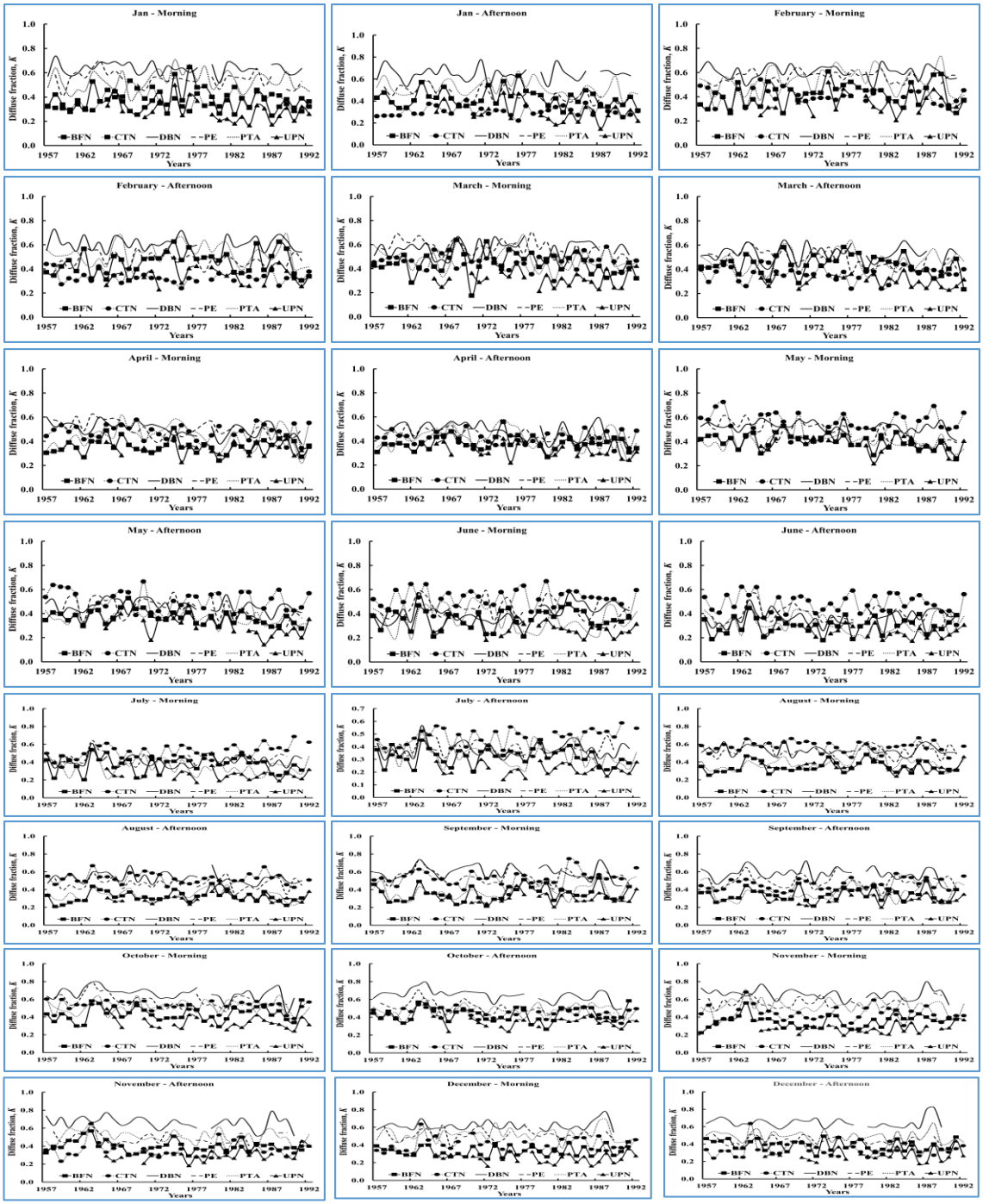

Fig. 2: Morning and afternoon diffuse fraction at various locations in South Africa between 1957 and 1992 during the months July to December

References

Allen, R.G., Trezza, R. and Tasumi, M., 2006. Analytical integrated functions for daily solar radiation on slopes. *Agricultural and Forest Meteorology*, *139*(1-2), 55-73.

Kvalevåg, M.M. and Myhre, G., 2007. Human impact on direct and diffuse solar radiation during the industrial era. *Journal of Climate*, 20:19, 4874-4883.

Power, H.C. and Mills, D.M., 2005. Solar radiation climate change over Southern Africa and an assessment of the radiative impact of volcanic eruptions. *International journal of climatology*, 25:3, 295-318.

Román, R., Antón, M., Valenzuela, A., Gil, J.E., Lyamani, H., De Miguel, A., Olmo, F.J., Bilbao, J. and Alados-Arboledas, L., 2013. Evaluation of the desert dust effects on global, direct and diffuse spectral ultraviolet irradiance. *Tellus B: Chemical and Physical Meteorology*, *65*(1), 19578.

Stjern, C.W., Kristjánsson, J.E. and Hansen, A.W., 2009. Global dimming and global brightening—An analysis of surface radiation and cloud cover data in northern Europe. *International Journal of Climatology: A Journal of the Royal Meteorological Society*, 29:5, 643-653.

Streets, D.G., Yan, F., Chin, M., Diehl, T., Mahowald, N., Schultz, M., Wild, M., Wu, Y. and Yu, C., 2009. Anthropogenic and natural contributions to regional trends in aerosol optical depth, 1980–2006. *Journal of Geophysical Research: Atmospheres*, 114(D10).

Tesfaye, M., Sivakumar, V., Botai, J. and Mengistu Tsidu, G., 2011. Aerosol climatology over South Africa based on 10 years of Multiangle Imaging Spectroradiometer (MISR) data. *Journal of Geophysical Research: Atmospheres*, 116(D20).

Tongwane, M.I., Savage, M.J., Tsubo, M. and Moeletsi, M.E., 2017. Seasonal variation of reference evapotranspiration and Priestley-Taylor coefficient in the eastern Free State, South Africa. *Agricultural water management*, 187, 122-130.

Tongwane, M.I., Savage, M.J. and Tsubo, M., 2019. Relationship between global and diffuse irradiance and their variability in South Africa. *Theoretical and Applied Climatology*, *137*(1-2), 1027-1040.

Unsworth, M.H. and Monteith, J.L., 1972. Aerosol and solar radiation in Britain. *Quarterly Journal of the Royal Meteorological Society*, *98*(418), 778-797.

Wang, J., 2019. *Angle dependent light scattering of functional nanoparticle composites.* Doctoral dissertation. Acta Universitatis Upsaliensis. ISBN 978-91-513-0559-2

Wild, M., 2009. Global dimming and brightening: A review. *Journal of Geophysical Research: Atmospheres*, 114(D10).

8. INSTRUMENTS AND DATA COLLECTION

Day-time and Night-time Ozone increase at Cape Point GAW Station as observed by ground based instruments

T. Mkololo[1,2], N. Mbatha[3], V. Sivakumar[2], C. Labuschagne[1],W. Jourbet[1], E.T. Mbambalala[1] and L. Martin[1]

[1]South African Weather Service, Global Atmosphere Watch Station, P.O. Box 320, Stellenbosch, 7599
[2]University of KwaZulu Natal, Private Bag x 54001, Westville campus, Durban, 4000
[3]University of Zululand, Department of Geography, KwaDlangezwa, 3886, South Africa

Corresponding author:

This study presents analysis of the variability and trends of the all-day, day-time and night-time ozone data measured at Cape Point Global Atmosphere Watch (GAW) station. Long term trends from 2000 to 2018 are investigated. The linear trend slope of 0.28 and 0.19 ppb/year are observed for the night-time and day-time data subsets, respectively. The observed higher linear slopes at night is evident in all seasons. In addition to linear trend analysis, Theil-Sen trend estimates an increase of 0.67 %/year and 0.02 %/year for night-time and night-time data subsets, respectively.

Keywords: Surface ozone, Day-time, Night-time, Trend analysis

Introduction

Cape Point Global Atmosphere Watch (GAW) is one of the World Meteorological Organization (WMO) GAW stations that monitor continuous surface ozone (O_3) to study background-level trends in the atmosphere. Approximately 90% of the total O_3 is located in the stratosphere and only 10% is located in the troposphere. Stratospheric O_3 acts as a shield that protects the Earth from harmful radiation. On the other hand, the tropospheric O_3 is formed through photochemical reactions of nitrogen oxides (NO_x) and volatile organic compounds (VOCs) or through downward movement of O_3 from the stratosphere to the troposphere. Nitrogen oxides and VOCs are emitted from anthropogenic sources such as fossil fuel power plants, industrial activities, and transportation as well as natural sources such as lightning and soil (NO_x). In the presence of sunlight, nitrogen dioxide (NO_2) undergoes photochemical reactions to produce oxygen atom (O), which reacts with oxygen molecule (O_2) to form O_3 (Lelieveld and Dentener, 2000). Meteorological parameters such as temperature, wind speeds, sunlight and the mixed layer depth plays a crucial role in O_3 mole fractions.

In general, O3 mole fractions are expected to be higher during day-time as compared to night-time because of photochemical reactions that take place during the day (Seinfeld and Padis, 2006). Night-time is characterised by low O_3 mole fractions, O_3 destruction by NO titration and deposition process (Ghosh et al., 2013). Earlier studies reported that it is advisable to separate day and night-time O_3 analysis due to different influencing factors that take place during these times (Abdul-Wahab et al., 2005; Özbay et al., 2011).

Ghosh et al. (2013), reported the important role of (nitrogen dioxide) NO_2-(nitrate) NO_3- (dinitrogen pentoxide) N_2O_5 cycle in the night-time O_3 chemistry as the cycle strongly affects the depletion process. Therefore, the Cape Point O_3 data is separated into day and night-time data in order to investigate if the observed O_3 increase occurs in both data subsets or is related to photochemical reactions that occurs in day-time.

Remarkably, a study by Oltmans et al., (2013) reported O_3 increase at Cape Point and other GAW stations in the southern hemisphere (Cape Grim and Lauder) in recent years.

Data and method

The Cape Point GAW station was established in 1978. The surface ozone long-term monitoring program began in 1983 from a 30m air intake line. In 1996, a second instrument was installed from the 4m air intake. Since then, the surface O_3 mole fractions have been monitored using two Thermo Electron (Teco) analyzers based on an ultraviolet (UV) detection technique. Daily zeroes are performed to check the long-term stability of the instruments. Furthermore, instrumental verifications are performed quarterly using the primary calibrator (TEI 49i-PS) traceable to WMO World Calibration Centre (WCC-EMPA) based in Switzerland.

In addition to the site verifications, calibrations are performed by WCC-EMPA every four years as from 1997. The latest O_3 instrument performance audit was performed in 2015.

The main aim of this study is to investigate day and night-time surface O_3 variability and trends. The trends and its significance are investigated using the Mann–Kendall trend test statistic. This method is defined as a non-parametric, rank-based method which is commonly used to extract monotonic trends in the time series of climate data, environmental data or hydrological data. Mann-Kendall test statistics was computed using the formula:

$$S = \sum_{k=1}^{n-1} \sum_{j=k+1}^{n} sign(X_j - X_k)$$

where,

$$sign(x) = \begin{cases} +1, & \text{if } x > 1 \\ 0, & \text{if } x = 0 \\ -1, & \text{if } x < 1 \end{cases}$$

average value of S is $E[S] = 0$, and the variance σ^2 is given by the equation:

$$\sigma^2 = \{n(n-1)(2n+5) - \sum_{j=1}^{p} t_j(t_j-1)(2t_j+5)\}/18$$

$$S = \sum_{k=1}^{n} \sum_{j=k+1}^{n} sng(X_j - X_k)$$

where

$$sgn(x) = \begin{cases} 1 & \text{if } x > 1 \\ 0 & \text{if } x = 0 \\ -1 & \text{if } x < 1 \end{cases}$$

In respect to the above-defined Z-transformation equation, this study reflects a 5% confidence level, where the null hypothesis of no trend is rejected if |Z| > 1.96.

Results and discussion

As indicated in Fig. 1, surface O_3 mole fractions show a minimum of 23.9 ± 6.9 ppb at 09:00 am and start to increase after the morning peak hour (09:30 am) reaching a maximum of 27.2 ± 7.7 ppb at 03:00 pm. Such an increase is followed by a decrease after 05:00 pm. Therefore, the current study uses local time intervals of 11:00 am - 04:00 pm and 11:00 pm - 04:00 am for day and night-time, respectively. However, the actual day and night-time vary with seasons.

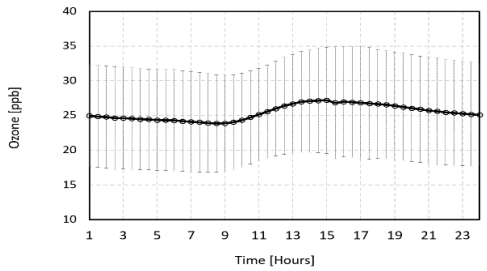

Figure 1. The average diurnal cycle of all year average surface O_3 mole fractions during 2000 to 2018.

As shown in Fig. 2, day-time surface ozone mole fractions are slightly higher than the night-time ozone mole fractions with all-day being the average of the day and night-time. The mean mole fractions of day and night-time are 26.6 ppb and 24.9 ppb, respectively. Slightly higher variations are observed in day-time compared to night-time as indicated by standard deviation of 6.0 ppb and 5.3 ppb for day and night-time, respectively. The observed results of higher surface ozone during the day is in agreement with previous studies that reported the occurrence of photochemical reactions in day-time (e.g. Reddy et al., 2011; Alghamdi et al., 2014). However, due to the geographical location of the station, there is less ozone destruction by NO during night-time (as compared to a city environment, for example). Hence, night-time O_3 mole fractions at Cape Point are not as low as in sub-urban and urban stations. Similar findings were reported in a study by Nzotungicimpaye et al., (2014). In general, all seasons indicate a higher average in day-time data subsets. The summary of this statistic is shown in Table 1.

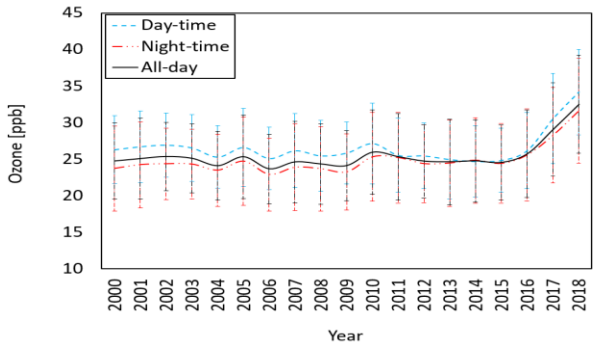

Figure 2. The average and the standard deviation (error bars) of all year average surface O_3 mole fractions for the all-day (diamond), day-time (circle) and night-time (tri-angle) data subsets during 2000 to 2018.

Table 1. The average and the standard deviation of all year and seasonal average surface O_3 mole fractions for the all-day, day-time and night-time data subsets during 2000 to 2018.

Data set	All year	Summer	Autumn	Winter	Spring
All-day	25.4±5.4	18.2±5.2	24.6±5.8	30.7±5.6	27.9±5.1
Day-time	26.5±5.7	20.0±5.8	26.0±6.2	31.0±5.4	28.9±5.2
Night-time	24.8±5.0	17.3±4.5	23.9±5.5	30.4±5.5	27.6±4.7

Oltamans et al. (2013) reported O_3 increase at Cape Point and other GAW stations in the southern hemisphere. However, in recent years, a strong increase in surface O_3 mole fractions has been observed, especially in the time period of 2016 to 2018. An average of 25.5, 26.6 and 24.9 ppb has been recorded over the study period for all-day, day and night-time, respectively. In 2018, O_3 average exceeds the long-term average by 7.1, 7.6 and 6.8 for all-day, day and night-time, respectively. The observed increase in surface ozone might be related to meteorological factors such as wind speed and direction dynamics. As indicated in Fig. 3, the prevailing winds from 2007 to 2013 are South-easterlies that brings clean air from the ocean to the station. As from 2014 to 2018, a change in the average observed wind direction from south-east to east is observed. In the years that seem to indicate an increase of ozone at Cape Point station, the year 2016 is only year that seem to indicate a normal south-east direction. Moreover, Tarasova and Karpetchko (2003) reported that winds with low speed, high solar radiation, high temperatures and low humidity promotes O_3 increase. It is worth to also mention that wind speeds at Cape Point seem to have reduced in recent years. Also, Cape Town and its surrounding areas was affected by a massive drought in 2015-2017 which provides another factor that could lead to increasing trends of ozone via a process of increasing trends of terrestrial temperatures.

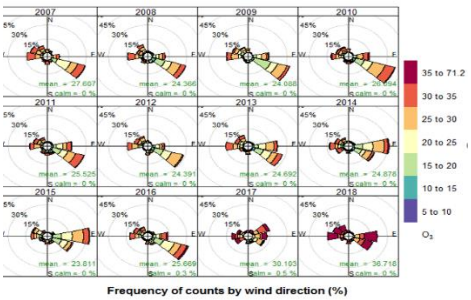

Figure 3. Percentage frequency occurrence of surface O_3 mole fraction relative to wind direction from 2007 to 2018.

As indicated in Table 2, the increase in surface O_3 is evident in all data subsets, with stronger increase observed in the night-time data. The linear trends reached 0.19, 0.14 and 0.22 ppb/year for all-day, day and night-time, respectively, with the strongest z-score of 3.30 observed with night-time data. With the exception of day-time, time series indicates a significant increase of ozone trends with positive z-score which are above 1.96 (95% confidence level). The Theil-Sen trend in Fig 4 (a), (b) and (c) shows a similar strong increase of 0.66 %/year in the night-time data, while it indicate an increase of 0.39 %/year and 0.01 %/year in the all-day and day-time data, respectively. However, when excluding 2017 and 2018 data, the Theil-Sen trend shows an increase of 0.28 and 0.03 %/year in the night-time and all-day, respectively. While a decrease of -0.34 %/year is observed for day-time. Similar results on high night-time trends relative to day-time were reported by Xu et al. (2016) at the Mt Waliguan GAW station in China.

Table 2. The linear slope, z-score and the p values of all year surface ozone mole fraction for the all-day, day-time and night-time data subsets during 2000 to 2018.

Data subset	Linear slope	Z-score	P-value
All-day	0.19	2.82	0.0048
Day-time	0.14	1.71	0.0872
Night-time	0.22	3.30	0.0010

(a)

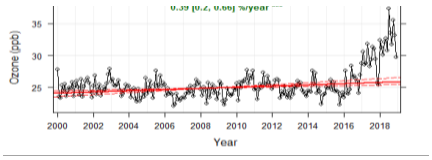

(b)

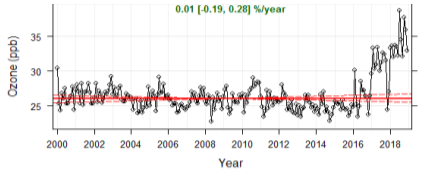

(c)

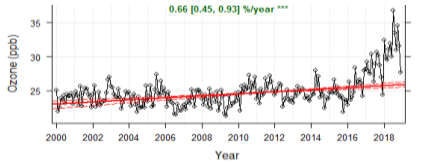

Figure 4. Theil-Sen trend estimates of surface O_3 mole fraction for the all-day (a), day-time (b) and night-time (c) data subsets during 2000 to 2018.

Conclusions

The observed O_3 increase at Cape Point occurs in all three data subsets. The changes in wind direction over the last years could potentially be the reason for the observed surface O_3 increase. Moreover, further investigation is required on:

- Meteorological parameters such as temperature and solar radiation as they play a big role in O_3 increase.
- Seasonal trends need to be investigated further by using similar trend analysis used for day and night-time data.
- Ozone data from other southern hemisphere stations need to be analysed for trends in order to know if the current O_3 increase is the southern hemisphere phenomenon.
- Furthermore, ozone data from Cape Town stations such as Goodwood and Molteno need to be analysed for trends in order to know if the current O_3 increase is related to 2017 Cape Town drought.

Acknowledgements

We are grateful to South African Weather Service for making their ozone data available for this research. Furthermore, we are indebted to Danie Van Der Spuy for his continued support in maintaing the instruments. We would also like to acknowledge the David Carslaw for his openair R packages, and the support by the NRF-CNRS Protea project.

References

Alghamdi, M., Khoder, M., Harrison, R. M., Hyvärinen, A.-P., Hussein, T., Al-Jeelani, H., Almehmadi, F. 2014: Temporal variations of O3 and NOx in the urban background atmosphere of the coastal city Jeddah, Saudi Arabia. *Atmospheric environment*, 94, 205-214.

Ghosh, D., Lal, S., & Sarkar, U. 2013: High nocturnal ozone levels at a surface site in Kolkata, India: Trade-off between meteorology and specific nocturnal chemistry. *Urban Climate*, 5, 82- 103.

Lelieveld, J. and Dentener, F. J. 2000: What controls tropospheric ozone? *Journal of Geophysical Research* 105, 3531-3551.

Nzotungicimpaye, C-L., Abiodun, B. J. and Steyn. D. G. 2014: Tropospheric ozone and its regional transport over Cape Town. *Atmospheric Environment,* 87, 228-238.

Oltmans, S. J., Lefohn, A. S., Shadwick, D., Harris, J. M., Scheel, H. E., Galbally, I., Tarasick, D. W., Johnson, B. J., Brunke, E. G., Claude, H., Zeng, G., Nichol, S., Schmidlin, F., Davies, J., Cuevas, E., Redondas, A., Naoe, H., Nakano, T., Kawasato, T. 2013: Recent tropospheric ozone changes e A pattern dominated by slow or no growth. *Atmospheric Environment*, 67, 331- 351.

Özbay, B., Keskin, G. A., Doğruparmak, Ş. Ç., & Ayberk, S. 2011: Multivariate methods for ground-level ozone modeling. *Atmospheric Research*, 102(1), 57-65.

Tarasova, O. A. and Karpetchko, A. Y. 2003: Accounting for local meteorological effects in the ozone time-series of Lovozero (Kola Peninsula). *Atmospheric Chemistry Physics Discussion*, 3, 655–676.

Reddy, B. S. K., Reddy, L., Cao, J.-J., Kumar, K. R., Balakrishnaiah, G., Gopal, K. R., Ahammed, Y. N. 2011: Simultaneous Measurements of Surface Ozone at Two Sites over the Southern Asia: A Comparative

Seinfeld, J. H. and Pandis, S. N. 2006: From Air Pollution to Climate Change. *Atmospheric Chemistry and Physics*. John Willey and Sons, New Jersey. Study. Aerosol and Air Quality Research, 11(7), 895-902.

Xu, W., Lin, W., Xu, X., Tang, J., Huang, J., Wu, H. and Zhang. X. 2016: Long-term trends of surface ozone and its influencing factors at the Mt Waliguan GAW station, China – Part 1: Overall trends and characteristics. *Atmospheric Chemistry and Physics*, 16, 6191-6205.

Evaluation of three models for estimating daily net radiation within the FAO Penman-Monteith method in southern Africa

Lindumusa Myeni[1, 2], Mokhele Moeletsi[1, 3] and Alistair Clulow[2]

[1]Agricultural Research Council - Institute for Soil, Climate and Water, Private Bag X79, Pretoria 0001, South Africa
[2]Soil-Plant-Atmosphere Continuum Research Unit, Agrometeorology Discipline, School of Agricultural, Earth and Environmental Sciences, University of KwaZulu-Natal, Private Bag X01, Scottsville 3209, Pietermaritzburg, South Africa
[3]Risks and Vulnerability Assessment Centre, University of Limpopo, Private Bag X1106, Sovenga 0727, South Africa

Corresponding author: myenil@arc.agric.za

ABSTRACT

Evaluation of different models for estimating net radiation flux (R_n) is indisputable for identification of the most accurate model. In this study, two new R_n models were evaluated, relative to the procedure recommended by Food and Agriculture Organization for estimation of R_n (FAO56-R_n) in southern Africa. The proposed model performed better than all the evaluated models at four sites, with regression coefficient (r^2) values greater than 0.90 and index of agreement (d) values greater than 0.97. These findings suggest that the proposed model presented here is a promising approach to estimate R_n in southern Africa with minimum input data.

Keywords: Calibration, Net radiometer, Modelling, Radiative flux, Reference crop evapotranspiration, Validation

Introduction

Accurate quantification of crop water use is critical for crop-yield modelling and efficient use of water resources (McMahon et al., 2013). Crop water use is often estimated based on the concept of reference evapotranspiration (ET_0). However, in situ measurements of ET_0 are only available in well-equipped and specific research sites (McMahon et al., 2013). Therefore, ET_0 is often estimated using FAO Penman-Monteith equation (Allen et al., 1998). The FAO-56 PM equation requires measurements of R_n, which are often not readily available from standard weather stations in developing countries in particular (Carmona et al., 2017). Therefore, R_n is often estimated from standard meteorological data using different empirical models, which often differ in procedures used to compute clear-sky solar radiation, cloud cover, net outgoing longwave radiation, atmospheric emissivity and actual vapour pressure of the air (Allen et al., 1998; Kjaersgaard et al., 2007; Irmak et al., 2010).

Improved estimation of R_n can provide more accurate prediction for ET_o in regions facing data scarcity, in southern Africa in particular (Sabziparvar and Mirgaloybayat, 2015). There is a vital need identify the most accurate and robust model that could be used to estimate R_n for improved estimation of ET_o with minimal data input requirements. Within this context, evaluation of different models to estimate R_n, relative to the recommended FAO56-R_n model and in situ measurements of R_n is indisputable. The availability of in situ R_n data at five sites, representing different climatic and land cover conditions of southern Africa enables the unique opportunity for the evaluation three models to estimate R_n within the FAO-56 PM equation. The main aim of this study was to develop and evaluate two new alternative procedures with relative minimum input data requirements to estimate R_n without any site-specific calibrations, relative to the recommended FAO56-R_n model and in situ measurements of R_n in southern Africa.

Materials and methods

Modelling net irradiance

Proposed net radiation model

According to Arya (2001), R_n (MJ m^{-2}) is expressed as:

$$R_n = R_s - rR_s + L_d - L_u \quad (1)$$

where r (dimensionless) is a reflection coefficient of the grass surface (approximately 0.23), L_d (MJ m^{-2}) is the incoming infrared irradiance flux emitted by the atmosphere and L_u (MJ m^{-2}) is the outgoing infrared irradiance flux emitted by the earth surface.

L_d is calculated based on theoretical Stefan–Boltzmann relation:

$$L_d = \varepsilon_e \sigma {T_{air}}^4 \quad (2)$$

According to Crawford and Duchon (1999), ε is the emissivity of the earth surface and is generally expressed as:

$$\varepsilon_e = C_f + ((1 - C_f)\varepsilon_0) \quad (3)$$

where C_f is the cloudiness factor (dimensionless) and ε_0 (dimensionless) is the effective emissivity of the atmosphere (under clear-sky conditions). According to Crawford and Duchon (1999), C_f is determined as:

$$C_f = 1 - R_s/R_{s\,clear} \quad (4)$$

In this paper we propose two models which differ only in the procedures used to compute ε_0 i.e. Eq.(5) utilize the Idso and Jackson (1969) equation while Eq.(6) uses the procedure of Brutsaert (1975):

$$R_n = 0.77R_s + [C_f + ((1 - C_f) \times (1 - (0.261 \exp(-7.77 \times 10^{-4}) \times (273.15 - T_{air})^2))] - \varepsilon\sigma {T_{air}}^4 \quad (5)$$

$$R_n = 0.77R_s + [C_f + ((1 - C_f) \times 1.24 \left(\frac{e_{air}}{T_{air}}\right)^{\frac{1}{7}}] - \varepsilon\sigma {T_{air}}^4 \quad (6)$$

where R_s is the solar irradiance (MJ m^{-2}), T_{air} is the air temperature at screen height of 2 m (K), e_{air} is the actual saturation vapour pressure (kPa), ε is the emissivity of the earth surface, σ is the modified daily time-scale Stefan-Boltzmann constant (4.9×10^{-9} MJ m^{-2} K^{-4}).

2.1.2 Procedure of estimating $\boldsymbol{R_n}$ within the FAO-56 PM equation

According to Allen et al. (1998), the FAO56-R_n model is as follows:

$$FAO56 - R_n = [R_s(1 - r)] - [4.903 \times 10^{-9} {T_{air}}^4 (0.34 - 0.14\sqrt{e_{air}}) \left(1.35 \frac{R_s}{R_{s\,clear}} - 035\right)] \quad (7)$$

Data collection

Five sites which represent a wide range of elevations, climatic conditions and land cover conditions across southern Africa were selected for models evaluations (Table 1). These sites were selected based on availability of quality R_n data and corresponding meteorological data. Data from UKZN were downloaded from the AIM system (http://agromet.ukzn.ac.za:5355/index.html). Data from Two Streams were collected as part of the South African Water Research Commission (WRC) research project K5/2022: The long term impact of *Acacia mearnsii* trees on evaporation, streamflow, low flows and ground water resources (Clulow et al., 2011). Data from Mfabeni Mire and Embomveni Dunes sites were collected as part of WRC research project K5/1704: Evapotranspiration from the Nkazana Swamp Forest and Mfabeni Mire (Clulow et al., 2012). Data from Letseng site, data were acquired from the UKZN database collected by a postgraduate student and are not officially been published previously. All collected were summed to daily time step to allow comparisons with outputs from R_n models.

Results and discussion

To evaluate the performance of the new R_n models (Eq. 5 and6) and FAO56-R_n model (Eq. 18), comparisons were made between the daily estimates (R_{ne}) and R_n at all five sites. A summary of statistical results of the comparisons between R_n and R_{ne} values from three R_n models at all five sites is presented in Table 2.

Table 2: Site-wise ranking of statistical results of the comparisons between R_n and R_{ne} values from three R_n models (models were ranked based on RMSE).

Site	Model	RMSE	MBE	r^2	d
Embomve-ni Dunes	Eq. 5	1.09	0.62	0.96	0.98
	FAO56 -R_n	1.67	1.38	0.96	0.96
	Eq.6	3.45	3.26	0.94	0.87
Letseng	Eq. 5	1.48	1.16	0.95	0.97
	FAO56 -R_n	1.87	1.59	0.94	0.94
	Eq. 6	4.92	4.73	0.95	0.74
Mfabeni Mire	FAO56 -R_n	1.71	0.11	0.96	0.98
	Eq. 5	1.82	-0.65	0.96	0.98
	Eq. 6	3.59	1.97	0.95	0.94
Two Streams	Eq. 5	1.30	-0.18	0.90	0.97
	FAO56 -R_n	1.56	0.71	0.89	0.96
	Eq. 6	3.34	2.76	0.82	0.86
UKZN	Eq. 5	2.27	-0.64	0.92	0.97
	FAO56 -R_n	2.63	-0.59	0.89	0.96
	Eq. 6	5.27	2.32	0.87	0.89

The observed differences between R_{ne} from FAO56-R_n and R_n may be attributed to the poor estimation of L_d as a result of using coefficients proposed by Allen et al. (1998) without site-specific calibrations at our sites. These results were consistent with previous studies (e.g. Kjaersgaard et al., 2007; Sabziparvar and Mirgaloybayat, 2015; Carmona et al., 2017). Therefore, this study confirmed the need for site-specific calibrations of coefficients in the FAO56-R_n model for accurate R_n estimates.

However, lack of long-term quality radiative fluxes data hindered the site-specific calibrations of coefficients used in the FAO56-R_n model at our sites.

The results also revealed that the proposed new model Eq. (5), with less site-specific empirical coefficients performed better than all the evaluated models at four sites, except at humid coastal conditions of Mfabeni Mire. Despite the similarity of the equations utilised in both proposed models, which only differed in the procedures used to compute ε_0, there were significant differences between their R_{ne}. The observed relative poor performance of Eq. (6) may be attributed to the poor estimation of L_d as a result of using 1.24 as an empirical coefficient in Brutsaert's equation, which could have lacked the validity under climatic conditions of southern Africa. Previous studies have demonstrated the need for site-specific calibration of Brutsaert's coefficient which varies with climatic conditions to attain best R_{ne} (Carmona et al., 2014; Cheng and Nnadi, 2014). However, lack of long-term profile measurements of e_{air} and T_{air} often hinders the site-specific calibrations of Brutsaert's coefficient (Cheng and Nnadi, 2014).

Conclusions

The results of this study indicated that R_n can be estimated well from standard weather station data using the FAO56-R_n model and the two proposed models. Results also confirmed the need for site-specific calibrations of coefficients used in the FAO56-R_n and Eq. 6 models to attain the best R_{ne}, which limit their applicability in southern Africa where long-term profile measurements of radiative fluxes, e_{air} and T_{air} data required for calibrations are lacking. The findings of this study suggested that the proposed model Eq. (5) presented here is the most promising, alternative and appropriate to estimate R_n in the FAO-56 PM equation with minimum input data in southern Africa without any site-specific calibrations.

Acknowledgments

Financial support from the European's Union H2020 research and innovation program under Grant Agreement No. 727201, Agricultural Research Council (ARC), University of KwaZulu-Natal (UKZN) and National Research Foundation (NRF) is gratefully acknowledged. The UKZN and Water Research Commission (South Africa) are gratefully acknowledged for provision of data.

References

Allen, R. G., Pereira, L. S., Raes, D., & Smith, M. (1998). Guidelines for computing crop water requirements-FAO Irrigation and Drainage Paper 56, FAO-Food and Agriculture Organisation of the United Nations, Rome (http://www. fao. org/docrep) ARPAV (2000), La caratterizzazione climatica della Regione Veneto, Quaderni per. *Geophysics*, *156*, 178.

Brutsaert, W. (1975). On a derivable formula for long-wave radiation from clear skies. *Water Resources Research*, *11*(5), 742-744.

Carmona, F., Rivas, R., & Caselles, V. (2014). Estimation of daytime downward longwave radiation under clear and cloudy skies conditions over a sub-humid region. *Theoretical and Applied Climatology*, *115*(1-2), 281-295.

Carmona, F., Rivas, R., & Kruse, E. (2017). Estimating daily net radiation in the FAO Penman–Monteith method. *Theoretical and Applied Climatology*, *129*(1-2), 89-95.

Cheng, C. H., & Nnadi, F. (2014). Predicting downward longwave radiation for various land use in all-sky condition: Northeast Florida. *Advances in Meteorology*, *2014*, 1-12.

Clulow, A. D., Everson, C. S., & Gush, M. B. (2011). The long-term impact of *Acacia mearnsii* trees on evaporation, streamflow and ground water resources. *Water Research Commission report no. TT 505/11*. Water Research Commission, Pretoria, South Africa. Available at: http://researchspace.csir.co.za/dspace/handle/10204/6064 [Accessed 18 June 2018].

Clulow, A. D., Everson, C. S., Mengistu, M. G., Jarmain, C., Jewitt, G. P. W., Price, J. S., & Grundling, P. L. (2012). Measurement and modelling of evaporation from a coastal wetland in Maputaland, South Africa. *Hydrology and Earth System Sciences*, *16*(9), 3233-3247.

Idso, S. B., & Jackson, R. D. (1969). Thermal radiation from the atmosphere. *Journal of Geophysical Research*, *74*(23), 5397-5403.

Irmak, S., Mutiibwa, D., & Payero, J. O. (2010). Net radiation dynamics: Performance of 20 daily net radiation models as related to model structure and intricacy in two climates. *Transactions of the ASABE*, *53*(4), 1059-1076.

Kjaersgaard, J. H., Cuenca, R. H., Plauborg, F. L., & Hansen, S. (2007). Long-term comparisons of net radiation calculation schemes. *Boundary-Layer Meteorology*, *123*(3), 417-431.

McMahon, T. A., Peel, M. C., Lowe, L., Srikanthan, R., & McVicar, T. R. (2013). Estimating actual, potential, reference crop and pan evaporation using standard meteorological data: a pragmatic synthesis. *Hydrology and Earth System Sciences*, *17*(4), 1331-1363.

Sabziparvar, A. A., & Mirgaloybayat, R. (2015). Evaluation of some existing empirical and semi-empirical net radiation models for estimation of daily ET0. *Journal of Advanced Agricultural Technologies Vol*, *2*(1).

Evaluating the Wet Bulb Globe Temperature Index at Irene Weather Office

Siphesihle Sithole[1], Katlego Ncongwane[1,2], Joel Botai[1,2,3]

[1]South African Weather Service, Centurion,
[2]School of Chemistry and Physics, University of KwaZulu Natal, Westville Campus
[3]Department of Geography, Geoinformatics and Meteorology, University of Pretoria

*Corresponding author:

Occupational heat strain has direct health and productivity outcomes. We evaluate Wet Bulb Globe Temperature (WBGT) heat index for the Irene weather office outdoor workers. The results show that outdoor workers were exposed to WBGT index values between 26°C to 32°C, representing moderate to high heat strain risk for 633 daytime hours for the period May 2018 to March 2019. Interventions such as the introduction of protective clothing and rescheduling of work are important options in managing heat strain, maintain productivity levels and ensure the overall wellbeing of outdoor workers exposed to heat stress conditions.

Keywords: Outdoor workers, Occupational Heat strain, Productivity, Human health, Climate change

Introduction

As the impact of climate change and variability intensifies, measurement of meteorological parameters and the knowledge of the associated impacts on human health and the environment becomes important. The fifth assessment report (AR5) of the Intergovernmental Panel on Climate Change (IPCC) indicates that during the 21st century, the global surface temperature is expected to rise from 1.1 to 2.9°C for the lowest greenhouse gas emission scenario and from 2.4 to 6.4°C for the highest greenhouse gas emission scenario (IPCC, 2014). These projections have a negative implication for human health, ranging from respiratory and cardiovascular effects to death (Wright, 2014). Outdoor workers are most at risk due to exposure to direct sunlight and other weather elements i.e. ultraviolet radiation. Further, un-acclimatized workers face a greater risk of heat strain than acclimatized workers whose bodies will take an extended time to regulate (Park, Kim and Oh, 2017).

This work evaluates Wet Bulb Globe Temperature (WBGT) heat index for outdoor workers at the Irene weather office and those in the surrounding i.e. the Agricultural Research Council (ARC) animal production division. The results of this study will inform SAWS management if it is necessary to put measures in place to protect workers from occupational heat strain as required by the South African Occupational Health and Safety Act No 85 of 1993 section 8 which states that every employer shall provide and maintain, as far as is reasonably practicable, a working environment that is safe and without risk to the health and safety of his employees.

The WBGT index has been approved as an International Standard through the International Organization for Standardization (ISO) (ISO, 7243) for heat load assessment in an occupational setting and sports applications (ISO, 1989). The WBGT combines, within a single index, temperature, humidity, wind speed, and heat radiation, all of which affect rates of heat transfer from the body (Kjellstrom, et al, 2016). Outdoor workers exposed to heat experience heat strain and have losses in productivity that increased by 2.6% for every degree increase beyond 24°C WBGT, more especially during hotter months (Flouris, et al. 2018). In a study by Mathee et al. (2010), outdoor workers in selected study settings reported heat strain symptoms such as sunburn, sleeplessness, irritability, and exhaustion on days where daily maximum temperatures reached 40°C, these weather conditions resulted to difficulties in maintaining work productivity. The health effects from weather exposure will vary from person to person. It is noted that individuals have different baseline propensities to feel hot or cold and that depends on their physiology, circadian and metabolic cycles which vary dramatically across individuals (Obermeyer, Samra and Mullainathan, 2017).

Instrumentation and Methodology

There are six main components of weather measurements including temperature, atmospheric pressure, wind, humidity, precipitation, and cloudiness (WMO, 2008). In order to assess human biometeorological conditions, the South African Weather Service (SAWS) has introduced additional sensors including Campbell Scientific BlackGlobe-L which is one of the most common instruments used for assessment of heat stress. The system also includes erythemal irradiance and solar radiation measurements on a horizontal surface. Together, these components describe the weather at any given time and influence how we feel and our productivity level in the workplace.

The field study was conducted at the Irene weather office (25.5°S; 28.1°E). The weather office, shown in Figure 1, is a technical centre for SAWS and it's located within the city of Tshwane Metropolitan Municipality, 20 km southeast of Pretoria. Personnel working in this office are mostly meteorological technicians as well as two tradesmen aid responsible for routine functions such as garden maintenance as well as cleaning and maintenance repairs of the weather office yard over extended hours. Observers spend approximately 15 min every hour or longer depending on the weather, for 24 hours daily

collecting weather observations, mainly on the roof top at 360-degree view.

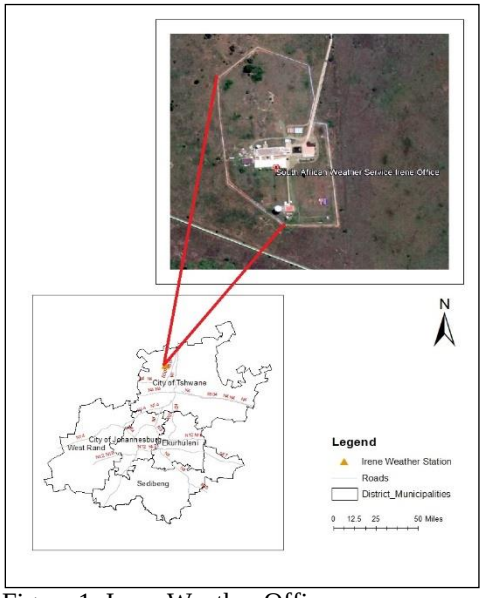

Figure 1: Irene Weather Office

Eleven months of data from May 2018 to March 2019 was used in this study. The data is sampled every 10 seconds using Campbell Scientific data logger (CR1000) and further averaged to hourly and daily time intervals.

The station measures relative humidity (%), wind speed (m s^{-1}) and direction, rain (mm), solar radiation (W m^{-2}), erythemal irradiance (W m^{-2}) that measure ultraviolet radiation (UVB), air temperature (*Twnb*) (°C), natural wet-bulb temperature (*Ta*) (°C), and the globe temperature (*Tg*) (°C), using a Black Globe Temperature Sensor. The measurements are done at the height below 1.5 m, corresponding to the average height of the center of gravity for adults (Mayer and Hoppe, 1987). The WBGT is computed from air temperature (*Tnw*) (°C), globe temperature (T_g) (°C), and the natural wet-bulb temperature (T_a) (°C) for outdoors (*See Eq. 1*).

$$WBGT = 0.7T_{nw} + 0.2T_g + 0.1T_a \quad (1)$$

Where:

T_{nw} Air temperature/dry bulb temperature, °C;

T_g: Black globe temperature measured by a globe 15cm in diameter, °C; and

T_a : Natural wet bulb temperature, °C

T_{nw} and T_g combines the effects of solar radiation, humidity, air temperature and wind (Havenith and Fiala 2016). The occupational health standards risk categories are followed where (WBGT <25°C: low risk; 26-33°C: moderate to high; and +34°C: extreme risk (ISO, 7243). Hourly rest periods are recommended when WBGT reaches 26°C for heavy labour and no work when WBGT reaches 34°C (Hyatt, 2010). The proportions of work and rest or no work will vary per individual, more and longer periods of rest are necessary as WBGT risks increase.

Results and Discussion

An annual WBGT index for Irene is presented in Figure 2. A clear variation is shown were the WBGT index is high during spring and summer and much lower in winter. During winter, the maximum WBGT index recorded was 23.06°C.

In spring and summer, the maximum WBGT index recorded at Irene was 29.78°C and 31.7°C respectively.

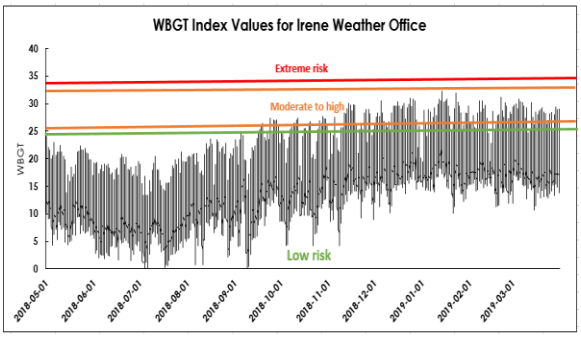

Figure 2: Wet Bulb Globe Temperature index time series for Irene

Between September and March, WBGT index values range between 26°C to 32°C, representing moderate to high heat strain risk. For the diurnal cycle, WBGT index values of 30°C are noted most frequent between 13:00 to 15:00 in the afternoon for the months November to March. The tradesmen's aid who spend extended hours outdoors as well as meteorological technicians are most at risk, in particular in the afternoon during the hottest hours of the day. Table 1 shows the hourly WBGT index heat strain risk for outdoor workers at Irene.

Table 1: WBGT index values and hours of exposure

Heat Strain Risk category	Hours of exposure	Months of exposure
<25°C: Low risk	7407 night hours included	April to August
26-33°C: Moderate to high	633	September to March
+34°C: Extreme risk	0	

For 633/8040 daytime hours, workers were exposed to moderate to high heat strain between 10:00 to 17:00 from the month of September to March. Moderate to high risk exposure can result in heat strain which can cause a wide variety of health disorders, including heat stroke, more especially for the un-acclimatized workers and workers doing heavy physical work. During the study period, the WBGT index value of 34°C was never reached at this location. Maximum WBGT recorded was 32°C, representing moderate to high risk. To reduce or avoid heat strain for outdoor workers, in particular, those exposed for extended

hours, SAWS management must introduce protective strategies such as protective clothing, make provision for frequent breaks or reschedule work for a time of day that is cooler or to delay the job altogether without compromising work productivity. Management must also ensure appropriate access to water and shading to offer relief from the heat. Furthermore, develop an early warning and surveillance system or a hazard communication alert using internal resources to inform workers of dangerous heat stress conditions. Training of workers to recognise the warning signs of heat strain is essential for effective heat strain risk management.

Conclusions

The WBGT index is the heat stress index of preference in the Occupational Health and Safety Act, No. 85 of 1993. The results of this study show that outdoor workers were exposed to moderate to high heat strain during the 633 daytime hours. Such WBGT index values require management interventions that will not compromise work productivity and the health of outdoor workers.

Acknowledgements

The authors acknowledge South African Weather Service personnel for support.

References

Cheuvront S.N, Caruso E.M, Heavens K.R, Karis A.J, Santee W.R, Troyanos C, D'Hemecourt P. (2015). Effects of WBGT Index measurement location on heat stress category classification. Official Journal of the American College of Sports Medicine. www.acsm-msse.org

Flouris A D, Dinas P C, Ioannou L G, Nybo, L Havenith G, Kenny,G P, Kjellstrom T.(2018). Workers' health and productivity under occupational heat strain: a systematic review and meta-analysis. Lancet Planet Health; 2: e521–31

Havenith G, Fiala D. (2016). Thermal Indices and thermophysiological modeling for heat stress. American Physiological Society. Compr Physiol. 6:255-302

Hyatta O, M, Lemke B, Kjellstrom T. Regional maps of occupational heat exposure: past present, and potential future, Global Health Action, 3:1,5715. DOI: 10.3402/gha.v3i0.5715

IPCC, (2014): Climate Change: Synthesis Report. Contribution of Working Groups I, II and III to the Fifth Assessment Report of the Intergovernmental Panel on Climate Change [Core Writing Team, R.K. Pachauri and L.A. Meyer (eds.)]. IPCC, Geneva, Switzerland, 151 pp.

ISO (1989). Hot environments - estimation of the heat stress on working man, based on the WBGT-index (wet bulb globe temperature) – ISO 7243 Standard. Geneva, Switzerland: International Organization for Standardization.

ISO 7243. (1989). Hot environments: estimation of the heat stress on working man, based on the WBGT-Index (Wet Bulb Globe Temperature). Geneva: International Organisation for Standardisation; Environmental Research and Public Health, 12(10), pp. 12577–12604. doi: 10.3390/ijerph121012577.

Kjellstrom T, Lemke B, Hyatt O. (2014). Climate change and occupational health: A South African perspective. S Afr Med J 2014; 104(8):586.DOI:10.7196/SAMJ.8646

Kjellstrom T, Briggs D, Freyberg C, Lemke B, Otto M, Hyatt O. (2016). Heat, Human Performance,and Occupational Health: A Key Issue for the Assessment of Global Climate Change Impacts. Annu. Rev. Public Health.37:97-112

Mathee A, Oba J, Rose A. (2010). Climate change impacts on working people (the HOTHAPS initiative): findings of the South African pilot study. Global Health Action 2010, 3: 5612 - DOI: 10.3402/gha.v3i0.5612

Mayer H, Hoppe P. (1987). Thermal comfort of man in different urban environments. Theoretical and Applied Climatology. https://www.researchgate.net/publication/225206098

Obermeyer Z, Samra JK, Mullainathan S. (2017). Individual differences in normal body temperature: longitudinal big data analysis of patient records. BMJ 2017; 359:j5468.http://dx.doi.org/10.1136/bmj.j5468

Park J, Kim Y, Oh I. (2017). Factors affecting heat-related diseases in outdoor workers exposed to extreme heat. Annals of Occupational and Environmental Medicine (2017) 29:30

South African Government. Environmental Regulations for Workplaces, 1987. Online available at URL: http://www.labour.gov.za/DOL/legislation/regulations/occupational-health-and-safety/regulation-ohs-environmental-regulation-for-workplaces

South Africa. Occupational Health and Safety Act No 85 of 1993 and its Regulations. Johannesburg: Lex Patria Publishers; 1993.

WMO. (2008). Guide to Meteorological Instruments and Methods of Observation WMO-No. 8 Seventh edition 2008

Wright C, Garland, R.M, Norval, M. Vogel, C. (2014). Human health impacts in a changing South African climate. S Afr Med J; 104(8):579-582. DOI:10.7196/SAMJ.860

9. REMOTE SENSING APPLICATIONS

Combining data mining and MODIS fire data for characterisation of fires in the Richards Bay area

P. Govender[1,*], V. Sivakumar[2] and Z.P. Mtshali[3]

[1,2]School of Chemistry and Physics, University of KwaZulu-Natal, Durban, 4000, South Africa
[3]School of Agriculture, Earth and Environmental Science, University of KwaZulu-Natal, Durban, 4000, South Africa

*Corresponding author: paulenegovender@gmail.com; Tel.: +27 31 260 7661

The aim of this study was to classify and characterise fires in the Richards Bay area using a data mining approach and MODIS fire data. A clustering algorithm was applied to 227 days of brightness temperatures which revealed three categories i.e. low, moderate and high intensity days. Fires in the Richards Bay area may be characterised by these categories. The largest proportion of days were found to be low intensity days, where brightness temperatures ranged from 306-338 K. These categories may be useful for fire prediction models and fire management strategies, in terms of efficient resource allocation.

Keywords: Clustering; Intensity; Temperature; Vegetation

Introduction

Southern Africa has been identified as a region having some of the most extensive biomass burning in the world (Roy *et al*. 2005). According to Strydom and Sauvage (2016), the African continent has been termed "the fire continent" due to the high number of fires experienced (more than 30 000 reported during the 2008 and 2009 fire seasons). Monitoring of fires is therefore an important environmental issue as they have a negative impact on plant and animal life, as well as are a threat to society due to the risk of fatalities. Remote sensing technologies such as satellites have become a valuable tool that enables the monitoring and analysis of fires over large regions. The Moderate Resolution Imaging Spectroradiometer (MODIS) satellite product is one such example, whereby the monitoring of active fires is possible by the use of hotspot detection algorithms. In most cases the MODIS satellite detects vegetation fires, which is of interest for the present study (Roy *et al*. 2005). More specifically, this study aims to characterise vegetation fires from MODIS using a data mining approach. Data mining can be simply described as the process of discovering patterns in data. Cluster analysis (or clustering) is a well-known and commonly-used data mining method that was employed for this study. Clustering groups together similar data observations with the aim of finding patterns, where it is often the case that these patterns may have been previously unnoticed. Clustering has found application across a wide variety of fields including atmospheric and Earth sciences. One of the uses of clustering is classification, and for this study, clustering was applied for the classification of MODIS fire data. Considering the negative impact fires can have on vegetation, soil, atmosphere, animal and human life, increasing our knowledge on fires is certainly required.

Chen *et al*. (2017) successfully applied clustering to establish fire regimes for China using MODIS active fire data. For South Africa, previous studies focusing on the analysis of fires, for all or some parts of the country, were conducted by Strydom and Sauvage (2016) and Shikwambana *et al*. (2019). Although these studies utilised satellite data, they did not make use of data mining methods for the analysis.

The aim of the present study to provide a classification and characterisation of vegetation fires in the Richards Bay area, using a data mining approach and MODIS fire data. KwaZulu-Natal is one of three provinces experiencing the most severe fire season, i.e. during August, due to the native vegetation, climate and topography (Strydom and Sauvage, 2016). Richards Bay, located on the eastern coast of South Africa, within the KwaZulu-Natal province, experience fires mainly during the period of May-November, peaking during the month of August.

Instrumentation and Method

MODIS fire data

Archived fire data for the Richards Bay (27.659S; 32.395E) area was obtained from NASA's Fire Information for Resource Management System (FIRMS), obtained from the MODIS instrument. From the available options, the MODIS C6 fire product was used. This product makes use of the most up-to-date algorithms and processing extends to oceans and other large bodies. The Richards Bay area often has fires due to the vegetation burning and was thus selected as the

region of interest. The selected time period was from January to December 2015. Significant land damage due to a fire in the north areas of Richards Bay was within this period (Zululand Observer, 2015). Pre-processing was applied to the original retrieved data file. This included the removal of night time measurements, as only day time fire data were included for the analysis. For each day the measurement with the highest confidence level was used. A total of 227 days were retained for the analysis. The detection of fires is indicated by the brightness temperature, given in Kelvin (K), where temperatures above 330 K were considered to be active fires (Justice *et al.* 2004).

Data mining approach: Clustering

The *k*-means algorithm (MacQueen, 1967) is a well-known clustering technique in data mining. Among the many clustering algorithms available, the reason for choosing *k*-means is because of its simplicity, ease of implementation and computational speed. Given a set of *n* objects, the method constructs *k* partitions of the data, where each partition represents a cluster and where *k* *n*. The partition divides the data into *k* groups such that each group contains at least one object. The *k*-means technique was used here for the classification of fires, and was applied to the brightness temperature variable. The *k*-means algorithm aims to minimise the following objective function:

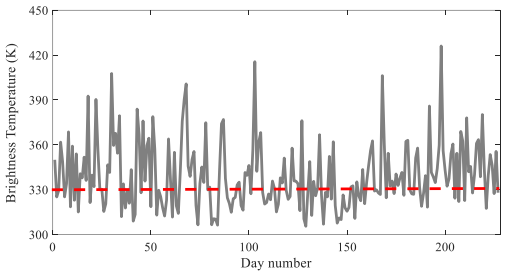

Figure 1: Sequence of days with corresponding brightness temperature. Red line indicates 330 K.

$$E_D = \sum_{i=1}^{c} \sum_{x \in C_i} d(x, m_i) \qquad (1)$$

where is the criterion function, is the center of the cluster and is the Euclidean distance between a point *x* and . For further details of the algorithm, the reader is referred to (Everitt, 2011). The value of *k* in the algorithm has to be chosen in advance. For the present study, a silhouette analysis was used to determine the optimal number of clusters. Silhouette values are in the range [-1;1], where 1 indicates the best clustering result and -1 the worst (Kaufman and Rousseeuw, 2005). The optimal number of clusters was found to be $k = 3$.

Results and Discussion

The sequence of days and corresponding brightness temperatures for year 2015 is shown in Fig. 1. Of the 227 days analysed, 58% experienced fires. The highest brightness temperature that occurred during the analysis period was found to be 426 K (i.e. 5 November 2015). Clustering was applied to the set of 227 days, producing 3 clusters as the optimal solution. The silhouette plot (Fig. 2) produced by the silhouette analysis shows the mean silhouette value for each cluster. For the $k = 3$, all clusters have silhouette values more than 0.6, indicating a good clustering solution. Shown in Figs. 3, 4 and 5 are the histograms of the individual clusters. These show the frequency of days for the range of brightness temperatures. Cluster 1 contains days with the brightness temperatures ranging from 306 K to 338 K. These days can be considered to be "low intensity" days, since most of the temperatures do not reach 330 K. This cluster contains a mixture of days where some days did not experience fires and some days did. Cluster 2 contains days with the brightness temperatures ranging from 339-369 K.

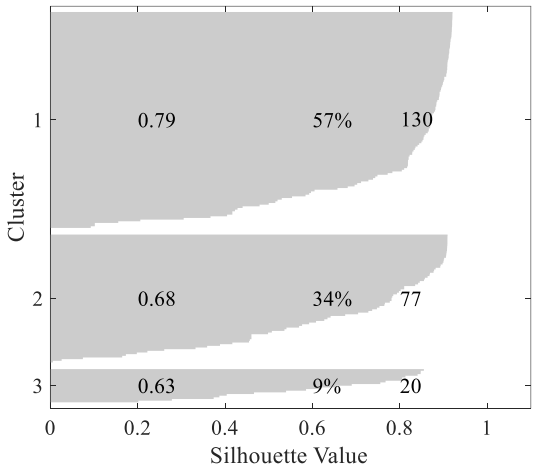

Figure 2: Silhouette plot with mean values, percentage and frequency of days for each cluster.

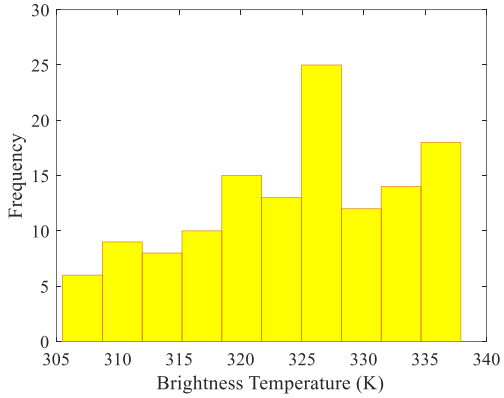

Figure 3: Histogram for low intensity days. A total of 35 and 95 days have a brightness temperature below 330 K and above 330 K, respectively.

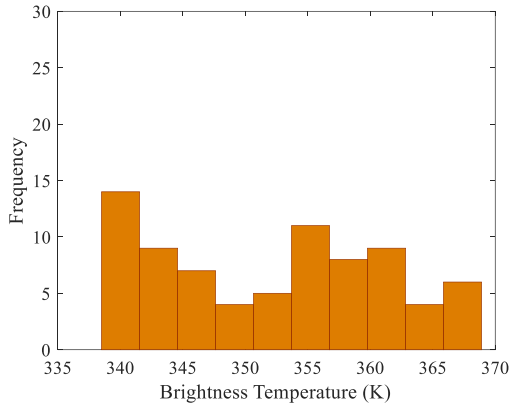

Figure 4: Histogram for moderate intensity days. Days are mostly evenly distributed across the temperature range of 339 K and 369 K.

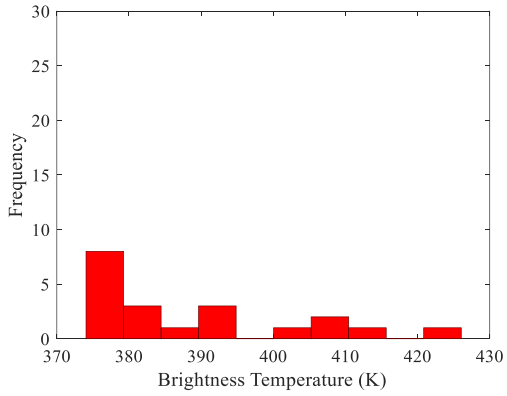

Figure 5: istogram for high intensity days. The highest frequency were days with a temperature of 377 K

These days can be considered to be "moderate intensity" days. All days in this category experienced fires. Lastly, Cluster 3 contains days with the highest brightness temperatures i.e. 374-426 K, and thus can be regarded as "high intensity" days. For the cluster containing low intensity days, a temperature of 327 K had the highest frequency (25) of days in this category, followed by temperature 336 K with 18 days. For the cluster containing moderate intensity days, a temperature of 340 K had the highest frequency of days (14) in this category, followed by temperature 355 K with 11 days. For the cluster containing high intensity days, a temperature of 377 K had the highest frequency (8) of days. Temperatures of 382 K and 392 K have equal frequencies. Temperatures above 400 K constitute 25% of all days in the high intensity category.

These three fire day categories: low, moderate and high intensity, therefore characterises the fires in the Richards Bay area over the period under analysis. It provides useful information on the range and frequency of brightness temperature in each cluster. The proposed method for classification of fires into categories may be useful for fire prediction models and fire management strategies. For example, if the category of day can be predicted, then resources may be allocated more efficiently.

The proportion of days in each category is given Fig. 6. It can be seen that the largest number of days were low intensity days, followed by moderate and high intensity. Therefore, low intensity days were found to be the most prevalent type in the Richards Bay area, and for many of these days there were no fires since brightness temperatures were below 330 K.

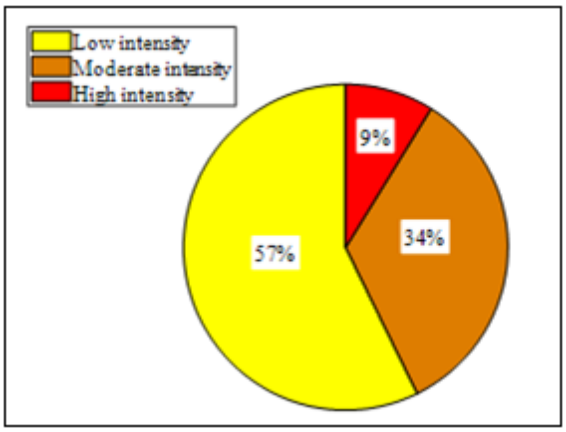

Figure 6: Proportion of days in each of the three categories.

Conclusions

This study proposed the use of a data mining approach (clustering) for the classification and characterization of fires in the Richards Bay area. For the analysis, a set of 227 days of MODIS fire data was used. Clustering applied to brightness temperatures showed three

categories of days that were classified as low, moderate and high intensity days. For low, moderate and high intensity days, temperatures of 327 K, 340 K and 377 K, had the highest frequency, respectively. For the Richards Bay area, the highest temperature for the analysis period was 426 K. Low intensity days were found to be the most frequently occurring category, comprising 57% of all days. These categories may be useful for the development of fire prediction models and fire management strategies, in terms of efficient resource allocation. For example, if the category can be predicted then resources may be allocated accordingly. However, this still remains to the explored in greater detail. Further work will include (1) investigating seasonality of the fires and correlation with the highest brightness temperatures, (2) correlating the fire category with the burned area to investigate the extent of burned area under low, moderate and high intensity days, and (3) applying the method to a larger data set. To the best of the authors knowledge, this is the first study in South Africa aimed at characterising MODIS fire data through a data mining approach.

Acknowledgements

We acknowledge NASA's Fire Information for Resource Management System (FIRMS) for providing fire data from the MODIS instrument. In addition, P. Govender acknowledges the National and Astrophysics Space Science Programme (NASSP) for bursary support.

References

Chen, D., Pereira, M.C. Jose, Masiero, A. and Piotti, F. (2017). Mapping fire regimes in China using MODIS active fire and burned area data. *Applied Geography*. 85: 14-26.

Everitt, B.S. Landau, S., Leese, M. and Stahl, D. (2011). *Cluster Analysis*, Wiley, London.

Justice, C.O., Giglio, L., Korontzi, S., Owens, J. O., Morisette, J.T., Roy, D., Descloitres, J., Alleaume, S. Petitcolin, F. and Kaufman, Y. (2002). The MODIS fire products. *Remote Sensing of Environment*. 83: 244-262.

Kaufman, L. and Rousseeuw, J.P. (2005). *Finding Groups in Data, an introduction to cluster analysis*, Wiley, New Jersey.

MacQueen, J.B. (1967). Some Methods for classification and analysis of multivariate observations. In Proceedings of the 5th Berkeley Symposium on Mathematical Statistics and Probability, Berkeley, University of California Press, 1, p. 281-297.

Roy, D.P., Frost, P.G.H., Justice, C.O., Landman, T., Le Roux J.L., Gumbo, K., Makungwa, S., Dunham, K., Du Toit, R., Mhwandagara, K., Zacarius, A, Tacheba, B., Dube, O.P., Pereira, J.M.C., Mushove, P., Morisette J.T., Santhana Vannan, S.K. and Davies, D. (2005). The Southern Africa fire network (SAFNnet) regional burned-area product-validation protocol. *International Journal of Remote Sensing*. 26(19): 4265-4292.

Shikwambana, L., Ncipha, X., Malahlela, O.E., Mbatha, N. and Sivakumar, V. (2019). Characterisation of aerosol constituents from wild fires using satellites and model data: a case study in Knysna, South Africa. *International Journal of Remote Sensing*. 40(12): 4743-4761.

Strydom, S. and Savage M.J. (2016) A spatio-temporal analysis of fires in South Africa. *South African Journal of Science*. 112(11/12): 1-8.

Zululand Observer (2015). Accessed at <https://zululandobserver.co.za/90348/large-areas- lost-to-fire/>

Temperature and chlorophyll response to spatial variability in upwelling favourable winds in False Bay

S.A.M. Seymour[1*], M. Krug[1,2,3], M. Smith[2], M. Rouault[1,3]

[1]Department of Oceanography, Ma-Re Institute, University of Cape Town, South Africa.
[2]Council for Scientific and Industrial Research (CSIR), Natural Resources and the Environment, Cape Town, South Africa.
[3]Nansen Tutu Centre for Marine Environmental Research, University of Cape Town, South Africa.

*Corresponding author: sian0seymour@gmail.com, +27 83 247 5464,

Coastal water dynamics are largely influenced by wind variability. Synthetic Aperture Radar (SAR) derived wind speeds are used together with Visible Infrared Imaging Radiometer Suite (VIIRS) sea surface temperature and chlorophyll-a data to explore the spatial wind variability and wind forcing in the coastal regions of False Bay and the Cape Peninsula. The region is dominated by an upwelling favourable south easterly wind regime. High spatial wind variability was found with stronger winds corresponding to colder waters and lower chlorophyll content and slower winds corresponding to warmer waters and higher chlorophyll concentrations.

Keywords: Sea surface temperature, Chlorophyll-a, Wind forcing, False Bay, Orography, Synthetic aperture radar

Introduction

False Bay and the greater Cape Peninsula region are important on both a conservational level as well as a human level. This area is home to a rich and diverse marine and coastal life, contains important fishing grounds and plays host to a variety of recreational activities (Gründlingh & Largier, 1991; van Ballegooyen, 1991). Wind is a primary driver of ocean dynamics within this region, and can affect both the physics and the biology of the bay (Gründlingh & Largier, 1991; Jury et al., 1985a; Jury et al., 1985b; Pitcher et al., 2010). Understanding the wind regime of this area is important for the continued co-existence between man and sea. False Bay is surrounded by a unique topography. It is flanked on the east by the Kogelberg Mountains and on the west by the Cape Peninsula Mountains. To the north lies a low lying area known as the Cape Flats. Mountain ridges create areas of wind shadow and wind acceleration within False Bay and off the Cape Peninsula during the predominantly south easterly (SE) winds. Wind shadows have been reported to occur in lee of the Cape Peninsula Mountains off the northern section of the Cape Peninsula as well as across False Bay in a West or North-westerly direction. Regions of accelerated winds have been observed off of Cape Point and Cape Hangklip as well as on either side of the afore mentioned wind shadows (Jury *et al*., 1985a; Jury *et al*., 1985b; Jury, 1987). These orographic effects influence wind variability in the area which in turn can affect other ocean dynamics (Jury et al., 1985a; Jury et al., 1985b; Wainman et al., 1987; Shannon et al., 1991).

Winds are a primary driving force of ocean variability along the west coast of South Africa (Jury *et* al., 1985a; Jury *et* al., 1985b; Jury, 1987; Wainman *et al*., 1987). Within False Bay and the greater Cape Peninsula, spatial wind variability can affect sea surface temperature (SST) through ocean driven processes such as upwelling, convergence and retention. This region is dominated by an upwelling favourable SE wind regime. The effect of these alongshore winds together with Coriolis forces move surface waters seaward, which are then replaced by cold, nutrient rich bottom waters (Wang *et al*., 2015). This process can result in localized upwelling fronts. Such upwelling fronts have been described off of Cape Hangklip and Cape Point during SE winds, with cooler waters observed during stronger SE winds (Jury *et* al., 1985a; Jury *et* al., 1985b; Jury 1987; Lutjeharms *et al.*, 1991) whereas warmer waters have been described during north-westerly (NW) winds (Jury 1987; Lutjeharms *et al.*, 1991).

Coastal winds can also affect the biology of coastal waters. Wind driven upwelling tends to be associated with higher nutrient content, while downwelling regions are associated with flow convergence and the formation of fronts such as the colour fronts often observed within False Bay (Shannon *et al*., 1991). However, this relationship is more complex than with temperature as biology is influenced by a large suite of factors. Upwelling systems such as False Bay and the greater Cape Peninsula are highly susceptible to Harmful Algal Blooms (HABs) with HABs having been linked to wind stress fluctuations within False Bay (Pitcher *et al*., 2010). Both these temperature and colour fronts can be observed using satellite imagery.

Historically, coastal winds were recorded using land-based anemometers or aerial surveys. However, these data have a low spatial resolution making it challenging to explore spatial wind variability (Holt, 2004; Dagestad et al., 2013). Currently, satellite based observations of surface roughness provide the primary source of ocean wind data (Long & Skouson, 1996). The recent launch of two Synthetic Aperture Radars (SARs) as part of the European Space Agency (ESA) Sentinel-1 mission with global coverage every six days (www.esa.int/Our_Activities/Observing_the_Earth/Copernicus/Sentinel-1/Introducing_Sentinel-1) provides free access to high resolution sea surface observations, from which wind estimates can be derived. This high spatial resolution wind speed data used in synergy with high resolution SST and chlorophyll-a (Chl-a) data opens up the opportunity for more studies looking at coastal wind variability and importantly how this drives other coastal dynamics.

Data and method

Selected case studies from the year 2017 were used to explore spatial variability in the wind field over False Bay and the Cape Peninsula region during the SE wind regime. The SE wind regime is dominant over this region and drives upwelling in coastal waters. Sentinel-1 SAR images of Interferometric Wide (IW) swath mode resolution were used. The CMOD5.n algorithm was used in conjunction with 9 km hourly ECMWF (European Centre for Medium-Range Weather Forecasts) wind directions to derive high resolution (1km) wind speeds. Additionally, Visible and Infrared Imaging Radiometer Suite (VIIRS) SST and VIIRS Chl-a data of a spatial resolution of 750 m where used to explore wind forcing on ocean temperature and biology within the region. VIIRS satellites collect data using infrared and the visible spectrum and are affected by cloud cover. Chl-a is used as a proxy for primary productivity. GEBCO gridded bathymetry data (GEBCO_2014 Grid) was used to explore the bathymetry within the bay as well as the topography of the surrounding land. A detailed description of the data and methods used can be found in Seymour (2019).

Within the year 2017 only 13 days where available where SE winds were blowing and SAR wind speed and VIIRS SST and Chl-a data were all available. Here a case of strong SE winds is presented to illustrate the impact of the orography on the spatial variability over the area.

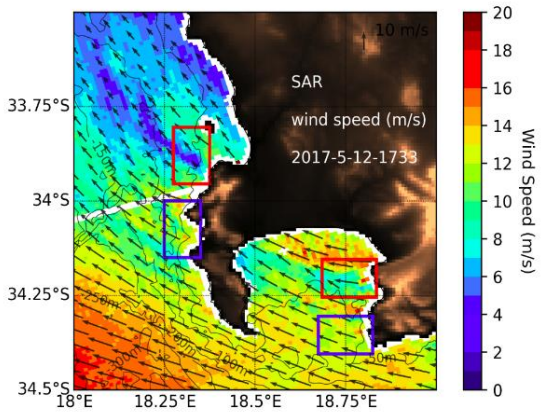

Figure 1: The position of the boxes used to calculate monthly mean sea surface temperature and chlorophyll concentrations for areas of upwelling (blue) and wind shadow (red) in False Bay and off the Cape Peninsula.

For each case, Ekman pumping was derived from the wind stress, which was calculated using the drag coefficient of Yelland and Taylor (1996). Ekman pumping represents the vertical transport induced by the wind stress at the ocean's surface where upwelling and downwelling is indicated by a negative and positive Ekman value, respectively (Tomczak & Godfrey, 2013). Equation 1 shows how Ekman pumping (ω) was calculated where τ_x and τ_y are the x and y components of the wind stress τ and f is the Coriolis force (Tomczak & Godfrey, 2013).

$$-\rho_0\omega = \text{curl}\,(\tau / f) = \partial(\tau_y / f) / \partial x - \partial(\tau_x / f) / \partial y \qquad (1)$$

A time series for the time period 2012 to 2017 was created using v-component ERA-interim wind speeds and VIIRS SST and Chl-a values averaged for a region of intensified (wind acceleration) and reduced wind speeds (wind shadows) off Cape Hangklip and Cape Point (Fig. 1). ERA-interim wind speeds have a spatial resolution of 80 km and a temporal resolution of 6 h. These wind speeds were rotated along a north-west to south-east axis to highlight potential upwelling favourable winds. Additionally, the difference in SST and Chl-a between the wind shadow and upwelling zones for both the Cape Hangklip and Cape Point regions were calculated and plotted as a time series.

Results and Discussion

Spatial variability was evident in the strong SE case with winds ranging from 6.7 m/s to 20.8 m/s (Fig. 2a). A clear wind shadow can be seen spreading across False Bay in a NW direction as well as off the northern section of the Cape Peninsula. Within False Bay this wind shadow seems to change orientation as the direction of the wind changes. The wind shadow off

the Cape Peninsula stretched as far as 62 km in one case. Areas of wind acceleration were observed adjacent to these areas of wind shadow as well as around Cape Hangklip and Cape Point (Fig. 2a). These wind shadows are likely a result of a capping inversion layer preventing wind from flowing over the tallest mountain ridges. Similarly, the wind acceleration is likely caused by vertical compression as wind is accelerated between this inversion layer and mountain ridges, as well as deflected seaward around Cape Hangklip and Cape Point. This capping effect and compression is linked to the southward ridging of the South Atlantic Anticyclone (SAA), which intern brings with it the SE winds (Atkins, 1970; Jury, 1987). In the VIIRS SST and Chl-a maps, cooler waters are seen in regions of intense wind speeds and warmer waters in wind shadow regions (Fig. 2b). Some correspondence was found between winds speed and Chl-a with higher concentration found in areas of decreased winds (Fig. 2c). However, this was not as distinct as with SST. Biology is more complex and is likely influenced by a large amount of factors.

The physical ocean is expected to be influenced by this strong spatial variability in the wind regime. Within False Bay SE winds and the effects of the Coriolis force result in Ekman transport away from the coast. High spatial variability in the wind regime results in areas of convergence (downwelling) and divergence (upwelling), shown as positive and negative Ekman pumping (Fig. 3). During the strong SE case, vertical upwelling velocities of up to 614.0 m/day and downwelling of up to 305.1 m/day were estimated (Fig. 3). Strong winds along the northern shores of False Bay resulted in strong upwelling. This upwelled water would be advected away from the coast towards the wind shadow zone. Here, weaker Ekman transport results in the slowing down of the movement of these waters and eventually downwelling, resulting in an area of convergence across the bay and the retention of waters within the northern half of False Bay (Fig. 3). Warmer waters have been described in the north of False Bay during prevailing SE winds (Lutjeharms *et al*., 1991). This convergence zone across the bay created by the wind shadow could explain this as SE winds result in upwelling along northern shores but the wind shadow prevents water from leaving the bay allowing it to warm up while preventing mixing with cooler waters at the mouth of the bay.

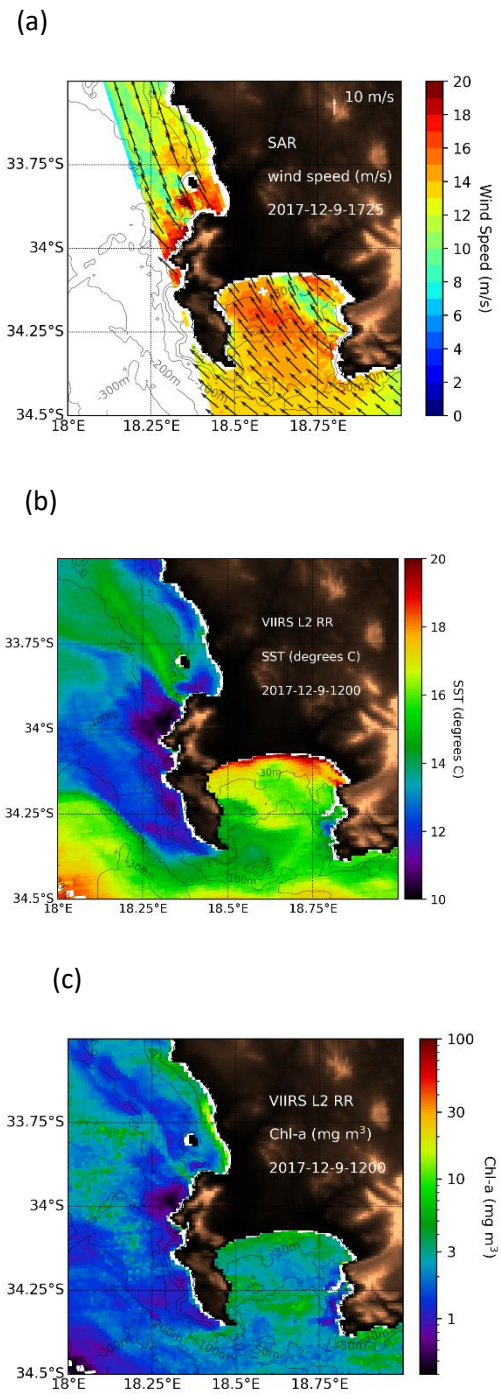

Figure 2: a) SAR derived wind speeds in m/s, b) VIIRS sea surface temperature (SST) map in °C, c) VIIRS chlorophyll-a (Chl-a) map in mg/m3 for a case of strong south-easterly winds (2017-12-09) in False Bay and the Cape Peninsula.

Seasonality can be seen within the time series, with SE wind predominantly occurring during summer months and corresponding to warmer waters and higher Chl-a values (Fig. 4). During winter months, NW winds dominate along with cooler waters and lower Chl-a. The difference in SST and Chl-a between wind shadow and upwelling regions was stronger during summer months and SE winds, with warmer waters and higher Chl-a found in wind shadow zones (Fig. 4). During winter months these differences were observably lower with upwelling regions reaching temperatures warmer than corresponding wind shadow regions in some cases. This is likely due to a decrease in upwelling favourable SE winds and a more dominant NW wind regime. On average, temperatures within False Bay were noticeably warmer than off the Cape Peninsula (Fig. 4). Again, this may be due to water retention within the bay as explained previously (Fig. 3). Additionally, on the Cape Peninsula side upwelling occurs in a more 'open' system and along a steeper bathymetry resulting in less water retention and deeper colder waters being brought to the surface.

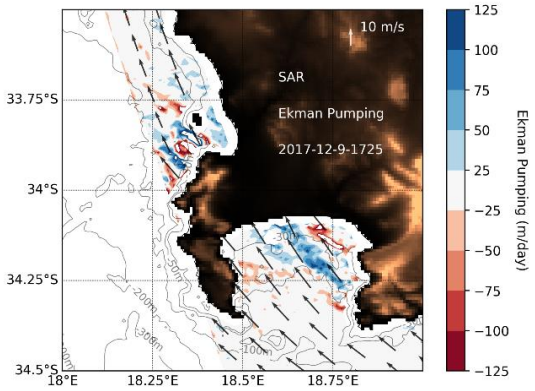

Figure 3: Ekman pumping maps in m/day over False Bay and the Cape Peninsula for a case of strong south-easterly winds (2017-12-09). Arrow length indicates SAR derived wind speed in m/s and arrow direction indicates ECMWF modelled wind direction

Conclusions

Most of human interaction with the sea occurs in coastal regions. Despite the importance of these areas, a large amount of coastal ocean-atmosphere interactions are understudied. The results from this study highlight the importance of understanding how coastal topography affects spatial wind variability, and in turn wind forcing. The SE wind regime of False Bay and the greater Cape Peninsula region is strongly influenced by the surrounding topography, with these orographic effects influencing other ocean dynamics. Surrounding mountain ranges cause areas of wind shadow and wind acceleration within False Bay and off the Cape Peninsula as a result of vertical compression and a capping inversion layer associated with the SAA. These wind shadows correspond to warmer ocean surface temperatures and higher Chl-a, whereas intense SE winds correspond to cooler SST and lower Chl-a values. Changes in SST and Chl-a are strongly linked to the prevailing wind regime, with higher values observed during summer months and SE winds, and lower values during winter months and NW winds. This study shows the potential to use SAR derived wind speeds in synergy with high spatial resolution SST and Chl-a data to better understand the spatial wind variability and wind forcing within the False Bay and greater Cape Peninsula region, as well as coastal regions as a whole.

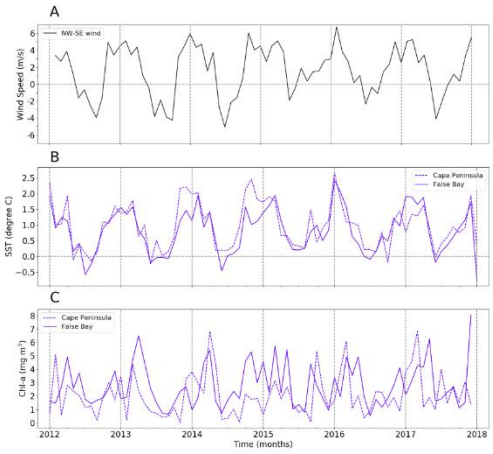

Figure 4: A time series of A) ERA-interim v-component wind speeds taken from a location offshore of False Bay (-34.5 S, 18.75 E) rotated along a northwest-southeast axis are compared to the difference between areas of wind shadow and upwelling for B) sea surface temperature (SST) in degrees Celsius and C) chlorophyll concentrations (Chl-a) in mg/m3 for False Bay (solid line) and off the Cape Peninsula (dashed line). A dashed grey vertical line indicates where the y-value is 0 and dashed horizontal lines indicate the years.

Acknowledgments:

Dr Alexis Mouche from IFREMER for the processing of SAR and ECMWF data.

References

Atkins, G. R. 1970. Winds and current patterns in False Bay. *Transactions of the Royal Society of South Africa*. 39(2): 139-148.

Dagestad, K.F., Horstmann, J., Mouche, A., Perrie, W., Shen, H., Zhang, B., Li, X., Monaldo, F., Pichel, W., Lehner, S. and Badger, M. 2013. Wind retrieval from synthetic aperture radar-an overview, in *4th SAR Oceanography Workshop (SEASAR 2012): Advances in SAR Oceanography*. European Space Agency.

Gründlingh, M. L., & Largier, J. L. 1991. Physical oceanography of False Bay: a review. *Royal Society of South Africa. Transactions TRSAAC*. 47(4/5).

Holt, B. 2004. SAR imaging of the ocean surface. *Synthetic aperture radar marine user's manual.* 25-80.

Jury, M. R. 1987. Aircraft observations of meteorological conditions along Africa's West Coast between 30–35 South. *Journal of climate and applied meteorology*. 26(11): 1540-1552.

Jury, M. R., Kamstra, F., & Taunton-Clark, J. 1985a. Diurnal wind cycles and upwelling off the northern portion of the Cape Peninsula in summer. *South African Journal of Marine Science.* 3(1): 1-10.

Jury, M. R., Kamstra, F., & Taunton-Clark, J. 1985b. Synoptic summer wind cycles and upwelling off the southern portion of the Cape Peninsula. *South African Journal of Marine Science*. *3*(1): 33-42.

Long, D. G., & Skouson, G. B. 1996. Calibration of spaceborne scatterometers using tropical rain forests. *IEEE Transactions on Geoscience and Remote Sensing.* 34(2): 413-424.

Lutjeharms, J. R. E., Olivier, J., & Lourens, E. 1991. Surface fronts of False Bay and vicinity. *Royal Society of South Africa. Transactions TRSAAC.* 47(4/5).

Pitcher, G. C., Figueiras, F. G., Hickey, B. M., & Moita, M. T. 2010. The physical oceanography of upwelling systems and the development of harmful algal blooms. *Progress in Oceanography*. 85(1-2): 5-32.

Seymour, S.A.M. 2019. Impact of Wind Driven Variability on Sea Surface Temperature and Ocean Colour in False Bay. MSc Thesis, Cape Town, University of Cape Town.

Shannon, L. V., Hennig, H. F. K. O., Shillington, F. A., Bartels, A., & Swart, D. H. 1991. Colour fronts in False Bay: origin, development and implications. *Royal Society of South Africa. Transactions TRSAAC.* 47(4/5).

Tomczak, M., & Godfrey, J. S. 2013. *Regional oceanography: an introduction*. Elsevier.

van Ballegooyen, R. 1991. The dynamics relevant to the modelling of synoptic scale circulations within False Bay. *Transactions of the Royal Society of South Africa*. 47(4): 419-432.

Wainman, C. K., Polito, A., & Nelson, G. 1987. Winos and subsurface currents in the False Bay region, South Africa. *South African Journal of Marine Science.* 5(1): 337-346.

Yelland, M., & Taylor, P. K. 1996. Wind stress measurements from the open ocean. *Journal of Physical Oceanography*. 26(4): 541-558.

Wang, Y., Castelao, R. M., & Yuan, Y. 2015. Seasonal variability of alongshore winds and sea surface temperature fronts in Eastern Boundary Current Systems. *Journal of Geophysical Research: Oceans*. 120(3): 2385-240.

Use of Satellite-Based NDVI Time Series to Detect Sugarcane Response to Climate Variability

Willard Zvarevashe[1*], Syamala Krishnannair[1] and Venkataraman Sivakumar[2]

[1]Department of Mathematical Sciences, University of Zululand, Private Bag X1001, KwaDlangezwa, 3886, South Africa
[2]Department of Chemistry and Physics, University of Kwazulu-Natal, Private Bag X54001, Durban, South Africa

*Corresponding author: wzvarevashe@gmail.com, *Tel: +27 633961263*

The Normalised Difference Vegetative Index (NDVI) is positively correlated to the yield in many crops. In recent times, it has been used to gauge the expected yield for crops. In this study, we have investigated the climate variability of sugarcane in a selected region in Felixton, Kwazulu-Natal province. The NDVI time series is decomposed to identify the seasonal, trend and random series. In order to find the periods and the impact of precipitation and temperature on the NDVI, a data adaptive method, ensemble empirical mode decomposition and synchronisation is applied. The results show that the seasonal rainfall and temperature variability has an influence on the NDVI. However, the rainfall variability has more direct impact. A non-linear regression model to find the effect of variability of precipitation, temperature, vapour pressure, cloud cover and soil moisture on the sugarcane growth is proposed.

Keywords: Precipitation, Temperature, Climate Change, Statistical Analysis, Sugarcane, Felixton

Introduction

The agriculture sector has not been spared from precipitation variability and warming climate. Driven by the growing concern about climate change impact on agricultural sector, there has been a growing interest on the subject. From 1990s onwards, there are a number of studies that have been carried out which mainly focused on the impact of climate variables such as air temperature, precipitation and CO_2 on the sugarcane yield (Jones & Singels, 2014; Linnenluecke et al., 2015; Miguez et al., 2018). Many of the studies used experimental analyses, agro-ecological models and process-based dynamic crop growth models and a few used statistical analysis (Kurma & Sharma, 2014; Jones & Singels, 2014; Zhao & Li, 2015; Linnenluecke et al., 2015). Therefore, there is need to carry out more statistical based analysis. Furthermore, a number of the statistical methods use yield or production as a basis of analysis of the impact of climate variability and do not look at the growth phase of the sugarcane.

The use of vegetation index to monitor crop progression and yield has increased over the years since it has been found to be positively correlated to yield for crops such as maize, soybean and sugarcane (Tarnavsky et al., 2008; Peralta, 2016; Sanches et al., 2018). One of the most commonly used index is Normalised Difference Vegetative Index (NDVI). Using this index, the stress on the leaves can be diagnosed through spectral responses. The NDVI can show nitrogen status and chlorophyll at micro level. Therefore, any limiting factors in the environment can be identified through the physiological stress in the leaves because of the variation in the concentration of nutrients (Lisboa et al., 2018).

The warming climate which has resulted in the increase of CO_2 has been found to have a positive correlation on the sugarcane by several studies (Jones & Singels, 2014; Zhao & Li, 2015; Linnenluecke et al., 2015). However, the variability of precipitation has had a negative impact on the growth of sugarcane (Kumar & Shamar, 2014). Sunlight, vapour pressure and soil moisture have all been found to have a significant influence on the plant growth (Zhao & Li, 2015; Miguez et al., 2018).

In this study, using the NDVI, the impact of climate variability on sugarcane of a selected region in Felixton, northern KwaZulu-Natal is shown. A data adaptive method, Ensemble Empirical Mode Decomposition and synchronisation is used to identify the variability at different time scales. A multiple non-linear regression model is proposed to find and predict the influence of air temperature, precipitation, vapour pressure, soil moisture and sunlight on NDVI.

Data and Method of Analysis

Study Area

A sugarcane production region located between -29ºS to -28.2ºS and 31.2ºE and 32.2ºE in Felixton, KwaZulu-Natal province was selected for the study (see Fig. 1). The Felixton area contributes about 10% of sugarcane yield in South Africa and has one of the largest mills in the country. In 2017/18 season about 1,7 million tons were crushed at the mill (SASA, 2019).

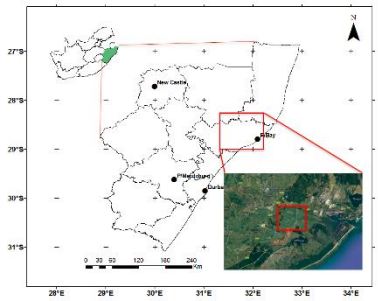

Figure 1: The location of study area in KwaZulu-Natal Province.

Data

In this study, monthly observations of precipitation, temperature, NDVI, vapour pressure, cloud cover and

soil moisture data for the period from 2000 to 2018 were used. For precipitation the Global Precipitation Climatology Project (GPCC) is used (Schneider et al., 2018). The GPCC, vapour pressure, cloud cover and soil moisture data are all freely available online on the Royal Netherlands Meteorological Institute (KNMI) website (https://climexp.knmi.nl) (Huang et al., 2014). The Global Historical Climatology Network version 2 and the Climate Anomaly Monitoring System (GHCN + CAMS) were used for temperature. The NDVI data set MOD13A3 version 6 was extracted from Appears Application (Didan, 2015). MOD13A3 version 6 provides Vegetation Index (VI) values at a per pixel basis at 500 meter spatial resolution and is taken every 16 days. The data set was averaged to find the monthly data.

Ensemble Empirical Mode Decomposition
Ensemble Empirical Mode Decomposition (EMD) is a data adaptive time-frequency representation method, which does not have a lot of underlying assumptions and it only requires that the data must consist of simple intrinsic oscillations (Huang et al., 1998). The NDVI is decomposed into intrinsic mode functions (IMFs) and a residual. The IMFs represents the original data at different time scale and the residual shows the general trend of the NDVI.

In order to investigate the variability of the NDVI at different time scales, the index was decomposed into different time scales using ensemble empirical mode decomposition. Five IMFs were derived and these were synchronised to temperature and precipitation and to identify the relationship between the time series.

Synchronisation of coupled oscillating systems means appearance of certain relations between their phases and frequencies (Rosenblum et al., 2001). Here, we use this concept in order to reveal the interaction between NDVI and the climatic variables precipitation and temperature. R package '*synchrony*' is used which measures phase synchrony between quasi-periodic times series (Cazelles & Stone, 2003).

Multiple Non-Linear Regression
Least squares method is used to find the linear and non-linear relationship between NDVI as dependent variable and independent variables; precipitation, temperature, vapour pressure, cloud cover and soil moisture. The general model is given by,

$$y = \beta_0 + \sum_{i=0}^{n} \beta_i f_i(x,t) \qquad (1)$$

Where y is the dependent variable NDVI, is error term, is a coefficient and is the independent climatic variables (Miguez et al., 2018).

Results and Discussion
Statistical Characteristics of the NDVI
Using the R package '*Forecast*' a simple additive statistical model was derived from the NDVI time series which is given by:

$$y_t = m_t + s_t + e_t \qquad (2)$$

where t=time, y_t is the observed time series, m_t is the trend series, s_t is the seasonal time series and e_t is the error term. The results of the decomposition using R-package '*Forecast*' is plotted in Fig. 2 below. The trend plot shows a dip in the NDVI around 2004 and 2015. The published results from Department of Agriculture, Fisheries and Forestry (DFF) shows that the yield for 2015/2016 dropped to 14,861 thousand tons from 17,756 thousand tons in 2014/2015 season (DAFF, 2016). This was mainly attributed to the drought that was experienced in South Africa (SASA, 2019).

Multi-scale Variability
Time series that are phase synchronised or locked exhibit a modal distribution with a prominent peak at a given phase difference, whereas unrelated times series are characterized by a uniform or diffuse distribution.

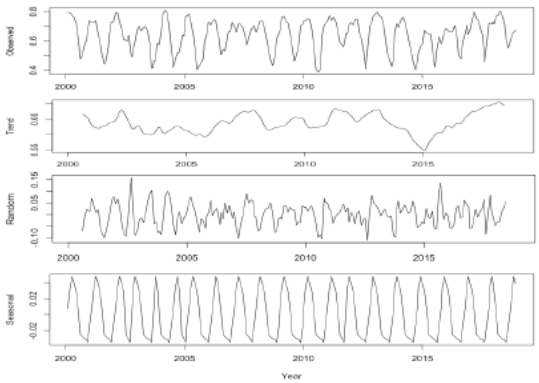

Figure 2. Plot of the decomposition of the NDVI time series into trend, random and seasonal series.

The results show that there is phase locking for IMF2 for precipitation since there is a clear peak (Fig. 3). IMF2 has a period of about 12 months which represents the annual period. However, there is weak coupling for all other IMFs. This shows that seasonal precipitation variability has a direct impact on the NDVI. This agrees with studies by Kumar & Shamar (2014) which showed the direct impact of rainfall variability. Fig. 4 reveals that temperature has an impact on the seasonal variability of NDVI, since a peak is also identified on the IMF2.

Impact of Environmental Variability
Multi non-linear regression was used to find the model of the environmental impact on the sugarcane growth. The percentage cloud cover was used to represent the sunlight. The model found is expressed as

$$y = 0.0826450 + 0.1790437x_1 - 0.0718855x_1^2 + 0.0038270x_2^2 + 0.0225784x_3 - 0.0063429x_4 + 1.4087915x_5$$

where x_1 is the precipitation, x_2 is temperature, x_3 is vapour pressure, x_4 is percentage cloud cover and x_5 is

soil moisture. The coefficients for vapour pressure, cloud cover and soil moisture were all found to be significant. The Pearson Coefficient of correlation for the model is . In order to evaluate the model a series of histogram are plotted and shown in Fig. 5.

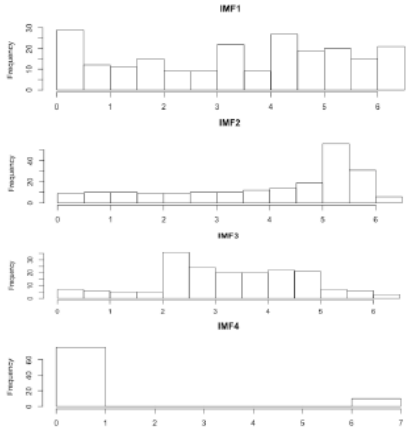

Figure 3. Histogram plot of synchronisation of NDVI and precipitation. The graphs show that there is clear peak for only IMF2 (second graph) which shows that there is phase locking.

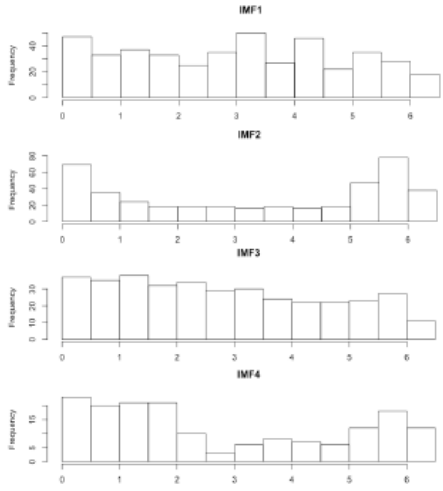

Figure 4. Histogram plot of synchronisation of NDVI and temperature. The graphs show a clear peak for only IMF2 (second graph) which shows that there is phase locking.

Residuals are values found from the difference between observed and expected values from the model. The points on the Residuals Vs Fitted plot are spread out and this shows that as a good model. The Normal Q-Q plot shows that the residuals are normally distributed, which is one of the assumptions that has to be met for a good model. The Scale-location plot is showing that the residuals are more spread out.

The Residuals vs Leverage plot helps to identify influential data points in the model. Points that are outside the dashed red Cook's distance line are influential on the model. The plot does not show any influential cases. Therefore, the model found to predict the plant growth using the cited external environmental factors.

The model provides further proof of the impact of climate variability as suggested by Zhao & Li (2015) which highlighted the direct influence of the environmental factors modelled here.

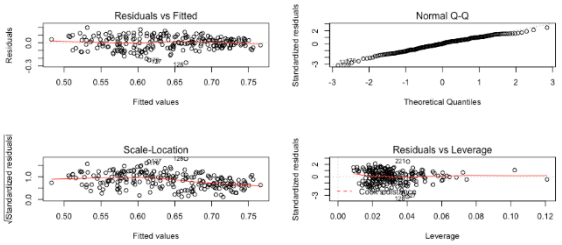

Figure 5. Residuals plots to evaluate the model. The plots are Residual vs Fitted (top left), QQ plot (top right), Scale-Location (bottom left) and Residuals vs Leverage (bottom right).

Conclusion

The NDVI was used to show the variability of the sugarcane at different time scales. This was done through decomposing the NDVI into different time scales and the resulted decomposed time series synchronised with precipitation and temperature. The variability of rainfall has more impact on the NDVI than temperature. A model which encompasses precipitation, temperature, vapour pressure, cloud cover and soil moisture was proposed.

Reference

Cazelles, B., & Stone, L. (2003). Detection of imperfect population synchrony in an uncertain world. *Journal of Animal Ecology*, 72(6), 953-968.

DAFF (Department of Agriculture, Forestry and Fisheries). (2016). A Profile Of The South African Sugar Market Value Chain. Pretoria. [Accessed online on 27 May 2019]. www.nda.agric.za.

Didan, K. (2015). *MOD13A1 MODIS/Terra Vegetation Indices 16-Day L3 Global 500m SIN Grid V006* [NDVI]. NASA EOSDIS Land Processes DAAC. doi: 10.5067/MODIS/MOD13A1.006

Huang, B., V.F. Banzon, E. Freeman, J. Lawrimore, W. Liu, T.C. Peterson, T.M. Smith, P.W. Thorne, S.D. Woodruff, and H.-M. Zhang. (2014): Extended Reconstructed Sea Surface Temperature version 4. NINO 3.4. doi:10.1175/JCLI-D-14-00006.1.

Huang, N. E., Z.Shen, S. R.Long, M. C. Wu, H. H. Shih, Q. Zheng, N. C. Yen, V. Tung, and H. H. Liu. (1998). 'The empirical mode decomposition and the Hilbert spectrum for nonlinear and non-stationary time series analysis,'. *Proceeding of the Royal Society of London*, Series A.

Jones, M. R., & Singels, A. (2014). A preliminary assessment of mid-century climate change

impacts on sugarcane production in South Africa. In *Proceedings of the Annual Congress-South African Sugar Technologists' Association* (No. 87, pp. 290-297). South African Sugar Technologists' Association.

Kumar, A., & Sharma, P. (2014). Climate change and sugarcane productivity in India: An econometric analysis. *Journal of Social and Development Sciences*, *5*(2), 111.

Linnenluecke, M. K., Nucifora, N., & Thompson, N. (2018). Implications of climate change for the sugarcane industry. *Wiley Interdisciplinary Reviews: Climate Change*, *9*(1), e498.

Lisboa, I. P., Cherubin, M. R., Lima, R. P., Cerri, C. C., Satiro, L. S., Wienhold, B. J., ... & Cerri, C. E. (2018). Sugarcane straw removal effects on plant growth and stalk yield. *Industrial crops and products*, *111*, 794-806.

Miguez, F., Archontoulis, S., & Dokoohaki, H. (2018). Nonlinear regression models and applications. *Applied statistics in agricultural, biological, and environmental sciences*, (appliedstatistics), 401-448.

Peralta, N., Assefa, Y., Du, J., Barden, C., & Ciampitti, I. (2016). Mid-season high-resolution satellite imagery for forecasting site-specific corn yield. *Remote Sensing*, *8*(10), 848.

Rosenblum, M., Pikovsky, A., Kurths, J., Schäfer, C., & Tass, P. A. (2001). Phase synchronization: from theory to data analysis. In *Handbook of biological physics* 4, 279-321. North-Holland.

Sanches, G. M., Duft, D. G., Kölln, O. T., Luciano, A. C. D. S., De Castro, S. G. Q., Okuno, F. M., & Franco, H. C. J. (2018). The potential for RGB images obtained using unmanned aerial vehicle to assess and predict yield in sugarcane fields. *International journal of remote sensing*, *39*(15-16), 5402-5414.

Schneider, U., Becker, A., Finger, P., Meyer-Christoffer, A., Ziese, M., (2018): GPCC Full Data Monthly Product Version 2018 at 0.25°: Monthly Land-Surface Precipitation from Rain-Gauges built on GTS-based and Historical Data. DOI: 10.5676/DWD_GPCC/FD_M_V2018_025.

SASA (South African Sugar Association). (2019). *Facts and figures.* [Accessed online on 29 May 2019]. www.sasa.org.za.

Tarnavsky, E., Garrigues, S., & Brown, M. E. (2008). Multiscale geostatistical analysis of AVHRR, SPOT-VGT, and MODIS global NDVI products. *Remote Sensing of Environment*, *112*(2), 535-549.

Zhao, D., & Li, Y. R. (2015). Climate change and sugarcane production: potential impact and mitigation strategies. *International Journal of Agronomy*, *2015*.

10. WEATHER FORECASTING AND CLIMATE MODELLING

Verification of meteorological variables simulated using different Planetary Boundary Layer (PBL) schemes in the WRF-ARW Model

Anzel de Lange*[1], Mogesh Naidoo[2], Rebecca M Garland[1,2], Liesl Dyson[1]

[1] Department of Geography, Geoinformatics and Meteorology, University of Pretoria
[2] Council for Scientific and Industrial Research (CSIR)

*Corresponding author: anzel.delange@up.ac.za, 082 779 8493

Numerical Weather Prediction models have for decades been used for the simulation of atmospheric variables, and frequently forms part of meteorological research. The accuracy of meteorological fields produced by these models are very much dependent on the choice of physical parameterization scheme. Any errors in simulations of meteorological fields will be passed on to subsequent processes (e.g. air quality models) and will have an effect on its outputs. Therefore, the realistic simulation of meteorological parameters is of utmost importance. The aim of the presented research is to evaluate the performance of Planetary Boundary Layer (PBL) schemes contained in the non-hydrostatic Advanced Research Weather Research and Forecasting (WRF-ARW) model. Four well-known and frequently used PBL schemes were investigated by conducting sensitivity experiments during June 2016 over the South African Highveld region. The simulations resulting from the different schemes were compared against each other, and statistically evaluated, by making use of observational meteorological data at five sites. Considering the performance indicators used, the MYNN schemes was identified as the best preforming in terms of temperature simulation. The MYNN scheme produced the smallest temperature biases at all but one site. Wind speed and direction were very well simulated by all schemes. Average wind speed biases for the period were small (<1ms^{-1}), and performance indicator results were similar between model setup. There is no clearly best-performing scheme in terms of wind speed and direction simulation, but MYJ produced slightly better results. Based primarily on performance when simulating temperature and wind speed, the two local schemes, MYJ and MYNN, are suggested as the preferred PBL schemes for the Highveld region during austral winter. Results from this study, and future research, will contribute to the establishment of a preferred PBL scheme in the WRF-ARW model, for use in the South African Highveld.

Keywords: South Africa, WRF-ARW model, PBL schemes, meteorological simulations, model evaluation

Introduction

Meteorological models have for decades been used for the simulation of atmospheric variables (Ritter et al., 2013), and frequently forms part of meteorological research. Numerical Weather Prediction (NWP) models are sensitive to a number of parameters, and uncertainties in the models can be attributed to physical parameterizations of atmospheric and surface processes, properties of the domain, and vertical and horizontal resolutions (Crétat et al. 2011; 2012; Crétat and Pohl, 2012).

Any errors in simulations of meteorological fields will be passed on subsequent processes (e.g. air quality models) and will have an effect on its outputs. Therefore, the accurate simulation of meteorological parameters, which are known to have an influence on pollution dispersion and chemistry, is of utmost importance (Gilliam et al., 2006). Planetary Boundary Layer (PBL) parameterization schemes are key when attempting to successfully simulate the boundary layer, and consequently, near surface air pollution concentrations levels. PBL schemes parameterize unresolved turbulent vertical fluxes of heat, momentum, and constituents such as moisture within the PBL and are responsible for the turbulent mixing throughout the atmosphere (Hu et al., 2010; Crétat et al., 2012).

In the presented research, we aim to evaluate the performance of PBL schemes in the Advanced Research Weather research and forecasting (WRF-ARW) model (Skamarock et al., 2008). Frequently used PBL schemes are investigated by conducting sensitivity experiments during a month in austral winter in the heavily polluted Highveld region of SA. Simulations are compared against each other, and evaluated by making use of observational (OBS) meteorological data.

Since accurately simulating meteorological processes, and subsequent pollution events, is of utmost importance in a region where South African National Ambient Air Quality

Standards (SA NAAQIS) are regularly exceeded, the results from this study contribute to the establishment of a preferred PBL scheme for use in South African Highveld region.

PBL and Surface Layer Schemes (SLS's)

The choice of PBL scheme does not only effect air quality related parameters like mixing height, but also has significant influence on other meteorological parameters (e.g. wind, temperature). Since different parameterization schemes in models affect the precision of simulated PBL height, and other meteorological parameters, it is necessary to validate these simulations with measurements (Korhonen et al. 2014).

The PBL schemes, their associated Surface Layer Schemes (SLS's), closure type, method for calculating PBL height, as well as threshold values, are listed in Table 1. These PBL schemes are popular internationally; with the YSU scheme being the most widely used, and the MYJ scheme following thereafter (Banks et al., 2016). However, MYNN2.5 and ACM2 are also popular. We consider two local closure schemes (MYJ and MYNN2.5) whereby a given point is only affected by vertical levels directly adjacent thereto, as well as two non-local schemes (YSU and ACM2), where multiple vertical layers can effect variables at a given point (Cohen et al. 2015).

Table 1. WRF-ARW PBL schemes, along with their associated SLS's, method of PBL height estimation and threshold, evaluated in this study (Adapted from Banks et al., 2016).

PBL scheme	Reference	Associated SLS	Closure	PBL height	Threshold
YSU	Hong et al., 2006	MM5 similarity	Non-local	Rib calculated from surface	0.00 (unstable) & 0.25 (stable)
MYJ	Janjic, 1994	Eta similarity	Local	Total Kinetic Energy (TKE) method	
MYNN2.5	Nakanishi and Niino, 2006	MYNN	Local	Total Kinetic Energy (TKE) method	
ACM2	Pleim, 2007	MM5 similarity	Non-local	Rib above neutral buoyancy level	0.25 (unstable & stable)

Model description and experimental design

a. Study region and case studies

The Highveld region (eastern Gauteng and western Mpumalanga) of SA experiences elevated pollution levels due to a variety of industrial and domestic emission sources.

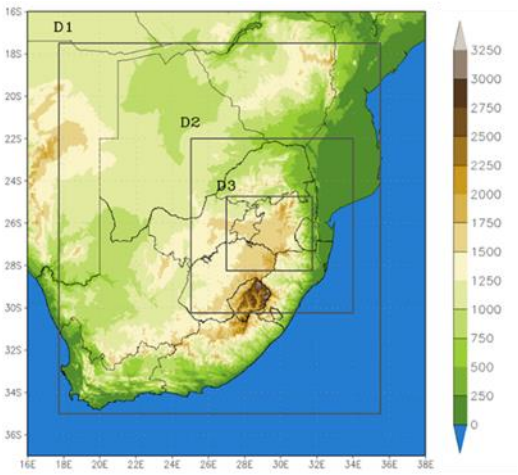

Figure 1. Domains for WRF-ARW model simulations over SA (D1=Domain 1, D2=Domain 2, D3=Domain 3).

Air pollutant levels in this region has led to the declaration of the Highveld Priority Area (HPA) (DEAT, 2007). Winters (JJA) in the HPA are characterized by clear skies, and cold and dry conditions (Lourens et al. 2011). Winters also exhibit stable atmospheric conditions; exacerbated by a semi-permanent high-pressure system over the region (Tyson and Preston-Whyte, 2000). Thus, the HPA often experiences poor atmospheric dispersion leading to the stagnation and accumulation of pollutants.

b. Model and domain

The WRF-ARW model requires two sets of external data in order to be successfully run for a real-world case. Static geographical land use and surface data (e.g. United States Geological Survey (USGS) topography) ranging from 10-min to 30-second resolutions for the 18 km, 6 km and 2km domains (Fig. 1) were used for surface parameters. Global model forecast data was used for initialization and boundary conditions; specifically, 6-hourly data at a 0.2° x 0.2° grid resolution from National Centers for Environmental Prediction (NCEP) Climate Forecast System Version 2 (CFSv2) (Saha et al., 2011).

Month-long WRF-ARW simulations, at a 1-hour temporal resolution, were used for model validation; this excludes the 15-day period allotted for model spin-up. The WRF-ARW model has multiple physics options, which require a choice of parameterization scheme. Besides the choice of PBL and SLS's, the simulations in this research were configured as follows; WRF single-moment six-class (WSM6) scheme for microphysics (Hong and Lim, 2004); Kain–Fritsch cumulus parameterization scheme (Kain, 2004); Rapid

Radiative Transfer Model scheme for longwave radiation (RRTMG-LW) and for shortwave radiation (RRTMG-SW) (Iacono et al., 2008), and the 4-layer NOAH unified land surface model (Tewari et al., 2004).

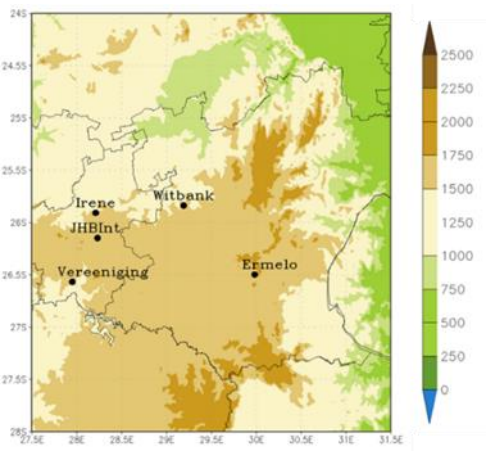

Figure 2. Location of the five sites chosen for this study in D3.

c. Meteorological observational data

Meteorological measurements originating from South African Weather Service (SAWS) stations were obtained, and data Quality Control (QC) applied. The five stations (Fig. 2) include three weather offices; Irene Ermelo, Johannesburg International Airport (JHB Int.), and two automated weather stations; Vereeniging and Witbank. Data availability for the period is more than 95% for all variables of concern; except wind speed and direction at Vereeniging (17.5%) which was not used in this analysis.

Table 2. Description and perfect score for the chosen statistical methods used to evaluate WRF-ARW model performance

Performance indicator	Description	Perfect Score
Pearson product-moment correlation coefficient (R)	Measure the degree of relationship between the observed and simulated data	1
Bias	Measures the sign and magnitude of the error of the simulations	0
Index of Agreement (IOA)	Standardized measure of degree of model prediction error	1
Mean Absolute Percentage Error (MAPE)	Measures the error of a simulation as a percentage (%)	0

d. Verification methods

Model evaluation in this study is focussed on the simulated wind speed, wind direction and temperature. Visual and statistical methods are used to evaluate the performance of the WRF-ARW model with different PBL scheme setups. Statistics used in the verification of the simulation results are summarized in Table 2.

Results and Discussion

a. Temperature

A summary of performance indicator results for temperature are presented in Table 3. The relationships between observed and simulated temperatures are strong (R>0.88) for all schemes at all sites. The weakest correlations are found at Vereeniging, this site also produced the largest bias for the period (2.47 °C, 3.38 °C, 1.74 °C and 2.50 °C for setup 1 to 4, respectively) as well as most inaccurate simulations (MAPE>100%).

In terms of correlation strength, IOA and MAPE, the site where simulations performed best was Irene. JHB Int. performed very well when considering bias, with all simulations producing average biases of less than 1°C for the period considered. Here we notice high agreement between observed and simulated temperature (IOA>0.95), and relatively low MAPE. Considering the data presented in Table 3, all schemes produce strong correlations and IOA. MAPE and biases are also quite similar between schemes, but MYNN does out-perform the other schemes with the smallest absolute biases and MAPE scores across the sites considered.

Table 3. Summary of performance indicator results for temperature simulated with the WRF-ARW model for different setups.

Station	Performance indicator	YSU (1)	MYJ (2)	MYNN (3)	ACM (4)
Ermelo	R	0.95	0.95	0.93	0.95
	Bias	1.01	1.22	0.44	1.05
	IOA	0.96	0.96	0.96	0.96
	MAPE	18.69	21.23	18.53	18.99
Irene	R	0.96	0.95	0.94	0.96
	Bias	-1.03	-0.15	-1.79	-1.05
	IOA	0.97	0.97	0.93	0.97
	MAPE	12.11	9.42	16.26	12.12
JHB Int.	R	0.92	0.93	0.91	0.92
	Bias	-0.12	0.64	-0.56	-0.06
	IOA	0.96	0.96	0.95	0.96
	MAPE	13.04	13.42	14.88	13.33
Vereeniging	R	0.93	0.88	0.92	0.93
	Bias	2.47	3.38	1.74	2.50
	IOA	0.91	0.85	0.93	0.91
	MAPE	129.32	185.79	103.72	129.03
Witbank	R	0.94	0.92	0.91	0.94
	Bias	0.95	1.58	0.26	0.98
	IOA	0.96	0.93	0.95	0.96
	MAPE	15.58	21.47	17.00	15.89

Average bias for the period is low for all sites except Vereeniging, where hourly temperature biases were high (greater than 2°C in most cases). In Fig. 3, average hourly temperature bias is plotted for one of the best-performing sites, JHB Int. It is clear that temperature bias is affected by the diurnal cycle. Most schemes tended to under-predict temperature during the night up to noon (approximately 12:00 SAST), and over-predicted temperatures as temperatures were cooling down (13:00 to 20:00 SAST). The one scheme that deviates from this patterns is MYJ.

This pattern of over and under-prediction is present at all sites to differing degrees, except at Ermelo and Vereeniging. Here, on average, temperatures are over-predicted by all model setups for most of the day. Considering absolute biases across all sites, MYNN is the best performing PBL scheme in terms of temperature simulation.

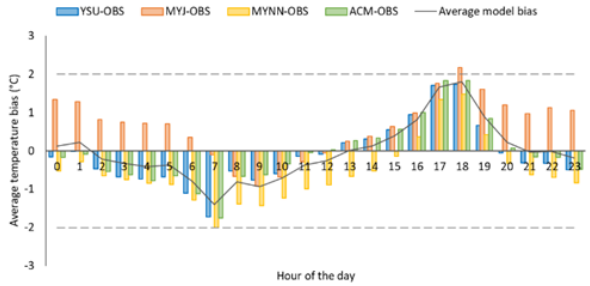

Figure 3. Hourly average temperature bias (Modelled – Observed temperature) at JHB Int. for all experimental setups.

b. Wind speed and direction

A summary of performance indicator results for wind speed is presented in Table 4. The relationships between observed and simulated wind speeds are relatively strong (R>0.65) for all schemes at all sites. Average wind speed biases are all less than +/- 1 ms^{-1} and mostly negative, except for Witbank where all model setups produced positive biases (meaning that the wind speeds were over-estimated by the model).

MAPE is less than 45% throughout model setups and sites. MAPE is low at Ermelo, indicating that the absolute percentage errors of the simulation are relatively low (< 30%). Considering the data presented in Table 4, there is no clearly best performing scheme in terms of wind speed simulations. In general, all schemes produce strong correlations, small biases and high IOA. The only performance indicator which truly differentiates between these schemes is MAPE, here MYJ shows slightly better results than the other schemes.

Table 4. Summary of performance indicator results for wind speed simulated with the WRF-ARW model for different setups.

Station	Performance indicator	YSU (1)	MYJ (2)	MYNN (3)	ACM (4)
Ermelo	R	0.72	0.73	0.75	0.72
	Bias	-0.32	-0.62	-0.52	-0.28
	IOA	0.84	0.82	0.84	0.84
	MAPE	29.70	29.64	27.92	29.49
Irene	R	0.72	0.71	0.68	0.69
	Bias	-0.33	0.15	-0.36	-0.21
	IOA	0.82	0.83	0.80	0.81
	MAPE	40.10	36.64	40.35	41.47
JHB Int.	R	0.67	0.67	0.66	0.65
	Bias	-0.23	-0.45	-0.30	-0.20
	IOA	0.81	0.78	0.79	0.80
	MAPE	34.22	32.46	35.16	35.32
Witbank	R	0.73	0.73	0.74	0.74
	Bias	0.38	0.21	0.40	0.33
	IOA	0.84	0.85	0.85	0.84
	MAPE	42.13	35.41	38.83	40.25

Wind roses for JHB Int. are plotted in Fig. 4. Wind roses assist in the identification of frequently occurring wind directions and speeds for each model setup. The dominant observed and simulated wind direction at JHB Int. is Westerly to North-Westerly (270° to 315°).

The occurrence of the dominant wind direction is very well simulated by all schemes at this site. The pattern of wind speed distribution is also well simulated by WRF-ARW. The only disagreement is the slight under-simulation of 2 to 4 ms^{-1} and over-simulation of 0.5 to 2 ms^{-1} winds.

Ermelo, Irene, and Witbank (not shown) also show good agreement between observed and simulated wind speed and directions. Hourly average biases were acceptable for this study (<1 ms^{-1}) for the majority of hours during the day as shown in Fig. 5 for Witbank.

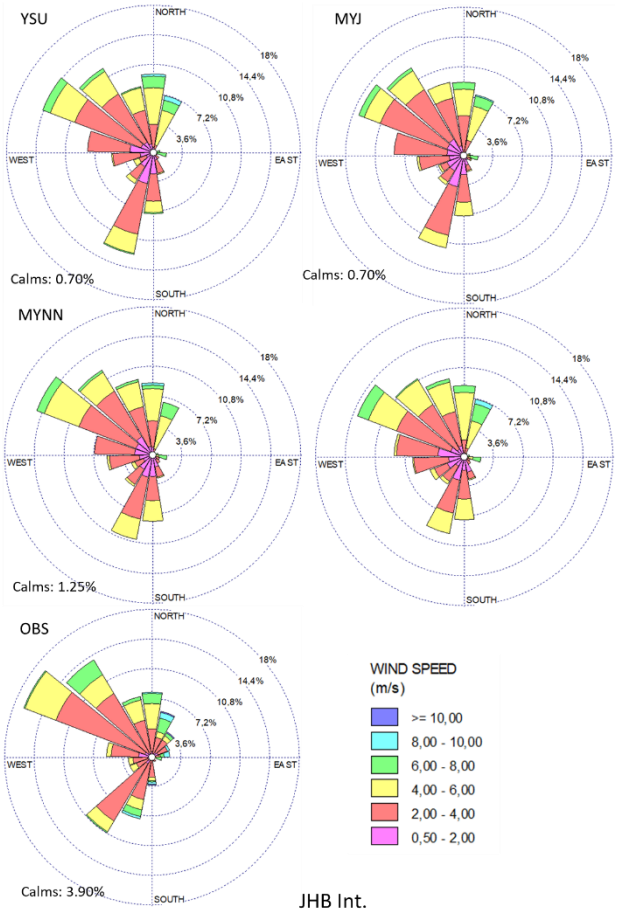

Figure 4. Wind roses at JHB Int. for the period.

Conclusions

Since experiment 1 to 4 were all configured in the same way, any variances in meteorological output can be attributed to the PBL and SLS's alone. The WRF-ARW model, with all tested configurations, reproduced the variation in temperature well for the chosen HPA sites.

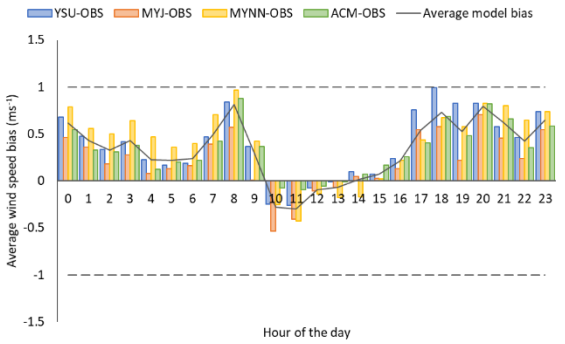

Figure 5. Hourly average wind speed bias (Modelled–Observed wind speed) at Witbank for all experimental setups.

Correlations between simulated and observed temperatures ranged between R=0.88 and 0.96, and indicated strong relationships. However, hourly biases are significant and largely affected by the diurnal cycle. When considering performance indicator results, MYNN was identified as the best performing scheme.

Wind speed and direction were very well simulated by all schemes. Hourly biases in wind speed were on average less than $1ms^{-1}$, and performance indicator results were very similar between model setups. Here, the scheme presenting slightly better results than the others, was MYJ.

The two local schemes (Table 1), MYJ and MYNN which uses the TKE method, are suggested as the preferred PBL schemes for the Highveld region during austral winter. These schemes likely represent stable conditions better as the coupling in the vertical is not as enhanced as in the summer.

Further research includes applying the presented method to a period in austral summer (November 2016), and a comparison of simulated upper-air profile data and PBL heights with atmospheric profiles, and PBL heights at Irene.

Acknowledgements
We would like to acknowledge SAWS for providing measured meteorological data for all sites for June 2016. We extend appreciation to the Laboratory for Atmospheric Studies (LAS) at the University of Pretoria. We also thank the CSIR Centre for High Performance Computing (CHPC) for the provision of computational resources.

References

Banks, R., Tiana-Alsina J., Baldasano J., Rocadenbosch F., Papayannis A., Solomos S. and Tzanis C. 2016, Sensitivity of boundary-layer variables to PBL schemes in the WRF model based on surface meteorological observations, lidar, and radiosondes during the HygrA-CD campaign. *Atmospheric Research*, 176-177:185-201.

Cohen A., Cavallo S., Coniglio M. and Brooks H. 2015, A Review of Planetary Boundary Layer Parameterization Schemes and Their Sensitivity in Simulating Southeastern U.S. Cold Season Severe Weather Environments. *Weather Forecasting*, 30:591-612.

Cre´tat J., Macron C., Pohl B. and Richard Y. 2011, Quantifying internal variability in a regional climate model: a case study for Southern Africa. *Climate Dynamics*, 37:1335–1356.

Crétat J., Pohl B., Richard Y. and Drobinski P. 2012, Uncertainties in simulating regional climate of Southern Africa: sensitivity to physical parameterizations using WRF. Climate Dynamics, 38(3–4):613–634.

Crétat J. and Pohl B. 2012, How Physical Parameterizations Can Modulate Internal Variability in a Regional Climate Model. *Journal of Atmospheric Science*, 69:714–724.

Department of Environmental Affairs and Tourism (DEAT). 2007, Declaration of the Highveld as Priority Area in terms of Section 18(1) of the National Environmental Management: Air Quality Act, 2004 (Act no.39 of 2004). Government Gazette No. 30518

Gilliam R., Hogrefe C. and Rao S. 2006, New methods for evaluating meteorological models used in air quality applications. *Atmospheric Environment*, 40(26):5073-5086.

Hong S. and Lim J. 2006, The WRF Single-Moment 6-Class Microphysics Scheme (WSM6). *Journal of the Korean Meteorological Society*, 42:129-151.

Hong S., Noh Y., and Dudhia J. 2006, A new vertical diffusion package with an explicit treatment of entrainment processes. *Monthly Weather Review*, 134:2318–2341.

Hu X., Nielsen-Gammon J.W., Zhang F. (2010). Evaluation of Three Planetary Boundary Layer Schemes in the WRF Model. J. *Journal of Applied Meteorology and Climatology*, 49:1831–1844.

Iacono M., Delamere J., Mlawer E., Shephard M., Clough S. and Collins W. 2008. Radiative forcing by long–lived greenhouse gases: Calculations with the AER radiative transfer models. *Journal of Geophysical Research*, 113:D13103.

Janjic Z. 1994, The Step–Mountain Eta Coordinate Model: Further developments of the convection, viscous sublayer, and turbulence closure schemes. *Monthly Weather Review*, 122:927–945.

Kain J. 2004, The Kain–Fritsch convective parameterization: An update. *Journal of Applied Meteorology*, 43:170–181.

Korhonen K., Giannakaki E., Mielonen T., Pfüller A., Laakso L., Vakkari V., Baars H., Engelmann R., Beukes J. P., Van Zyl P. G., Ramandh A., Ntsangwane L., Josipovic M., Tiitta P., Fourie G., Ngwana I., Chiloane K. and Komppula M. 2014, Atmospheric boundary layer top height in South Africa:

measurements with lidar and radiosonde compared to three atmospheric models. *Atmospheric Chemistry and Physics*, 14:4263-4278.

Lourens A., Beukes J., van Zyl P., Fourie G., Burger J., Pienaar J., Read C. and Jordaan J. 2011, Spatial and temporal assessment of gaseous pollutants in the Highveld of South Africa. *South African Journal of Science*, 107.

Nakanishi M. and Niino H. 2006, An improved Mellor–Yamada level 3 model: its numerical stability and application to a regional prediction of advecting fog. *Boundary Layer Meteorology*, 119:397–407.

Pleim J. 2007, A Combined Local and Nonlocal Closure Model for the Atmospheric Boundary Layer. Part I: Model Description and Testing. *Journal of Applied Meteorology and Climatology*, 46:1383–1395.

Ritter M., Muller M., Jorba O., Parlow E. and Sally Liu, L. 2013, Impact of chemical and meteorological boundary and initial conditions on air quality modeling: WRF-Chem sensitivity evaluation for a European domain. *Meteorology and Atmospheric Physics*, 119:59-70.

Saha S., Moorthi S., Wu X., Wang J., Nadiga S., Tripp P., Behringer D., Hou Y., Chuang H., Iredell M., Ek M., Meng J., Yang R., Mendez M. P., van den Dool H., Zhang Q., Wang W., Chen M. and Becker E. 2011, NCEP Climate Forecast System Version 2 (CFSv2) 6-hourly Products. Research Data Archive at the National Center for Atmospheric Research, Computational and Information Systems Laboratory.

Skamarock W., Klemp J., Dudhia J., Gill O., Barker D., Duda M., Huang X., Wang W. and Powers J. 2008, A Description of the Advanced Research WRF Version 3. NCAR Technical Note.

Tewari M., Chen F., Wang W., Dudhia J., LeMone M., Mitchell K., Ek M., Gayno G., Wegiel J. and Cuenca R. 2004, Implementation and verification of the unified NOAH land surface model in the WRF model. 20th conference on weather analysis and forecasting/16th conference on numerical weather prediction, 1–15.

Tyson P. and Preston-Whyte R. 2000, The weather and climate of Southern Africa. Oxford University Press Southern Africa, Cape Town, South Africa. ISBN: 978-0-195-71806-5.

Towards implementing a mesoscale hydrological model at SAWS: Initial results

Jaco de Wit[1], Christina M. Botai[1], Joel Botai[1,2], Kgalalelo Letshwiti[1]

[1]South African Weather Service, Private Bag X097, Pretoria 0001
[2]Department of Geography Geoinformatics and Meteorology, University of Pretoria

Corresponding author: jaco.dewit@weathersa.co.za, Tel: 012 367 6243

The South African Weather Service (SAWS) is implementing a hydrological model to be used for various hydrological research activities. The Mesoscale Hydrological Model (mHM) is an open-source grid-based model that has been tested and applied in various hydrological research activities. This contribution aims to present initial results of the mHM over two secondary catchments in the Vaal and Inkomati drainage regions. The Nash-Sutcliffe Efficiency (NSE) scores were computed and analysed for various streamflow points throughout each catchment. Initial model setups are being robust in estimating streamflow in the Inkomati catchment as opposed to the Vaal catchment. For the Inkomati catchment ~64% stations showed positive NSE scores meaning the model is a better estimate for streamflow than simply using the mean of the observed data at those points. In contrast the Vaal catchment showed worse results with only ~6% stations exhibiting a positive NSE score, albeit very small. This shows a clear discrepancy in the models ability to accurately model the streamflow of the two different catchments. The differences in model performance across the two catchments could be attributed to the inherent differences in e.g., the quality of input data sets and catchment hydrological processes. As a result, much more work and research is needed in understanding the various input data which feeds the model. This study shows the initial work towards an operational hydrological model that can firstly forecast streamflow and secondly monitor drought conditions throughout South Africa.

Keywords: Mesoscale Hydrological Model, streamflow forecast

Introduction

The South African Weather Service (SAWS) is a Meteorological Authority organization that is driven by three main pillars, namely the science, services and technology. The organization is tasked with providing weather and climate services to all the South African citizens, thereby providing solutions related to the top risks associated with extreme weather, natural disasters and climate action (SAWS Strategic Plan, 2019/2020-2023/24).

In order to effectively provide services to the water sector, SAWS is joining most of the national meteorological and hydrological services in terms of implementing and operationalising a hydrological modelling system. Now-a-days the requirements and demands for hydrological models have significantly increased due to the recurring natural hazards that result in extreme damages to property and infrastructure, including the loss of lives. This has led to significant improvements in the development of these models, e.g. from simple conceptual hydrological models (Burnash et al., 1973; Bergstrom, 1995) to more complex and spatially distributed models (Wood et al., 1997; Schulla and Jasper, 2007). These improvements also require an increase in computational power.

The SAWS is in the process of implementing the Mesoscale Hydrological Model (mHM) (www.ufz.de/mhm) system for hydrological research and applications. SAWS plans on achieving the first operational streamflow forecasts by the end of March 2020 for the preliminary catchments selected in this study.

The mHM is a spatially distributed open-source model developed by the Helmholtz Centre for Environmental Research – UFZ in Germany. This grid-based conceptual model has been tested in more than 30 basins in Germany, see for example, Samaniego et al. (2010). Other studies that have utilized the mHM for various hydrological research include Samaniego et al. (2011), Kumar et al. (2013), Thober et al. (2015), Samaniego et al. (2013), Baroni et al. (2017), Pechlivanidis et al. (2017), Visser-Quinn et al. (2019) and many others. SAWS decided on this model because of the robustness of the model in handling any time period and any spatial resolution. Since it is an open-source model there are little limitations in which input data can be ingested into the model as long as it complies with the temporal and/or spatial resolution of the catchment. At SAWS, the mHM will be used for, but not limited to, drought monitoring and prediction, streamflow and runoff forecasts.

Study area

Two catchments were identified for the first model implementation and evaluation of the first results. The two secondary catchments that were selected are: the C1 of the upper Vaal drainage region and X2 in the Inkomati drainage region, see Fig. 1. The C1 secondary catchment was identified because of the socio-economic activities in the Vaal region. For instance, there are numerous dams, mining, agricultural and industrial activities in the region which withdraws or deposits flow (depending on the

activities) from the rivers and are likely to alter the hydrological flow directly/indirectly. On the other hand, Inkomati drainage region exhibits more natural flow characteristics and it is less influenced by dams and other activities.

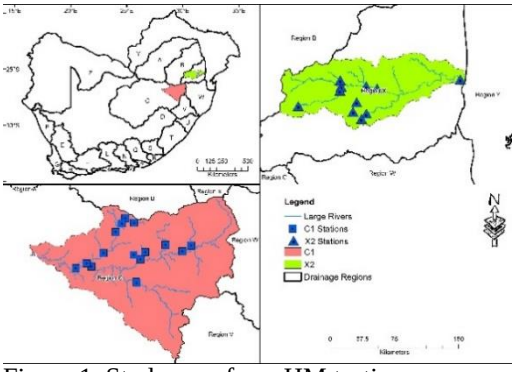

Figure 1. Study area for mHM testing

Data and Methodology

The mHM is an open-source grid-based hydrological model which is based on accepted hydrological conceptualizations (Kumar et al., 2013). The model is able to reproduce as accurately as possible not only observed discharge hydrographs at any point within a basin but also the distribution of soil moisture among other state variables and fluxes (Kumar et al., 2013). For the purpose of this study only discharge or streamflow is of interest out of the model outputs. There are no spatial or temporal resolution limitations to the model and as long as the resolutions are uniform for all the datasets the model can be set up. The model is driven by daily or hourly precipitation and temperature fields together with various morphological data (elevations, land cover, soil types and geological types) describing the local environment. The mHM model was set-up using the input data as described in Table 1 in the processed dataset column. The table also describes briefly the processing which had to be done on the original datasets to obtain the desired uniform spatial resolution. The processing involves re-projecting and resampling the data to a new spatial resolution.

The time period of historical meteorological information is defined by the period of historical streamflow observations. The C1 catchment has limited streamflow data in that area and thus limited the time period. In particular, C1 has 16 streamflow stations which have data from 1997 to 2018 (21 years). Thus for the C1 catchment the input meteorological data also had to reflect the same time period of 1997 to 2018. On the other hand, X2 catchment has a much larger streamflow dataset and has 11 streamflow stations with data from 1979 to 2018 (40 years). Similarly for the X2 catchment the meteorological data was also adapted to the time period of 1979 to 2018. The model uses these two time periods for each catchment respectively to compare the model estimated streamflow with the observed. Which is then used to optimise and calibrate a parameterization set which most accurately describe each catchment. The streamflow stations were identified and picked as such in order to obtain as many streamflow points as possible with at least 20 years' worth of data. Both catchments met the minimum model requirement of 20 years' worth of input data for the purpose of optimizing and parameterizing a catchment.

Table 1. Summary of original and processed datasets as per the model requirement: Orig. Res. = Original Resolution; Proc. Res. = Processed Resolution; prec. = precipitation; temp. = temperature; NLCM = National Land Cover Map; HWSD = Harmonized World Soil Database

Original dataset	Orig. Res.	Processed dataset	Proc. Res.
Hourly ERA5 reanalysis prec.	0.25^0	Daily accumulated prec	0.25^0
Hourly ERA5 reanalysis 2m temp.	0.25^0	Daily minimum, maximum and average temp	0.25^0
Global Multi-resolution Terrain Elevation Data (GMTED) 2010	7.5 arc-second (about 0.0021^0)	Hydrological reconditioned DEM; fill DEM; slope; aspect; flow direction; flow accumulation	0.0025^0
HWSD V1.2	1 km	Soil classes for catchments (% clay, % sand, bulk density, top soil and sub soil layers)	0.0025^0
DEA SA NLCM 1990 and 2013/14 – 35 classes	30 m	Reclassified land cover types as needed by the model	0.0025^0
DWAF streamflow gauge locations	No original, data had to be created	Streamflow points in raster format fitted on top of the flow accumulation lines	0.0025^0
Watershed of the catchment	No original, data had to be created	Computed the watershed area using the outflow streamflow point and the flow direction data	0.0025^0

Initially by default the mHM uses a default global parameterization set for every catchment which has been obtained by the developers of the model through global setups of the model. The model then estimates streamflow based on the input data and default global parameterization. After that the model compares the estimated streamflow with the historically observed streamflow. In order to fit model estimated streamflow to the observed data, the mHM and the parameter sets have to be recalibrated and optimized for each catchment. These calibrated and optimized parameterization sets result in calibrated and optimized streamflow variables for that catchment which then serve as the basis for evaluation of each catchment.

The predictive power of a hydrological model is mainly described by two efficiency coefficients namely the Nash-Sutcliffe efficiency coefficient

(NSE) and the Kling-Gupta efficiency coefficient (KGE). The NSE is the most popular for estimating the forecasting capabilities of a hydrological model (Kumar et al., 2013). The NSE is the main interest of this study and will serve as the main measure of how well the model can estimate streamflow at various points using all the morphological and meteorological data provided as inputs. The formula for NSE is described as per Eq. 1

$$NSE = 1 - \frac{\sum_{t=1}^{T}(Q_m^t - Q_o^t)^2}{\sum_{t=1}^{T}(Q_o^t - \overline{Q_o})^2} \qquad \text{Eq.1}$$

where is the mean observed streamflow, is the modelled streamflow and corresponds to the observed streamflow at time *t.* The NSE values can range from -∞ to 1, with NSE = 1 corresponding to a perfect match of modelled streamflow to the observed streamflow. An efficiency of 0 indicates that the model estimates are equal to the mean of the observed streamflow. It is suggested that threshold values of NSE >= 0.5 indicates sufficient model estimation quality.

There are four main optimization methods available and numerous objective functions which are implemented in the model. The Dynamically Dimensioned Search (DDS) optimization routine or method was used because DDS is known to improve the objective within a small number of iterations (Kumar et al., 2013). The other optimization functions are the Monte Carlo Markov Chain, simulated annealing and shuffled complex evolution. The objective function implemented was the "0.5*(NSE+lnNSE)" function which weighs both NSE and lnNSE by 50%. This function roughly fits high and low flows and describes the basic mean or median flow conditions.

Ideally the more iterations possible the better the optimization results for a catchment, but that also increases computational efforts. Both catchments were calibrated and optimized through 1000 iterations with the settings described above to keep consistency. The results were compared and analysed.

Results

The NSE scores which have been obtained by using the same input datasets and optimization method for the two different catchments C1 and X2 are shown in Table 2 and Table 3 respectively. It can be noted from Table 2 that most of the stations in catchment C1 exhibit negative NSE scores. The only exception is station 2 which has a very small positive NSE score of 0.02. As described in the methodology, an efficiency score of 0 (NSE = 0) indicate that the model estimates are as accurate as the mean of the observed data. This suggests that for station 2 the model estimates are as accurate as the mean of the observed data. All the other station locations show negative NSE scores suggesting that the model estimate is a worse predictor than simply using the mean of the observed streamflow. Stations 14, 15 and 16 show very small negative NSE scores which can also be interpreted as close or similar to the mean. This gives us an indication that the model is not accurate in estimating the real flow in this area.

Table 2. Catchment C1 station NSE scores.

ID	Station Name	Lat	Lon	NSE
1	C1H002 Sterkfontein	29.2	-27.2	-31.4
2	C1H004 Branddrift	29.0	-26.6	0.02
3	C1H005 Welbedacht	29.3	-26.9	-72.5
4	C1H006 Rietvley	29.5	-26.8	-7.7
5	C1H007 Goedgeluk	29.7	-26.8	-3.8
6	C1H008 Elandslaagte	28.9	-26.9	-72.2
7	C1H012 Nooitgedacht	28.8	-27	-7.1
8	C1H015 Sterkfontein	29.2	-27.2	-12.5
9	C1H017 Villiers	28.6	-27	-23.1
10	C1H019 Grootdraai	29.3	-26.9	-2.4
11	C1H020 Grootdraai	29.2	-26.9	-28.2
12	C1H027 Tweefontein	29.8	-26.8	-31.3
13	C1H030 Wolwfontein	28.7	-27	-22.9
14	C1H033 Secunda	29.2	-26.5	-0.03
15	C1H041 Evander	29.1	-26.5	-0.05
16	C1H042 Embalenhle	29.1	-26.6	-0.03

The results from catchment X2, which are shown in Table 3, indicate more positive NSE scores than negative. The catchment X2 produced 7 positive NSE scores, which is more than half of the station locations. The negative scores are also very small however, much smaller than that compared with catchment C1. Four of the station locations depict NSE scores larger than 0.1 which gives the indication that the model estimates are becoming better than the mean of the observations. One significant result is station 5 which is at the 0.5 NSE threshold. These results indicate that the model is much better in estimating streamflow for X2 than it is for C1, given the same input datasets.

Table 3. Catchment X2 station NSE scores.

ID	Station Name	Lat	Lon	NSE
1	X2H016 Tenbosch	-25.4	31.9	0.1
2	X2H006 Karino	-25.5	31.1	-0.01
3	X2H013 Montrose	-25.4	30.7	-0.1
4	X2H005 Boschrand	-25.4	30.9	0.04
5	X2H014 Sudwalaskraal	-25.4	30.7	0.5
6	X2H015 Lindenau	-25.5	30.7	-0.1
7	X2H012 Geluk	-25.7	30.3	0.01
8	X2H024 Glenthorpe	-25.7	30.8	-0.2
9	X2H010 Bellevue	-25.6	30.9	0.2
10	X2H031 Bornmans	-25.7	30.9	0.2
11	X2H008 Sassenheim	-25.8	30.9	0.1

These results were obtained using very basic physical classifications parameters like elevation, land use, soil and geomorphology for South Africa. Improving and properly classifying the various physical classifications would improve the models ability to estimate streamflow over South Africa. Running the optimization routines for a much larger set of iterations would also improve the parameterization and calibration sets the model uses for each catchment. This however will take much more time and computational efforts. All of these ideas will form part of future work towards improving and operationalizing the mHM model.

Conclusion

The X2 catchment showed good results with 7 out of 11 stations resulting in positive NSE scores. Four of those stations exhibit more significant NSE scores. In contrast, the C1 catchment showed mostly negative NSE scores with only 1 very slightly positive score. The results which were obtained using a very basic optimization and calibration methodology and using the same input datasets indicate that the mHM model is better in estimating streamflow for X2 than it is for C1. This also gives an indication that the mHM model is much better in estimating streamflow for a catchment which exhibits more natural flow characteristics as compared to one which is more influenced by human or socio-economic activities. These results demonstrate the very basic capabilities of the mHM model as well as the initial stages towards building an operational hydrological forecasting and drought monitoring model. Much more work is needed in many aspects of the model implementation in a bid to accurately set up catchments throughout South Africa.

References

SAWS Strategic Plan for 2019/20 – 2020/24 (Internal document)

Visser-Quinn, A., Beevers, L., Collet, L., Formetta, G., Smith, K., Wanders, N., Thober, S., Pan, M., and Kumar, R. (2019). Spatio-temporal analysis of compound hydro-hazard extremes across the UK. Advances in Water Resources, 130: 77-90.

Samaniego, L., Bárdossy, A. and Kumar, R. (2010) Streamflow prediction in ungauged catchments using copula-based dissimilarity measures. Water Resour. Res. 46, W02506.

Samaniego, L., Kumar, R and Jackisch., C. (2011) Predictions in a data-sparse region using a regionalized grid-based hydrologic model driven by remotely sensed data. Hydrological Research

Kumar, R., Samaniego, L., & Attinger, S. (2013). Implications of distributed hydrologic model parameterization on water fluxes at multiple scales and locations. Water Resources Research, 49(1), 360–379. doi:10.1029/2012WR012195

Samaniego, L., Kumar, R., & Zink, M. (2013). Implications of Parameter Uncertainty on Soil Moisture Drought Analysis in Germany. Journal of Hydrometeorology, 14(1), 47–68. doi:10.1175/JHM-D-12-075.1

Thober, S., Kumar, R., Sheffield, J., Mai, J., Schaefer, D., & Samaniego, L. (2015). Seasonal Soil Moisture Drought Prediction over Europe Using the North American Multi-Model Ensemble (NMME). Journal of Hydrometeorology, 16(6), 2329–2344

Baroni, G., Zink, M., Kumar, R., Samaniego, L., & Attinger, S. (2017). Effects of uncertainty in soil properties on simulated hydrological states and fluxes at different spatio-temporal scales. Hydrology and Earth System Sciences, 21(5), 2301–2320. doi:10.5194/hess-21-2301-2017

Pechlivanidis, I.G., Arheimer, B., Donnelly, C., Hundecha, Y., Huang, S., Aich, V., Samaniego, L., Eisner, S. and Shi, P., (2017): Analysis of hydrological extremes at different hydro-climatic regimes under present and future conditions. Climatic Change, 141(3), pp.467-481

Burnash, R., Ferral, R., McGuire, R.M. (1973), A generalized streamflow simulation system: Conceptual modelling for digital computer. U.S. Dept. of Commerce, National Weather Service, and State of California, Dept. of Water Resources

Bergström, S. (1995), The HBV model. In: Singh, V.P., Ed., Computer Models of Watershed Hydrology, Water Resources Publications, Highlands Ranch, Colorado, 443-476.

Wood, E.F., Letternmaier, D., Liang, X., Nijssen, B., Wetzel., S.W. (1997), Hydrological modeling of continental-scale basins. Annu. Rev. Earth Planet. Sci., 25: 279-300

Schulla, J., Jasper, K. (2007), Model description WaSiM-ETH (Water Balance Simulation Model ETH). ETH Zurich, Zurich, Switzerland.

Seasonal cycle attributes of S2S predictive skill over the westerly and easterly weather regime regions of southern Africa

Christien J. Engelbrecht[1,2]

[1]South African Weather Service, Centurion, South Africa
[2]Department of Geography, Geoinformatics and Meteorology, University of Pretoria, Pretoria, South Africa

Corresponding author:

The subseasonal deterministic prediction skill of atmospheric circulation relevant to the southern African region is assessed by utilizing daily reforecasts of the NCEP CFSv2 model. The predictive skill is assessed over the westerly and easterly wind regime regions respectively. Over the westerly wind regime region, skill in predicting weekly mean circulation is the highest during the summer months, whereas over the easterly wind regime region, the lowest skill is apparent towards mid-summer.

Keywords: Subseasonal prediction, southern Africa, weather regimes

Introduction

Weather and climate predictions on the subseasonal timescale have the potential to serve decision making in sectors that are of economic and societal importance. Over southern Africa, the agricultural sector can in particular benefit from useable subseasonal predictions, as the time scale of some critical operational decisions that need to be made falls within this time scale. Disaster management is another sector that can benefit from subseasonal forecasts.

Subseasonal weather prediction is relatively new and an almost unexplored field for the southern African region (Fig. 1). In this study, the predictability of low-level atmospheric circulation that affect the weather and climate of southern Africa is assessed. The weather and climate over southern Africa are influenced by weather systems embedded in both the easterly (e.g. tropical lows, tropical cyclones) -and westerly (e.g. cold fronts, ridging high pressure systems) wind regimes (e.g. Taljaard 1985; Reason and Rouault 2005; Malherbe et al. 2012) as well as by interactions across these weather regimes such as tropical-temperate troughs (e.g. Hart et al. 2010). The approach of assessing the predictive skill over regions that are representative of the westerly -and easterly wind regimes is followed for comparison purposes of the seasonal cycle of predictive skill over these two distinct weather regimes.

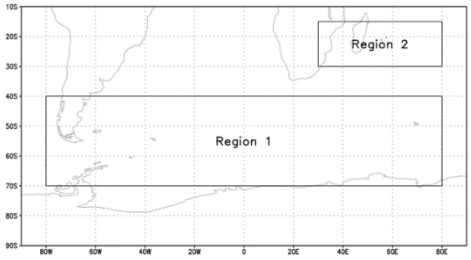

Figure 1. Region 1 and Region 2 is representative of the westerly -and easterly wind regime regions respectively.

Data and Methodology

The 850 hPa geopotential height hindcasts with a daily start date over the period 1999 to 2010 from the fully coupled National Centers for Environmental Prediction (NCEP) Climate Forecast System, version 2 (CFSv2) are used in this study (Saha et al, 2014). This hindcast dataset is available from the S2S ECMWF data portal and consists of four ensemble members per day, initialized at 6-hourly intervals. A deterministic assessment is performed here, and the ensemble mean is therefore used to calculate a 7-day moving average over the full period of 1999 to 2010 from which the Anomaly Correlation Coefficient (ACC) is calculated and presented as a domain average for Region 1 and 2 (Fig. 1). To assess the seasonal cycle of the predictive skill for these two weather regimes, the ACC is presented as monthly means. The climatological fields required by the ACC, are functions of both the lead time and start date. The moving average approach based on daily start dates results in forecasts with lead times from 1 out to 21 days. Here, the assessment of the week 2, 3 and 4

forecasts are shown as represented by the 8, 15 and 21 day lead time forecasts.

Results and Discussion

The ACC for both the westerly -and easterly wind regime regions for week 2, 3 and 4 forecasts is shown in Fig. 2. As expected, the ACC is in general higher for the easterly wind regime region. In all of the months and for all three lead times with the exception of the week 3 forecast for January, the ACC is exceeding 0.6. In contrast, the ACC never exceeds 0.6 over the westerly wind regime region. Whereas there is a striking deterioration between the week 2 and week 3 forecast over the westerly wind regime region, this is not the case over the easterly wind regime region.

In terms of the seasonal cycle of predictive skill, the summer months exhibit higher skill over the westerly wind regime region, in particularly for the week 3 and 4 forecasts. The week 2 forecast shows different behaviour during the winter months compared to the week 3 and 4 forecasts with no clear fall in the ACC for the mid-winter months. Over the easterly wind regime region, a seasonal cycle in the skill is also evident. Here, the month of January seems to have the lowest predictive skill of 850 hPa weekly mean circulation, in particularly for the week 3 forecast. In general, for this region, predictive skill seem to peak during the transitioning seasons.

Conclusions

The deterministic skill of weekly averaged 850 hPa geopotential height circulation has been assessed over a period of twelve years (1999 to 2010) by making use of CFSv2 hindcasts. The seasonal cycle in skill has been explored over two regions that is representative of the westerly -and easterly wind regime. The general lower skill during the winter months over the westerly wind regime region (in particular for the week 3 and 4 forecasts) is likely due to deeper extratropical cyclones during that time of the year, whilst the relatively better skill for the week 2 forecast can quite likely be attributed to the initial conditions still having an influence on the downwind weather systems. The general high ACC over the easterly wind regime region for the week 2, 3 and 4 forecasts are an indication that skill scores where the reference forecast is climatology is not the best skill score to be used over tropical regions. A skill score where the reference forecast is based on persistence might be more useful. Even so, the skill as shown by the ACC, provides some insight into the seasonal cycle of skill.

.

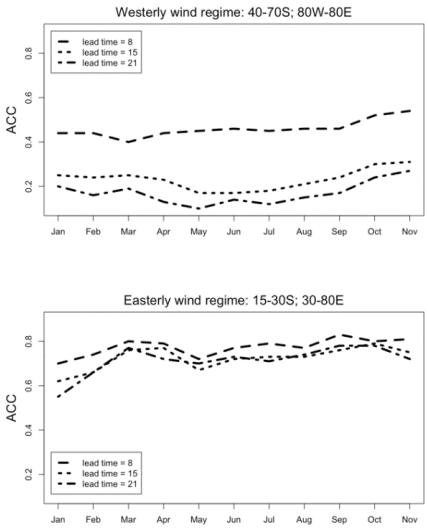

Figure 2. Monthly mean ACC for Region 1 and Region 2 for week 2 (lead time = 8 days), week 3 (lead time = 15 days) and week 4 (lead time = 21 days) 850 hPa geopotential height forecasts.

Acknowledgements

This work is part of the ACyS-ACCESS project that is funded by the NRF

References

Hart, N.C.G., Reason, C.J.C. and Fauchereau, N. (2010) Tropical-extratropical interactions over Southern Africa: three cases of heavy summer season rainfall. Monthly Weather Review 138:2608-2623

Malherbe, J., Engelbrecht, F.A., Landman, W.A. and Engelbrecht, C.J. (2012) Tropical systems from the southwest Indian Ocean making landfall over the Limpopo River Basin, southern Africa: a historical perspective. International Journal of Climatology 32: 1018-1032, doi:10.1002/joc.2320

Reason, C.J.C. and Rouault, M. (2005) Links between the Antarctic Oscillation and winter rainfall over western South Africa. Geophysical Research Letters 32: L07705. doi:10.1029/2005GL022419

Saha, S. and co-authors. (2014) The ncep climate forecast system version 2. Journal of Climate 27(6): 2185-2208, doi:10.1175/JCLI-D-12-00823.1

Taljaard, J.J. (1995) Atmospheric circulation systems, synoptic climatology and weather phenomena of South Africa. Part 2: atmospheric circulation systems in the South African region. South African Weather Bureau, Technical paper 28

Stratospheric Ozone time series prediction and forecasting using LSTM and Hybrid ARIMA-ANN approach

N. Mbatha[1], H. Bencherif[2,3], V. Sivakumar[3] and T. Mkololo[3,4]

[1]University of Zululand, Department of Geography, KwaDlangezwa, 3886, South Africa
[2]Laboratoire de l'Atmosphère et des Cyclones, UMR 8105 CNRS, Université de la Réunion, Météo-France, Réunion, France
[3]School of Chemistry and Physics, Discipline of Physics, University of KwaZulu Natal, Durban, South Africa
[4]South African Weather Service, Global Atmosphere Watch Station, P.O. Box 320, Stellenbosch, 7599

Corresponding author:

The prediction and forecasting of stratospheric ozone is of great significance as it can explain the dynamics of the slowly self-recovering ozone layer in the stratosphere. The data used in this study is a the stratosphere averaged ozone measured over three sites operating in the framework of the Southern Hemisphere Additional Ozonesodes (SHADOZ), namely Irene (25.88°S, 28.22°E), Nairobi (1.29°S, 36.82°E), and Reunion Island (21.11°S, 55.53°E), by the Sounding of the Atmosphere using the Broadband Emission Radiometry (SABER) instrument on-board the Thermosphere-Ionosphere-Mesosphere Energetic and Dynamics satellite (TIMED). In general, there is a 0.18%/year ozone layer recovery at Irene and Reunion Island sites, while Nairobi recorded nearly the same rate, i.e., 0.2%/year ozone layer recovery. Three data-driven forecasting models namely the autoregressive integrated (ARIMA) and artificial neural networks (ANN) Hybrid, long short-term memory networks (LSTM), and discrete wavelet transform (DWT) denoised LSTM (WD-LSTM) were used here. The results indicate that the WD-LSTM deep learning method achieved the best forecast, compared to other models.

Keywords: Ozone, forecasting, LSTM, ARIMA, NN

Introduction

A number of atmospheric chemistry research groups have been closely monitoring the slow self-recovery of stratospheric ozone for some time. The difficulty about this slow recovery is that there is nothing that human beings can do as this recovery process depends solely on self-recovery of ozone. And also, the recovery of the stratospheric ozone layer is strongly dependent on the continued decline in the atmospheric concentration of ozone-depleting gases such as chlorofluorocarbons (CFC) (Rigby *et al*., 2019). However, it is concerning that a recent paper by Rigby *et al*., (2019) has reported that the recent slowing down of the stratospheric ozone layer recovery is largely associated to the continual emission of trichlorofluoromethane (CFC-11) in the northeast China.

The suggestion of a decrease in stratospheric ozone recovery and the continuation of the ozone decline in the lower stratosphere have been presented by other authors (e.g. Ball *et al.,* 2018). A study by Ball *et al*. (2018) indicated that while stratospheric ozone layer has stopped declining across the globe, there is no clear increase observed at latitudes between 60°S and 60°N outside the polar region (60-90°). Therefore, it is for this reason that models that can predict and also forecast the dynamics of the stratospheric ozone are imperative.

The performance of linear models such as Autoregressive Integrated Moving Average (ARIMA) and non-leaner models such as Artificial Neural Networks (ANN) autoregressive in time series forecasting has strengthened its popularity (e.g. Khandelwal *et al*., 2015). But, a hybrid model which is built by combining the two methods (leaner and non-leaner) has been shown to produce better results than the individual models (e.g. Khandelwal *et al*., 2015). Moreover, long short-term memory networks (LSTM) Recurrent Neural Networks (RNNs) which was proposed by Hochreiter and Schmidhuber (1997) has been proven to be one of the improved variants of RNNs which can learn the information contained in time series data more directly. Therefore, in this study, we assess the performance of the hybrid ARIMA-ANN and LSTM models in predicting stratospheric ozone amounts. The study also proposes the use of discrete wavelet transform (DWT) for denoising the time series before the use of the LSTM model.

The rest of the paper is outlined as follows. The next section describes the instruments and data used in this study, and an overview of models used here. This is followed by empirical results and the conclusion in the final section.

Instrument and Method

In this study, we opted to use stratospheric ozone mixing ratio data averaged in the 20-50 km altitude range from ozone profiles as measured by the Sounding of the Atmosphere using the Broadband Emission Radiometry (SABER) instrument on-board the Thermosphere-Ionosphere-Mesosphere Energetic and Dynamics (TIMED) satellite. The data used in this investigation covers 17 years (January 2002 – December 2018) of SABER overpasses (within ±5° in latitude and longitude shift) for three station, namely Irene (25.88°S, 28.22°E), Nairobi (1.29°S, 36.82°E), and Reunion Island (21.11°S, 55.53°E). This locations were chosen because they are part of the Southern Hemisphere Additional Ozonesondes (SHADOZ) sites operated by National Aeronautics and Space Administration (NASA) Goddard Space Flight Center (GSFC). More details about the SABER instrument and TIMED satellite can be found in other studies (e.g. Remsberg *et al*., 2003; Bègue *et al*., 2017). For the purpose of this research, the data was averaged to monthly means. The map of the study area is shown in Fig. 1.

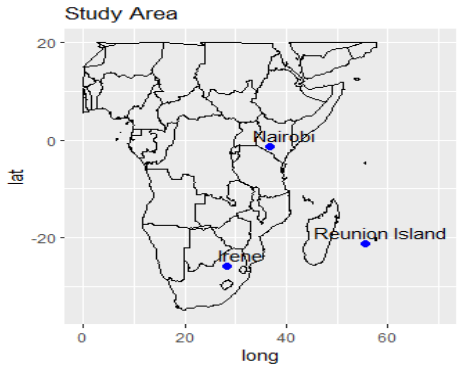

Figure 1. Map showing the location of SHADOZ stations used in this study.

One popular method that enables one to detect both linearity and nonlinearity during time series prediction and forecasting is to develop a hybrid ARIMA-ANN model (e.g. Zhang *et al*., 2003; Khandelwal *et al*., 2015). ARIMA model is a linear model that is based on the fundamental principles that the future values of the time series are produced from a linear function of the previous values and white noise terms. It assumes that the time series can be stationarized by transformations such as differencing, where the order () is classified as follows:

- is the number of autoregressive terms
- is the number of non-seasonal differences
- is the number of lagged forecast errors in the prediction equation

A more detailed mathematical explanation of the ARIMA model can be found in other studies (e.g. Zhang *et al*., 2003; Khandelwal *et al*., 2015). On the other hand, autoregressive ANNs are an alternative to ARIMA for time series forecasting because they can estimate any nonlinearity up to any desired degree of accuracy (Khandelwal *et al*., 2015). In this study, we opted to use a single hidden layer feedforward ANN with one output node, which is commonly used in forecasting. More details about this type of ANN can be found in a study by Zhang *et al*., (2003).

This study also utilizes a deep learning Recurrent Neural Networks (RNNs) method called long short-term memory networks (LSTM). In general, RNNs are improved multilayer networks that have internal connections that can pass the processed signal from the current moment to the future. More details about RNNs can be found in a study by Giles *et al*. (2001). LSTMs are family of RNNs that are often used with deep neural networks. In summary, as illustrated by Fig. 2, a LSTM is made up of three gates, a forget gate (*f_t*) which controls if/when the context is forgotten, an input gate (*i_t*) which controls if/when a value should be remembered by the context, and an output gate (*o_t*) which controls if/when the remembered value is allowed to pass from unit. This exclusive structure of the LSTM is capable to effectively solve the problem of gradient loss and gradient explosion problem during the training procedure (Hochreiter and Schmidhuber, 1997).

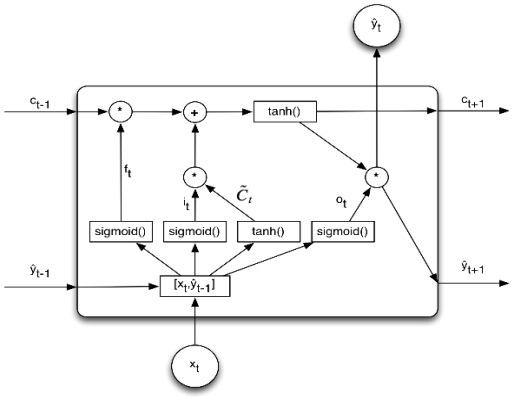

Figure 2. The structure of the long short-term memory (LSTM) unit.

In a mathematical form, the above diagram (Fig. 2) can be represented in this form:

$$f_t = S\left(W_f \cdot [\hat{y}_{t-1}, x_t] + b_f\right) \quad (1)$$
$$i_t = S(W_i \cdot [\hat{y}_{t-1}, x_t] + b_i) \quad (2)$$
$$\tilde{C}_t = tanh(W_C \cdot [\hat{y}_{t-1}, x_t] + b_C) \quad (3)$$
$$C = f_t \cdot C_{t-1} + i_t \cdot \hat{C}_t \quad (4)$$
$$o_t = S(W_o \cdot [\hat{y}_{t-1}, x_t] + b_o) \quad (5)$$
$$\hat{y}_t = o_t \cdot tanh(C_t) \quad (6)$$

In the set of equations in Eq. (1,2,3,5) are the corresponding weight matrix connecting the signal , and represents the element level multiplication. and are the signal activation function and the state of cell, respectively.

For the purpose of this study, we first apply the LSTM in the original time series as it is, and then applied the LSTM in a denoised time series in order to investigate whether denoising the time series does improve the model performance. The denoising process was performed by employing the discrete wavelet transform (DWT). A detailed explanation about the DWT and its application in the preparation of a signal before it is pushed into an LSTM RNNs is explained by Liu *et al*., (2019). For the purpose of this study, we label the LSTM that uses the DWT denoised signal a WD-LSTM, while the one which did not use the denoising step is called LSTM. For both LSTM models, the time series is first normalized using the maximum and minimum (max/min) method before it is pushed into the LSTM, and the LSTM output is denormalized using the same method at the end. The flow chart indicating steps which are taken when creating the WD-LSTM is shown in Fig. 3.

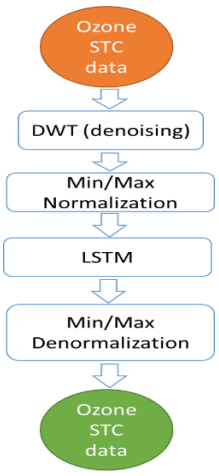

Figure 3. The architecture of the WD-LSTM model.

Results

As mentioned above, the experiment was conducted with stratospheric averaged ozone mixing ratio data measure over three sites, namely Irene, Nairobi, and Reunion Island. The time series of stratospheric ozone are depicted in Fig. 4. In general, stratospheric ozone seems to be stronger in lower latitudes (Nairobi) compared to the tropics (Irene and Reunion Island). By using the Theilsen method, it was observed that the stratospheric ozone layer is recovering by 0.20%/years over Nairobi since 2002, while the recovery is 0.18%/years for both Irene and Reunion Island sites, respectively.

Three different forecasting models were used in the data set in Fig. 4. The LSTM system used here is a Python TensorFlow LSTM system which was run in a miniconda. And, the hybrid ARIMA-ANN was designed using the Forecasting: Principle and Practice (fpp2) package in R. For denoising, this study used a Daubechies (db8) wavelet family in the PyWavelets wavelet transform software for Python. This family of wavelets was selected because it performed better than

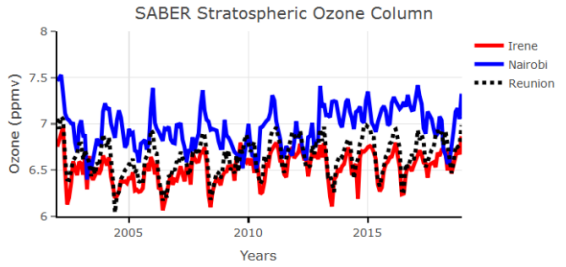

others in terms of the model accuracy.

Figure 4. Stratospheric ozone for Irene (red), Nairobi (blue), and Reunion Island (black dashed) sites.

Fig. 5 (a-c) depicts the actual testing datasets (black line) and its forecasts (black dashed line: LSTM, blue line: WD-LSTM, and red line: ARIMA-ANN) for Irene (a), Nairobi (b), and Reunion Island (c) stratospheric ozone. It is notable that the three models give different forecast results of the monthly mean ozone data series from the three study stations. But, the WD-LSTM seems to outperform the other two models while the ARIMA-ANN model is the least performing model. As expected, the ARIMA-ANN model seems to hardly catch the sudden changes in the original time series, while the WD-LSTM model seems to overcome this drawback. The application of DWT denoising to the data before it is pushed into the LSTM significantly improved the LSTM model.

For a comprehensive presentation, the three data-driven predictive models were examined using graphical demonstration of Taylor diagram, as displayed by Fig. 5(d-f). The Taylor diagram is informative as it assist by visualisation of the comparative strength of the models to the actual target variable. In the Taylor diagram, the two different statistical metrics (i.e., correlation coefficients and standard deviations of each model) are used to quantifying the comparability between the models and the actual data. The distance from the reference point is a measure of the RMSE. Based on the Taylor diagram representation presented in Fig. 5(d-f) for the three data-driven models used in this study, WD-

LSTM outperformed the other two models in all the study sites.

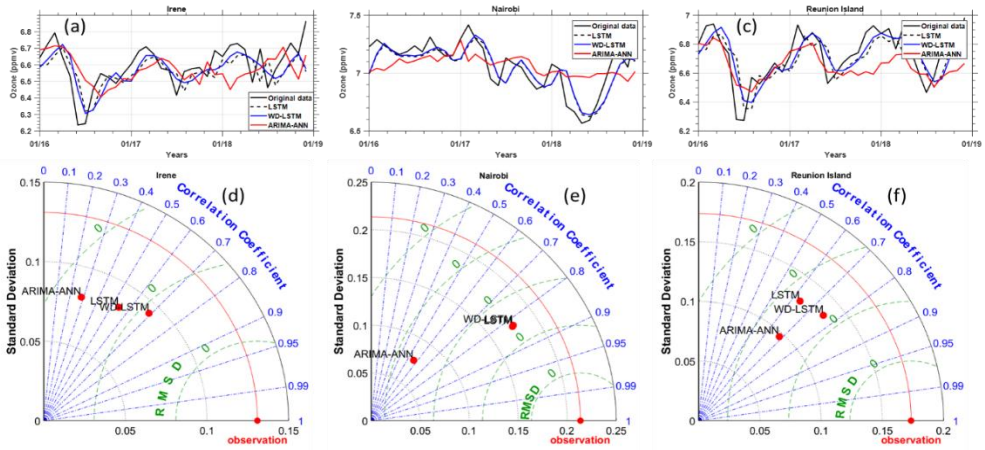

Figure 5. Testing sets and forecasts using LSTM, WD-LSTM, and Hybrid ARIMA-ANN for: (a) Irene, (b) Nairobi, and (c) Reunion Island. Taylor diagram graphical representation for the three models for: (d) Irene, (e) Nairobi, and (f) Reunion Island.

Conclusion

When investigating the trends of stratospheric ozone data used in this study, it was observed that there is a slow recovery of the ozone of approximately 0.18% - 0.20% per year for the study sites (Nairobi, Irene and Reunion Island).

It is acceptable that achieving reasonably accurate forecasts of time series is an important yet challenging task. However, this study has shown that denoising the time series before pushing them into the LSTM deep learning method enhance the model accuracy. The Hybrid ARIMA-ANN model which is a machine learning system seems to have failed to capture the nature of the time series compared to a deep learning LSTM method. Therefore, this study has also shown the superiority of deep learning methods when compared with machine learning methods.

Acknowledgements

This work is undertaken within the framework of the French-South Africa International Research Group LIA – ARSAIO (International Associated Laboratory – Atmospheric Research in Southern Africa and Indian Ocean) supported by CNRS and NRF and by the Protea program. The authors would especially like to thank the staff of the team working on the SABER measurements (http://saber.gats-inc.com/data.php).

References

Giles, C. L., Lawrence, S., & Tsoi, A. C. (2001). Noisy time series prediction using recurrent neural networks and grammatical inference. *Machine learning*, *44*(1-2), 161-183.

Ball, W. T., Alsing, J., Mortlock, D. J., Staehelin, J., Haigh, J. D., Peter, T., ... & Bourassa, A. (2018).

Evidence for a continuous decline in lower stratospheric ozone offsetting ozone layer recovery. *Atmospheric Chemistry and Physics*, *18*(2), 1379-1394.

Hochreiter, S., & Schmidhuber, J. (1997). Long short-term memory. *Neural computation*, *9*(8), 1735-1780.

Remsberg, E., Lingenfelser, G., Harvey, V. L., Grose, W., Russell III, J., Mlynczak, M., & Marshall, B. T. (2003). On the verification of the quality of SABER temperature, geopotential height, and wind fields by comparison with Met Office assimilated analyses. *Journal of Geophysical Research: Atmospheres*, *108*(D20).

Bègue, N., Mbatha, N., Bencherif, H., Loua, R. T., Sivakumar, V., & Leblanc, T. (2017). Statistical analysis of the mesospheric inversion layers over two symmetrical tropical sites: Réunion (20.8° S, 55.5° E) and Mauna Loa (19.5° N, 155.6° W). In *Annales Geophysicae* (Vol. 35, No. 6, pp. 1177-1194).

Khandelwal, I., Adhikari, R., & Verma, G. (2015). Time series forecasting using hybrid ARIMA and ANN models based on DWT decomposition. *Procedia Computer Science*, *48*, 173-179.

Liu, Y., Guan, L., Hou, C., Han, H., Liu, Z., Sun, Y., & Zheng, M. (2019). Wind Power Short-Term Prediction Based on LSTM and Discrete Wavelet Transform. *Applied Sciences*, *9*(6), 1108.

Rigby, M., Park, S., Saito, T., Western, L. M., Redington, A. L., Fang, X., ... & Fraser, P. (2019). Increase in CFC-11 emissions from eastern China based on atmospheric observations, *Nature*, *569*(7757), 546.

Zhang, G. P. (2003). Time series forecasting using a hybrid ARIMA and neural network model. *Neurocomputing*, *50*, 159-175.

Investigating the role of non-quasigeostrophic forcing during Cut-off low onsets over South Africa

Tsholanang S Rammopo and Thando Ndarana

Department of Geography Geoinformatics and Meteorology, University of Pretoria

*Corresponding author:

The roles of non-quasigeostrophic (NQG) forcing during three Cut-off low (CoL) onsets over South Africa (SA) were elucidated using an extended quasigeostrophic height tendency equation at 500hPa. Advection terms reflected a cohesive pattern preceeding CoL 2 (10 March 2019) onset which weakened thereafter when the advection of ageostrophic vorticity (Fv2) and the advection of absolute vorticity by the ageostrophic wind (Fv3) had opposing effects. The advection of geostrophic absolute vorticity (Fv1) was dominant during CoL 2 formation with the quasigeostrophic (QG) thermal advection (FT1) playing a similar but secondary role. Forcing time and area averages revealed that tilting (Ftilt) and horizontal divergence (Fdiv) consistently forced height falls and rises respectively. Poor forcing evolution average correlations between the CoLs were established while a possible implication on predictability is discussed briefly.

Keywords: Cut-off low, Diagnostics, Height tendency, Ageostrophic

Introduction

Hazardous high-impact weather events such as floods associated with Cut-off low pressure systems (CoLs) (Favre, 2013; Engelbrecht, 2015) as well as the increased frequency of occurrence of such weather systems over South Africa (SA) (Favre, 2013) suggest that considerable efforts have to be devoted to the development of forecasting tools that may add value to the forecasting process of such weather systems. Through the use of diagnostic equations, one can gain insight into the important aspects of the development of such extra-tropical systems as they unfold, in a qualitative and mostly approximate manner to complement the Numerical Weather Prediction (NWP) guidance (Nielsen-Gammon and Gold, 2006).

The quasigeostrophic (QG) theory (Bluestein, 1993; Holton, 2004) is often preferred in studies as opposed to finding solutions to the primitive equations due to its simplicity and ability to describe slow evolving synoptic waves in the mid-latitudes where the Rossby number is very small ($Ro<<1$) and linear wave theory is assumed (Andrews et al., 1987; Gall, 1977). However, several drawbacks of this framework are attributable to the assumptions made in the formulation of the theory, effectively hampering its utility. These include; the assumption that the horizontal wind is purely geostrophic, thus ignoring ageostrophic processes, the exclusion of diabatic processes and friction effects (Tsou et al., 1987; Colucci and Dong, 2015), collectively referred to as non-quasigeostrophic (NQG) forcing.

Indeed, owing to the imposed restrictions, several studies have found traditional QG diagnostics to be inadequate for the description of some extra-tropical and mid-latitude weather systems such as cyclones and blocking high pressure systems (Tsou et al., 1987; Colucci and Dong, 2015), giving rise to the need for the relaxation of some of the imposed assumptions, which extends the traditional QG equations.

Several extended forms of the QG height tendency equation have been derived and found to approximate the evolution of extra-tropical systems with improved accuracy as compared to their traditional form (Colucci and Dong, 2015; Tsou et al., 1987). These include the effects of NQG processes such as the horizontal wind (which also accounts for the ageostrophic wind) (Colucci and Dong, 2015; Lupo, 2001) in their formulation as well as a three dimensionally varying static stability parameter, which are not assumed in the traditional QG framework (Colucci and Dong, 2015; Tsou et al., 1987) while retaining the simplicity and usability the QG theory is known for.

The main objectives of this study were as follows; to diagnose CoLs over SA using an extended form of the QG height tendency equation, to assess the role of NQG forcing with particular interest on the ageostrophic wind related forcing during the onset of three CoLs as well as to establish and assess patterns relating to the terms in the NQG equation during the period preceding the onset of CoLs, which may inform aspects of predictability studies. The CoL events of interest were; the 10 August 2018, 10 March and 22 April 2019 events hereafter referred to as CoL1, 2 and 3 respectively.

Data and Methodology

The calculations were done using the 6 hourly 2.5□x 2.5□ grid resolution, with 17 pressure levels (1000hPa-10hPa) re-analysis dataset from the National Centre for Environmental Prediction (NCEP) for: air temperature, U and V horizontal winds, geopotential height and vertical velocity (omega) fields. Attention was focused on the 500 hPa level due to the growth in QG calculated geopotential tendency errors at higher tropospheric levels and the stratosphere (Colucci and Dong, 2015).

Basic variables such as □ are as described in (Holton, 2004), while terms appearing in Eq. (1) are defined as:

- **:** The geopotential height tendency,
- **FV1**: QG vorticity advection,
- **FV2**: Ageostrophic relative vorticity by the geostrophic wind,
- **FV3:** Absolute vorticity due to the ageostrophic wind,
- **FT1:** QG thermal advection term,
- **FT2:** Thermal advection due to ageostrophic wind,
- **Fageo:** Ageostrophic vorticity tendency,
- **Fvert:** Vertical advection of relative vorticity,
- **Fdiv:** Horizontal divergence term,
- **Ftilt:** Tilting term.

Eq. (1) (Colucci and Dong, 2015) was the chosen diagnostic on the basis of its consideration of ageostrophic processes and previous successful application in Southern Hemispheric (SH) Rossby Wave Breaking (RWB) studies such as blockings (which are associated with CoLs) (Colucci and Dong, 2015, Hoskins and Tyrlis, 2007, Ndarana and Waugh, 2010). This is important because of the extra-tropical location of SA, where departures from pure geostrophy can be expected. Onsets were defined as the first hour of the day (00z) of CoL onset for each events. The onset day was defined as the day of the first occurrence of the cut-off closed low pressure, following (Molekwa, 2013).

The onset region was defined as the region completely enclosing the west flank of the cyclone spanning at least 20□ latitudes and longitudes so as to include the area of maximum inward curvature characteristic of RWB to capture the behaviour of the terms during the evolution by calculating both area and time averages of the forcing terms during the evolution of each of the three CoLs. Onset regions (27.5º-47.5º S; 10 º W-15º E), (25º -45º S; 5º W-20º E) were defined for CoLs 1, 2, and 3 respectively (same region for CoLs 2 and 3).

All unknown variables appearing in Eq. (1) forcing terms were approximated numerically using finite differencing (central differentiation) in both the horizontal and verticals over 5 days prior and post onset) with zero upper and lower boundary conditions for the pressure levels. Each forcing term was computed separately so as to isolate and assess its individual contribution (forcing) to . This is warranted by the fact that for sinusoidal disturbances, the Laplacian of the function obtains a maximum value where the function is a minimum (Holton, 2004), resulting in Eq. (2). For purposes of visual interpretation, Eq. (2) was solved after calculations.

A 9-point averaging filter was applied to each grid point to produce smooth results. Furthermore, extreme outliers, defined for this study as those points with values two orders of magnitudes higher than its 8 surrounding members were removed and replaced by an interpolated value obtained by averaging 8 neighbouring points for each removed grid point.
The calculated area and time averages of the forcing terms were then used to produce time series plots for each CoL. To compare the association between the evolution of the three CoLs, each CoL time series was correlated linearly with the other two CoLs under investigation, for example, CoL 1 was correlated with CoL 2, then correlated with CoL 3 to produce three correlation coefficients.

Results

Forcing for for the three CoL events were calculated and compared against one another. Generally, all the terms displayed fairly similar behaviour during each of the three events, therefore only CoL 2 is extensively reported on. This is to avoid repetition, and due to the fact that CoL 2 has properties relating to both CoL 1 and CoL 2, e.g CoL 1 propagated zonally at a fairly consistent rate, while CoL 3 was quasi-stationary for some time after onset, while CoL 2 moved relatively slower as compared to CoL 1, but at an increased speed relative to CoL 3. Therefore, CoL 2 is considered as the average of the CoLs in this study.

Fig. 1 reveals the spatial distribution of Fv1 prior and during CoL 2 onset. This is the most prominent term at the 500 hPa level as found in previous studies (Colucci and Dong, 2015; Tsou, et al., 1987), while FT1 is at a maximum in the lower troposphere (not shown). For ease of interpretation of the terms, negative values coincide with height falls (< 0) while positive values represent height rises > 0). This indicates that Fv1 was the most influential term during CoL 2's life cycle. Prior to CoL 2 onset, terms: Fv1, Fv2, Fv3, FT1 and FT2 acted in cohesion as the mechanisms responsible for the north eastward

propagation (Fv1, Fv2 and Fv3) and intensification (FT1 and FT2) of the trough-ridge system through cold cyclonic advection on the west flank of the trough and warm anticyclonic vorticity advection on the east flank of the trough associated with height rises and falls respectively.

This is because the collocation of vorticity terms' (Fv1, Fv2 and Fv3) maxima and minima with the trough-ridge axes implies that vorticity does not contribute towards the intensification, therefore suggesting that it is responsible for system motion. Furthermore, zero thermal advection (FT1 and FT2) along the trough-ridge axes is associated with the intensification of the system (Holton, 2004).

Fig. 1 reveals the spatial distribution of Fv1 prior and during CoL 2 onset. This is the most prominent term at the 500 hPa level as found in previous studies (Colucci and Dong, 2015; Tsou, et al., 1987), while FT1 is at a maximum in the lower troposphere (not shown). For ease of interpretation of the terms, negative values coincide with height falls (< 0) while positive values represent height rises (> 0).

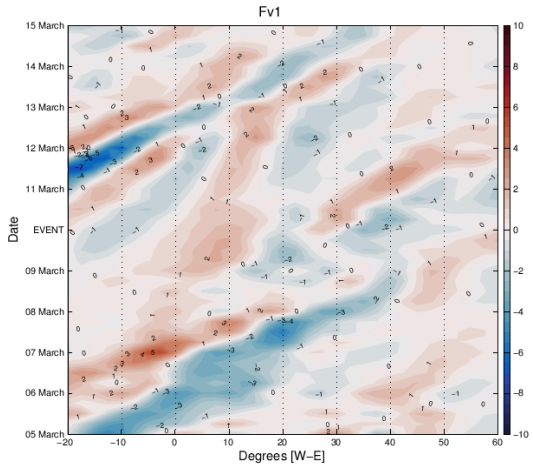

Figure. 1(a): Hövmöller diagram showing the evolution of Fv1 during and after CoL 2 averaged over region (20°- 40° **S**), units: $10^{15} \times s^{-2}$.)

This indicates that Fv1 was the most influential term during CoL 2's life cycle. Prior to CoL 2 onset, terms: Fv1, Fv2, Fv3, FT1 and FT2 acted in cohesion as the mechanisms responsible for the north eastward propagation (Fv1, Fv2 and Fv3) and intensification (FT1 and FT2) of the trough-ridge system through cold cyclonic advection on the west flank of the trough and warm anticyclonic vorticity advection on the east flank of the trough associated with height rises and falls respectively.

This is because the collocation of vorticity terms' (Fv1, Fv2 and Fv3) maxima and minima with the trough-ridge axes implies that vorticity does not contribute towards the intensification, therefore suggesting that it is responsible for system motion. Furthermore, zero thermal advection (FT1 and FT2) along the trough-ridge axes is associated with the intensification of the system (Holton, 2004).

The pattern persisted until the onset when Fv2 and Fv3 played opposing roles Figs. 2(a) and (b) as the magnitude of Fv1 decreased on both sides of the cyclone, having a net balancing effect on height changes as the CoL remained quasi-stationary, consistent with Godoy et al., (2011). The same pattern was observed for FT1 and FT2 (not shown).

Table. 1: Area averages of all forcing terms averaged over a 48 hour pre-onset period, Forcing units: 10^{15} x s^{-2}, units: 10^{3} m x $6h^{-1}$.

Forcing Term	CoL 1	CoL 2	CoL 3	Average
Fv1	1.0563	0.6155	0.9547	0.8755
Fv2	0.517	0.4039	0.3496	0.4235
Fv3	0.2697	0.422	0.3697	0.3538
FT1	0.2295	0.5961	-0.4517	0.124633
FT2	-0.6607	-0.3754	0.0219	-0.33807
Fageo	-0.1246	-0.0991	-0.1	-0.1079
Fvert	-0.5934	-0.6677	-0.2754	-0.51217
Fdiv	-0.1428	-0.2235	0.0064	-0.11997
Ftilt	0.4336	0.4734	0.1769	0.3613
Height Tendency	2.5531	2.2458	3.66	2.819633

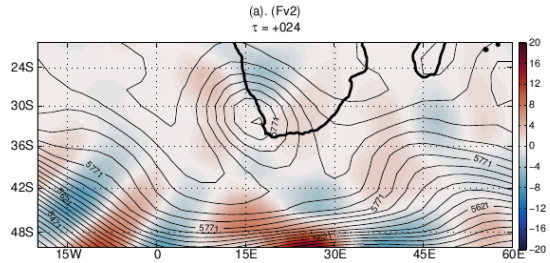

Figure. 2(a): 500 hPa geopotential heights (black contours) overlaid with Fv2 24 hours post CoL 2 onset at 00z, units: 10^{15} x s^{-2}.

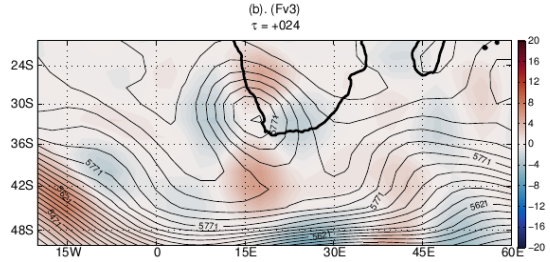

Figure. 2(b): 500 hPa geopotential heights (black contours) overlaid with Fv3 24 hours post CoL 2 onset at 00z, units: 10^{15} x s^{-2}.

Most notable of the NQG forcing is Fvert's persistent forcing towards height falls over the onset region 48 hours prior to onset followed by FT2 on average for

the three cases (Table. 1). In contrast, Ftilt was the leading positive term, persistently forcing height rises. Table. 1 also reveals a difference in behaviour between two classes of CoLs, those that remain quasi-stationary for a prolonged period of time (CoL 3), and those that propagate continuously (CoLs 1 and 2). FT1 contributes significantly towards height falls for quasi-stationary types while in contrast with the propagating type, FT2 and Fdiv contribute negligibly towards height rises.

Table. 2: Correlations (CoL1 and CoL2, CoL2 and CoL 3, etc) of the evolution of forcing terms during the 5-day pre-onset period.

Forcing Term	CoL 1+2	CoL 1+3	CoL 2+3	Mean
Fv1	0.7886	0.9602	0.7839	0.8442
Fv2	0.3217	0.1634	0.0548	0.1800
Fv3	0.3449	0.7528	0.4025	0.5001
FT1	0.1577	0.7033	0.0069	0.2893
FT2	-0.0928	0.3781	-0.0824	0.0676
Fageo	0.2333	0.1108	0.2797	0.2079
Fvert	0.0399	0.1084	-0.5466	-0.1327
Fdiv	0.0721	-0.1351	-0.2728	-0.1119
Ftilt	-0.1710	-0.2371	0.4216	0.0045

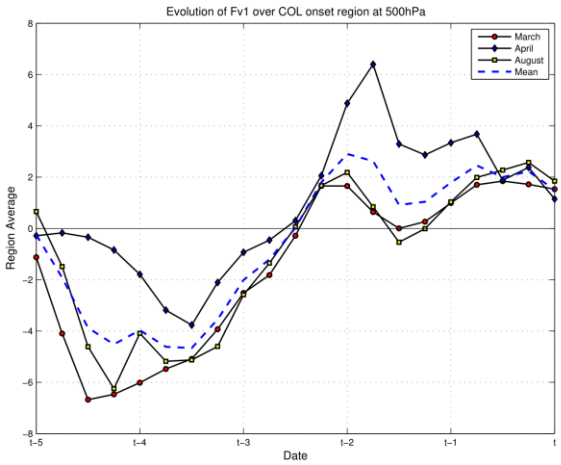

Figure. 3: A comparison of the evolution of Fv1 over the 5 day pre-onset period between the three CoLs.

Fig. 3 represents a consistent sinusoidal signature of Fv1 during the 5-day pre-onset period over the onset region for all three CoLs. High and positive average correlations were found for Fv1 and Fv3 between the three CoLs (Table. 2), the generally poor correlations being attributable to the variability shown by CoL 2. It is noteworthy that generally speaking, the forcing evolution patterns for the three CoLs reflect a similar structure, pattern and shape, however the lack of synchronicity between the patterns contributes negatively to the linear correlation. As part of the on-going CoL predictability studies, perhaps an issue of interest in light of the observed term evolution signatures could be related to the extent to which Ensemble Prediction Systems (EPS) can predict them.

It is worth noting that CoL 1, saw a largely negative contribution by Fv1, indicating significant anticyclonic vorticity advection over the onset region 5-days before onset. This may be due the fact that CoL 1 was not quasi-stationary as opposed to CoLs 1 and 2 which saw propagation mechanisms playing relatively smaller roles. In contrast with Fv1, Fvert together with FT2 (also in CoL 2) had consistent, large negative contributions during the period. In addition, in all the cases analysed, FT2, Fvert as well as Fdiv forced height falls over the onset region while the rest of the terms generally contributed positively.

Conclusion

Three CoL events were diagnosed over SA using an extended form of the QG geopotential height tendency equation (Colucci and Dong, 2015) in line with the objectives of this study. Consistent with previous studies, it is found that for the analyzed CoLs, QG advection processes (Fv1 and FT1) dominate trough-ridge development while NQG terms play occasional secondary roles. NQG equivalents assumed a complementary role to have a net influence on . The roles of NQG unrelated to advection were also analysed. Fvert and Ftilt contributed on average significantly towards height falls and rises over time in within the onset region. An evolution pattern of the forcing terms was established and found to be approximately consistent throughout the three CoLs which then then begs the question, how useful could the pattern be for predictability studies? The finding of the study serves as testament that there is some knowledge to be gained from the utility of simple, traditional diagnostics in research.

References

Andrews, D. G., Leovy, C. B., & Holton, J. R. (1987). *Middle atmosphere dynamics* (Vol. 40). Academic press.

Berrisford, P., Hoskins, B., & Tyrlis, E. (2007). Blocking and Rossby wave breaking on the dynamical tropopause in the southern hemisphere. *Journal of the Atmospheric Sciences*, *64*(8), 2881–2898.

Bluestein, H. B. (1993). *Synoptic-dynamic meteorology in midlatitudes. volume ii. observations and theory of weather systems*. New York, NY (United States); Oxford University Press.

Dong, L., & Colucci, S. J. (2015). The role of nonquasi-geostrophic forcing in southern hemisphere blocking onsets. *Monthly Weather Review*, *143*(4), 1455–1471.

Engelbrecht. (2016). *Dynamics of climate variability over the all-year rainfall region of South Africa* (Unpublished doctoral dissertation). University of Pretoria.

Favre, A., Hewitson, B., Lennard, C., Cerezo-Mota, R., & Tadross, M. (2013). Cut-off lows in the south africa region and their contribution to precipitation. *Climate dynamics*, *41*(9-10), 2331–2351.

Gall, R. (1977). Some non-quasigeostrophic effects in linear baroclinic waves. *Monthly Weather Review*,*105*(8), 1039–1051.

Holton, J. R. (2004). *An introduction to dynamic meteorology* (Vol. 41) (No. 5). AAPT.

Molekwa, S. (2013). *Cut-off lows over south africa and their contribution to the total rainfall of the eastern cape province* (Unpublished master's thesis). University of Pretoria.

Ndarana, T., & Waugh, D. W. (2010). The link between cut-off lows and rossby wave breaking in the south- ern hemisphere. *Quarterly Journal of the Royal Meteorological Society*, *136*(649), 869–885.

Tsou, C. H., Smith, P. J., & Pauley, P. M. (1987). A comparison of adiabatic and diabatic forcing in an intense extratropical cyclone system. *Monthly weather review*, *115*(4), 763-786.

Africanes, often unidentified but never to be underestimated

A closer look at how often these synoptic scale weather systems occur over southern Africa

Elizabeth M. Webster[1,2], Liesl L Dyson[2]

[1]South African Weather Service, Pretoria, 0001, South Africa
[2]Department of Geography, Geoinformatics and Meteorology, University of Pretoria, Pretoria 0001, South Africa

Corresponding author:

The atmospheric circulation over South Africa is generally dominated by extra-tropical weather systems. However, during the summer months, tropical weather systems track further south and contribute to the rainfall in the region. Due to the less frequent occurrence of tropical weather systems, they are often overlooked and sometimes not even identified. One such system is the Africane. Africanes are warm cored, synoptic scale low pressure systems that are unique to southern Africa This research demonstrates an objective identification method that can be used to recognize a tropical weather system that has received very little attention up to now.

Keywords: Rainfall, Synoptic Weather Systems, Climatology, Southern Africa, Flooding

Introduction

The tropics can generally be defined as the area positioned between the Tropic of Cancer (23.5˚N) and the Tropic of Capricorn (23.5˚S) (Asnani, 2005). South Africa is positioned such that the Tropic of Capricorn is situated over the north-eastern parts of the country, thus tropical weather systems often reach this region during the summer months (Dyson and van Heerden, 2002). Even though tropical weather systems do affect the Republic, the dominant weather systems are extra-tropical. Consequently, forecasters are very familiar with the forecasting of extra-tropical weather systems, but often lack the necessary experience to identify and forecast tropical weather systems.

The main tropical weather systems affecting southern Africa include tropical cyclones, tropical low pressures, tropical temperate troughs (TTTs) and the inter-tropical convergence zone (ITCZ). Taljaard (1994) defines the ITCZ as an area of low pressure that lies in close proximity to the equator. Harrison (1986) added that the location of the ITCZ has a major influence on the rainfall in southern Africa. The ITCZ is furthest south during late summer. During this time, there is often a low-level tropical/subtropical low pressure that extends a trough towards South Africa (Williams *et al.*,1984). This low pressure was named by Mulenga (1998) as the Angola low and defined by Reason *et al.,* (2006) as a shallow heat low situated over southern Angola/northern Namibia that starts to develop in October, strengthening by January and February.

Very limited research has been dedicated to tropical weather systems over southern Africa, except for the period between 1940 and 1970 known as the "golden period of African tropical meteorology" where a substantial amount of research was devoted to tropical and subtropical Africa (van Heerden and Taljaard, contributing to Karoly and Vincent, 1998). Even though there is limited research and understanding of tropical weather systems over Africa, they are notorious for the devastation they cause across southern Africa. The extreme amounts of rainfall associated with these systems often results in widespread flooding. During January 2017, one such system, a Continental Tropical Low pressure (CTL), which was not identified by forecasters, devastated parts of southern Africa (SAWS, 2018).

There has been very limited research dedicated to CTLs from a forecasting perspective with just a handful of documented work available (Taljaard, 1996; Dyson and van Heerden, 2002 and recently Webster, 2018). The only known similar weather system to exist elsewhere in the world, is found in Australia, where it is informally referred to as a landphoon (Tang *et al.,* 2016 and May *et al.,* 2008) or an agukabams (Emanuel *et al.,* 2008). Due to the exclusiveness of CTLs to southern African, they will henceforth be referred to as Africanes.

As such, this paper aims at highlighting the occurrence of Africanes over southern Africa by first explaining the identification process used to recognize Africanes and then creating a climatology over southern Africa. A brief look at the rainfall contribution of Africanes will demonstrate the significance of these weather systems. This paper also aims at increasing forecasters' awareness of these weather systems so that they can identify them timeously in future.

Data and Methodology

Using reanalysis data from the National Centers for Environmental Prediction (NCEP) (Kalnay *et al.*, 1996), Webster (2018) recently developed an identification method that objectively identifies Africanes over southern Africa. This method is broadly based on work done by Dyson and van Heerden (2002) who developed a Model for the Identification of Tropical weather Systems (MITS). While using MITS to identify tropical weather systems, the semi-permanent Angola Low pressure was frequently identified. Therefore, to identify Africanes and exclude the Angola Low, Webster (2018) uses four very strict criteria that consider the long term means. Engelbrecht *et al.*, (2013) stated that tropical low pressures have a scale of 500-1000 km, therefore NCEP reanalysis data (Kalnay *et al.*, 1996), will adequately be able to resolve these weather systems as the horizontal resolution is 2.5° (approximately 250km) with a vertical resolution of 17 levels. In addition, NCEP reanalysis data is available every 6 hours. NCEP is used here in the same way as previous work done on synoptic scale weather systems over South Africa (see Singleton and Reason, 2007; Malherbe et al., 2012; Favre et al., 2012, 2013; Engelbrecht et al., 2014).

The first criteria relates to classifying a favourable tropical area (FTE). This is done by identifying a grid point that meets the following conditions:

- Negative vorticity values need to exist at 850 and 500 hPa and be replaced by positive values at 300 hPa;
- Precipitable water values in the 850-300 hPa layer need to exceed 20 mm;
- Precipitable water values also need to exceed the long-term average for the particular month;
- The average 500-300 hPa temperatures need to be higher (warmer) than the average for that month;
- The average tropospheric total static energy values also need to be higher than the long-term average for that month;
- The negative vorticity values representing cyclonic circulation at 850 and 500 hPa is required to be stronger than the norm while the positive values at 300 hPa are required to be higher than the norm at this level for the particular month.

Once an FTE is recognised, the next criteria is two-fold and requires that a warm core (in the 500-300 hPa layer) and closed low (at 500 hPa) are identified and that they are within two grid points of each other. Once this is met, the low is now termed a warm low. Following this, the third criteria states that the FTE and warm low are within two grid points. If this is true, the low pressure is now called a warm FTE low. The fourth and final criteria is that two warm FTE lows exist within 18 hours of each other and are within two grid points. Once a certain grid points meets all these criteria, the position of the closed low pressure is used as the location of the Africane. Further fine tuning has taken place to take into account larger Africanes that extend over more than a single grid point. What this means is that if more than one Africane is identified at the same time step, the grid point closest to the average position of the Africanes is used as the location of the Africane and therefore only one Africane is counted at that time. This eliminates the possibility of a large Africane being counted multiple times.

Results

This study focuses on the summer months, December to March for the period December 1979 to March 2018 for the area over southern Africa, south of 15˚S. During this time, the identification method recognized 2346 events. This equates to roughly 587 Africane days (Africane events grouped in a 24-hour period with a possibility of 4 events being recognized per day) during the period and an average of 15 Africane days per year.

It is found that Africanes favour the extreme south-eastern parts of Angola (Fig. 1) with the occurrences decreasing rapidly southwards. Africanes are also found to occur more frequently over the eastern parts of southern Africa, with far less occurrences in the west. Over the South Africa region (area enclosed in a box in Fig. 1), the highest number of Africane occurrences is found in the extreme north-eastern part of the region (border of Limpopo Province and Mozambique). There is a steady decrease in events towards the south-western parts. The higher number of events in the north-east can be attributed to landfalling tropical cyclones that move eastwards over southern Africa and weaken, taking on Africane characteristics. The furthest south an Africane was found is occur is at 32.5˚, which only occurred once during this study period on 23 January 2011.

Africanes are found to occur most frequently in January (35.4%), followed very closely by February (34.4%) (Fig. 2). These results are similar to those found by Dyson *et al.*, (2015) who stated that during late summer months (January to March), the atmosphere over Gauteng transforms and becomes noticeably tropical. Almost equal number of Africanes occur during December and March months (Fig. 2).

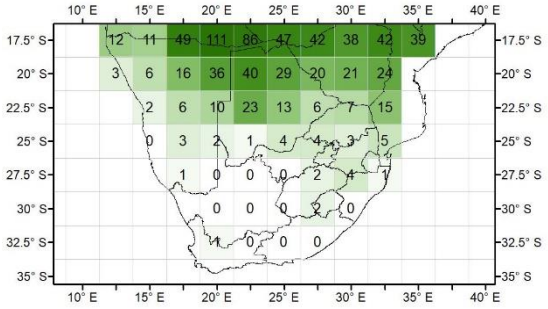

Figure 1: The total number of Africanes over southern Africa per grid point for December to March 1979-2017. 2346 events were identified in total. The area enclosed is referred to the South African region.

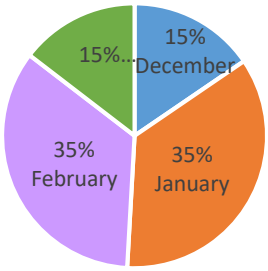

Figure 2: Percentage of occurrence of the total number of Africanes over the entire domain per month for 1979-2017.

The geographical distribution of Africanes over southern Africa varies slightly each month (Fig. 3). Africanes are confined to the extreme eastern and north-eastern parts of South Africa during December months (Fig. 3a). In January (Fig. 3b) there is a westward shift in the distribution and by February (Fig. 3c), Africanes occur over the northern parts of the Northern Cape. During March months (Fig. 3d), the least number of Africanes are found to occur in the east, however, there is a clear increase in the number of Africanes in the western parts of South Africa. This shift in the distribution between the months coincides with the westward movement of the 50 mm isohyet over South Africa during the summer months (Taljaard, 1996).

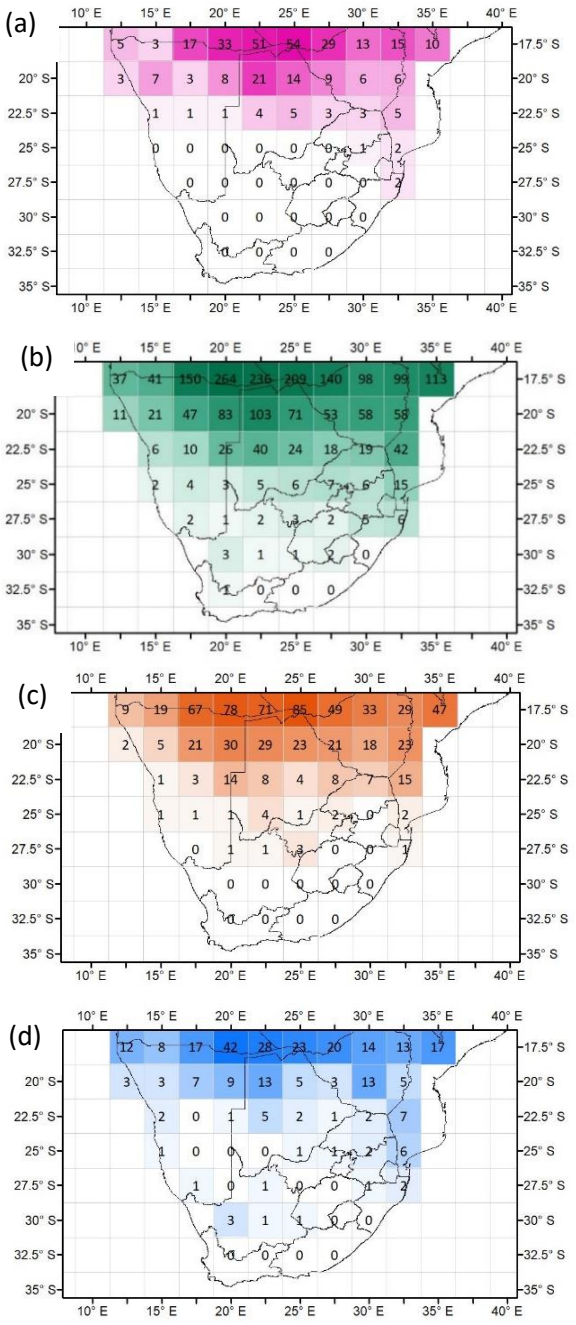

Figure 3: Geographical distribution of the total number of Africane events over southern African during the months (a) December, (b) January, (c) February and (d) March.

Contribution to rainfall
Using CPC rainfall data, the contribution Africanes have to rainfall over southern Africa is investigated.

CPC rainfall is a global unified gauge-based analysis of daily rainfall on a 0.5 by 0.5° resolution. The rainfall is available daily from 1979 to current and over 30 000 land based stations rainfall data is incorporated into the product (https://www.cpc.ncep.noaa.gov/). The rainfall for each Africane day is calculated and a composite map is presented in Figure 4. The results show that the highest rainfall amounts are generally located to the east of the position of the Africane (Fig. 4) with considerably less rainfall to the west with the south-west regions receiving the lowest rainfall.

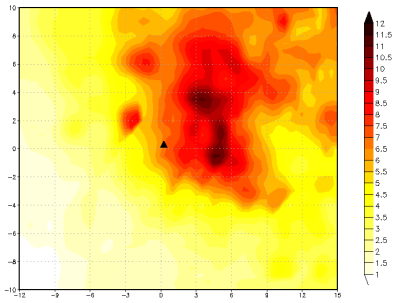

Figure 4: A composite average rainfall map showing the rainfall distribution around an Africane. The location of the Africane is in the centre of the image.

It is also found that topography plays a very important role, influencing rainfall amounts. As an example, figure 5 is the average rainfall for all events when the Africane was situated at 25 S and 27.5 E. The higher rainfall amounts can clearly be seen over the escarpment of South Africa and Zimbabwe.

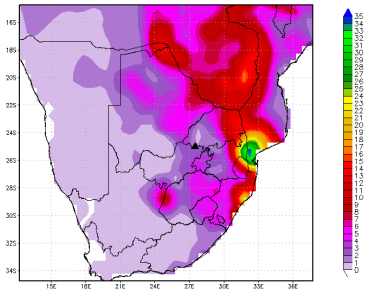

Figure 5: Average rainfall for all events when the Africane was located at 25 S and 27.5 E.

Conclusion
Africanes favour southern Zambia and Angola with a rapid decrease in number of events further southwards. Africanes also occur most frequently during January and February months. It is during March months, that Africanes extend over more of South Africa. The development of a climatology of Africanes over southern Africa, will create an increased awareness in the existence of these weather systems. Forecasters will therefore be able to confidently and accurately identify them. The rainfall distribution around an Africane has higher rainfall amounts to the east of the central Africane position, however topography can influence the location of the heaviest rainfall. This information is of vital importance to a forecaster, as an area of concern for heavier rainfall can easily be identified and kept a close watch on.

Acknowledgements
The authors of this research would like to thank the Water Research Council for providing the necessary funds to complete this research.

References
ASNANI GC (2005) Tropical Meteorology. Revised Ed. Pashan, Pune, India, Indian Institute of Tropical Meteorology, 1. ISBN 81-900400-7-3.

DYSON LL and VAN HEERDEN J (2002) A model for the identification of tropical weather systems over South Africa. Water SA, 28(3), pp. 249-258.

DYSON LL, VAN HEERDEN J and SUMNER (2015) A baseline climatology of sounding-derived parameters associated with heavy rainfall over Gauteng, South Africa. *International Journal of Climatology*, 35, pp. 114-127. doi:10.1002/joc.3967

EMANUEL K, CALLAGHAN J and OTTO P (2008) A Hypothesis for the Redevelopment of Warm-Core Cyclones over Northern Australia. American Meteorological Society. DOI: 10.1175/2008MWR2409.1

ENGELBRECHT CJ, ENGELBRECHT FA and DYSON LL (2013) High resolution model projected changes in tropospheric closed-lows and extreme rainfall events over southern Africa. International Journal of Climatology, 33(1), pp. 173-187.

ENGELBRECHT CJ, LANDMAN WA, ENGELBRECHT FA and MALHERBE J (2014) A Synoptic Decomposition of Rainfall over the Cape south coast of South Africa. Clim. Dynamics. DOI 10.1007/s00382-014-2230-5

FAVRE A, HEWITSON B, TADROSS M, LENNARD C and CEREZO-MOTA R (2012) Relationships between cut-off lows and the semiannual and southern oscillations. Clim. Dynamics 38, pp. 1473–1487. 95

FAVRE A, HEWITSON B, LENNARD C, CEREZO-MOTA R and TADROSS M (2013) Cut-off lows in the South Africa region and their contribution to precipitation. Clim. Dynamics 41, pp. 2331–2351.

HARRISON MSJ (1986) A synoptic climatology of South African rainfall variations. Unpublished PhD Thesis. University of the Witwatersrand, 341pp.

KALNAY E and co-authors. (1996) The NCEP/NCAR 40-year reanalysis project, Bulletin of the American Meteorological Society 77:437-470. DOI:http://dx.doi.org/10.1175/1520-0477 (1996)077<0437:TNYRP>2.0.CO;2

KAROLY DJ and VINCENT DG (1998) Meteorology of the Southern Hemisphere 27 (49). *American Meteorological Society*. Boston. 410pp.

MALHERBE J, ENGELBRECHT FA, LANDMAN WA and ENGELBRECHT CJ (2012) Tropical systems from the southwest Indian Ocean making landfall over the Limpopo River Basin, southern Africa: a historical perspective. International Journal of Climatology DOI: 10.1002/joc.2320.

MAY PT, MATHER JH, VAUGHAN G, JAKOB C, MCFARQUAR GM, BOWER KN, MACE GG (2008) The tropical warm pool international cloud experiment. *American Meteorological Society*. DOI:10.1175/BAMS-89-5-629

MULENGA HM (1998) Southern African Climatic Anomalies, Summer Rainfall and the Angola Low. Dissertation, University of Cape Town, South Africa.

REASON CJC, LANDMAN W and TENNANT W (2006) Seasonal to Decadal Prediction of Southern African Climate and its Links with Variability of the Atlantic Ocean. *Bulletin American Meteorological Society*, 87, pp. 941-955.

SINGLETON AT and REASON CJC (2007) Variability in the characteristics of cut-off low pressure systems over subtropical southern Africa. International Journal of Climatology, 27, pp. 295–310.

SOUTH AFRICAN WEATHER SERVICE (2018) Climate Summary of South Africa, January 2017. ISSN 1992-2566. Volume 28, No.1.

TALJAARD JJ (1994) Atmospheric Circulation Systems, Synoptic Climatology and Weather Phenomena of South Africa. Part 1 Controls of the Weather and Climate of South Africa. *South African Weather Service Technical Paper*, 27, South African Weather Service, Private Bag X97, Pretoria, 0001. 45pp.

TALJAARD JJ (1996) Atmospheric Circulation Systems, Synoptic Climatology and Weather Phenomena of South Africa. Part 6 Rainfall in South Africa. *South African Weather Service Technical Paper*, 32, South African Weather Service, Private Bag X97, Pretoria, 0001. 98pp

TANG S, SMITH RK, MONTGOMERY MT, GU M (2016) Numerical study of the spin-up of a tropical low over land during the Australian Monsoon. *Royal Meteorological Society. 142:2021-2032.* DOI:10.1002/qj.2797

WEBSTER EM (2018) A synoptic climatology of Continental Tropical Low pressure systems over southern Africa and their contribution to rainfall over South Africa. Unpublished M.Sc. Dissertation, University of Pretoria, South Africa.

WILLIAMS FR, RENARD RJ, JUNG GH, TIMKINS RD and PICARD RR (1984) Forecasters Handbook for the Southern African Continent and Atlantic/Indian Ocean Transit. Department of Meteorology Naval Postgraduate School. Monterey, California

A New User-Orientated Severe Weather Warning System for South Africa

Elizabeth M. Webster[1,2], Kate Turner[1]

[1]South African Weather Service, Pretoria, 0001, South Africa
[2]Department of Geography, Geoinformatics and Meteorology, University of Pretoria, Pretoria 0001, South Africa

*Corresponding author:

The South African Weather Service in collaboration with the National Disaster Management Centre are in the final stages of developing and implementing a new weather warning system for the country. This warning system will completely change the conventional threshold-based warnings into colour-coded warnings that are easier to understand. Pilot phases have been used to test the warnings in real time and to fine-tune the warning process with disaster managers only. The feedback received from the disaster managers has been extremely positive thus far.

Keywords: Severe Weather, Impacts, Warnings, Impact-Based Warning System

Introduction

The forecasting of severe weather hazards has improved significantly over the past few years, however an accurate and timely warning does not guarantee the safety of life (WMO, 2015). Severe weather related hazards frequently occur over South Africa. It is when this severe weather has negative impacts that disasters occur. The extent of the impact is dependent on the vulnerability of the affected area with certain areas being more vulnerable to a certain weather hazard than others.

Currently the South African Weather Service (SAWS) issues warnings based on meteorological thresholds. As such once the weather conditions are expected to meet the specific threshold criteria, a warning is issued, without considering the vulnerability of the area affected. The general public have difficulty in understanding these threshold based warnings. For example, the general public struggle to relate to a gale force wind warning of 70 km h^{-1}, as they do not understand what this means.

There is a need for the warnings to be useful, concise and easy to understand. Internationally this has also been noticed by other meteorological institutions and consequently the World Meteorological Organisation (WMO) has started a movement to promote severe weather warnings to be impact-based. Weather related warnings need to evolve from *what the weather will be* to *what the weather will do*.

SAWS together with the National Disaster Management Centre (NDMC) have embarked on developing and implementing an Impact-Based (ImpB) Severe Weather Warning System (SWWS) for South Africa. The main focus of this ImpB SWWS is to change the focus of the early warning service from a weather prediction to a people-centred risk prediction, which is tailored to South African conditions.

This multi-year project, included the hosting of stakeholder workshops with disaster managers from Provincial and District level from across the country. At these workshops, the concept of the ImpB SWWS was explained and input provided by the disaster managers was included in the system. This warning system is a completely different approach for forecasters and requires a paradigm shift in the way the warnings are dealt with, as such all the forecasters also underwent training.

Impact-Based Severe Weather Warning System

The ImpB SWWS combines the severity level of the impact with the likelihood of the impact occurring (Fig. 1). The impact levels are determined in conjunction with the local disaster managers, thus making this a joint warning.

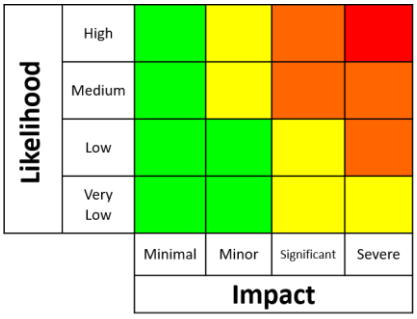

Figure 1: Warning Risk Matrix showing the combination of the impact levels on the horizontal axis with the likelihood on the vertical axis.

Pilot phases started at SAWS head office in 2016 with the issuing of ImpB warnings for Gauteng for the summer season. Since then the pilot phases have extended across the remainder of the country and will

continue until the ImpB SWWS is operational. Through these pilot phases the new warning system is thoroughly tested.

Lesson learnt

In June 2017, an intense cut-off low pressure which notoriously became known as the #CapeStorm affected the Cape provinces. Gale force winds reaching strong gale force (64-87 km h^{-1}) were expected across most parts of the Western Cape during #CapeStorm, however an additional sensitivity that was initially not completely accounted for was the possibility of runaway fires. On Tuesday 6 June 2017, winds started picking up and small fires in the Knysna area quickly became out of control and caused widespread devastation along the Cape south coast.

More recently, in June 2019, a cold front was expected to move over the Western and Eastern Cape resulting in strong to gale force winds (64-87 km h^{-1}) along the coast as well as over the interior. This proved to be a perfect opportunity to once again test the effectiveness of the new warning system.

Case Study: 21-22 June 2019

Throughout the pilot phase, each forecasting office issues an outlook to the local disaster managers every Monday for the upcoming week. This is to provide an indication to the disaster managers on any potential hazardous weather. The Cape Town and Port Elizabeth forecasting offices issued the weekly outlooks on Monday 17 June 2019. In these outlooks, there was no mention of the possible intense cold front, but it was mentioned that strong north-westerly winds were expected on Friday. However, later on in the week, the Numerical Weather Prediction (NWP) models started showing signs of a severe cold front making landfall over the south-western Cape on Friday 21 June 2019.

Numerical Weather Prediction Models

Each day that week leading up to the event, the NWP's projection of the cold front intensified, whereby higher wind speeds and rainfall amounts were anticipated. Consequently, warnings were issued from Wednesday, 19 June 2019.

The cold front, supported by a steep upper air trough, was projected to develop into a cut-off low pressure system late on Friday. What made this cold front so unique and intense was the central position of the low pressure that was expected to pass unusually close to the South African south coast. This resulted in extreme wind conditions ahead of the cold front over the Western, Northern and Eastern Cape as well as off the south-west coast and later, along the south coast. Also associated with this front were very rough sea conditions and possible storm surge.

Heavy downpours were possible with the passage of the front during Friday afternoon and into the next morning which could lead to flooding and flash flooding in areas. Accumulated rainfall expected from the Friday afternoon over the south-western parts of the Western Cape were between 20-30mm reaching 40-60mm over the western mountain ranges.

Relating to winds, strong to gale force and gusting winds (50-70 km h^{-1}) were expected over most of the Western Cape interior however reaching 80-100kmh^{-1} during the Friday afternoon and evening. Off the south-west coast, gale to strong gales of 65-80kmh^{-1} reaching 100-120 km h^{-1} were anticipated throughout the afternoon and into the evening. These north-westerly winds were projected to swing south-westerly early on Saturday morning.

Significant wave heights generated in the deep sea were expected to be between 6-9m along the Western Cape south-west coast during Friday night and Saturday morning. These swells were to spread along the south coast, but drop to 5-6 m. The high wave heights and strong onshore winds would aid in pushing water further up the beachfront resulting in possible storm surge. Additionally, the storm coincided with the winter solstice, subsequently resulting in spring tides. It would thus be around high tide times where the most damage was possible.

Impact-Based Severe Weather Warnings Issued

The first ImpB warning was issued on Wednesday 19 June 2019 for most of the Western Cape and western parts of the Eastern Cape. The anticipated hazard was winds where significant impacts were expected. Warnings relating to rain impacts as well as coastal winds and waves were also issued on the Wednesday. On Thursday 20 June, once the NWP models were more in agreement with their prognoses, a number of warnings were upgraded to include severe impacts for wind (Fig. 2). These warnings were valid for the 21st and 22nd of June. Yellow and orange warning levels (Fig. 2), were issued for wind (over the interior), rain, rough seas, storm surge as well as coastal winds.

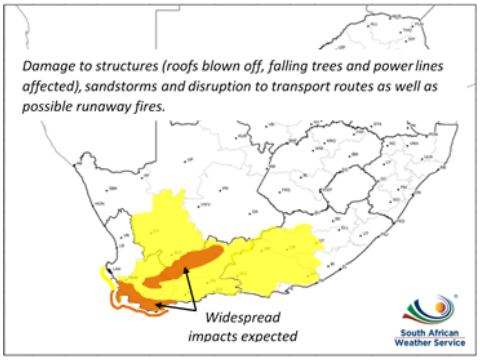

Figure 2: Graphical display of the new ImpB warning for wind issued on Thursday 20 June, valid for Friday 21 to Saturday 22 June 2019. Severe impacts indicated in orange and significant impacts in yellow.

The hazard that was the main cause for concern were the strong winds. The impacts that were expected as a result of the winds were damage to structures with the possibility of roofs blowing off, trees and power lines falling and blocking roads. This could then also result in transport routes being disrupted. Sandstorms were also likely to cause traffic disruption. The possibility of runaway fires was also highlighted as a risk and in an attempt to prevent history repeating itself, in relation to the infamous #CapeStorm, the local disaster managers were contacted and alerted to the possibility of active fires becoming uncontrollable and rapidly spreading. It was advised that if there were any active fires, these needed to either be extinguished or closely monitored. The disaster managers confirmed that measures had been taken to prevent any runaway fires and had also put a ban in certain areas on fire breaks being conducted. These possible impacts were captured within the ImpB warning issued.

Communication with Disaster Management

The set-out procedure regarding the ImpB SWWS, agreed upon with disaster management is that once any orange (or red) warnings are considered, the Provincial Disaster Management Centre (PDMC) has to be contacted telephonically. The expected weather conditions and possible impacts were discussed, and an agreement reached with regards to warning levels. These warnings were thereafter compiled and issued. This telephonic communication allowed disaster managers to have an early indication before the warnings were issued. They were then able to call an emergency meeting to discuss the required measures to be put in place.

Summarised warnings were also sent to disaster managers via an instant messaging application, WhatsApp, for immediate access to weather warnings even if they are in the field. For this particular case, disaster managers contacted the Cape Town office early on Friday morning for clarity regarding the warnings and for an update in the expected conditions. The two way communication is vital for the success of this new warning system.

Weather updates were sent via the WhatsApp platform on the day of the event and disaster managers provided feedback of impacts using situation reports, via the same platform.

Actual Conditions and Impacts

As the front passed over the Western Cape, rainfall set in from late afternoon on Friday, 21 June 2019. The frontal band and rainfall spread further inland overnight and over most of the Western Cape and western parts of the Northern Cape by the Saturday morning. However, the bulk of the rainfall accumulations were confined to the western mountain ranges of the Western Cape. The highest rainfall accumulations for the 21-22 June 2019 are depicted in Table 1.

Table 1: Selected stations rainfall (mm) accumulation for the period 21 to 22 June 2019.

Rainfall (mm)	**Total**
Stellenbosch	**76.4**
Kirstenbosch	**56.6**
Ceres	**44.6**
Molteno	**42.0**
Moreesburg (Langewens)	**31.6**
Elgin Grabouw	**28.6**

Although heavy downpours did occur, the strong and gusty winds were of higher concern. Even though slightly delayed in timing, these winds did materialise and at times even exceeded 100kmh^{-1} gusts along the coastal areas as well as in places over the Western Cape interior (Fig 3). Even though the average winds were weaker than expected, generally between 40-70 km h^{-1}, the gusts did the most damage. The gusts reached between 50-90 km h^{-1} with certain areas such as along the south-west coast (Cape Point, Slangkop and parts in the City of CapeTown) reaching between 90-130 km h^{-1}. Over the interior, areas such as Worcester and Ladismith also reached gusts between 90-110 km h^{-1}.

According to reports from disaster management and various social media platforms several roofs were blown off, trees blown over, damaging formal and informal structures as well as pulling electricity lines down. Numerous areas across the City of Cape Town were without power for few days after the storm. A number of settlements were damaged and residents displaced. Severe rock falls occurred on the

Franschhoek Pass, significantly damaging two cars and resulting in the closure of the Pass. A severe sandstorm occurred on the R321 between Grabouw and Villiersdorp, leaving cars stranded and the closure of the road.

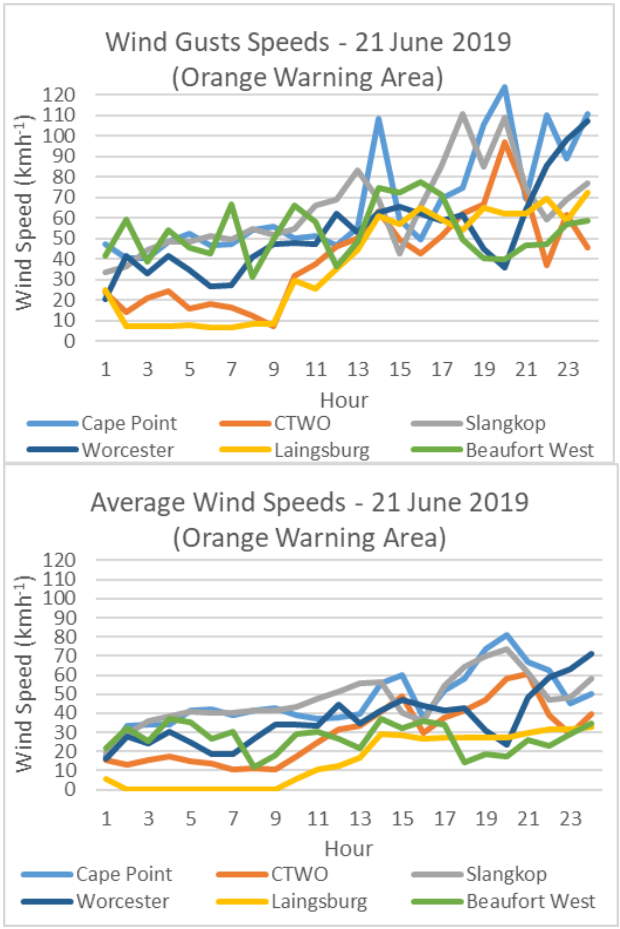

Figure 3: Graphs showing the average wind speeds (top) and wind gusts (bottom) of selected stations across the Western Cape on Friday 21 June 2019.

Verification of Warnings

In order to improve the warnings issued, each warning is verified by the local disaster managers. Since this is a very subjective method, work is currently also being done on finding ways to verifying these warnings objectively. The warnings are also verified using reports gathered through various media platforms, in order to determine whether the expected impacts actually did occur. Once the warning system is operational, verification will also be done by conducting surveys with the general public.

For this particular weather event, the feedback received from disaster managers indicated that warnings were mostly accurate, issued timeously and well communicated through the various platforms. However, warnings could have been clearer relating to the inclusion of more specific areas. The general consensus is that the ImpB SWWS is more user-friendly and an improvement to the threshold based warning system.

Conclusion

The development of an ImpB SWWS will result in a people-centred service delivery of severe weather warnings for South Africa. The message that disaster managers as well as the general public will receive will be more relevant and straight forward with less meteorological jargon. This should result the appropriate actions taken in order to mitigate the adverse effect of hydro-meteorological hazards.

This case study of the severe cold front that occurred during 21-22 June 2019, showed that two-way communication with disaster management is key. This case also shows that this warning system is feasible and valuable.

Acknowledgements

The authors of this research would like to thank the South African Weather Service for providing the time to compile this case study. The continuous support and collaboration with national, provincial and municipal disaster management is also very much appreciated.

References

World Meteorological Organisation (2015) WMO guidelines on Multi-hazard Impact-based Forecast and Warning Services. WMO-No. 1150, ISBN 978-92-63-11150-0